MINERAL SNOWFLAKES ON EXOPLANETS AND BROWN DWARFS

Dominic Bartholomew Singh Samra

University of
St Andrews

This thesis is submitted in partial fulfilment for the degree of

Doctor of Philosophy (PhD)

at the University of St Andrews

2022

"Aux yeux de ces amateurs d'inquiétude et de perfection, un ouvrage n'est jamais achevé, - mot qui pour eux n'a aucun sens, – mais abandonné"

Translation: In the eyes of those who anxiously seek perfection, a work is never truly completed - a word that for them has no sense - but abandoned

- Paul Valéry, *"La Nouvelle Revue Française"*, 1933

Declaration

Candidate's declaration I, Dominic Bartholomew Singh Samra, do hereby certify that this thesis, submitted for the degree of PhD, which is approximately 36,200 words in length, has been written by me, and that it is the record of work carried out by me, or principally by myself in collaboration with others as acknowledged, and that it has not been submitted in any previous application for any degree. I confirm that any appendices included in my thesis contain only material permitted by the 'Assessment of Postgraduate Research Students' policy.

I was admitted as a research student at the University of St Andrews in September 2018.

I received funding from an organisation or institution and have acknowledged the funder(s) in the full text of my thesis.

Date   25/03/2022   Signature of candidate

Supervisor's declaration

I hereby certify that the candidate has fulfilled the conditions of the Resolution and Regulations appropriate for the degree of PhD in the University of St Andrews and that the candidate is qualified to submit this thesis in application for that degree. I confirm that any appendices included in the thesis contain only material permitted by the 'Assessment of Postgraduate Research Students' policy.

Date   25/03/2022   Signature of supervisor

Permission for publication

In submitting this thesis to the University of St Andrews we understand that we are giving permission for it to be made available for use in accordance with the regulations of the University Library for the time being in force, subject to any copyright vested in the work not being affected thereby. We also understand, unless exempt by an award of an embargo as requested below, that the title and the abstract will be published, and that a copy of the work may be made and supplied to any bona fide library or research worker, that this thesis will be electronically accessible for personal or research use and that the library has the right to migrate this thesis into new electronic forms as required to ensure continued access to the thesis.

I, Dominic Bartholomew Singh Samra, confirm that my thesis does not contain any third-party material that requires copyright clearance.

The following is an agreed request by candidate and supervisor regarding the publication of this thesis:

Printed copy

No embargo on print copy.

Electronic copy

No embargo on electronic copy.

Date   25/03/2022   Signature of candidate
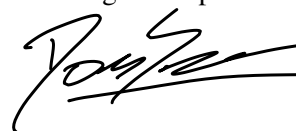
Date   25/03/2022   Signature of supervisor

Underpinning Research Data or Digital Outputs

Candidate's declaration

I, Dominic Bartholomew Singh Samra, understand that by declaring that I have original research data or digital outputs, I should make every effort in meeting the University's and research funders' requirements on the deposit and sharing of research data or research digital outputs.

Date   25/03/2022   Signature of candidate

Permission for publication of underpinning research data or digital outputs

We understand that for any original research data or digital outputs which are deposited, we are giving permission for them to be made available for use in accordance with the requirements of the University and research funders, for the time being in force.

We also understand that the title and the description will be published, and that the underpinning research data or digital outputs will be electronically accessible for use in accordance with the license specified at the point of deposit, unless exempt by award of an embargo as requested below.

The following is an agreed request by candidate and supervisor regarding the publication of underpinning research data or digital outputs: No embargo on underpinning research data or digital outputs.

Date   25/03/2022   Signature of candidate

Date   25/03/2022   Signature of supervisor

"Je n'ai fait celle-ci plus longue que parce que je n'ai pas eu le loisir de la faire plus courte."
Translation: I have made this longer than usual because I have not had time to make it shorter.

- Blaise Pascal, *Lettres Provinciales*, 1657

Abstract

The diversity of exoplanets and brown dwarfs provides ideal atmospheric laboratories to investigate novel physico-chemical regimes. Furthermore, the atmospheres of exoplanets act as the history books of planetary system. However, as observational data improves, the contributions of cloud particles in exoplanet and brown dwarf atmospheres must be adequately accounted for. Microphysical modelling of cloud formation provides the best method to investigate the potentially observable properties of clouds in these atmospheres. Most observed gas-giant exoplanets have been suggested to host mineral clouds which could form 'snowflake-like' structures through condensation and constructive collisions. Cloud particle porosity, size and number density are influenced by constructive and destructive collisions. In this thesis, we expand our kinetic non-equilibrium cloud formation model to explore the effects of non-compact, non-spherical cloud particles on cloud structure and their spectroscopic properties. Additionally, we investigate the effects on clouds of collisional growth and fragmentation. The impact of these affects is assessed on prescribed 1D (T_{gas}-p_{gas}) profiles in DRIFT-PHOENIX model atmospheres of brown dwarfs and exoplanets. We utilise Mie theory and effective medium theory to study cloud optical depths, where we additionally represent non-spherical cloud particles with a statistical distribution of hollow spheres. We find that micro-porosity can affect the distribution of cloud particles in an exoplanet atmosphere, and that irregular particle shape impacts the optical depth in the near- and mid-infrared. However, we also find that cloud particle collisions driven by turbulence result in fragmentation of cloud particles for exoplanet atmospheres, which also impacts optical depths in the optical and mid-infrared regions. The global distribution and properties of clouds is also important as observations begin to allow for treating exoplanets in their full 3D nature. We therefore apply a hierarchical approach to global cloud formation modelling. We also apply our 1D cloud formation model to profiles extracted from results of 3D General Circulation Models (GCM) for the gas-giant exoplanet WASP-43b and the ultra-hot Jupiter HAT-P-7b, revealing a dramatic difference in the distribution of clouds between these types of exoplanets as a result of stellar radiation heating the day-side of the ultra-hot planets. This results in an asymmetry in cloud structures for the terminators of WASP-43b and more significantly for HAT-P-7b, observable in the optical depth of the clouds at these points, further complicating retrieval of cloud properties from spectra.

"All of us have special ones who have loved us into being. Would you just take, along with me, ten seconds to think of the people who have helped you become who you are. Those who have cared about you and wanted what was best for you in life. Ten seconds of silence."

- Fred Rogers, Daytime Emmy Awards, 1997

Acknowledgements

I dedicate this thesis to my grandparents; Mohan Samra, Gurmit Samra, John Firth and Gladys Firth. Without whose many sacrifices I would not be in the privileged position to pursue my dreams and ambitions, and who I wish dearly were all still here to share in this achievement.

To my family: your love, care and support has gotten me through these - at times particularly tough - past three and a half years. Dad, thank you for your determination, dedication, and drive. Without your passion for academic excellence, I undoubtedly wouldn't have endeavoured in a career in academia. It also helped that you had a habit of taking Ben and I to the Science Museum in London as children (I suspect for the free child care)! I'm sorry, the 'rocket hall' was just that much cooler than the medical exhibits. Mum, you have always given me the permission to pursue whatever I found most interesting, for that I am eternally grateful. After all these years I am still just trying my best and being happy and I don't think it's possible to forget your love for me. Especially not whenever you spell check my work, or when you are sending me endless travel updates. Ben and Daisy, thank you for always being at the end of a phone to chat about just about anything and everything I wanted to talk about, and for putting up with my ramblings. You're my two closest friends, no matter how many miles separate us.

I would be horribly remiss if I did not next express my deepest gratitude to my supervisor Christiane Helling. Thank you for your endless patience and for all the opportunities you have provided me. I look very much forward to continuing on in our collaboration together and I cannot wait to see where it takes us. My sincere thanks also to Peter Woitke and Martin Dominik for their detailed discussion and help with research problems in group meetings and beyond. I would also like to also thank the summer and Masters students who joined the group throughout the years for your interesting science and your endless enthusiasm.

Next I must thank all the friends and colleges who have helped me during my PhD. Thank you to Carl, Chris, Original Dom, and all the Staff in the School of Physics and Astronomy for making me feel so welcome at St Andrews from the moment I arrived. Thank you to Elliot, Camilo (my Lord), Fran, Juan, Meng, Nicole, Tatiana, Tom, and Yiuri for the company at Friday Lunches in BrewCo, or the evenings in BrewCo. Thank you to the Cupar Crew: Sam, James, Alistair, and Kristin, you were essential at times to my sanity, with the winter walks along the

Eden and the BBQs in the summer. Thank you to the CHAMELEONs and associates: Emma, Helena, J.P., Thorsten, Till (Steven), and Sandra, who joined the group in St Andrews in the midst of a particularly dour global situation and added a considerable amount of colour. May your drives always find the fairway wherever in the world you find yourself. I also thank all those at the IWF who made a very out of place Brit feel at home in Austria.

Finally, saving best until last. An immense thank you to the rest of the 'Holy Trinity' Oliver and Patrick, thank you for sharing in all the tribulations and triumphs, the drinks to every paper submission (and re-submission), and your patience while I take far too long to play a card in Skat. Patrick, thank you for hosting me on so many occasions after a Luvians tasting, or after EuroVision, for the delicious bread and other baking goodies. Oliver (LaTeX-google), it has been a heck of a few years! From the first weeks and Cloud Academy, until writing up this very thesis, thank you for your support and your optimism. By the way, did I also mention there may have been a few drinks here or there? Here's to many more years of success in academia, if our livers can handle it.

General acknowledgements
Funding

"Out of the cradle
onto dry land
here it is
standing:
atoms with consciousness;
matter with curiosity.

Stands at the sea,
wonders at wondering: I
a universe of atoms
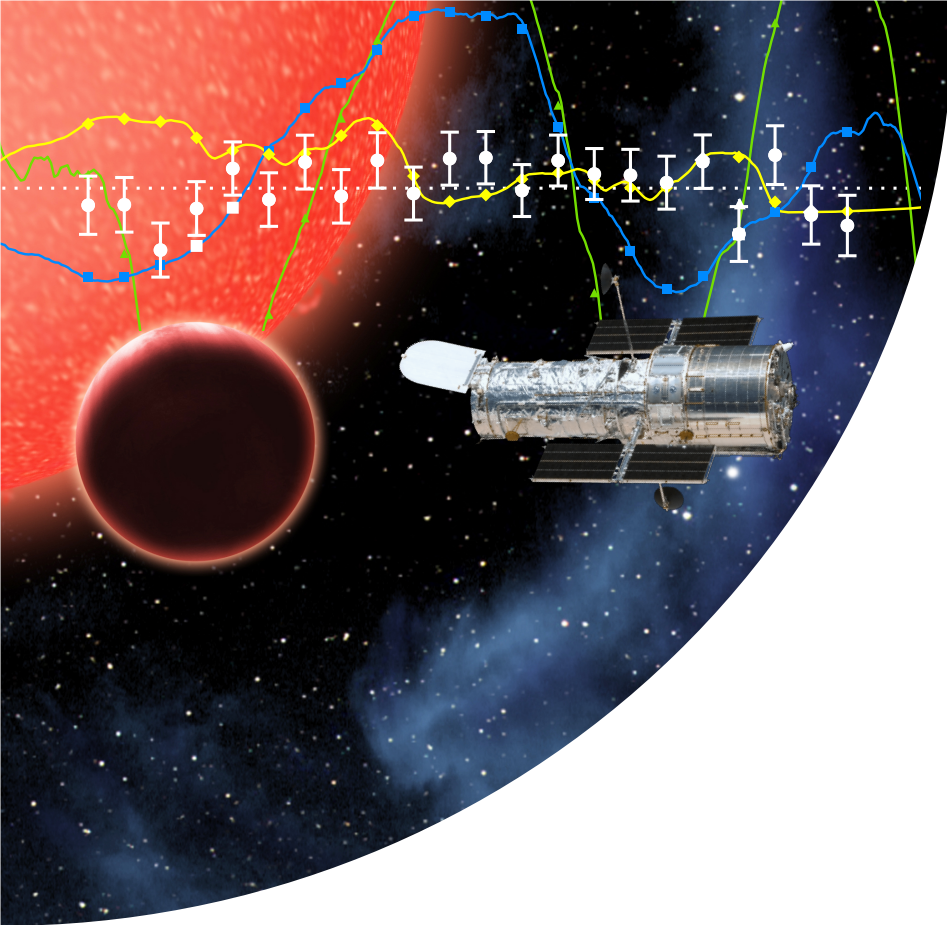*an atom in the Universe."*

        - Richard Feynman

Contents

"Tiger got to hunt, bird got to fly;

Man got to sit and wonder 'why, why, why?'

Tiger got to sleep, bird got to land;

Man got to tell himself he understand."

\- Kurt Vonnegut, *Cat's Cradle*, 1963

1

Introduction

1.1 Declaration

This chapter includes original text as well as material adapted from two publications:

- 'Mineral snowflakes on exoplanets and brown dwarfs: Effects of micro-porosity, size distributions, and particle shape', Samra, D., Helling, Ch., Min, M. 2020, A&A, 639, A107. All co-authors provided comments on the final manuscript of the paper.

- 'Mineral snowflakes on exoplanets and brown dwarfs: Coagulation and fragmentation of cloud particles with HyLandS', Samra, D., Helling, Ch., Birnstiel, T. 2022, A&A, Accepted. All co-authors provided comments on the final manuscript of the paper.

1.2 Exoplanet Zoo: Discovery and Detection

The beginning of the field of exoplanets started with science-fact seeming more like science-fiction. The first recognised exoplanet; PSR 1257+12b, was discovered in 1992 (Wolszczan & Frail 1992) orbiting a pulsar - the collapsed remnants of a star which emits high-energy beams of radiation. It was later followed by the first confirmed discovery of an exoplanet orbiting a main-sequence star in 1995 (Mayor & Queloz 1995); Pegasi 51b, a Jupiter size planet in a 4.2 day orbit
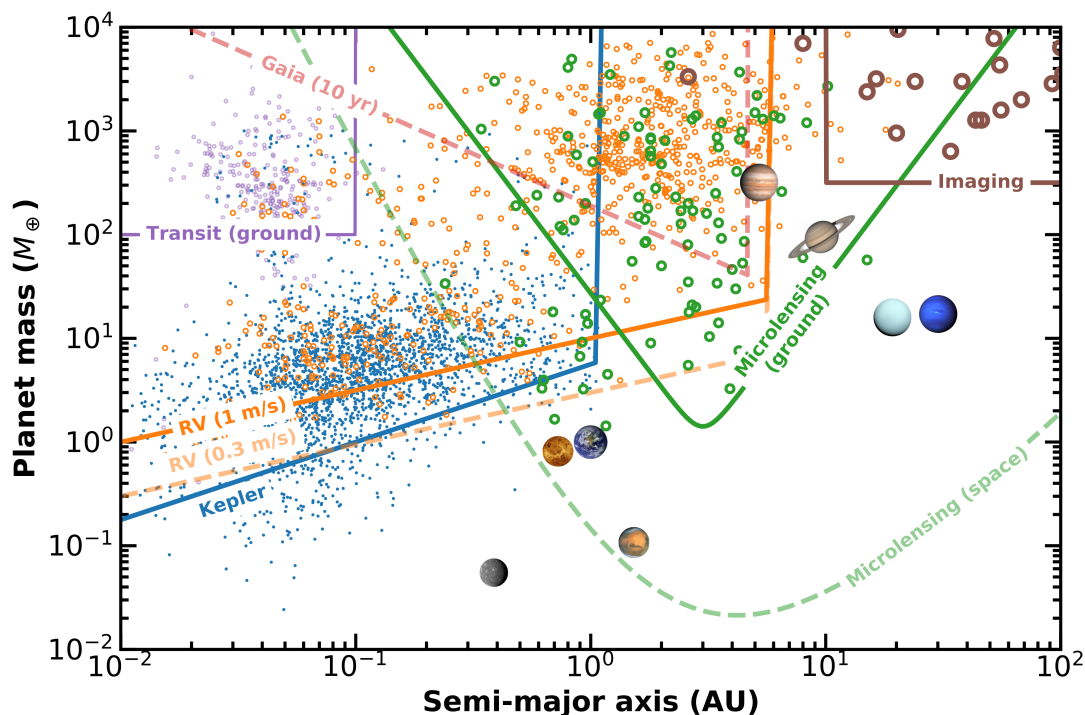
Figure 1.1: Taken from Zhu & Dong (2021). Planetary mass (in Earth masses $M_\oplus$) against semi-major axis (in AU) for discovered exoplanets as of the beginning of September 2021. Detection methods are shown in different colours: radial velocity (orange), transit (blue and purple), microlensing (green), and imaging (brown). Approximate current detection limits for the respective methods are shown by the solid lines. Similarly, dashed lines show future potential limits (for details see Zhu & Dong (2021)). Some masses are estimated using the Chen & Kipping (2017) relation. Solar system planets are shown in their respective locations, images courtesy of NASA.

around its star[1]. These two systems were highly unusual in that they challenged the understandings of planetary system formation and evolution. This set a precedent for the next three decades of discoveries that challenged traditional expectations of planets and planetary systems.

There are now nearly 5000 confirmed exoplanets[2]. These span a huge range of parameter space, for example the oft-used planetary mass vs orbital radius space (see Fig. 1.1). The first and most notable thing about these detected planets is the relative lack of overlap with the Solar System planets in the parameter space shown. However, this can be seen to result from the sensitivity levels and biases of current detection methods, which prevent longer period detections. So far planets have been detected spanning everything from: K2-137b the exoplanet with the shortest semi-major axis so far of just 0.0058 ± 0.0006 AU, out to orbital radii out to ~ 2000 AU for GU Psc b, identified by Naud et al. (2014). Discovered exoplanets also range in mass from 0.066–8654 $M_\oplus$,

---

[1] The detection of which would later win Didier Queloz and his then supervisor Michel Mayor the 2019 Nobel Prize in Physics, shared with James Peebles

[2] Taken from NASA Exoplanet Archive, available at `http://exoplanet.eu/`, retrieved 02/02/2022

for Kepler-138b (Jontof-Hutter et al. 2015) and KELT-1b (Siverd et al. 2012) respectively.

The majority of early detections were by the radial velocity method (see right of Fig. 1 in Adibekyan 2019), for example with ground based instruments such as HARPS (High Accuracy Radial velocity Planet Searcher; Rupprecht et al. 2004). The radial velocity (or Doppler spectroscopy) method uses the fact that the mass distribution in an exoplanet-star system results in the system barycentre being located away from the centre of the star. As both the planet and the star orbit around this centre, the light emitted from the star is red- and blue-shifted relative to the observer at different points in the orbit. By detecting this oscillation it is possible to infer the existence of the orbiting exoplanet and also put bounds on the exoplanet's mass, although this is degenerate with the inclination of the system with respect to the observer.

The second method that produced the bulk of exoplanet detections is the transit method: as an exoplanet passes in front of its host star, it obscures some of the light. This dip in brightness is detectable at Earth. From the ground the contrast required for such transits is high in order to overcome atmospheric noise, thus only the largest planets were detected. Nonetheless such searches could be undertaken from the ground with relatively inexpensive equipment, for example HATnet Exoplanet Survey (Hungarian Automated Telescope Network; Bakos et al. 2004) and WASP/SuperWASP (Wide Angle Search for Planets; Pollacco et al. 2006).

However the real game-changer came first with the *Kepler* (Borucki et al. 2010) and now TESS (Transiting Exoplanet Survey Satellite; Ricker et al. 2015) space missions, which have increased the number of known exoplanet systems by an order of magnitude. More recently, transit missions such as CHEOPS (CHaracterising ExOPlanet Satellite; Broeg et al. 2013), have also been launched specifically to further support exoplanets detected by other methods, providing accurate radii measurements in order to constrain the planets bulk density. Planned missions such as PLATO (PLAnetary Transits and Oscillation of stars; Rauer et al. 2014) will push towards $\sim 1\,M_{\oplus}$ exoplanet detections.

As can be seen in Fig. 1.1, both the radial velocity and transit method have greater sensitivity for larger mass exoplanets. Radial velocity does however have the advantage that it does not require observations over many orbital periods in order to determine the orbital properties of an exoplanet. This allows it to detect longer orbital period planets than the transit method. Additional, smaller contributions to our knowledge of exoplanetary systems are by direct imaging and gravitational microlensing. However, crucially, such techniques occupy different

regions of the parameter space shown. Direct imaging with coronographic techniques finds exoplanets at large orbital distances, for example SPHERE (Spectro-Polarimetric High-contrast Exoplanet REsearch; Beuzit et al. 2008) and GPI (Gemini Planet Imager; Macintosh et al. 2008).

Gravitational microlensing - the bending of the light of a background star by an unseen star-exoplanet(s) system - is a unique technique as it is unbiased to local or distant exoplanets or particular directions within the galaxy (Dominik 2010). The upcoming Nancy Grace Roman Telescope (Spergel et al. 2015) will be able to do both direct imaging of exoplanets in reflected light (Carrión-González et al. 2021) as well as free-floating planets that have been ejected from their host system through gravitational microlensing (Johnson et al. 2020). Fischer et al. (2014) provide a detailed review of these detection methods. [3]

Exoplanet atmosphere observations are important for understanding the formation mechanisms of planets, which leave a 'fingerprint' on the exoplanet atmosphere abundances (e.g. C/O) based on the region(s) of the protoplanetary disc in which the planet formed (Öberg et al. 2011; Madhusudhan et al. 2014; Helling et al. 2014). Furthermore, population studies based on the vast numbered of detected exoplanets reveal a number of interesting clues to such mechanisms. One such clue is a correlation between stellar metallicity and planetary occurrence rates (Marcy et al. 2005; Adibekyan 2019). However, the metallicity and atmosphere abundances of exoplanet atmospheres are also affected by cloud formation. We now turn to the exoplanet types with atmospheric observations investigated in this work.

1.2.1   Hot and Ultra-hot Jupiters

The first observations of an exoplanet atmosphere was the detection of a sodium line for the planet HD 209458b, a hot Jupiter planet, by Charbonneau et al. (2002). Hot Jupiters are gas giant planets with masses $\gtrsim M_{\text{Jup}}$, the mass of Jupiter, up to the transition into brown dwarfs (see Sect. 1.2.3). Hot Jupiters orbit in tight orbits around their host star with periods on the order of a few days (Dawson & Johnson 2018). As gas giant planets, their atmospheres are dominated by H/He elemental abundances. They are the exoplanets most frequently observed for spectroscopic characterisation, owing to their large atmospheric scale height, due to the low mean molecular weight of their atmospheres. In addition hot Jupiters' proximity to their host star maximises the amount of star light intercepted by the planets atmosphere and thus increases the overall signal

---

[3] A nice mnemonic for the main detection methods of exoplanets: radial velocity, transit, gravitational microlensing and direct imaging, is wobbles, dips, blips, and pics. (Credit: Calum McAndrew, Public Engagement Officer, University of St Andrews.)

from absorption by atmospheric molecules and clouds.

The proximity of the planet to the star leads to hot Jupiters being universally tidally locked, therefore there is a dichotomy between the dayside and nightside of the planet, in terms of stellar irradiation, chemistry, and cloud formation. Notable observations of hot Jupiter atmospheres include the detection of water and clouds on 10 hot Jupiters (Pinhas et al. 2019), as well as the detection of TiO_2 gas and thermal inversions (Sedaghati et al. 2017). Ultra-hot Jupiters are typically defined as hot Jupiters with temperatures on the dayside $\gtrsim 2200\,K$ (Parmentier et al. 2018)[4]. With such hot daysides, ultra-hot Jupiters exhibit extreme effects like the total dissociation of H_2 to atomic H in the upper atmosphere of the dayside. This is important as it increases the atmospheric scale height of this hemisphere, which affects observations when considering 3D atmospheres (Lacy & Burrows 2020a; MacDonald & Lewis 2021).

1.2.2 Cooler gas giants

Most of the known exoplanets are orbiting their star very closely, but direct imaging efforts have increased the number of known gas giants orbiting their host star at large distances (Desidera et al. 2021; Langlois et al. 2021). Such large-orbit exoplanets in particular allow comparisons with brown dwarfs. It is difficult to study exoplanet of similar types and different ages, however this is possible for brown dwarfs (e.g. Scholz et al. 2018; Vos et al. 2020).

Atmospheric characterisation of some such exoplanets has been achieved in the near-infrared, these tend to be massive and young planets, so that their emission is detectable in contrast to the star. The best known system HR 8799, has produced detection of H_2O, CH_4, and CO gas (Barman et al. 2015). In the future, direct emission spectroscopy on such systems in the mid-infrared with the James Webb Space Telescope (JWST) Mid-Infrared Instrument (MIRI; Wright et al. 2004) could allow for constraining the abundances of these molecules (Patapis et al. 2022). As planets that are more easily observed by direct emission are much younger ($< 100\,Myr$) than those observed in transmission and eclipse, this would provide a much closer link between atmospheric abundances and formation history (Barman et al. 2015).

---

[4]One fears the end-state evolution of such terminology, which by now includes hot Jupiters, warm Saturns (Brahm et al. 2018), and disintegrating super-Mercurys (Rappaport et al. 2012). It is only a matter of time before we are confronted with tepid Neptunes (Credit: Simon Ebo).
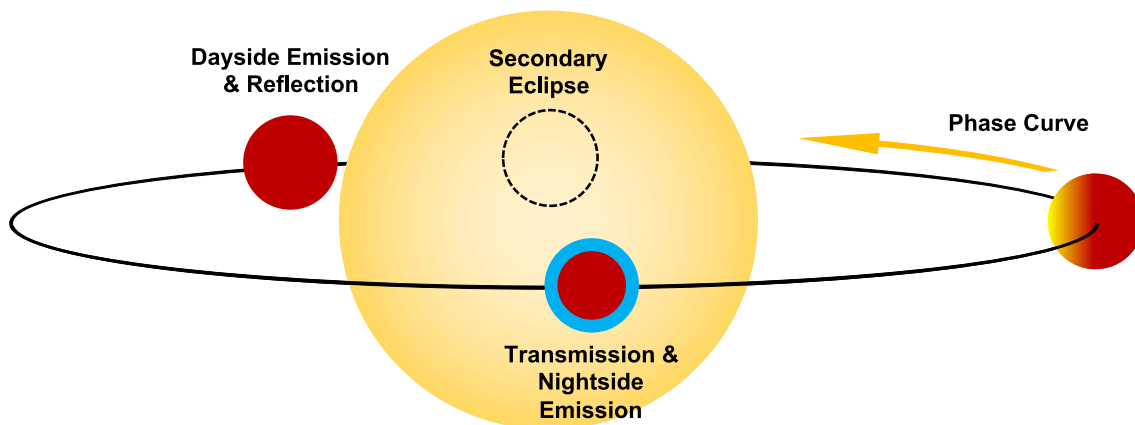
Figure 1.2: Taken from Gao et al. (2021), schematic diagram of observational techniques for an exoplanet atmosphere.

1.2.3   Brown Dwarfs

Brown dwarfs bridge the gap between exoplanets and stars. However, the boundary between planets and brown dwarfs is somewhat blurred. For example the exoplanet KELT-1b has a mass of 27.23 M_{Jup}, well above the IAU accepted 'limit' of 13 M_{Jup} for brown dwarfs, which is where theoretical predictions indicate the onset of thermonuclear deuterium fusion (Boss et al. 2003). This limit is not universally accepted as some prefer formation mechanism based distinctions and suggest that there is rather an overlap of exoplanet and brown dwarfs masses (Chabrier et al. 2014). At the upper mass limit, brown dwarfs are generally considered to be objects below the hydrogen-burning minimum mass ($\sim 0.07\,\mathrm{M}_\odot$ – solar masses – see Chabrier et al. 2000).

Brown dwarfs are interesting objects for comparison to exoplanets given their likely different formation mechanism. They also have complex cloud dynamics across their population, with the transition between L- and T-type brown dwarfs (Kirkpatrick 2005) associated with changes in near-infrared colours, with L-type exhibiting CO absorption, while T-type shows CH_4 absorption. The presence of clouds in L-type atmospheres accounting for this transition (Ackerman & Marley 2001). Variability in brown dwarf observations is also associated with cloud dynamics (e.g. Biller et al. 2015). Helling & Casewell (2014) provide a detailed review of brown dwarf atmospheres. It has been noted that brown dwarfs in orbit around white dwarf stars may also offer analogues to ultra-hot Jupiters (Lothringer & Casewell 2020).

1.3 Atmosphere Observation Techniques

The atmosphere of Earth is extremely shallow in its extent; if the Earth was the size of an apple, the atmosphere would be approximately the thickness of the skin[5], on the order of $\sim 1/100$. The same is actually true for gas giant exoplanets as well: for example HAT-P-7b has a radius of $1.4\,R_{\rm Jup}$ ($\sim 10^{10}$ cm) and a typical General Circulation Model (GCM) might model the regime for $p_{\rm gas} = 10^2$–10^{-6} bar, which extends over $\sim 10^8$ cm, leading to the same ratio of $\sim 1/100$ for the atmosphere height to planet radius ratio. However, because the ratio of the radius of a gas giant to its host star is much larger than an Earth-sized planet to a Sun-like star, its much easier to observe gas giant atmospheres. Here we introduce three primary means of atmospheric characterisation (as shown in Fig. 1.2): transit spectroscopy, emission and scattered light spectroscopy (around secondary eclipse), and phase curves. Madhusudhan et al. (2014) provides a detailed review of atmosphere observation techniques.

1.3.1 Transmission Spectra

Characterisation of the atmospheric properties of exoplanets can be done through transmission spectroscopy (Seager 2010), in which starlight passes through the atmosphere of a planet as it moves in front of its host star as viewed from Earth (called a transit). This leads to light being blocked by the planet and its atmosphere. The ratio of flux during and out of transit is given by:

$$\frac{F_{\rm in}(\lambda)}{F_{\rm out}(\lambda)} = 1 - \left(\frac{R_{\rm p}(\lambda)}{R_*}\right)^2 , \tag{1.1}$$

where $F_{\rm in}(\lambda)/F_{\rm out}(\lambda)$ is the ratio of flux between when the exoplanet is transiting (in) and when it is not (out), at a wavelength λ, otherwise known as the transit depth. $R_{\rm p}(\lambda)/R_*$ is the ratio of the effective planetary radius (including opaque atmosphere) at wavelength λ and the stellar radius. $R_{\rm p}(\lambda)$ is dictated by opacity sources in the planetary atmosphere including gas phase and aerosol opacities (Barstow & Heng 2020). The changing transit depth with respect to wavelength obtained by observations can be used to reconstruct the atmospheric properties of the atmosphere such as temperature profile and elemental abundances by the retrieval method (Madhusudhan & Seager 2009). Because of the geometry of transits, the light rays pass through the atmosphere of

---

[5]This frequently repeated fact (e.g. Neil DeGrasse Tyson's twitter: `https://twitter.com/neiltyson/status/723534428916486144?s=20&t=XsepCHkmfk8K8Lnf80lBcA`.) is really only an order of magnitude illustration, considering an apple to have a radius of approximately 35 mm and a skin of 0.3 mm

the exoplanet on a 'slant path' and thus are more sensitive to the upper atmosphere (Fortney 2005).

Additionally, as a result of the tidally locked nature of hot and ultra-hot Jupiters, most transit observation probe two narrow regions that divide the dayside and nightside of the exoplanet called the terminator regions (Lacy & Burrows 2020a). H_2-He dominated atmospheres of gas giants and mini-Neptunes give them large atmospheric extensions (due to the low mean molecular weight of the atmosphere) and therefore large $R_p(\lambda)$, making them ideal targets for transmission spectra (Barstow 2020). So far some of the major discoveries with transit spectra include detection of water on a number of exoplanets (Pinhas et al. 2019), a plethora of atomic gas species detections (e.g. Hoeijmakers et al. 2020), and patchy cloud coverage (Line & Parmentier 2016; MacDonald & Madhusudhan 2017).

1.3.2 Secondary Eclipse: Emission and Scattered Light

As hot and ultra-hot Jupiters orbit their stars so closely they have high effective temperatures (T_{eff}, the temperature of a blackbody that outputs the same amount of electromagnetic radiation as the body in question). This is particularly true on the dayside (see Sect. 1.2.1), thus they radiate in the infrared. The ratio of this flux compared with the star is given by (Alonso 2018):

$$\frac{F_p}{F_*} = \left(\frac{R_p}{R_*}\right)^2 \frac{B(\lambda, T_{p,\text{eff}})}{B(\lambda, T_{*,\text{eff}})} \tag{1.2}$$

where $B(\lambda, T_{i,\text{eff}})$ is the blackbody function of a body with effective temperature $T_{i,\text{eff}}$. The flux F_p can be determined by comparing the flux just before and after an exoplanet moves behind its host star relative to the observer (secondary eclipse, see Fig. 1.2).

The earliest detections of secondary eclipse emission spectra for exoplanets came from the *Spitzer* space telescope (e.g. Deming et al. 2013). Emission spectra observations are taken when viewing the planet face-on (rather than the slant geometry viewed by transit spectra), this allows for probing deeper into the exoplanet atmosphere. However, the depth seen is also dictated by where aerosols are becoming optically thick, as this dictates the temperature observed. Emission spectra can therefore also attempt to infer the chemistry of aerosol formation, based on the temperature of the cloud deck(Gao & Powell 2021), provided there are clouds present on the dayside. Although, such inferences rely on model assumptions. Indications of this in population studies of *Spitzer* data has already been found (Baxter et al. 2020). The degeneracies in emission spectra can be hard to untangle, particularly between the atmospheric composition and temperature structure

(Madhusudhan & Seager 2009; Griffith 2014). Such degeneracies however can be probed through combined transmission and emission observations, or through phase curve observations (Griffith 2014).

For reflected light from an exoplanet atmosphere at orbital distance (r) the flux ratio is given by:

$$\frac{F_\mathrm{p}}{F_*} = \left(\frac{R_\mathrm{p}}{r}\right)^2 A_\mathrm{g} \tag{1.3}$$

where A_g is the geometric albedo, a measure of scattered light in comparison to a reference 'Lambertian disk' when observed face on (Seager 2010). Scattered light observations of hot and ultra-hot Jupiters often reveal little or no reflected flux, indicating very dark daysides for these exoplanets. An example of this is Pegasi 51b, for which Spring et al. (2022) were only able to place an upper limit on reflected light flux. Similarly, Fraine et al. (2021) inferred a very low geometric albedo for WASP-43b, which they suggest is difficult to reconcile with the presence of clouds. Note also that Eq. 1.3 is inversely proportional to the square of the semi-major axis r, thus this technique works better on closely orbiting exoplanets, which is why direct imaging instead has to rely on young self-luminous planets rather than reflected light.

1.3.3 Phase Curves

Phase curves show photometry with changing phase – which longitude of the planet faces the observer – rather than spectrally resolved observations which integrate over time (i.e. transit, emission, and scattered light spectra). However, here phase curves at different wavelength bands (e.g. visible vs thermal) can provide a powerful diagnostic tool for global atmosphere dynamics of exoplanets and brown dwarfs, probing both depth and longitude (Knutson et al. 2009). It also allows for mapping of exoplanets and brown dwarfs (Crossfield et al. 2014). One of the main results from phase curve observations is the presence of a 'hotspot offset', that is to say that the hottest point in the highly irradiated ultra-hot Jupiter atmospheres is not located at the point directly underneath the star. The detection of a number of eastward shifted hotspots (i.e. with planetary rotation) have been used as an indication of strong equatorial jets in the atmospheres of some ultra-hot Jupiters (Stevenson et al. 2014, 2017). A similar technique of longitudinally resolved spectra provides the possibility of characterisation of hot and ultra-hot Jupiter atmospheres in even greater detail (Irwin et al. 2020; Cubillos et al. 2021).

1.4 Aerosols in Atmospheres

1.4.1 Clouds and Haze and Dust: Aerosol Definitions

The naming conventions for particles suspended in an atmosphere are often quite muddled, with each individual field using its own jargon freely. This often leaves little hope for those from another field to understanding the specific nuances of the definitions used. Exoplanet atmosphere modelling has developed out of these many fields (see Sect. 1.4.2) and thus the nomenclature can, at times, be similarly confused.

Generally *aerosols* are used as an all-encompassing term for particles suspended in a gas, both solid and liquid phase particles (Gao et al. 2021), and as such it is similarly used in this work.[6] The term *dust* is best avoided entirely due to its broad usage across the astrophysical community, from protoplanetary discs (Birnstiel et al. 2016), the interstellar environment (Draine 2003), AGB stars (Gail et al. 2009), and occasionally for exoplanets (e.g. Pont et al. 2013). From the Earth atmosphere community, *dust* is used to explicitly describe material swept up from the surface, for example sand from deserts (Kok et al. 2012).

For *hazes/clouds* there can be a clash between observations and theoretical modelling. The former generally favour a naming convention where *clouds* are used to mean *aerosols* producing a grey opacity (flat across a range of wavelengths), whereas a *haze* produces an opacity dependent on wavelength (Pinhas & Madhusudhan 2017). We instead adopt a nomenclature based on the *aerosol* formation (Marley et al. 2013; Madhusudhan et al. 2016; Barstow 2020; Gao et al. 2021): *Hazes* form through photochemical reactions, they are expected to be largely made of hydrocarbons (Kawashima & Ikoma 2018; Morley et al. 2013), similar to those on Titan (Hörst 2017) or hydrocarbon ices as on Pluto and Triton (Ohno et al. 2021; Lavvas et al. 2021), although their exact composition is uncertain (Gao et al. 2021). They are often modelled with either 'soot'-like spectral properties (Morley et al. 2013) or those of so-called 'Tholins' (Khare et al. 1984). *Clouds* are defined as *aerosols* formed by condensation of gas phase species, either through direct phase changes or chemical reactions. Their formation is governed by the available surface for condensation and thermal stability of the condensing material. It is *cloud particles* that are the focus of this work.

---

[6]Although even this is not universal: we, over the past two and a bit years, have sadly become all too familiar with the alternative epidemiological definition of an aerosol as a $\lesssim 5\,\mu m$ particle. Although see Randall et al. (2021) for the scientific dubiousness of this often touted figure.

1.4.2 Aerosol Formation Modelling

As clouds became established as a regular feature of sub-stellar atmospheres, many research groups developed models using very different inspirations: based on terrestrial cloud formation (Ackerman & Marley 2001; Cooper et al. 2003), from the point of view of planetary science (Rossow 1978; Marley et al. 1999), of asymptotic giant branch (AGB) stars (Helling et al. 2001; Woitke & Helling 2003, 2004), and based on practical considerations (Tsuji et al. 1996a,b; Allard et al. 2001).

Broadly the approaches to cloud formation modelling for exoplanets fall into two categories; equilibrium models based on thermal stability of the condensate, and non-equilibrium kinetic models (Helling et al. 2008a). Equilibrium models have the advantage of being computationally cheap, which allows for fitting of observations to model parameters. Taking the Ackerman & Marley (2001) equilibrium model as an example, this makes use of a 'sedimentation efficiency' f_{sed} for the vertical extent of clouds, with smaller values of f_{sed} resulting in a greater vertical extent of clouds in the atmosphere. This parameterised approach allows for easy fitting to observations, as has been done for brown dwarfs and mini-Neptunes (Morley et al. 2012, 2013) for example. However, it incorporates multiple physical effects into a single parameter, such the strength of vertical gas mixing in an atmosphere, the surface gravity and material composition of cloud particles (Gao et al. 2018). Thus more complex atmospheric dynamics are somewhat lost in the tuning of this single parameter (Gao et al. 2021).

Kinetic aerosol formation models treat microphysical formation (such as nucleation, bulk growth, evaporation, and gravitational settling, see Chap. 2) processes explicitly. Within microphysical modelling there are two approaches to particle size distributions, the binning method or the moment method. The binning method has discrete 'bins' which track the certain number of particles of a given particle mass, it therefore allows for direct understanding of particle size distribution. An example of the binning method applied to exoplanet atmospheres for cloud modelling is the CARMA model (Community Aerosol and Radiation Model for Atmospheres; Toon et al. 1979; Turco et al. 1979). This model was adapted from an Earth-focused model for exoplanet atmospheres (see Gao et al. 2018; Gao & Benneke 2018). The advantage of such models is the ability to resolve the cloud/haze particle size distribution without an assumed functional form of the particle size distribution, which may be multi-modal (Powell et al. 2018).

11

However, a sufficient number of bins is required for numerical accuracy (Krueger et al. 1995), these bins must also typically span a many orders of magnitude in mass space. We note that mass does not uniquely relate to the size (radius) of cloud particles in exoplanet and brown dwarf atmospheres as it is reasonable to expect that various mixes of materials may result in the same value of mass density. The smallest bin size may have an assumed number density as in protoplanetary disc modelling or is calculated from nucleation theory. For example, Gao et al. (2018) use 65 particle mass bins, starting at a radius of 10^{-8} cm and doubling in mass for each subsequent bin. The largest bin contains the particles of $\sim 2 \times 10^{-2}$ cm. A consequence of this is that this method is computationally expensive and cannot accommodate mixed material condensation due to element conservation requirements see Lavvas & Koskinen (2017); Gao & Benneke (2018); Kawashima & Ikoma (2018).

The moment method, in contrast, integrates over the particle size distribution. Thus no form of the particle size distribution is assumed, but average properties of cloud particles can still be derived (Helling et al. 2008b; Ohno & Okuzumi 2017; Ormel & Min 2019). Furthermore, moment method kinetic cloud formation models are capable of treating the condensation of many cloud materials at once whilst maintaining element conservation. The advantage of this method is that it requires only a small number of moments to be used to represent the particle size distribution $f(V)$. The number of moment equations required to be solved scales with the number of materials considered (≈ 20) regardless of the range of particle sizes covered by the distribution. The lower integration boundary requires a model for which, for example, a kinetic nucleation approach may be chosen (e.g. Lee et al. 2015a; Köhn et al. 2021). See Sect. 2.2.1 for a detailed description of the moment method used in this work.

1.4.3 Flatlining?: Aerosol Observations

The study of clouds in exoplanet atmospheres may be the only case where a flatline was an indication of good health. The most famous example of this being the spectra of GJ 1214b (Kreidberg et al. 2014, see Fig. 1.3). The very first detection of an exoplanet atmosphere showed diminished sodium spectral lines for the hot Jupiter HD 209458b (Charbonneau et al. 2002). This was in line with the expectation that interpreting the transmission spectra of exoplanets would require careful consideration of condensates (Seager & Sasselov 2000). Muted spectral features can be suggestive of clouds in the atmosphere as they obscure deeper parts of the atmospheric column. Similarly, the importance of clouds had previously been recognised for brown dwarf
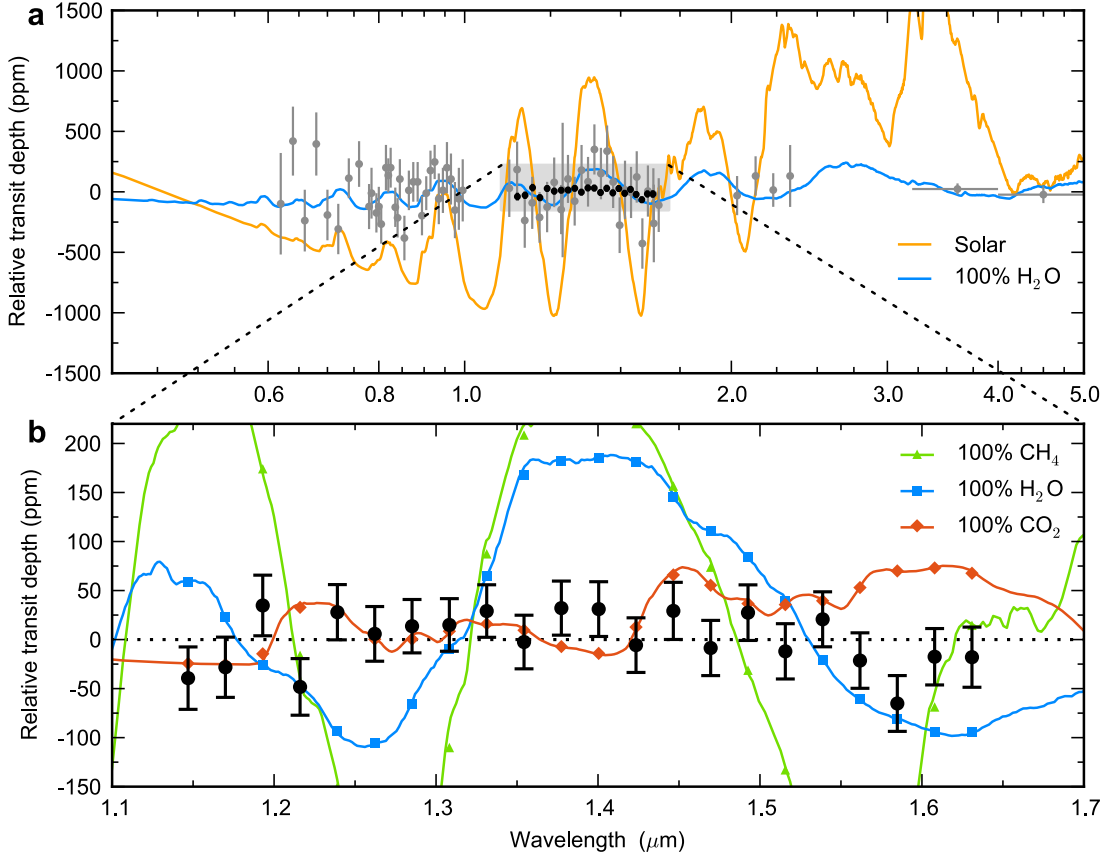
Figure 1.3: Taken from Kreidberg et al. (2014), the spectra of GJ-1214b at optical and near-infrared wavelengths using *Hubble*, over-plotted are models for various mean-molecular weight atmospheres.

atmospheres (Lunine et al. 1986; Tsuji et al. 1996a,b), where they play a crucial role in the transition between L- and T-type brown dwarfs. Since the first detection of truncated spectral features, spectra indicative of cloud particles have been found for many exoplanets (e.g. Benneke & Seager 2012; Crossfield et al. 2013; Deming et al. 2013; Kreidberg et al. 2018).

However, the spectra of aerosols in exoplanet atmospheres is not always flat, for small enough aerosols, they enter the Rayleigh regime where $Q_{\text{ext}} \propto \lambda^{-4}$ (Kerker 1969). This has been observed for a number of gas giant exoplanets (Sing et al. 2016). Furthermore, Ohno & Kawashima (2020) showed that hazes could actually produce super-Rayleigh slopes (steeper than λ^{-4}) in atmospheres with strong mixing.

In contrast to both the kinetic and equilibrium cloud modelling described in Sect. 1.4.2, fitting to observations often use highly parametrised models for clouds, often without consideration for material composition or particle size, but instead implementing simple optical properties such as opacity power laws in wavelengths (see Barstow & Heng 2020, for a review of

exoplanet retrieval methods). However, more recent retrieval models (e.g. Mollière et al. 2019; Benneke et al. 2019; Taylor et al. 2020) allow for retrievals with properties of the cloud particles, like material composition, size and irregular shape. Benneke et al. (2019) included Mie theory into a retrieval (see Sect. 2.3.1), but in a later study, the authors also found that a grey cloud model for the habitable zone planet K2-18b (Benneke et al. 2019) was a better fit to the data. This highlights the limitations of the low-resolution spectra that are currently available. Barstow (2020) showed that other parameters retrieved from exoplanet observations, such pressure-temperature structure, are not too badly affected by simple cloud model assumptions, for optical wavelengths, though of course the information gained about cloud properties are limited. However, there are known degeneracies between sub-solar atmospheric metallicities and high altitude clouds (MacDonald & Madhusudhan 2017).

1.4.4   Exoplanet Aerosols: The Multi-Wavelength Era

On December 25th 2021 at 12:20 UTC, the Arianne 5 rocket carrying JWST leapt off the launchpad. This marked the start of the truly multi-wavelength era for spectroscopic characterisation of exoplanet atmospheres. As the next generation of missions instruments arrive, such as JWST (Greene et al. 2016), but also in the future ARIEL (Tinetti et al. 2018; Venot et al. 2018) and CRIRES+ (Follert et al. 2014), the range of wavelengths at which atmospheres are observed will allow the investigation of cloud particles properties such as particle size and composition (Helling et al. 2006; Wakeford & Sing 2015; Burningham et al. 2021; Luna & Morley 2021).

Unlike the flat, or simple power law optical wavelength observations, in the mid-infrared we potentially get to see the blip that indicates the beating heart of cloud formation on gas giant exoplanets. As shown by Wakeford & Sing (2015) (see Fig. 1.4), in the mid-infrared wavelengths, JWST MIRI, will be able to begin to see the spectral features of different cloud material compositions, potentially between different silicate types (Luna & Morley 2021).

Lothringer et al. (2020) showed the potential of UV observations to discriminate between scattering slopes (such as hazes) and atomic gas phase absorbers such as Fe, Ti, Ni, V, Cr, and SiO. Wakeford et al. (2020) showed it is possible to do near-UV exoplanet observations with the *Hubble* UVIS grism, and detected H^- likely from disequilibrium processes (Lewis et al. 2020). Future space missions such as the LUVOIR (Large UV/Optical/IR Surveyor; The LUVOIR Team 2019) and HabEx (the Habitable Exoplanet Observatory; Gaudi et al. 2020) will enable UV observations
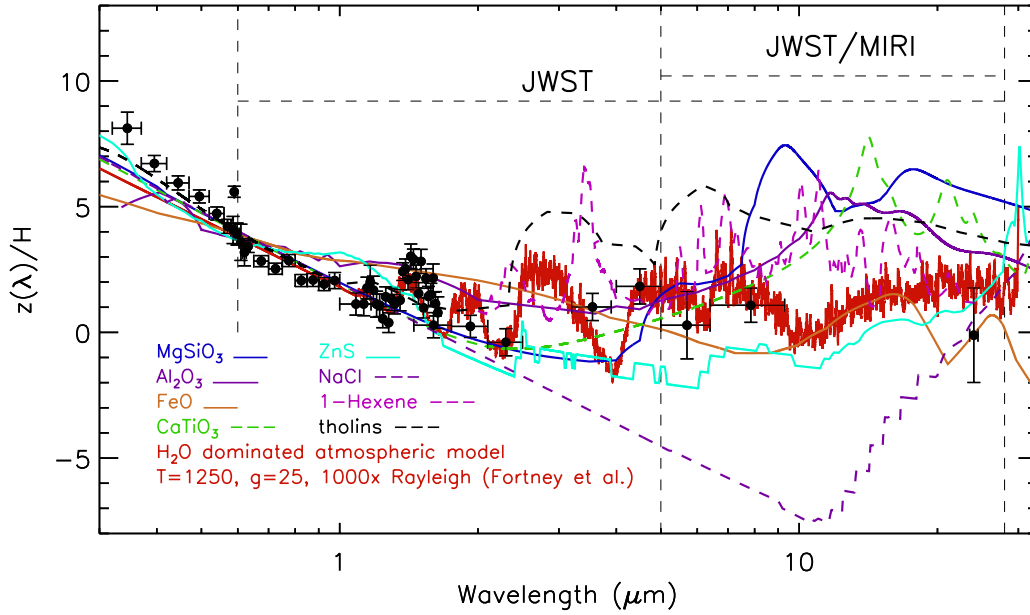
Figure 1.4: Spectra of various condensate species for particle sizes of 0.025 μm, using the (Fortney et al. 2010) model for the gas giant exoplanet HD 189733b. Black points show the observations of Pont et al. (2013) and McCullough et al. (2014). Taken from Wakeford & Sing (2015)

of exoplanet atmospheres. CUTE (Colorado Ultraviolet Transit Experiment; Sreejith et al. 2019) will also do UV transmission spectra of hot Jupiters.

Finally an additional tool for characterising exoplanet aerosols is polarisation of light. Light emitted from stars is un-polarized. However, depending on the atmosphere of an exoplanet and its contained aerosols, the polarisation of reflected light is altered (Stam et al. 2004). Thus by investigating specific polarisations the contrast between stellar light and reflected light from the exoplanet atmosphere is enhanced. This enables better characterisation of the atmosphere but also requires detailed understanding of aerosol characteristics (Stolker et al. 2017; Sanghavi et al. 2021).

1.5 Thesis Aim, Outline, and Research Questions

This thesis seeks to highlight the complex nature of microphysical cloud modelling. In particular, the ways in which including additional microphysical effects and processes affects the distribution, physical properties, and spectral properties of cloud particles in the atmospheres of gas giant exoplanets and brown dwarfs. Chapter 2 describes the moment method and the 1D kinetic non-equilibrium model of static cloud formation used throughout this work, as well as the basics of Mie theory for mixed material cloud particles used to investigate their spectral properties.

Chapter 3 introduces a simple mode to explore micro-porous cloud particles and their impact of cloud particle distribution in an atmosphere. It further investigates the spectral properties of clouds including a cloud particle size distribution, inclusion of porosity into Mie theory calculations using effective medium theory, and irregularly shaped cloud particles using a statistical distribution of hollow spheres. Chapter 4 presents HyLandS, a hybrid two bin and moment method for consistently modelling cloud particle collisions alongside nucleation, condensational growth and settling for mixed material cloud particles, whilst maintaining element conservation. The model incorporates a parameterised collision model with collisions driven by turbulence and differential gravitational settling. The chapter explores various parameters of the model as well as presenting some of the spectral effects of including coagulation / fragmentation of cloud particles.

Chapter 5 demonstrates a hierarchical approach to modelling global cloud particle formation for hot and ultra-hot Jupiters. The chapter explores potential asymmetry of cloud formation for two typical gas giants: HAT-P-7b an ultra-hot Jupiter, and WASP-43b a cooler gas giant. Also investigated are the optical depth of clouds at the terminators of these planets.

Finally, Chapter 6 summaries the results and discusses potential future work leading on from this thesis. Here we further briefly state the research questions that are addressed by each of the results chapters (Chapters 3, 4, and 5).

Chap. 3 Mineral Snowflakes: Irregular, Micro-porous and Non-Monodisperse Cloud Particles

- How does the porosity of cloud particles affect their distribution in gas giant exoplanet and brown dwarfs?

- Does the size distribution of cloud particles in the atmosphere dramatically impact the spectral properties of microphysically modelled clouds?

- Can the microphysics of cloud particle formation (affecting particle shape and porosity) affect the cloud optical properties, for example cloud particle albedo?

Chap. 4 Clashing Clouds: Coagulation and Fragmentation with HyLandS

- How can collisional processes be consistently incorporated into microphysical cloud formation modelling, allowing for mixed materials whilst maintaining element conservation?

- For which gas giant exoplanets and brown dwarfs do particle-particle collisions impact cloud formation, and what processes drive these collisions?

- How do the results of collisions alter the optical properties of cloud particles, and can such effects confound interpretations of cloud material composition?

Chap. 5 Sunny Days?: Global Cloud Formation on Hot and Ultra-hot Jupiters

- How is global cloud distribution different for ultra-hot Jupiters compared to more temperate hot Jupiters?

- Can the asymmetries in cloud formation on such planets have implications for observations, in particular as hot and ultra-hot Jupiters begin to be treated fully in 3D?

- What are the implications of the different distributions of clouds for these worlds on results of population studies of hot and ultra-hot Jupiters which will be enabled by future observations?

$$\rho L_j = \int_{V_l}^{\infty} f(V) V^{j/3} \mathrm{d}V \qquad a_0^2(K_2^2 - K_1 K_3)$$
$$+ a_0(K_1 K_4 - K_2 K_3) \qquad \rho L_0 = n_0 + n_1$$

$$\frac{\partial}{\partial t}(\rho L_j) + \nabla(\boldsymbol{v}_{\mathrm{gas}} \rho L_j) = \quad + (K_3^2 - K_2 K_4) \qquad n_1 = \frac{K_1 K_3 - K_2^2}{a_0(K_3 - 2a_0 K_2 + a_0^2 K_1)}$$

$$- \nabla \int_{V_l}^{\infty} f(V) V^{j/3} \mathring{\boldsymbol{v}}_{\mathrm{dr}} \mathrm{d}V \qquad = 0$$
$$n_0 = \frac{(a_0 K_1 - K_2)^3}{(a_0 K_2 - K_3)(K_3 - 2a_0 K_2 + a_0^2 K_1)}$$

$$+ \int_{V_l}^{\infty} \sum_k R_k V^{j/3} \mathrm{d}V$$
$$-\frac{\mathrm{d}}{\mathrm{d}z}\left(\rho_s \frac{L_4^s}{c_T}\right) = \frac{1}{\xi_{\mathrm{lKn}}}\left(V_l^{j/3} J(V_l) + \frac{j}{3}\chi_{\mathrm{lKn}}^{\mathrm{net}} \rho L_2 - \frac{\rho L_3^s}{\tau_{\mathrm{mix}}}\right)$$

$$K_j = \int_{a_l}^{\infty} f(a) a^j \mathrm{d}a$$
$$-\frac{\mathrm{d}}{\mathrm{d}z}\left(\rho_s \frac{L_{j+1}}{c_T}\right) = \frac{1}{\xi_{\mathrm{lKn}}}\left(V_l^{j/3} J(V_l) + \frac{j}{3}\chi_{\mathrm{lKn}}^{\mathrm{net}} \rho L_{j-1} - \frac{\rho L_j}{\tau_{\mathrm{mix}}}\right)$$

$$= \left(\frac{3}{4\pi}\right)^{j/3} \rho L_j \qquad \frac{H_p}{\langle v_z \rangle}$$

$$\tau_{\mathrm{mix}} = \log_{10}(\tau_{\mathrm{mix}}^{\mathrm{inn}}) + \beta \max[0, \log_{10}(p_0) - \log_{10}(p(z))] \qquad \tau_{\mathrm{mix}} = \frac{H_p}{\langle v_z \rangle}$$

$$Q_{\mathrm{ext}} = \frac{2}{x^2}\sum_{i=1}^{\infty}(2i+1)\mathfrak{R}(a_i + b_i) \qquad \frac{n_{\langle H \rangle}(\epsilon_i^0 - \epsilon_i)}{\tau_{\mathrm{mix}}} = \nu_{i,0} N_l J_*$$

$$x = \frac{2\pi a}{\lambda} \qquad + \rho L_2 \chi_{i,s,\mathrm{lKn}}^{\mathrm{net}}$$

$$Q_{\mathrm{sca}} = \frac{2}{x^2}\sum_{i=1}^{\infty}(2i+1)(a_i a_i^* + b_i b_i^*) \qquad A_S(\lambda) = \frac{Q_{\mathrm{sca}}}{Q_{\mathrm{ext}}}$$

$$\kappa_{\mathrm{ext}} = \frac{Q_{\mathrm{ext}} \pi a^2 n_d}{\rho} \qquad \Sigma_s \left(\frac{V_s}{V_{\mathrm{tot}}}\right)\frac{\epsilon_s - \epsilon_{\mathrm{eff}}}{\epsilon_s + 2\epsilon_{\mathrm{eff}}} = 0$$

$$\tau(z') = \int_0^{z'} \kappa_{\mathrm{ext}} \rho \, dz$$

"All models are wrong but some are useful"

- George E.P. Box, *Robustness in Statistics*, 1978

2

Background Theory

2.1 Declaration

This chapter includes material adapted from two publications:

- 'Mineral snowflakes on exoplanets and brown dwarfs: Effects of micro-porosity, size distributions, and particle shape', Samra, D., Helling, Ch., Min, M. 2020, A&A, 639, A107. All co-authors provided comments on the final manuscript of the paper.

- 'Mineral snowflakes on exoplanets and brown dwarfs: Coagulation and fragmentation of cloud particles with HyLandS', Samra, D., Helling, Ch., Birnstiel, T. 2022, A&A, Accepted. All co-authors provided comments on the final manuscript of the paper.

2.2 Kinetic Cloud Formation Theory

The principle problem of cloud formation is the efficient conversion of gas phase material into bulk, solid cloud particles. This requires an abundance of condensable [1] species in the gas phase, favourable local thermo-chemical conditions, and sufficient time for the necessary reactions to occur. Four processes govern whether these conditions are satisfied: *nucleation, bulk*

---

[1] Here condensation/evaporation are somewhat abused terminology, delineating the general processes of material leaving/entering the gas phase onto/from the cloud particles (also referred to as condensates).
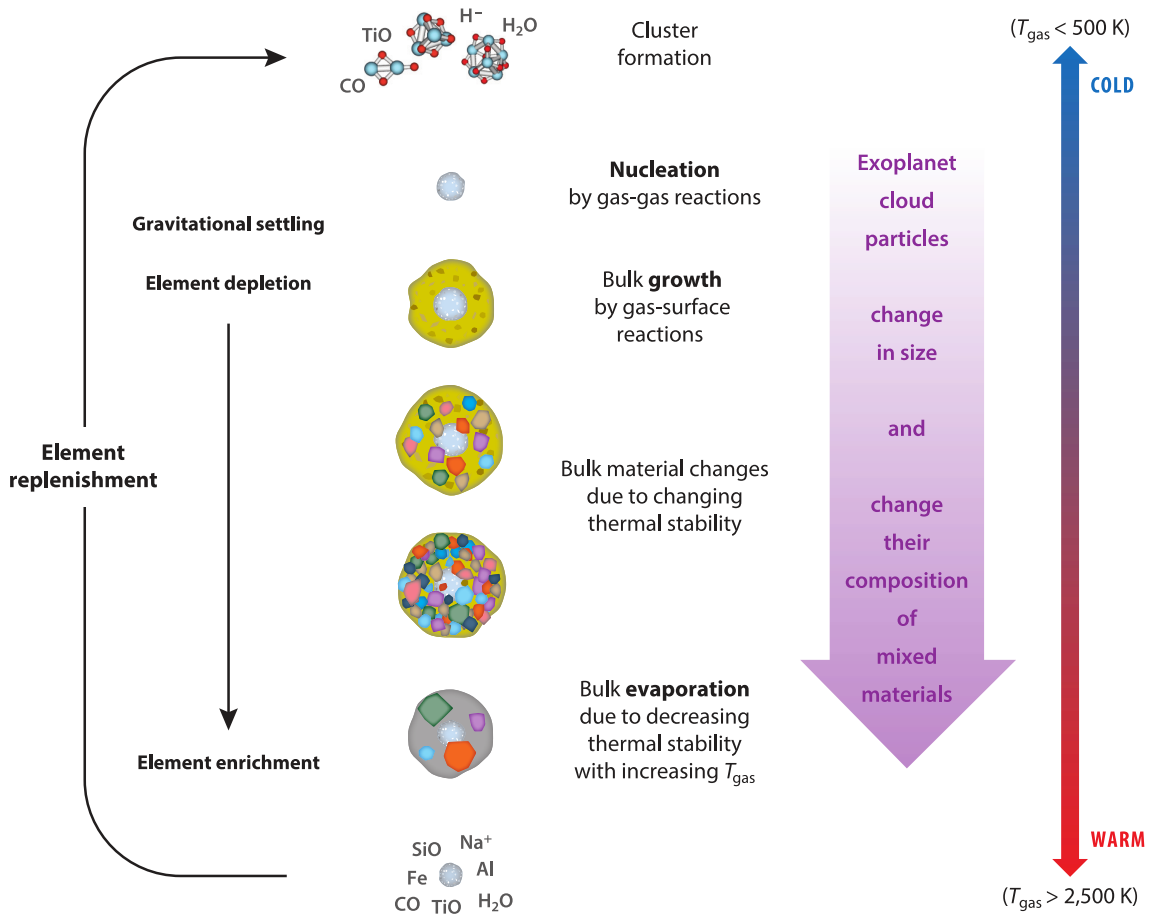
Figure 2.1: Schematic of cloud formation in a 1D atmospheric model, where temperature increases with depth from the top of atmosphere. High in the atmosphere, at low pressure and temperature, only nucleation occurs. These condensation nuclei settle deeper into the atmosphere where many materials become thermally stable and thus heterogeneously condense onto the cloud particle surfaces. At the lowest levels, materials are no longer thermally stable and hence evaporate. Turbulent mixing replenishes the upper atmosphere with condensable gas, without which cloud formation would eventually cease. Taken from Helling (2019).

growth/evaporation, gravitational settling, and turbulent mixing. Fig. 2.1 illustrates where these processes typically occur in a 1D atmospheric model.

Nucleation consists of interactions between gas molecules, termed monomers, with each interaction adding an additional monomer to the larger molecule. Materials not present in the gas phase, but for which there are abundant precursors may also nucleate provided the conditions for the necessary reactions are favourable. The cluster eventually reaches a critical size wherein the energy required for the addition of the next monomer is at a minimum. After this size, further monomers are easily added and the the cluster 'snowballs', becoming large enough to be well characterised by the bulk properties of the material, at which point it is termed a 'cloud condensation nucleus' (Helling & Fomins 2013). Nucleation typically occurs near the top of the

atmosphere (TOA), where the low temperature aids nucleation and low pressures prevent bulk growth. This is because the gas has to be in a state of extreme supersaturation in order for a material to form clusters directly from the gas phase, $S \gg 1$. Where S is the supersaturation ratio of the nucleating monomer gas, defined as the gas pressure over the vapour pressure of the nucleating species. For this to occur the gas must be much cooler than the temperature required for saturation of that species (Goeres 1996; Helling 2019)

Bulk growth is the net deposition of material from the gas phase onto the surface of existing cloud particles. For this to happen, the material must be thermally stable as a condensate (Helling & Fomins 2013), that is, the rate of condensate evaporation is lower than the deposition rate (equivalent to $S > 1$). Condensation onto the surface of a cloud particle is significantly more energy efficient than nucleation, and therefore only mild supersaturation is required. This leads to bulk growth dominating over nucleation and rapidly exhausting the gas phase of a species, provided there is a sufficient supply of cloud seeds at a given layer in the atmosphere.

Evaporation is the inverse process to bulk growth and occurs when cloud particles containing a condensed material reach the point in the atmosphere where that particular material is no longer thermally stable ($S < 1$). In these regions the deposition rate of the material is therefore exceeded by the evaporation rate, and the material evaporates from the cloud particles.

Gravitational settling occurs when the frictional forces exerted on cloud particles by the gas are no longer sufficient to couple them to the gas, and thus the particles fall out of that layer of the atmosphere. The velocities at which the cloud particles settle in the atmosphere with respect to the gas quickly reach an equilibrium value called the 'drift velocity'. For a subsonic free molecular flow, this is given by Woitke & Helling (2003) as

$$\mathring{v}_{\mathrm{dr}} = \frac{\sqrt{\pi}}{2} \frac{g\rho_{\mathrm{s}}a}{\rho c_{\mathrm{T}}}, \tag{2.1}$$

which is dependent on the size of the cloud particle a, gas density ρ , and material density ρ_{s}. Consequently, large cloud particles or cloud particles of higher density will settle faster. The inverse proportionality to gas density and the modal gas molecule speed of a Maxwell-Boltzmann distribution $c_{\mathrm{T}} = \sqrt{2k_{\mathrm{B}}T/\mu}$, where μ is the mean molecular weight of the gas means that cloud particles settle from higher in the atmosphere to a lower layer because gas density and temperature typically increase with depth in an atmosphere. For a sufficiently high drift velocity, the cloud

particles settle faster than bulk growth can occur, resulting in the cloud particles remaining at a constant size and 'raining out' of the atmosphere, which means that they rapidly fall towards lower atmospheric layers before they evaporate. The combined processes of gravitational settling and evaporation naturally deplete the gas-phase element abundances of condensible material in regions where cloud particles initially form and conversely enriches it where cloud materials evaporate.

Turbulent mixing is necessary for sustained cloud formation; without replenishment of the upper atmosphere gas phase, cloud formation would cease because the necessary condensable species would be depleted (Woitke & Helling 2004). Large-scale convective motions provide a potential process for driving such mixing, but because this motion is inherently a 3D hydrodynamical effect, including it in 1D models requires parameterisations. Woitke et al. (2020) provide a detailed discussion of the details.

The master equation (Eq. 55 Woitke & Helling (2003)) captures these processes acting on the distribution function of cloud particles in volume space $f(V)$ [cm^{-6}], for cloud particles in the volume interval [V, $V + \mathrm{d}V$],

$$\frac{\partial}{\partial t}\left(f(V)\mathrm{d}V\right) + \nabla \cdot \left(\left[\boldsymbol{v}_{\mathrm{gas}} + \mathring{\boldsymbol{v}}_{\mathrm{dr}}(V)\right]f(V)\mathrm{d}V\right) = \sum_{k} R_{k}\mathrm{d}V, \qquad (2.2)$$

where $\boldsymbol{v_{gas}}$ is the hydrodynamic gas velocity. $\mathring{\boldsymbol{v}}_{\mathrm{dr}}(V)$ is the gas-particle relative velocity of the cloud particles of volume V, calculated as the velocity for a spherical grain where drag and gravity are in force balance (see Eq. 2.1). The left hand side terms express the time and spatial evolution of (cloud) particles of volume V moving with the (cloud) particle velocity expressed as $v_{\mathrm{gas}} + v_{\mathrm{dr}}(V)$. The right hand side is composed of the net rates of processes (R_{k}) causing cloud particles to grow/evaporate into/out of the volume interval [$V, V + \mathrm{d}V$].

Two approaches have been developed in order to solve Eq. 2.2: the binning method, and the moment method, as discussed in Sect. 1.4.2. We now turn to describing the moment method as used in this work.

2.2.1   The Moment Method

The moment method was initially developed by Gail & Sedlmayr (1988) and expanded to include mixed material cloud particles ('dirty grains') by Dominik & Tielens (1997). Woitke & Helling (2003) and Helling & Woitke (2006) expanded the method to enable the modelling of gravitational

settling of mixed-material cloud particles forming in exoplanet and brown dwarf atmospheres. A set of moment equations is derived by multiplying Eq. 2.2 by $V^{j/3}$ (j = 0, 1, 2, 3, ...) and integrating over the volume space of cloud particles resulting in the conservation equation

$$\frac{\partial}{\partial t}(\rho L_j) + \nabla \cdot (\boldsymbol{v}_{\text{gas}}\rho L_j) = \int_{V_1}^{\infty} \sum_k R_k V^{j/3} \mathrm{d}V - \nabla \cdot \int_{V_1}^{\infty} f(V) V^{j/3} \mathring{\boldsymbol{v}}_{\text{dr}} \mathrm{d}V. \tag{2.3}$$

Where each moment is is represented by one such conservation equation. The moments are defined by an integral over volume space:

$$\rho L_j = \int_{V_1}^{\infty} f(V) V^{j/3} \mathrm{d}V. \tag{2.4}$$

Where ρ is the local gas density, and V_1 is the minimum cloud particle volume considered. Here we define the size of a cloud condensation nucleus as 1000 times the volume of a TiO_2 molecule, and this size is then used as the lower bound of the integration. For the jth moment, the unit of ρL_j is $cm^{(j-3)}$. From Eq. 2.4 and the definition of the distribution function $f(V)$ it is clear that when j = 0,

$$n_{\text{d}} = \rho L_0 \, [\text{cm}^{-3}]. \tag{2.5}$$

Furthermore, average cloud particle properties can be similarly computed from the moments, such as the mean particle size ($\langle a \rangle$),

$$\langle a \rangle = \left(\frac{3}{4\pi}\right)^{1/3} \frac{L_1}{L_0} \, [\text{cm}]. \tag{2.6}$$

In addition higher order moments can be used to derive similar average quantities with different weighting. Of particular interest are $\langle a \rangle_{\text{A}}$, the surface-averaged mean particle size, and correspondingly the number density to $n_{\text{d},0} = n_{\text{d,A}}$, which are defined as

$$\langle a \rangle_{\text{A}} = \left(\frac{3}{4\pi}\right)^{1/3} \frac{L_3}{L_2}, \qquad \text{and} \qquad n_{\text{d,A}} = \frac{\rho L_2^3}{L_3^2}. \tag{2.7}$$

The solution of the moment equations provides us with information about the local mean

particle sizes (Eq. 2.6), the number density of cloud particles (Eq. 2.5), and also the material composition of the cloud particles. These all vary with height in the atmosphere because they depend on local thermodynamic conditions as this affects properties such as the supersaturation ratio of condensation species, affecting their thermal stability, resulting in either condensation or evaporation.

2.2.2 Kinetic Cloud Formation in a Subsonic, Free Molecular Flow

The atmospheres of exoplanets cover a large region of parameter space, which may result in many hydrodynamic regimes for cloud particles falling in the atmosphere. Two major discriminators for these regimes is between subsonic and supersonic flow for cloud particles falling in an atmosphere ($v_{dr} \ll c_T$ and $v_{dr} \gg c_T$ respectively[2]), and the Knudsen number $Kn = l_{mfp}/2a$. The Knudsen number characterises the cloud particle-gas interaction in regards to the drag force the cloud particle feels, where l_{mfp} is the mean free path of a gas molecule. Woitke & Helling (2003) have derived forms for the master equations for cloud formation in the case of the subsonic free molecular flow ($Kn \gg 1$) and the laminar viscous flow cases ($Kn \ll 1$). As Woitke & Helling (2004) have discussed the $Kn \gg 1$ is appropriate for most of the atmosphere of exoplanets and brown dwarfs, with an exception for the deep atmosphere (see their Sect. 4.1). However, treatment of this transition is non-trivial in the moment method as Kn depends on particle size. Thus different cloud particles in the size distribution, over which the moments are integrated, would undergo the transition from one Knudsen number regime to another at different points in the atmosphere. Thus for this model we assume $Kn \gg 1$. In a subsonic free molecular flow (large Knudsen numbers, lKn), and 1D plane parallel geometry (z direction only), Eq. 2.3 becomes (Woitke & Helling 2004)

$$\frac{\partial}{\partial t}(\rho L_j) + \frac{\partial}{\partial z}(v_{gas}\rho L_j) = V_1^{j/3} J(V_1) + \frac{j}{3}\chi_{lKn}^{net}\rho L_{j-1} + \xi_{lKn}\frac{\partial}{\partial z}\left(\frac{L_{j+1}}{c_T}\right). \tag{2.8}$$

The right-hand-side terms, in order, describe nucleation (seed formation, with $J(V_1)$ being the current of cloud particles through the lower boundary of integration in volume space), growth/evaporation of existing cloud particles (χ_{lKn}^{net} – net growth velocity, Eq. 66 in Woitke & Helling 2003) and gravitational settling (ξ_{lKn}– the drag force density).

---

[2]For consistency with (Woitke & Helling 2003) we stick with the above definitions of subsonic and supersonic regimes, the criterion of $v_{dr} \ll c_T$ and $v_{dr} \gg c_T$ comes from the asymptotic behaviour of the drag force relation used (Eq. 13 used by Woitke & Helling 2003), derived by Schaaf (1963). The modal gas molecule velocity c_T is related to the sound speed c_s by $c_s = \sqrt{\gamma/2}c_T$, where γ is the adiabatic index. For a diatomic gas $\gamma = 7/5$, this introduces a ~ 16% difference between the velocities.

2.2.3 Inclusion of Mixing to Form Static Clouds

Assuming a quasi-static atmosphere ($v_{\text{gas}} = 0$) with a stationary cloud particle population ($\partial L_j/\partial t = 0$), the left hand side of Eq. 2.8 is zero (Woitke & Helling 2004). This therefore leaves the moments only as dependent on z, thus from here on we use total derivatives with respect to height in the atmosphere. As all terms on the right hand side are positive, this leads to the trivial solution of no stable cloud can form in a static atmosphere (see Appendix A in Woitke & Helling 2004). However, since clouds do form and atmospheres are seldom truly static, a parameterisation for hydrodynamic mixing processes is introduced using a mixing timescale τ_{mix}. Details of the specific mixing parameterisations used in each chapter are discussed in Sect. 2.2.7. Thus Eq. 2.8 becomes

$$\frac{\rho L_j}{\tau_{\text{mix}}} = V_1^{j/3} J(V_1) \; + \; \frac{j}{3} \chi_{\text{lKn}}^{\text{net}} \rho L_{j-1} \; + \; \xi_{\text{lKn}} \frac{\mathrm{d}}{\mathrm{d}z} \left(\frac{L_{j+1}}{c_{\text{T}}} \right), \tag{2.9}$$

re-arranging arrives at (Eq. 7 in Woitke & Helling 2004):

$$-\frac{\mathrm{d}}{\mathrm{d}z} \left(\frac{L_{j+1}}{c_{\text{T}}} \right) = \frac{1}{\xi_{\text{lKn}}} \left(V_1^{j/3} J(V_1) \; + \; \frac{j}{3} \chi_{\text{lKn}}^{\text{net}} \rho L_{j-1} \; - \; \frac{\rho L_j}{\tau_{\text{mix}}} \right). \tag{2.10}$$

2.2.4 Closure Condition

A closure condition for L_0 is required for the set of Eqs. 2.10 to be solvable (Sect. 2.4.1 Woitke & Helling 2004). The shape of the distribution function of particles sizes is not known in the moment method, but assuming by assuming certain analytic forms one can be derived from the moments. For example, a double Dirac cloud particle size distribution function:

$$f(a) = n_0 \delta(a - a_0) \; + \; n_1 \delta(a - a_1). \tag{2.11}$$

Applying $V = (4\pi/3)a^3$ and using the definition of the moment in particle space (as in Dominik et al. 1989; Gauger et al. 1990):

$$K_j = \int_{a_1}^{\infty} f(a)a^j \mathrm{d}a = \left(\frac{3}{4\pi} \right)^{j/3} \rho L_j. \tag{2.12}$$

Integrating Eq. 2.12 results in $K_j = n_0 a_0^j + n_1 a_1^j$ for the double-Dirac $f(a)$ function. Therefore,

$$\rho L_0 = n_0 + n_1. \tag{2.13}$$

The four parameters of the distribution function $f(a)$; a_0, a_1, n_0, n_1 can be expressed in terms of the K_j-moments: a_0 is the positive root of $a_0^2(K_2^2 - K_1 K_3) + a_0(K_1 K_4 - K_2 K_3) + (K_3^2 - K_2 K_4) = 0$, from this n_0, n_1 follow as (Appendix A of Helling et al. 2008c):

$$n_0 = \frac{(a_0 K_1 - K_2)^3}{(a_0 K_2 - K_3)(K_3 - 2a_0 K_2 + a_0^2 K_1)}, \tag{2.14}$$

$$n_1 = \frac{K_1 K_3 - K_2^2}{a_0(K_3 - 2a_0 K_2 + a_0^2 K_1)}. \tag{2.15}$$

This condition is used in this work, the same as by Helling et al. (2008c), where Equations 2.13, 2.14, and 2.15 provides the closure condition for L_0.

2.2.5 Heterogeneous Cloud Particles

Within an atmosphere, the thermodynamic conditions are not homogeneous and may, for example, change with height. Consequently, the changing temperature will alter the equilibrium chemical composition of the atmosphere. Both, the locally changing temperature and the changing chemical composition causes a changing thermal stability for cloud particle condensates throughout the exoplanet and brown dwarf atmosphere. Each cloud particle is composed of condensate species s where each have the volume fractions V_s/V (Helling & Woitke 2006) defined as

$$V_s = \rho L_3^s = \int_{V_l}^{\infty} f(V) V \frac{V^s}{V} dV. \tag{2.16}$$

V^s is the volume of material species s in an individual cloud particle of volume V. It is assumed that all cloud particles have the same material composition in a given atmospheric layer, such that

$$V_{\text{tot}} = \sum_s V_s \quad \Rightarrow \quad L_3 = \sum_s L_3^s \tag{2.17}$$

The cloud particle mass density is defined as $\rho_s = \sum_i \rho_{s,i} V_i / V_{\text{tot}}$.[3] Thus in addition to the set

---

[3] Where here we use the dummy variable i for each condensate species to avoid confusion between ρ_s for cloud particle material density and the typical ρ_s for the material density of material species s.

of Eqs. 2.10 for $L_1, L_2, L_3, ...$ and the closure condition, an additional moment equation for each species s is solved,

$$-\frac{d}{dz}\left(\rho_s \frac{L_4^s}{c_T}\right) = \frac{1}{\xi_{lKn}}\left(V_1^{j/3}J(V_1) + \frac{j}{3}\chi_{lKn}^{net}\rho L_2 - \frac{\rho L_3^s}{\tau_{mix}}\right). \tag{2.18}$$

A closed set of equation that describes the formation of cloud particles in an atmospheric environment is therefore composed of Eq. 2.13 for L_0, Eqs. 2.10 for L_1, L_2, L_3, and Eqs. 2.18 for the L_3^s for each condensate material s.

2.2.6 Element Conservation

Throughout the processes of cloud formation, element conservation must be observed for both the gas phase and condensate phase together. From Eq. 8 (Woitke & Helling 2004) we have the condition for each element i:

$$\frac{n_{\langle H\rangle}(\epsilon_i^0 - \epsilon_i)}{\tau_{mix}} = v_{i,0}N_1 J_* + \rho L_2 \chi_{i,s,lKn}^{net} \tag{2.19}$$

where ϵ_i is the hydrogen normalised abundance of element i, ϵ_i^0 are the undepleted element abundances. $\chi_{i,s,lKn}^{net}$ is the growth velocity but with additions for each element i and reaction species s (cf Eq. 2 and Eq. 8 Woitke & Helling (2004) with Eq. 10 Helling et al. (2008c)).

2.2.7 Model Setups

The precise setup for the cloud condensate chemistry, linked to equilibrium gas-phase chemistry and mixing, changes slightly between the chapters of this work, these are detailed below.

For Chapters 3 & 4 nucleation rates use modified classical nucleation theory (see Lee et al. (2015c) for a detailed description). We calculated nucleation rates J_i for i = TiO$_2$[s], SiO[s], and C[s]. The sum of the three rates is the total nucleation rate $J_* = \Sigma_i J_i$ [cm^3 s^{-1}]. A total of 15 cloud condensation species are considered (TiO$_2$[s], Mg$_2$SiO$_4$[s], MgSiO$_3$[s], MgO[s], SiO[s], SiO$_2$[s], Fe[s], FeO[s], FeS[s], Fe$_2$O$_3$[s], Fe$_2$SiO$_4$[s], Al$_2$O$_3$[s], CaTiO$_3$[s], CaSiO$_3$[s], C[s]), which can condense by 126 gas-surface reactions.

For the gas phase, for 191 molecules, atomic and ionic species, chemical equilibrium is assumed and consistently linked with cloud formation through element depletion. The

undepleted element abundances are assumed to be solar (Grevesse et al. 1993). The local turbulent gas-mixing timescale is parameterised by the convective overshooting approach, where the mixing timescale τ_{mix} in Eq. 2.10 is calculated as in Eq. 9 of (Woitke & Helling 2004):

$$\tau_{\text{mix}} = \log_{10}(\tau_{\text{mix}}^{\text{min}}) + \beta \max[0, \log_{10}(p_0) - \log_{10}(p(z))]. \tag{2.20}$$

Where p_0 and $\tau_{\text{min}}^{\text{max}}$ are the pressure of the upper boundary of the convective region and the minimum mixing timescale in the convective region respectively. Here a value of $\beta = 1.0$ is used for Chapter 3, whilst for Chapter 4, $\beta = 2.2$ is used which is consistent with the Drift-Phoenix profiles. This does affect significantly the mass of clouds that condenses in the atmospheres and the extent of condensation in the atmosphere, as discussed in detail in comparison to a diffusive cloud model by Woitke et al. (2020).

For Chapter 5, solar abundances are also assumed for undepleted elements, however (Asplund et al. 2009) values are taken. Furthermore, KCl[s] is included as a nucleation and condensate species for WASP-43b. Thus an additional 3 gas-phase species are included (K, Cl, and KCl) along with the gas-surface reactions for condensing/evaporating KCl[s]. The mixing timescale is defined as the ratio of the pressure scale height H_p and local vertical gas velocity from the GCM results $\langle v_z \rangle$:

$$\tau_{\text{mix}} = \frac{H_p}{\langle v_z \rangle}. \tag{2.21}$$

2.3 Observable Properties of Cloud Particles

Cloud particles in atmospheres and aerosols in general (e.g. including hazes) can have significant impact on radiative transfer in the atmosphere as they scatter and absorb photons. Scattering and absorption for any medium is defined by its cross sections C_{sca}, C_{abs} [cm^2].[4] The extinction cross section of the medium is then defined as the sum of these cross sections, $C_{\text{ext}} = C_{\text{sca}} + C_{\text{abs}}$. It is quite common then to express these cross sections in terms of 'efficiency factors' by dividing by the cross sectional area of the particle. With homogenous (one material consistent throughout), monodisperse, spherical cloud particles of radius a this gives the total extinction efficiency as

---

[4]Quite frequently these are represented by σ_{sca}, σ_{abs}, but for consistency with previous work here we stick with this alternative notation.

$$Q_{ext} = \frac{C_{ext}}{\pi a^2} = \frac{C_{sca}}{\pi a^2} + \frac{C_{abs}}{\pi a^2}. \qquad (2.22)$$

The efficiency factors for scattering and absorption (Q_{sca}, Q_{abs}) are similarly defined. From the definition of the extinction efficiency, follows the concept of optical depth τ, which is the discriminator between whether a medium is opaque ($\tau \gg 1$) or transparent ($\tau \ll 1$). The optical depth is (again for a medium of monodisperse spherical particles of radius $a(z)$) defined as

$$\tau(z') = \int_0^{z'} Q_{ext}(\lambda, a)\pi a^2(z)n_d(z)dz. \qquad (2.23)$$

The form of this equation is reminiscent of that of the collisional mean free path of a particle moving through a medium of particles distributed with some number density n_d, reconsigning $Q_{ext}(\lambda, a)\pi a^2 = C_{ext}$ in the above equation represents the 'effective cross sectional area' of extinction by the scattering/absorbing particles. This similarity naturally explains the meaning of an optical depth of unity $\tau(z) = 1$, z in this case is the physical distance that a photon can travel through the medium before experiencing an absorption or scattering event. Often for convenience with Eq. 2.23, the 'mass extinction coefficient' κ_{ext} [$cm^2\,g^{-1}$] is defined as,

$$\kappa_{ext} = \frac{Q_{ext}\pi a^2 n_d}{\rho}. \qquad (2.24)$$

Where this now defines the extinction coefficient for cloud particles per unit mass of gas in the atmosphere. It can easily be shown that $n_d/\rho = N/(\mu m_H)$ (i.e. the number of cloud particles N per mass of gas molecules in the atmosphere μm_H). Thus Eq. 2.23 becomes

$$\tau(z') = \int_0^{z'} \kappa_{ext}\rho dz. \qquad (2.25)$$

The optical depth is an important concept for radiative transfer in an atmosphere as it dictates which regions of the atmosphere are accessible to radiation, both from a planet's host star and for internal heat. It is also important for observations as only the region where $\tau < 1$ is observable. However, so far we have not described the methods used to calculate the extinction/scattering/absorption efficiency factors of cloud particles central to the calculations above.

2.3.1 Calculating Scattering and Extinction Efficiencies of Cloud Particles

To asses the observational impact of the cloud particles we use Mie theory, an analytic model for the opacity of spherical cloud particles (Mie 1908). Mie theory is a 'bridging theory' between the regime of Rayleigh scattering and geometric optics. These regimes are discriminated by the size parameter:

$$x = \frac{2\pi a}{\lambda} \tag{2.26}$$

for a particular size of particle a and wavelength λ.

$x \ll 1$ is the Rayleigh regime, in this case the scattering efficiency is $Q_{\text{sca}} \propto a^6 \lambda^{-4}$ and the absorption efficiency is $Q_{\text{abs}} \propto a^3 \lambda^{-1}$. However, the total extinction efficiency ($Q_{\text{ext}} = Q_{\text{sca}} + Q_{\text{abs}}$) is often dominated by the scattering rather than absorption for cloud particles in gas giant exoplanet atmospheres. This is because the imaginary part of the refractive index (k) is orders of magnitude smaller than the real part (n) for typical cloud materials (e.g. $MgSiO_3$[s]) at optical wavelengths, where they have been previously observed, for example by Lecavelier Des Etangs et al. (2008). $x \gg 1$ is the geometric optics regime, in this limit the extinction efficiency Q_{ext} tends towards 2 for large enough size parameter. Thus the cross section is twice the geometric cross section of the cloud particle (Min 2015).

Between these regimes ($x \sim 1$) Mie theory is necessary to calculate the efficiency factors accurately. Using notation based on (Bohren & Huffman 1983), the extinction and scattering cross sections can be written as:

$$Q_{\text{ext}} = \frac{2}{x^2} \sum_{i=1}^{\infty} (2i + 1) \Re(a_i + b_i) \tag{2.27}$$

$$Q_{\text{sca}} = \frac{2}{x^2} \sum_{i=1}^{\infty} (2i + 1)(a_i a_i^* + b_i b_i^*) \tag{2.28}$$

where a_i, b_i are complex functions composed of Ricatti-Bessel functions, however we neglect a further detailed discussion of the the computation here (see Bohren & Huffman 1983). It is worth reiterating here that all that has been discussed here assume homogeneous cloud particles, which are spherical of a radius a, such simplifications are examined in Chapter 3. From the extinction

and scattering efficiencies it is also possible to compute the single scattering albedo (A_S) for a distribution $n_d(a)$ (see Wolf & Voshchinnikov 2004),

$$A_S(\lambda) = \frac{\int_{a_{\min}}^{a_{\max}} n_d(a)\, C_{\text{sca}}(\lambda, a)\, da}{\int_{a_{\min}}^{a_{\max}} n_d(a)\, C_{\text{ext}}(\lambda, a)\, da}.$$

(2.29)

For a monodispere (Dirac delta) distribution the above simplifies to

$$A_S(\lambda) = \frac{Q_{\text{sca}}}{Q_{\text{ext}}}.$$

(2.30)

2.3.2 Effective Medium Theory

Mie theory assumes homogeneous cloud particles, that is to say the entire particle consists of one consistent material with a single complex refractive index ($n + ik$) for a given wavelength. However, we have heterogeneous cloud particles with volume V_{tot} and volume fractions V_s/V_{tot} of different solid species s. In order to model these with Mie theory we produce an 'effective refractive index' of the cloud particles weighted by the respective volume fraction of each of the condensate species. Two methods for calculating this are used, the method of Bruggeman (1935) is the default and the method by Looyenga (1965) used for cases of non-convergence of the former. The Bruggeman mixing rule (Bruggeman 1935) gives

$$\Sigma_s \left(\frac{V_s}{V_{\text{tot}}} \right) \frac{\epsilon_s - \epsilon_{\text{eff}}}{\epsilon_s + 2\epsilon_{\text{eff}}} = 0$$

(2.31)

where ϵ_s is the dielectric constant of an individual condensate material in the cloud particle (therefore the refractive index of the material is $m_s = n + ik = \sqrt{\epsilon_s}$). The desired effective dielectric constant is ϵ_{eff} and it is found by solving Eq. 2.31 iteratively with the Newton-Raphson method.

2.3.3 Refractive Indices of Cloud Condensates

We used established Mie theory routines to calculate cloud particle opacities for log-linearly spaced wavelengths spanning the range $\lambda = 0.1$–$1000\,\mu$m. We used optical constants identical to those used by Helling et al. (2019) (reproduced in Table 2.1 and shown in Figs. 2.2 and 2.3). Materials where the experimental data does not cover the full wavelength grid are treated as

31

described by Lee et al. (2016). In the cases where the experimental source data does not extend to short enough wavelengths, constant refractive index values are assumed. For non-conducting materials, where experimental source data does not cover long enough wavelengths the real part of the refractive index n is assumed to be constant, the imaginary part k reduces linearly with increasing wavelength. For conductors (Fe[s] and C[s]) at longer wavelengths the data is extrapolated linearly in log-log space. The extrapolated regions can be seen as dashed lines in Figs. 2.2 and 2.2. Our data largely consists of values for amorphous materials. Whilst Kitzmann & Heng (2018) have argued for the use of amorphous condensates, Helling & Rietmeijer (2009) previously suggested that exoplanet cloud particles can be crystalline at temperatures exceeding 900 K because the thermal energy is sufficient to allow for lattice rearrangement within the cloud particle. The internal structure of the cloud particle material has implications for the spectra of hot and ultra-hot Jupiters at wavelengths that will be observable by JWST MIRI, particularly for the sharpness and shape of the 9.7 μm and 18 μm silicate features.

Table 2.1: References and wavelength coverage of optical constants for condensate materials.

Material Species	Reference	Wavelength Range (μm)
TiO_2[s] (rutile)	Zeidler et al. (2011)	0.47–36
SiO_2[s] (alpha-Quartz)	Palik (1985), Zeidler et al. (2013)	0.00012–10000
SiO[s] (polycrystalline)	Philipp in Palik (1985)	0.0015–14
$MgSiO_3$[s] (glass)	Dorschner et al. (1995)	0.20–500
Mg_2SiO_4[s] (crystalline)	Suto et al. (2006)	0.10–1000
MgO[s] (cubic)	Palik (1985)	0.017–625
Fe[s] (metallic)	Palik (1985)	0.00012–285
FeO[s] (amorphous)	Henning et al. (1995)	0.20–500
Fe_2O_3[s] (amorphous)	Amaury H.M.J. Triaud (priv. comm.)	0.10–1000
Fe_2SiO_4[s] (amorphous)	Dorschner et al. (1995)	0.20–500
FeS[s] (amorphous)	Henning (unpublished)	0.10–100000
$CaTiO_3$[s] (amorphous)	Posch et al. (2003)	2–5843
$CaSiO_3$[s]	No data - treated as vacuum	N/A
Al_2O_3[s] (glass)	Begemann et al. (1997)	0.10–200
C[s] (graphite)	Palik (1985)	0.20–794
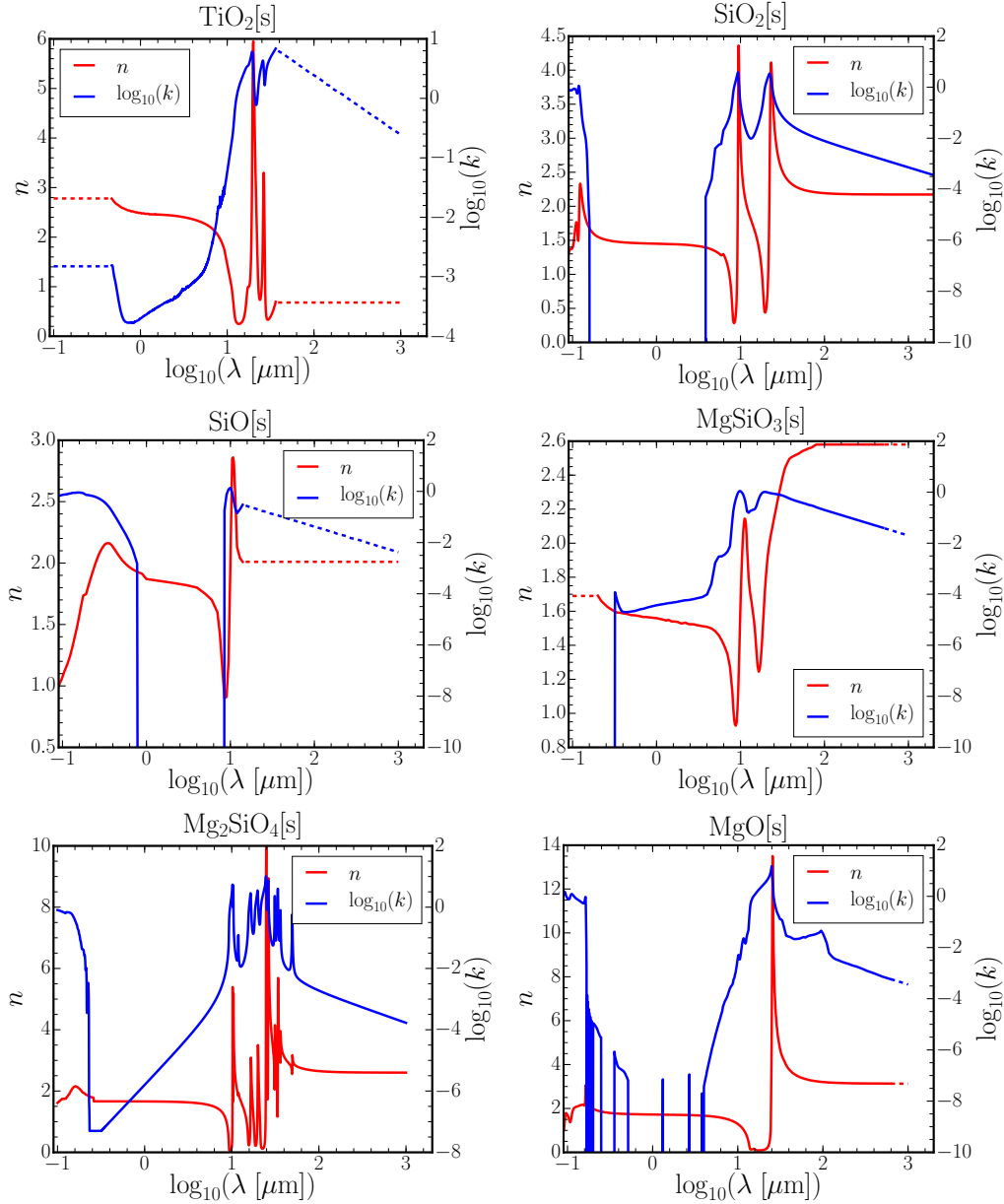
Figure 2.2: Real (*n*) and imaginary (*k*) refractive indexes (red and blue, respectively) for the condensate materials, shown across the wavelength range 0.1–1000 μm. Solid lines indicate regions for which reference data exists, and dashed lines indicate regions that were extrapolated. References are found in Table 2.1. Continues overleaf.
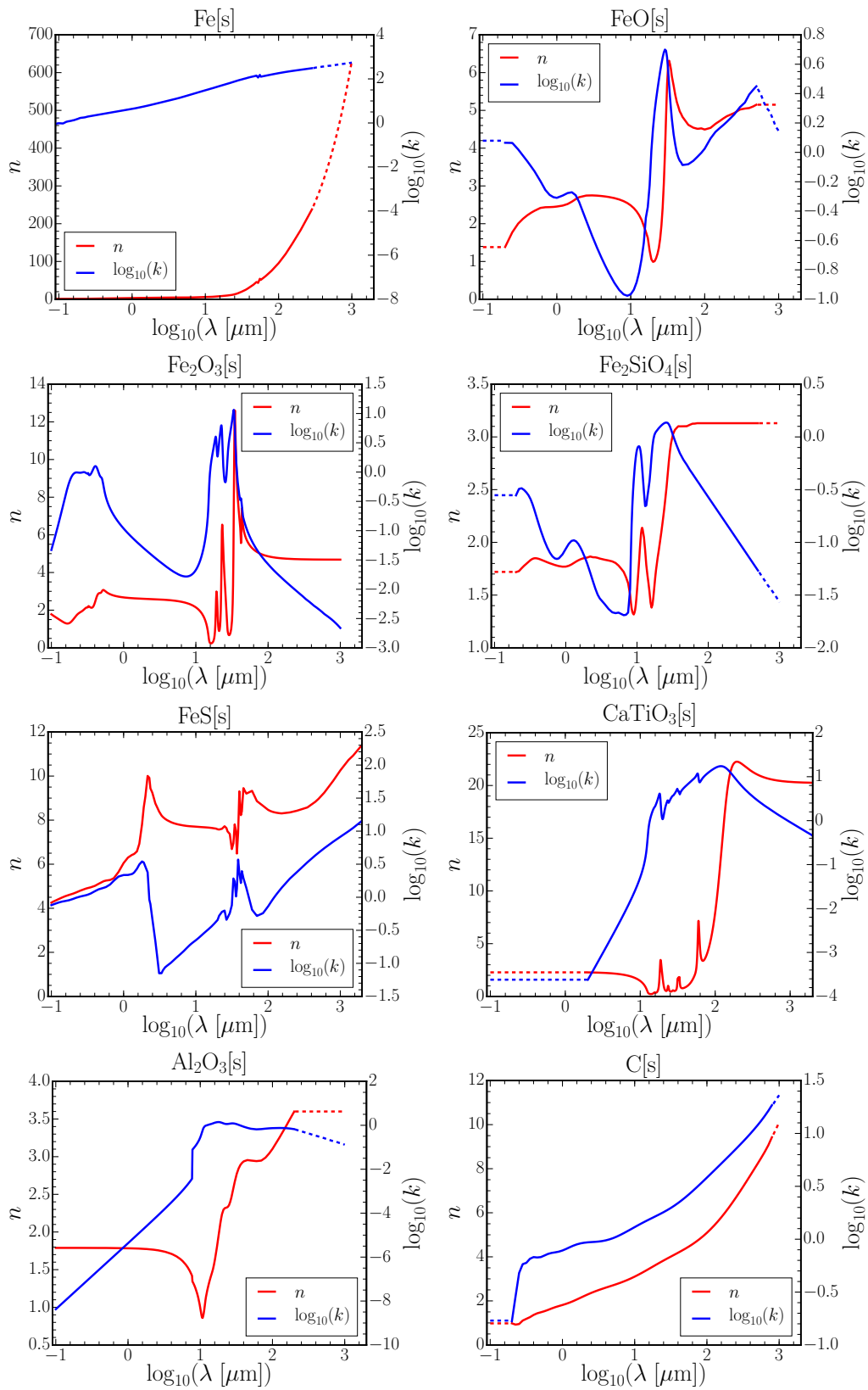
Figure 2.3: Continuation of Fig. 2.2.

"A mote of dust suspended in a sunbeam."

- Carl Sagan, *Pale Blue Dot: A Vision of the Human Future in Space*, 1994

3

Mineral Snowflakes: Irregular, Micro-porous and Non-Monodisperse Cloud Particles

3.1 Declaration

This chapter is adapted from:

- 'Mineral snowflakes on exoplanets and brown dwarfs: Effects of micro-porosity, size distributions, and particle shape', Samra, D., Helling, Ch., Min, M. 2020, A&A, 639, A107. All co-authors provided comments on the final manuscript of the paper.

3.2 Introduction

Micro-porosity is the porosity arising from the organisation of the condensate monomers (e.g. Mg_2SiO_4 in $Mg_2SiO_4[s]$) within a cloud particle during growth. This is different from the porosity that can be used to characterise aggregates that originate from particle-particle collision processes (coagulation, e.g. Dominik & Tielens (1997); Blum & Wurm (2000)), which we do not consider here but address in Chap. 4.

On Earth, the material density of water ice is dependent on the ambient temperature at formation. Snowflakes are known to form many types of crystal structures that can be up to 84%

porous for millimetre-sized cloud particles when compared to ice material density (Hales 2005), leading to the possibility of altitude-dependent porosity in terrestrial snow clouds. Earth-like exoplanets, mini-Neptunes, and T-type brown dwarfs may form water clouds, composed of liquid or solid particles, but warmer planets and brown dwarfs of L-type and later have been shown to form cloud particles made of a mix of materials that is dominated by Mg, Si, Fe, and O and to a lesser extent by Ti, Al, K and other elements (e.g. Witte et al. 2009; Lee et al. 2015b; Helling et al. 2019). There are many ways in which this micro-porosity might be incorporated into mineral cloud particles, for example lattice faults at the interfaces between two different condensation species owing to the different lattice structures.

Even for homogeneous growth, single species often have multiple crystal structures (Sood & Gouma 2013), which can also generate lattice faults at their interfaces. For example, the TiO_2[s] rutile and anatase forms are both stable at atmospheric pressures for temperatures greater than 1100 K (Jung & Imaishi 2001; Hanaor & Sorrell 2010). Additionally, within crystal structures, there are many known types of defect that might further decrease material density (e.g. Schottky defects in TiO_2[s] and MgO[s] crystals; Ménétrey et al. 2004).

Furthermore, because cloud particles made of a mix of many thermally stable materials fall into warmer atmospheric regions, the low-temperature materials (such as SiO[s], MgSiO3[s]) become thermally unstable, they evaporate and leave behind a skeleton made of high-temperature materials (such as Fe[s], TiO2[s], Al2O3[s]). Whilst this may be a source of micro-porosity of cloud particles, Juncher et al. (2017) noted that this may also lead to a reduction in micro-porosity because the structural integrity of the particle is weakened and dangling structures break off. These micro-porous mineral cloud particles we call 'mineral snowflakes'.

Outside of the binning method, which has previously been discussed in Sect. 1.4.2, cloud particle size distributions in the literature often use assumed distribution forms, where the value of the parameters describing the distribution are derived from the observational data. Using again the example of the Ackerman & Marley (2001) model, this uses a fixed log-normal distribution for particle size. Here we are also interested in the effects of a particle size distribution on the cloud spectral properties. Because of practical considerations, retrievals of exoplanet atmospheres try to limit the parameter space as much as possible, often assuming particle sizes a-priori or modelling clouds as a grey cloud deck (e.g. Madhusudhan et al. (2011); Benneke & Seager (2012); Kreidberg et al. (2014)). Within the moment method kinetic cloud formation modelling it is possible to derive

a size distribution (Sect. 3.3.3). We therefore investigate the possible nature of cloud particle size distributions arising from microphysical modelling of the clouds.

This chapter discusses how simplifying assumptions about cloud particles, such as sphericity, homodispersity (monodisperse size distribution), and compactness, affect the physical and spectral properties of clouds. This is important as future instruments will be capable of providing higher resolution spectra, such as the next-generation CRIRES+ (CRyogenic high-resolution InfraRed Echelle Spectrograph; Follert et al. 2014), or observations with a higher signal-to-noise ratio such as are expected from the JWST (James Webb Space Telescope; Gardner et al. 2006) and the ARIEL (Atmospheric Remote-sensing Infrared Exoplanet Large-survey; Tinetti et al. 2018), and this will require a better understanding of the effects of simplifying assumptions in models on the distribution and optical effects of clouds. We investigate this in the framework of our kinetic non-equilibrium cloud formation model. We confine the study to atmospheric models typical of brown dwarfs and Jupiter-size gas giant exoplanets, but we anticipate a wider applicability to other exoplanets such as mini-Neptunes, super-Earths, and lava worlds.

3.3 Approach

3.3.1 Inputs Profiles

For this chapter we use as input for our cloud formation model the 1D Drift-Phoenix atmosphere models (Dehn 2007; Helling et al. 2008b; Witte et al. 2009, 2011), where cloud feedback on the temperature pressure profiles was consistently included. The Drift-Phoenix models are the result of iterating between the kinetic cloud formation model (referred to as DRIFT) with the general-purpose atmosphere code Phoenix (Hauschildt & Baron 1999). Phoenix solves equilibrium chemistry, hydrostatic equilibrium pressure structure with convection included using Mixing Length Theory (MLT), and radiative transfer for a given p_{gas}-T_{gas} structure. Cloud effects are included as a depletion of gas-phase element abundances for the chemical equilibrium calculation, and additional opacity sources for the radiative transfer calculation, where cloud properties were calculated by Drift-Phoenix using the p_{gas}-T_{gas} from Phoenix.

This chapter uses a subset of the models covering a grid of T_{eff} = 1200, 1800, and 2400 K. We also used surface gravities $\log(g\,[\mathrm{cm\,s^{-2}}])$ = 3.0 and 5.0, which is representative of gas giant exoplanets, and brown dwarfs and young gas giant exoplanets (Witte et al. 2009).

3.3.2 Micro-porosity

The micro-porosity of cloud particles is modelled by introducing an effective material density for each material (ρ_s^{eff}). To do this, we modify the material density ρ_s by a 'micro-porosity fraction' (f_{por}), which for this study was assumed constant for all condensate materials (s) and atmospheric layers. Hence

$$\rho_s^{\text{eff}} = \rho_s \left(1 - f_{\text{por}} \right). \tag{3.1}$$

For opacity calculations we incorporate the additional volume introduced by the micro-porosity factor as vacuum (using the effective medium theory), with the complex refractive index $m = 1$ (i.e. $n = 1$, $k = 0$). This simple approach enables the investigation of the effect of micro-porosity on cloud spectral and material properties for a variety of f_{por} values. Previously, an effective medium approach was used for dust in protoplanetary discs (Woitke et al. 2016) assuming a value of $f_{\text{por}} = 0.25$.

3.3.3 Cloud Particle Size Distribution

The results of our cloud formation models for the moments L_j (Eq. 2.4) are used to reconstruct a cloud particle size density distribution function $f(a)$ [cm^{-4}] through the related moments in radius-space K_j (Eq. 2.12):

$$K_j = \left(\frac{3}{4\pi} \right)^{j/3} \rho L_j = \int_{a_l}^{\infty} f(a) \, a^j \mathrm{d}a. \tag{3.2}$$

Here we assume the particle size to be normally distributed such that particle size follows the Gaussian distribution:

$$g(a) = \frac{1}{\sigma \sqrt{2\pi}} \exp\left(-\frac{(a - \overline{a})^2}{2\sigma^2} \right). \tag{3.3}$$

Thus the actual density distribution function of particle size for a given atmospheric layer is given as $f(a) = n_{\text{d}}^{\text{Gauss}} g(a)$. The overall distribution function is specified by three parameters: the mean particle size $\overline{a}$ [μm], the standard deviation σ [μm], and the total number density of cloud particles $n_{\text{d}}^{\text{Gauss}}$ [cm^{-3}]. Following the approach by Helling et al. (2008c), substituting Eq. 3.3 into

Eq. 3.2 and integrating across all cloud particle radii (extending the lower limit of the integral to $-\infty$), the parameters of the distribution function can be written in terms of the moments in radius-space, K_j, $j = 0, 1, 2, 3, 4$, as

$$n_{\mathrm{d}}^{\mathrm{Gauss}} = \frac{4K_1^2}{3K_2 \pm \sqrt{9K_2^2 - 8K_1K_3}}, \tag{3.4}$$

$$\bar{a} = \frac{K_1}{n_{\mathrm{d}}^{\mathrm{Gauss}}}, \tag{3.5}$$

$$\sigma = \sqrt{\frac{1}{n_{\mathrm{d}}^{\mathrm{Gauss}} \left(K_2 - n_{\mathrm{d}}^{\mathrm{Gauss}} \bar{a}^2\right)}}. \tag{3.6}$$

The derived distribution does not feedback on the moments, and therefore the cloud formation is unaffected by its assumed form. In other words, the derived parameters represent the information encapsulated by the moments, but the moments remain the same regardless of the reconstructed size distribution. The mean particle size of the distribution $\bar{a}$ (Eq. 3.5) is distinct from the average particle size from the moments $\langle a \rangle$ (Eq. 2.6). Combining Eqs. 3.5 and 3.2, we can write

$$\bar{a} = \left(\frac{3}{4\pi}\right)^{1/3} \frac{\rho L_1}{n_{\mathrm{d}}^{\mathrm{Gauss}}}. \tag{3.7}$$

Comparing this with the mean particle size (Eq. 2.6), we see that $\bar{a} = \langle a \rangle$ only if $n_{\mathrm{d}}^{\mathrm{Gauss}} = \rho L_0 = n_{\mathrm{d}}$. This demonstrates that $n_{\mathrm{d}}^{\mathrm{Gauss}}$ must be related to the total local cloud particle number density for a monodisperse distribution (n_{d}). The zeroth moment, L_0, is used as the closure condition of the moment equations (Helling et al. 2008c, , Eq. 11), thus we did not use it to define $n_{\mathrm{d}}^{\mathrm{Gauss}}$. Hence, $\bar{a}$ and $\langle a \rangle$ are not analytically the same, but for the atmospheres considered here, we find that they differ by no more than 20% in the most extreme case (Fig. A.4).

3.3.4 Cloud Particle Opacity with a Size Distribution

The opacity of non-monodisperse cloud particles for each atmospheric layer is calculated using the effective medium theory and the Mie theory, as introduced in Chapter 2. This is used to determine the dimensionless efficiency factors $Q_{\mathrm{sca,ext,abs}}(a)$ as a function of particle size within

the distribution. Integrating over the size distribution gives the mean cross-sections for scattering, extinction, and absorption ($\langle C_{\text{sca,ext,abs}} \rangle$ [cm^2]) as

$$\langle C_{\text{sca,ext,abs}} \rangle = \frac{\int_{a_l}^{a_u} Q_{\text{sca,ext,abs}}(a) f(a) \pi a^2 da}{\int_{a_l}^{a_u} f(a) da}. \tag{3.8}$$

We numerically integrate Eq.3.8 by choosing upper and lower limits (a_l and a_u) symmetric about the mean of the distribution. We find $a_{u/l} = \bar{a} \pm 5\sigma$ to be sufficient to fully capture the distribution effects. For a monodisperse distribution, that is, $f(a) = \delta(a - \langle a \rangle)$, it can be seen that Eq. 3.8 simplifies back to

$$C_{\text{sca,ext,abs}} = Q_{\text{sca,ext,abs}}(a)\pi a^2. \tag{3.9}$$

The single-scattering albedo for the Gaussian distribution was similarly calculated using the integral forms as in Equation 3.8 and Eq. 2.30.

3.3.5 Irregular Particle Shape

Understanding the spectral properties of non-spherical cloud particles involves modelling the interaction between the electromagnetic field and individual segments of the particles, as well as the interactions of the segments with each other. For highly non-spherical particles, it is important to take both terms into account to accurately calculate the optical properties (Min et al. 2008). Methods such as the discrete dipole approximation (DDA) (Draine & Flatau 1994; Purcell & Pennypacker 1973) model the optical properties of cloud particles with individual segments being represented by multiple dipoles. However, for very porous particles DDA requires a large number of dipoles, $\sim 10^7$ (Min et al. 2008), and thus is computationally slow.

We use the statistical approach first proposed by Bohren & Huffman (1983), where the scattering and absorption effects of non-spherical grains are simulated by averaging over a distribution of simply shaped particles such as ellipsoids, spheroids, or hollow spheres (Min et al. 2003). This approach assumes that in averaging over a distribution of such shapes for a variety of parameters (e.g. major axes for an ellipsoid), the properties become approximately independent of the individual shapes used. Thus the results describe equally well what would be the case for a more thorough calculation of a distribution of irregularly shaped particles (Min et al. 2003). In

the context of dust in protoplanetary discs, Min et al. (2003, 2005) have assessed the benefits of various shape distributions. Ellipsoids, spheroids, and hollow spheres in the Rayleigh regime were described by Min et al. (2003), and spheroids and hollow spheres for larger particles by Min et al. (2005). The authors found good agreement between the three distributions considered for the Rayleigh regime (Min et al. 2003), and they further found that hollow spheres replicate laboratory experiments of irregularly shaped quartz particles well (Min et al. 2005) for larger particles. We used the distribution of hollow spheres because it can be calculated using an extension of the Mie theory and thus yields very fast results (Min 2015).

Hollow spheres are composed of two concentric spheres: a core and a mantle, with respective radii of a_{core} and a_{mant}. The core is treated as a vacuum inclusion with a refractive index $(n, k) = (1, 0)$, and the refractive index of the mantle is taken to be that of the mixed material cloud particles for each atmospheric layer. The total mass of the 'original' compact or micro-porous cloud particle of radius a (i.e. $4\pi a^3 \rho_s / 3$) is distributed into the mantle. An individual hollow sphere is defined by the fraction of its total volume taken up by this core and can therefore be specified by the parameter

$$f_{\text{hol}} = \frac{a_{\text{core}}^3}{a_{\text{mant}}^3}, \tag{3.10}$$

hence the volume of the mantle is given by

$$V_{\text{mant}} = \frac{4\pi}{3}(a_{\text{mant}}^3 - a_{\text{core}}^3). \tag{3.11}$$

When using Eqs. 3.10 and 3.11 with ρ_s = constant, the radius of the spherical core can be written in terms of the original cloud particle radius a and f_{hol}

$$a_{\text{core}} = \frac{a f_{\text{hol}}^{1/3}}{(1 - f_{\text{hol}})^{1/3}}. \tag{3.12}$$

Similarly the outer radius of the spherical shell (the mantle) can be written as

$$a_{\text{mant}} = \frac{a}{(1 - f_{\text{hol}})^{1/3}}. \tag{3.13}$$

41

For this chapter a is either taken to be the mean particle radius at an atmospheric layer, $\langle a \rangle$, or a particle radius derived from the cloud particle distribution. It follows from Eqs. 3.10, 3.12, and 3.13 that in the limit of f_{hol} approaching 1, the radii of both spheres tend to infinity. Furthermore, the fraction of the hollow sphere taken up by the core by definition approaches 1. This results in an unphysical, infinitely large particle consisting almost entirely of vacuum, with an infinitesimally thin mantle. This is computationally intractable for particles not in the Rayleigh regime (Min et al. 2005). Thus the distribution of hollow spheres is specified by the irregularity parameter $f_{\mathrm{hol}}^{\mathrm{max}}$ (the upper limit of f_{hol}), which should be set to a value sufficiently close to 1 so that the calculated spectral properties converge whilst still remaining computationally feasible. We find $f_{\mathrm{hol}}^{\mathrm{max}} = 0.85$ to be sufficient. We use the same approach as by Min et al. (2005) (who used $f_{\mathrm{hol}}^{\mathrm{max}} = 0.98$). We average over a distribution function $n(f_{\mathrm{hol}})$, with equal weighting between $f_{\mathrm{hol}} = 0$ and $f_{\mathrm{hol}} = f_{\mathrm{hol}}^{\mathrm{max}}$:

$$
n(f_{\mathrm{hol}}) = \begin{cases} 1/f_{\mathrm{hol}}^{\mathrm{max}}, & 0 \leq f_{\mathrm{hol}} < f_{\mathrm{hol}}^{\mathrm{max}} \\ 0, & f_{\mathrm{hol}} \geq f_{\mathrm{hol}}^{\mathrm{max}} \end{cases} . \tag{3.14}
$$

3.4 Mineral Snowflakes: Effects of Micro-porosity

We study how micro-porosity affects the cloud structure and properties of cloud particles in exoplanet and brown dwarf atmospheres. In Section 3.4.1 we discuss our results for the case of a warm gas giant atmosphere with $T_{\mathrm{eff}} = 1800\,\mathrm{K}$ and $\log(g\,[\mathrm{cm\,s^{-2}}]) = 3.0$. Section 3.4.2 discusses the spectral effects of micro-porous cloud particles for this atmosphere. Finally, Section 3.4.3 examines micro-porosity in the context of a grid of atmospheres across a range of effective temperatures and surface gravities. The 1D DRIFT-PHOENIX (p_{gas}-T_{gas}) profiles monotonically increase from 750–2500 K (Fig. A.1), much like nightside profiles for ultra-hot Jupiters such as WASP-18b (Helling et al. 2019) and HAT-P-7b (Helling et al. 2019).

3.4.1 Micro-porosity and Amplified Bulk Growth

For the warm gas giant atmosphere ($T_{\mathrm{eff}} = 1800\,\mathrm{K}$, $\log(g\,[\mathrm{cm\,s^{-2}}]) = 3.0$) we considered three values for the micro-porosity ($f_{\mathrm{por}} = 0.0, 0.5, 0.9$). Increasing the micro-porosity of the cloud particles leads to generally larger cloud particles (Fig. 3.1, middle left). In the upper atmosphere (10^{-12}–10^{-8} bar) this is due to the increased nucleation monomer size. At greater pressures, the mean cloud particle size increases at $\sim 10^{-8}$ bar for highly micro-porous cloud particles ($f_{\mathrm{por}} =$
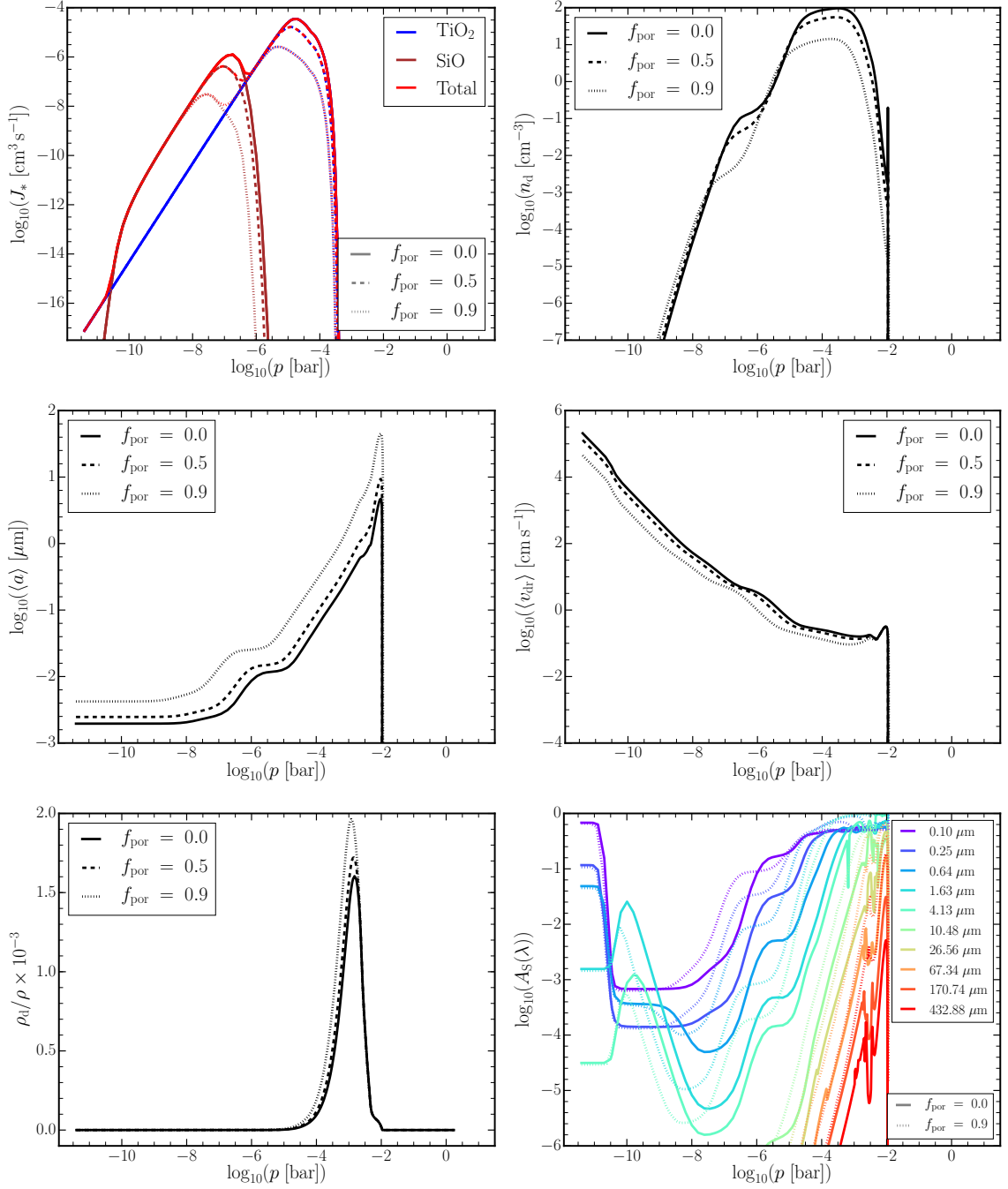
Figure 3.1: Material and spectral properties of cloud particles in an atmosphere representative of a warm gas giant, $T_{\text{eff}} = 1800\,\text{K}$, $\log(g\,[\text{cm s}^{-2}]) = 3.0$, for a cloud particle micro-porosity $f_{\text{por}} = 0.0, 0.5, 0.9$ (the bottom right panel shows only $f_{\text{por}} = 0.0, 0.9$ for clarity). **Top Left:** Nucleation rates for individual species $J_i\,[\text{s}^{-1}]$ i = TiO$_2$[s] (blue), SiO[s] (brown), and the total $J_* = \Sigma_i J_i$ (red). **Top Right:** Number density $n_d\,[\text{cm}^{-3}]$ of cloud particles. **Middle Left:** Mean cloud particle size $\langle a \rangle$ [µm]. **Middle Right:** Mean drift velocity $\langle v_{\text{dr}} \rangle$ [cm s^{-1}] for cloud particles of size $\langle a \rangle$. **Bottom Left:** Cloud particle mass load (ρ_d/ρ) scaled by a factor of 10^3. **Bottom Right:** Single-scattering albedo as defined in Eq. 2.30 for wavelengths $\lambda =$ 0.1, 0.25, 0.64, 1.63, 4.13, 10.48, 26.56, 67.34, 170.74, and 432.88 µm (colours as shown in the legend).

0.9) as opposed to $\sim 10^{-7}$ bar for compact particles (f_{por} = 0.0). This is due to the larger surface area of the cloud particles, which increases the altitude at which bulk growth begins.

Figure A.2 shows the material composition of cloud particles, the transition between cloud particles composed entirely of the nucleation species SiO[s] to cloud particles with a significant fraction of the bulk growth material MgO[s] also shifts to higher in the atmosphere. This transition shifts from $\sim 10^{-7}$ bar to $\sim 10^{-8}$ bar between the compact (Fig. A.2, left) and highly porous (Fig. A.2, right) cases. When we simplify this by assuming constant material composition, the drift velocity of a micro-porous particle can be expressed in terms of the compact drift velocity and the micro-porosity fraction (from Eqs. 2.1 and 3.1),

$$v_{\text{dr}}^{\text{por}} = \left(1 - f_{\text{por}}\right) v_{\text{dr}}^{\text{comp}}. \tag{3.15}$$

Lower drift velocities are therefore expected for higher micro-porosity, as shown in the middle right panel of Fig. 3.1. This furthermore allows the cloud particles to remain longer in an atmospheric layer and thus to experience more bulk growth. It therefore causes greater particle sizes. However, as seen in Fig. 3.1, bottom right, this does not lead to a significant increase in cloud particle mass load (the ratio of cloud particle mass density to gas mass density, ρ_{d}/ρ) because it is balanced by a reduced number density. Overall, with increasing micro-porosity there are fewer large cloud particles in any given atmospheric layer.

The micro-porosity also affects the number of seed particles that form, that is, the nucleation rate (Fig. 3.1, top left). The nucleation rates of TiO$_2$[s] and SiO[s] decrease with increased cloud particle micro-porosity. However, the micro-porosity must reach 90% for the nucleation rate to decrease significantly, and below 50% micro-porosity, the effect remains within an order of magnitude for all pressures. Micro-porosity does not affect the rate at which cloud particles form in the low-pressure atmosphere. The point at which the nucleation rate deviates from the compact particle rate (f_{por} = 0.0) is dependent on the cloud particle micro-porosity and occurs at lower pressures for increased micro-porosity. This is due to competitive bulk growth rates for the nucleation elements. Because bulk growth needs substantially less supersaturation of the gas phase than nucleation, the bulk growth rate quickly exceeds the nucleation rate when the material becomes thermodynamically stable. This depletes the gas phase of Si-, Ti-, and O-bearing molecules and thus limits the nucleation rates. A higher particle micro-porosity increases the area that is available for gas-surface reactions and thus improves the bulk growth rate at all layers,
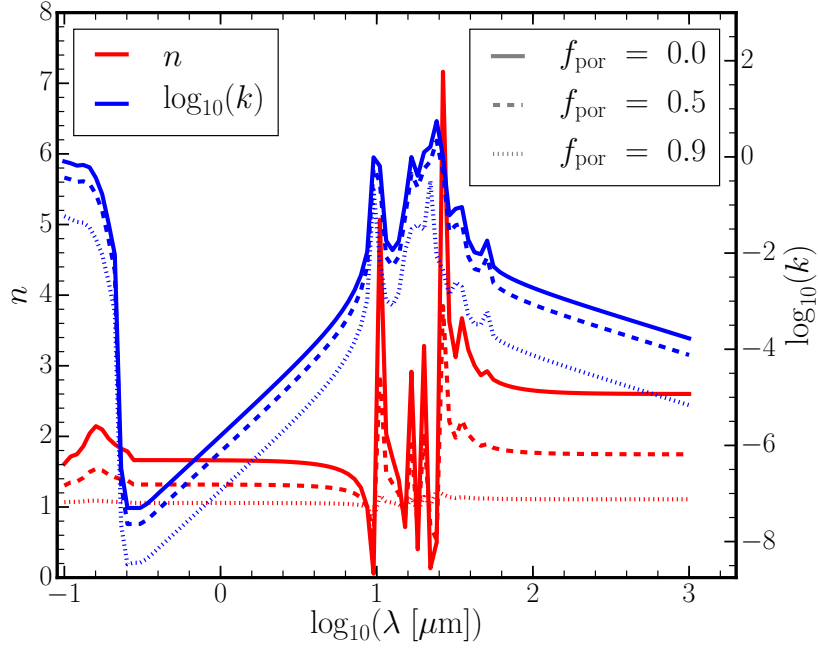
Figure 3.2: Real (n) and imaginary (k) refractive indices calculated based on the effective medium theory (red and blue lines, respectively) for cloud particles consisting of crystalline $Mg_2SiO_4[s]$ and vacuum, for micro-porosity fractions f_{por} = 0.0, 0.5, 0.9.

which means that it becomes stronger than nucleation at higher altitudes (lower pressures) than in the compact case. The reduction in nucleation rate leads to the reduced peak number density of cloud particles in the atmosphere (Fig. 3.1, top right).

3.4.2 Increased Albedo from Micro-porosity of Cloud Particles

In order to discuss the spectral effects of micro-porosity on cloud particles, it is illuminating to first briefly consider homogeneous cloud particles that are composed of only one material and vacuum through the effective medium theory. Figure 3.2 shows that as f_{por} increases, the refractive index tends towards vacuum values, with the real part of the refractive index (n) becoming more uniform (diminishes spectral features) and tending to 1, whilst the imaginary part (k) also decreases uniformly, although it maintains its shape, and tends towards zero.

For the warm gas giant atmosphere, the shape of the single-scattering albedo ($A_S(\lambda)$, Eq. 2.30) 'spectrum' (Fig. 3.1, bottom right) is defined by the material composition of the cloud particles. The sudden drop in $A_S(\lambda)$ at 10^{-10} bar for wavelengths λ = 0.1, 0.25, and 0.64 µm is associated with the transition between the dominant nucleation species. The material composition changes from cloud particles consisting entirely of $TiO_2[s]$ seeds to particles that largely comprise $SiO[s]$,

which aligns with the dominant nucleation rates (Fig. 3.1, top left). The exact values of the albedo in this region and the transition is dependent on the extrapolation used for $TiO_2[s]$ because the refractive index data does not cover this wavelength range (see Fig. 2.2). Further work on obtaining the refractive indices for materials such as $TiO_2[s]$ over a broader range of wavelengths would greatly benefit many theoretical studies.

The increase in albedo for all wavelengths between 10^{-8} and 10^{-7} bar is associated with a change to heterogeneous cloud particles of mixed composition, with a majority iron and magnesium silicate (fayalite $Fe_2SiO_4[s]$ and forsterite $Mg_2SiO_4[s]$) composition. Figure A.2 shows detailed material composition changes across the atmosphere for the compact and highly porous cases. For pressures $< 10^{-7}$ bar, the albedo for wavelengths smaller than $10.48\,\mu m$ shows a general trend corresponding to the mean grain size. Most notably, this explains the shift of the flat part of the spectrum from around 10^{-6} bar for the compact case to 10^{-7} bar for the highly micro-porous case. In this flattened region the effects of micro-porosity are directly visible on the albedo, with increased values for all wavelengths except $0.1\,\mu m$. For the highly micro-porous particles the effective refractive index tends towards that of vacuum and the extinction efficiency of the particles (Q_{ext}) is therefore reduced, increasing the albedo. Whilst the extinction efficiency of the cloud particles is reduced, the extinction cross-section Eq. 3.9 of micro-porous cloud particles can still increase because of their larger size (see Fig. 3.7).

3.4.3   Effect of Micro-porosity for Different T_{eff} and $\log(g)$

The trends in n_d, $\langle a \rangle$, and ρ_d/ρ as previously observed for the $T_{eff} = 1800\,K$ gas giant atmosphere qualitatively hold for a wider set of global atmospheric parameters (Fig. 3.3). For all atmospheres we investigated, the increased surface area of the micro-porous cloud particles leads to growth that occurs higher in the atmosphere and consequently to a reduced peak in number density n_d of cloud particles. In the upper atmosphere of each profile, the number density of micro-porous particles initially marginally exceeds the compact case, but when growth becomes efficient, it dominates nucleation for the necessary nucleation elements and thus dramatically reduces the nucleation rates and lowers the peak cloud particle number density.

The cloud particle mass load, ρ_d/ρ, peaks deeper in the atmosphere of cooler planets because the temperatures sufficient to evaporate the condensation species occur at greater pressure for these atmospheres. The cloud particle mass load sharply increases and peaks just above the cloud base (typically between 10^{-4} and 10^{-2} bar), because of cloud particles settling from higher
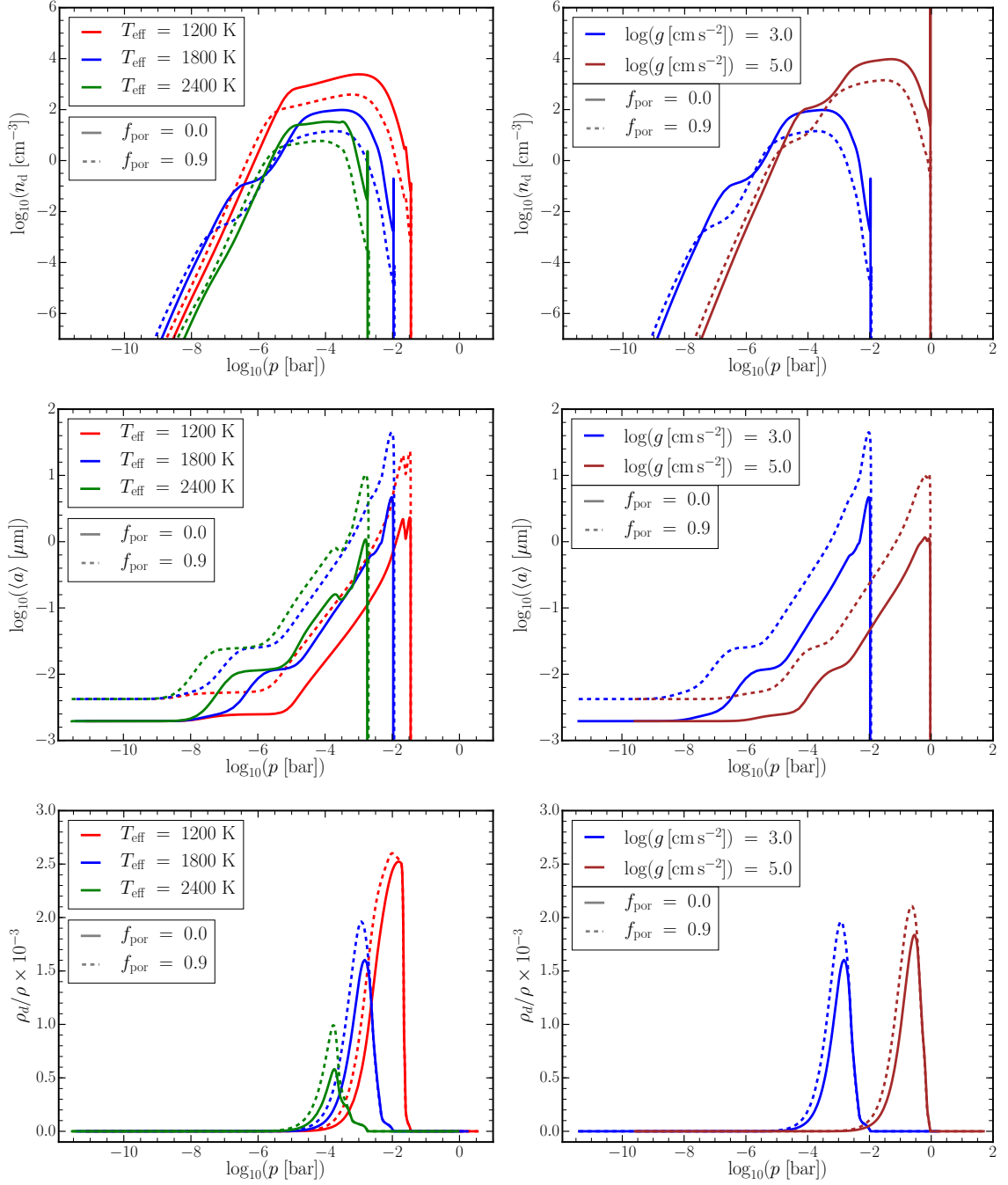
Figure 3.3: Material properties of cloud particles for micro-porosities of f_{por} = 0.0 (solid) and f_{por} = 0.9 (dashed) across a grid of effective temperatures and surface gravities. **Left:** Surface gravity $\log(g\,[\mathrm{cm\,s^{-2}}])$ = 3.0, representative of gas giant exoplanets, for T_{eff} = 1200, 1800, and 2400 K (red, blue, and green, respectively). **Right:** Surface gravities $\log(g\,[\mathrm{cm\,s^{-2}}])$ = 3.0 (blue) and 5.0 (brown), representative of brown dwarfs and young gas giants for T_{eff} = 1800 K. The blue lines in both columns are identical. **Top:** Number density of cloud particles $n_d\,[\mathrm{cm^{-3}}]$. **Middle:** Mean cloud particle size $\langle a \rangle\,[\mathrm{\mu m}]$. **Bottom:** Ratio of the cloud particle mass density and gas mass density ρ_d/ρ scaled by a factor of 10^3.
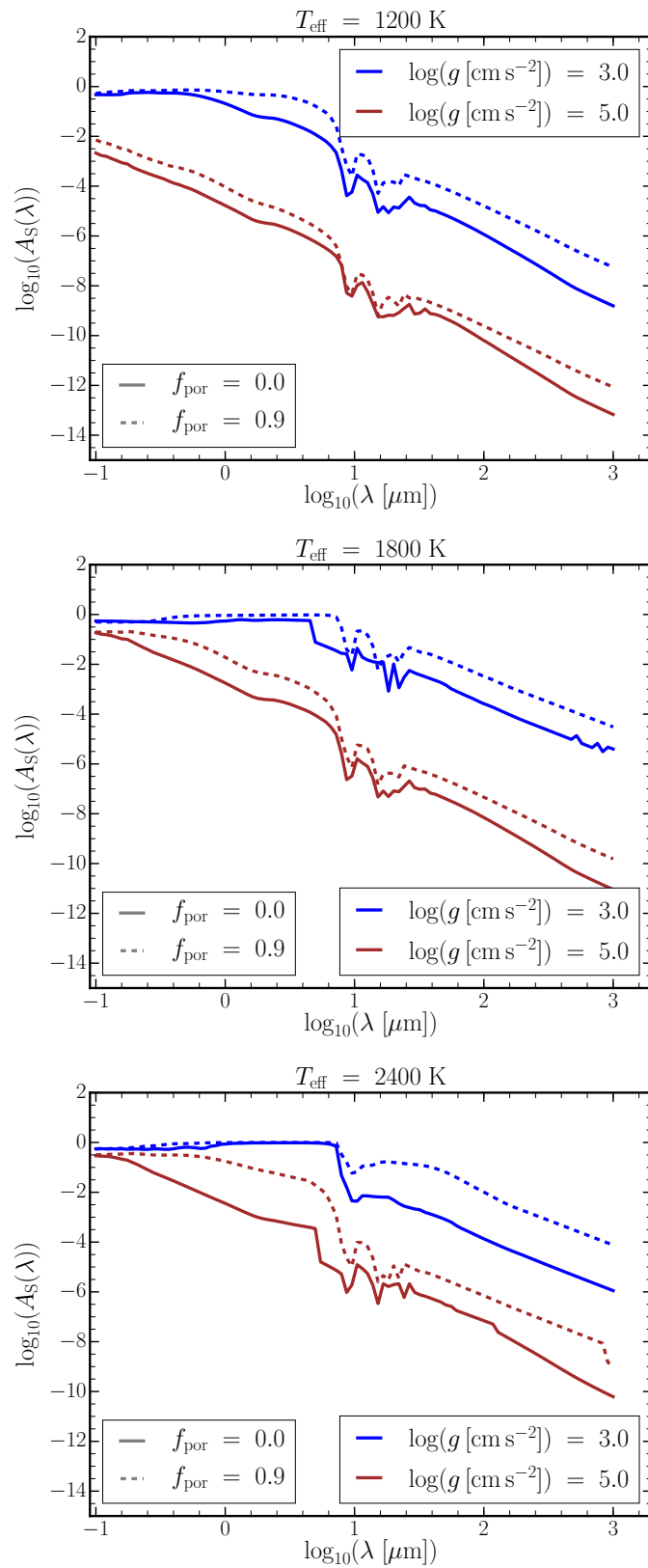
Figure 3.4: Single-scattering albedo $A_S(\lambda)$ as a function of wavelength from $0.1\,\mu m$ to $1000\,\mu m$ for $f_{por} = 0.0$ (solid) and 0.9 (dashed) at pressure level of 1 mbar. Surface gravities of $\log(g\,[\mathrm{cm\,s^{-2}}]) = 3.0$ (blue) and 5.0 (brown) are shown. **Top**, **Middle,** and **Bottom** panels are for $T_{eff} = 1200$, 1800, and 2400 K, respectively.

altitudes. Just prior to the cloud base is the perfect combination of sufficient surface of existing cloud particles raining in from above and efficient bulk growth, leading to a rapid increase in mass of material in the cloud particle phase. Because bulk growth rates and drift velocities are lower, warmer atmospheres are typically inefficient at sequestering mass into cloud particles and thus have a significantly lower ratio of cloud particle mass to gas mass, such as the $T_{\mathrm{eff}} = 2400\,\mathrm{K}$, $\log(g\,[\mathrm{cm\,s}^{-2}]) = 3.0$ profile. The bottom left plot of Figure 3.3 shows that in the compact case, the ratio of peak cloud particle mass load of this profile is about 0.5×10^{-3}, whereas in the highly micro-porous case the peak value is closer to 1×10^{-3}. This is an increase of a factor of 2. The increase for the $T_{\mathrm{eff}} = 1200\,\mathrm{K}$ profile, which is much more efficient at cloud particle formation in the compact case, is only minor.

Higher surface gravity causes cloud formation to occur deeper in the atmosphere (Fig. 3.3, right) because the gas pressure is higher. However, the increase in ρ_{d}/ρ remains roughly consistent for both cases. The average particle size similarly follows the change in cloud formation when $\log(g\,[\mathrm{cm\,s}^{-2}]) = 3.0$ and 5.0 are compared. Similarly, when we varied the effective temperature for $\log(g\,[\mathrm{cm\,s}^{-2}]) = 3.0$ profiles, the $T_{\mathrm{eff}} = 1600\,\mathrm{K}$ model and the $T_{\mathrm{eff}} = 2400\,\mathrm{K}$ model increase the average cloud particle size by about the same amount as for the $T_{\mathrm{eff}} = 1800\,\mathrm{K}$.

Figure 3.4 shows the spectral effects of micro-porous particles for our grid of atmospheres at the 1 mbar pressure level. This region of the atmosphere is typically probed by transmission observations for gas giant planets. Generally, the single-scattering albedo is enhanced for all profiles and across all wavelengths we considered, with the albedo for a brown dwarf profile always lower than that of a similar temperature gas giant profile. For wavelengths shorter than $10\,\mu\mathrm{m}$ in the $T_{\mathrm{eff}} = 2400\,\mathrm{K}$ brown dwarf model atmosphere, there is a peak increase of two orders of magnitude in albedo around $1\,\mu\mathrm{m}$. For all gas giant profiles, the albedo for wavelengths around $10\,\mu\mathrm{m}$ becomes flatter with micro-porosity. For longer wavelengths ($> 30\,\mu\mathrm{m}$), the micro-porous cloud particles show a trend of increased albedo over the compact case, with an increase of roughly two orders of magnitude for the hottest profiles at wavelengths of a few hundred microns. Lastly, we note an increased prominence of silicate features (which make up the bulk of the volume of cloud particles at these pressures) for all profiles in the micro-porous case.

Across the range of models we find that the increases in various material properties of the cloud particles across the atmosphere remain the same for various temperatures and surface gravities. This was expected because we chose to model micro-porosity by a constant factor. A parameter

dependent on local temperature and gas density would capture effects such as different evaporation rates of materials, leading to porous inclusions in the cloud particle. These effects would increase the micro-porosity deeper in the atmosphere.

3.5 Cloud Particle Size Distribution, High-altitude Cloud Material, and Spectral Properties

The spectral effects of a height-dependent cloud particle size distribution are shown in Fig. 3.5 for the T_{eff} = 1800 K, $\log(g\,[\text{cm s}^{-2}])$ = 3.0 atmosphere. The functional form assumed is a Gaussian distribution, derived from the solution of our kinetic cloud formation model as described in Section 3.3.3. For simplicity, we considered only compact cloud particles in this section. The coupled effects of micro-porosity and non-monodisperse cloud particles are discussed in Section 3.7.

3.5.1 Wide Particle Size Distributions due to Competitive Growth and Nucleation

The top left panel of Figure 3.5 shows the deviation of the Gaussian distributed particle sizes from a simple Dirac delta monodisperse ($a = \langle a \rangle$) size distribution. For the upper atmosphere ($< 10^{-8}$ bar) there are only cloud condensation nuclei, and thus the Gaussian distribution is almost a delta function around $\overline{a}$. Particles do not undergo bulk grow in this regime as the growth timescale is much longer than the gravitational settling timescale ($\tau_{\text{gr}} \gg \tau_{\text{sett}}$). The cloud particles therefore rapidly fall before significant growth can occur. The mean of the size distribution at each level in the atmosphere therefore remains at a constant value, the size of the cloud condensation nuclei, down to 10^{-8} bar, as was the case for monodisperse cloud particles. Furthermore, in this region we see the familiar effects of changing material composition on albedo, which remains unaffected by local particle sizes, as discussed in Section 3.4.2.

Around 10^{-8} bar, $\tau_{\text{gr}} = \tau_{\text{sett}}$, therefore cloud particles begin to grow through the condensation of thermally stable materials. In this region the mean cloud particle size begins to increase, but the nucleation rate remains high (Fig. 3.5, bottom left); the rate of SiO[s] nucleation does not peak until approximately 10^{-7} bar (brown line). Thus the inferred local variance of the Gaussian distribution from the moments increases significantly to account for both the small cloud condensation nuclei and for particles beginning to undergo substantial bulk growth in the same atmospheric layer. A similar broadening is found at 10^{-5} bar, where the TiO$_2$[s] nucleation rate

peaks (blue line). In between these two peaks, the nucleation rate briefly drops. This leads to a plateau in the particle number density (blue dashed line Fig. 3.5, top left). At this same point, the distribution narrows because the cloud particles grow rapidly. Any cloud particles falling from higher in the atmosphere in this regime (> 10^{-8} bar) rapidly grow, and thus a significant population of small particles is only supported by high nucleation rates. For pressures > 10^{-4} bar, the total nucleation rate drops rapidly and the Gaussian distribution converges towards the mean cloud particle size $\langle a \rangle$.

In regions where the local cloud particle size distribution is represented by a wide Gaussian distribution, the symmetrical nature of the Gaussian distribution can lead to unphysical inferred particle sizes that extend below the minimum particle size, and indeed even below zero, in attempting to represent the large particles produced by bulk growth. In the atmosphere we studied, this is the case even for particles within 3σ of the mean for the region between 10^{-6} and 10^{-4} bar. Cloud particle sizes below the minimum particle size are not included in any of the material property calculations because these rely on the moments, and using the distribution to calculate the spectral properties therefore produces a discrepancy between the methods. Cloud particles in the size distribution below zero size are excluded, and a further small discrepancy is therefore produced in the total number density of cloud particles. It is also unclear to what extent the upper bounds of the distribution are increased in attempting to compensate for the small cloud condensation nuclei over the true values for the larger cloud particles that have undergone bulk growth. Approaches to cloud particle and haze formation through the binning method have found evidence for multi-modal distributions, but these models rely on assumptions that simplify the formation of seed particles, material compositions, and growth processes (Powell et al. 2018; Kawashima & Ikoma 2018).

3.5.2 Increased Albedo due to Non-monodisperse Cloud Particle Size Distribution

At pressures where the Gaussian distribution is narrow, the integrated albedo over the size distribution is the same as for the monodispere case. For the broad distribution between 10^{-8} bar and 10^{-4} bar, the single-scattering albedo of the Gaussian distribution, $A_S^{Gauss}(\lambda)$, is always higher than that of the monodisperse case, $A_S^{Mono}(\lambda)$, (see the right two plots of Fig. 3.5). The increase for the initial broadening around 10^{-7} bar is wavelength independent and peaks at $A_S^{Gauss} = 1.5\,A_S^{Mono}$ (Fig. 3.5, bottom right). The second peak in the increase of the albedo from the monodispserse case to the Gaussian size distribution occurs at about 10^{-5} bar, and this time is
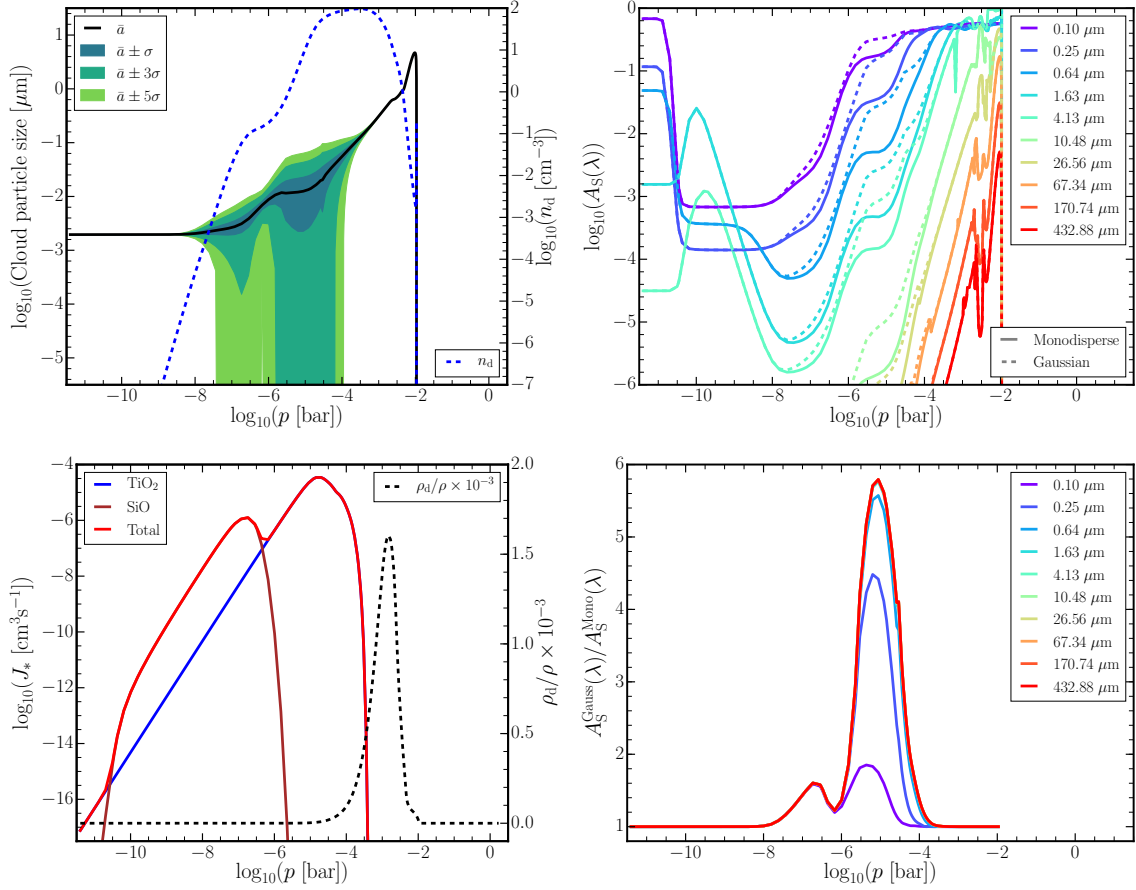
Figure 3.5: Gaussian cloud particle size distribution material and spectral effects (atmosphere of T_{eff} = 1800 K, $\log(g\,[\text{cm s}^{-2}])$ = 3.0). **Top Left:** Gaussian distribution mean cloud particle size $\bar{a}$ μm (solid black). Green contours show particle sizes 1σ, 3σ, and 5σ from the mean size (left axis). Cloud particle number density n_{d} [cm^{-3}] (dashed blue line, right axis). Below this we reproduce material property plots to facilitate comparison. These are identical to those shown in Fig. 3.1. **Bottom Left:** Nucleation rates (left axis) for individual species J_{i} [cm^3 s^{-1}] i = TiO$_2$[s] (blue), SiO[s] (brown), and the total $J_* = \Sigma_{\text{i}}J_{\text{i}}$ (red). Ratio of the cloud particle mass density and gas mass density ρ_{d}/ρ scaled by a factor of 10^3 (black dashed line, right axis). **Top Right:** Single-scattering albedo ($A_{\text{S}}(\lambda)$) for monodisperse cloud particles $\langle a \rangle$ [μm] (solid) and Gaussian size distribution (dotted) at wavelengths λ = 0.1, 0.25, 0.64, 1.63, 4.13, 10.48, 26.56, 67.34, 170.74, and 432.88 μm. **Bottom Right:** Ratio of the single-scattering albedo for a Gaussian and monodisperse size distribution ($A_{\text{S}}^{\text{Gauss}}/A_{\text{S}}^{\text{Mono}}$), i.e. a value exceeding 1 indicates an increase in the albedo when a particle size distribution is included.

wavelength dependent with a significantly lower increase of only a factor of 2 for $\lambda = 0.1\,\mu\text{m}$, as opposed to increases by a factor greater than 4 for all longer wavelengths. This is because in this region $\bar{a} \approx 10^{-2}\,\mu\text{m}$, and the fraction of cloud particles in the Rayleigh scattering regime ($Q_{\text{sca}} \propto \lambda^{-4}$) varies for each wavelength for a broad size distribution. Although an increase of half an order of magnitude in albedo seems substantial when the total extinction of the atmosphere is calculated, the peak extinction is dominated by regions with high mass fractions of cloud particles (ρ_{d}/ρ). The mass fraction of cloud particles peaks around the millibar level in the atmosphere, which does not significantly overlap with regions of high nucleation rates (Fig. 3.5, bottom left) where the local size distribution is broad. The size distribution therefore has little effect on properties such as optical depth (Fig. 3.9). Wakeford & Sing (2015) also found that for a log-normal distribution, the cumulative effect of transmission spectra of clouds is dominated by larger particles in the distribution. An asymmetric distribution, such as the log-normal distribution, has a greater number of large particles than the Gaussian distribution considered here, and may produce greater deviations from the monodisperse case. It has been found recently to have an effect on retrieved cloud particle size (Benneke et al. 2019). We note, however, that none of the size distributions used in retrieval approaches are based on a consistent cloud model, and therefore no conclusion can be drawn about the shape of the particle size distribution from such retrieval approaches.

3.6 Spectral Effects of Non-spherical Particles

To determine the spectral effect of non-spherical cloud particles, we return to the $T_{\text{eff}} = 1800\,\text{K}$, $\log(g\,[\text{cm}\,\text{s}^{-2}]) = 3.0$ atmosphere with compact, monodisperse cloud particles. When a distribution of hollow spheres is used, as described in Section 3.3.5, the albedo generally decreases compared to the compact, monodisperse case (Fig. 3.6, top right). This is due to the high f_{hol} end of the hollow sphere distribution, where the cloud particles have a large surface area (which is not conserved across the distribution of hollow spheres) and thus increase absorption (Min et al. 2003). Furthermore, Fig. 3.9 shows that for the compact case (red line), the inclusion of non-spherical particles leads to an increase in optical depth in the silicate features at $9.7\,\mu\text{m}$ and $18\,\mu\text{m}$. This result is in good agreement with the results by Min et al. (2005), who found that particles from the distribution with large f_{hol}, and thus thin mantles, act similarly to a collection of smaller particles that enhance spectral resonances. The result is more complex for hollow spheres coupled with already micro-porous particles, with little to no effect on the features

because the two methods (distribution of hollow spheres and effective medium theory) both attempt to capture the effects of non-compact particles. The implications of the combined effects are therefore unclear. This shows that the limited effect of hollow spheres in addition to highly micro-porous particles due to the diluted refractive indices that such particles have.

Our results are in qualitative agreement with the result found by Min et al. (2005), that the shape of the particles in an atmosphere also affect their spectral shape (illustrated also in Fig. 3.9). This also impacts the spectral properties, such as albedo, of the cloud particles and thus inferences of composition of the cloud particles (which changes throughout the atmosphere) also depends on assumptions of the distribution of shapes. However, total agreement with Min et al. (2005) is not possible because the model setups and sources of refractive index data were different. We show that the results of retrievals for particle sizes (Benneke et al. 2019) are greatly simplified with compact spheres and that this simplification can have a dramatic effect on the derived cloud properties. We note, however, that here we do not explore the additional effects of a distribution of hollow spheres on the polarisation of light in these atmospheres, which can also be significant. Because spheres are surface-minimising volumes, it is expected that the surface area increases for non-spherical particles.

3.7   Coupled Effects of Non-sphericity, Particle Size Distribution, and Micro-porosity

After examining each of the effects in isolation, we now investigate the effect on spectral properties for both compact and highly micro-porous (90%) particles; with and without a dispersed particle size distribution to represent the particle size, derived from our cloud model results; and for spherical and non-spherical grains as represented by a distribution of hollow spheres. All results are for the warm gas giant planet used throughout this chapter.

Figure 3.6 shows the single-scattering albedo and serves to highlight the relative contribution of each of the individual deviations from compact spheres. As noted in Section 3.5.2, the Gaussian distribution has the effect of maintaining a higher albedo at greater atmospheric altitude. In all cases the inclusion of non-spherical particles with a distribution of hollow spheres reduces the albedo for short wavelengths at pressures lower than 10^{-4} bar. For a wavelength of 0.1 µm, non-spherical particles have a more pronounced effect for the highly micro-porous case around 10^{-6} bar, but the reduction in albedo persists to even higher altitude only for the compact
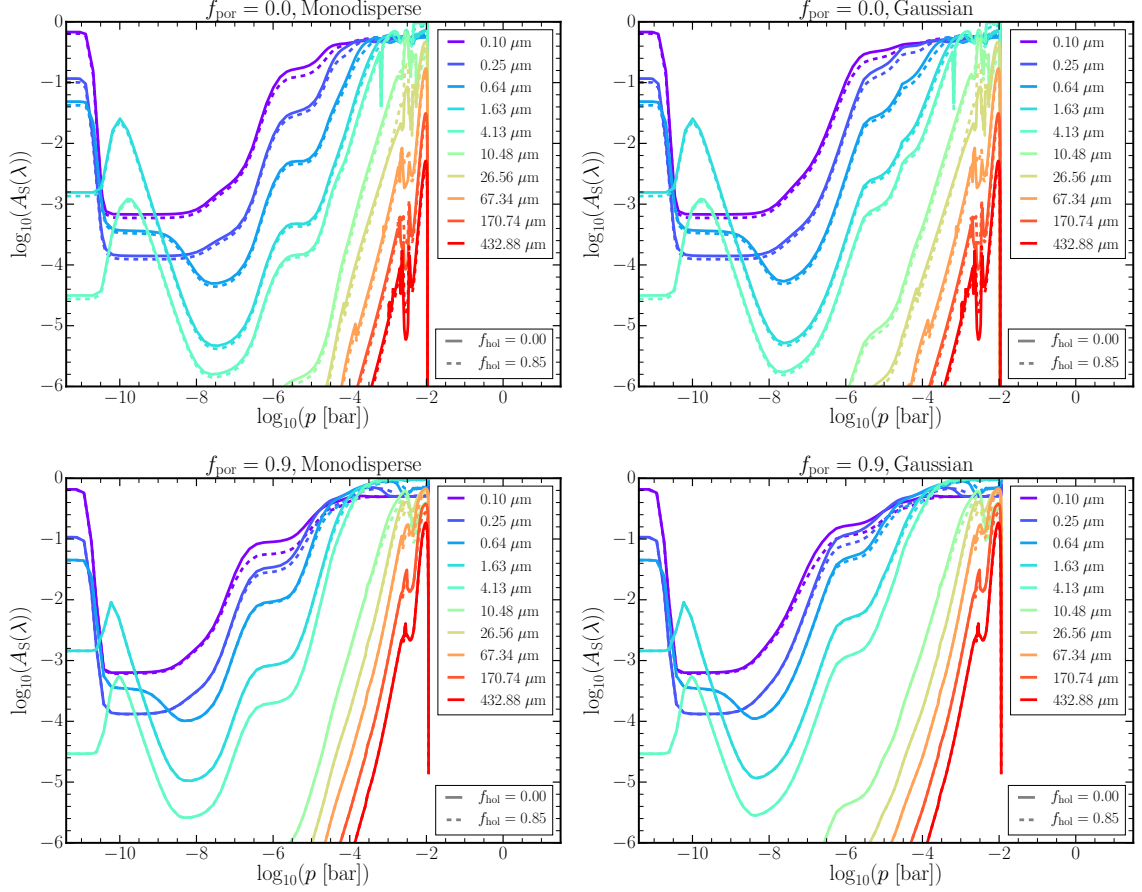
Figure 3.6: Single-scattering albedo $(A_S(\lambda))$ with (solid) and without (dashed) a distribution of hollow spheres for the atmosphere T_{eff} = 1800 K, $\log(g\,[\mathrm{cm\,s}^{-2}])$ = 3.0 at wavelengths λ = 0.1, 0.25, 0.64, 1.63, 4.13, 10.48, 26.56, 67.34, 170.74, and 432.88 μm. **Left:** For monodisperse cloud particles according to mean particle size $\langle a \rangle$ [μm]. **Right:** For the derived Gaussian cloud particle size distribution. **Top:** For compact cloud particles (f_{por} = 0.0). **Bottom:** For highly micro-porous (f_{por} = 0.9) cloud particles.

case.

Figure 3.7 shows the wavelength dependence of the single-scattering albedo as well as the extinction cross-section both with and without a distribution of hollow spheres for three critical pressure levels (10^{-10}, 10^{-5}, and 10^{-3} bar). As expected, the cloud particle size distribution has little observed differences for all except 10^{-5} bar, where the cloud particle size distribution expands significantly (see Fig. 3.5). Notably the hollow spheres have the effect of increasing the extinction cross-section for compact particles at higher pressures (10^{-3} bar), but marginally decreasing it for the highly micro-porous case for wavelengths between 1–10 μm. This is further highlighted by integrating across all wavelengths to determine the Planck mean opacity (Fig. 3.8). The Planck mean opacity (κ_{Pl}) is given by the equation

$$\kappa_{\mathrm{Pl}} = \frac{\int_0^\infty \kappa_\nu B(\nu, T_{\mathrm{gas}})\, \mathrm{d}\nu}{\int_0^\infty B(\nu, T_{\mathrm{gas}})\, \mathrm{d}\nu}, \tag{3.16}$$

where $B(\nu, T_{\mathrm{gas}})$ is the blackbody function for temperature T_{gas}, and κ_ν is the mass extinction coefficient in frequency ν space. The peak of the Planck mean opacity (which aligns with the cloud particle mass load, see Fig. 3.1, bottom left) is increased for the compact case, but reduced for the highly porous case. This agrees with previous work by Juncher et al. (2017), who found a reduced Planck mean opacity for highly micro-porous particles. This implies that estimates for the mass of cloud particles in an atmosphere from retrieval methods may be significant overestimates unless the cloud particles are sufficiently porous. For the warm gas giant atmosphere, the albedo of the cloud particles is generally very low, $\sim 1\%$ for the atmosphere above 1 mbar. This even holds with the enhancement of the albedo we described for the mineral snowflake clouds. This means that mineral snowflakes, like compact cloud particles, remain relatively poor reflectors and are much stronger absorbers. The extinction cross-section and single-scattering albedo both show the presence of silicate features at 9.7 μm and 18 μm, which are sensitive to the assumptions on the cloud particles shape and porosity.

The optical depth of clouds is investigated using the vertically integrated pressure level (from the top of the atmosphere, TOA) at which the optical depth of the clouds reaches unity (Figure 3.9), revealing all models follow a similar slope for less than 3 μm. However, the micro-porous and compact cases diverge at 3 μm, with the compact cases exhibiting clear silicate spectral features. The highly micro-porous cases suppress these features until ~ 8 μm. For cases where the optical depth never reaches unity, our integration reaches the bottom of the atmosphere at 2 bar. This
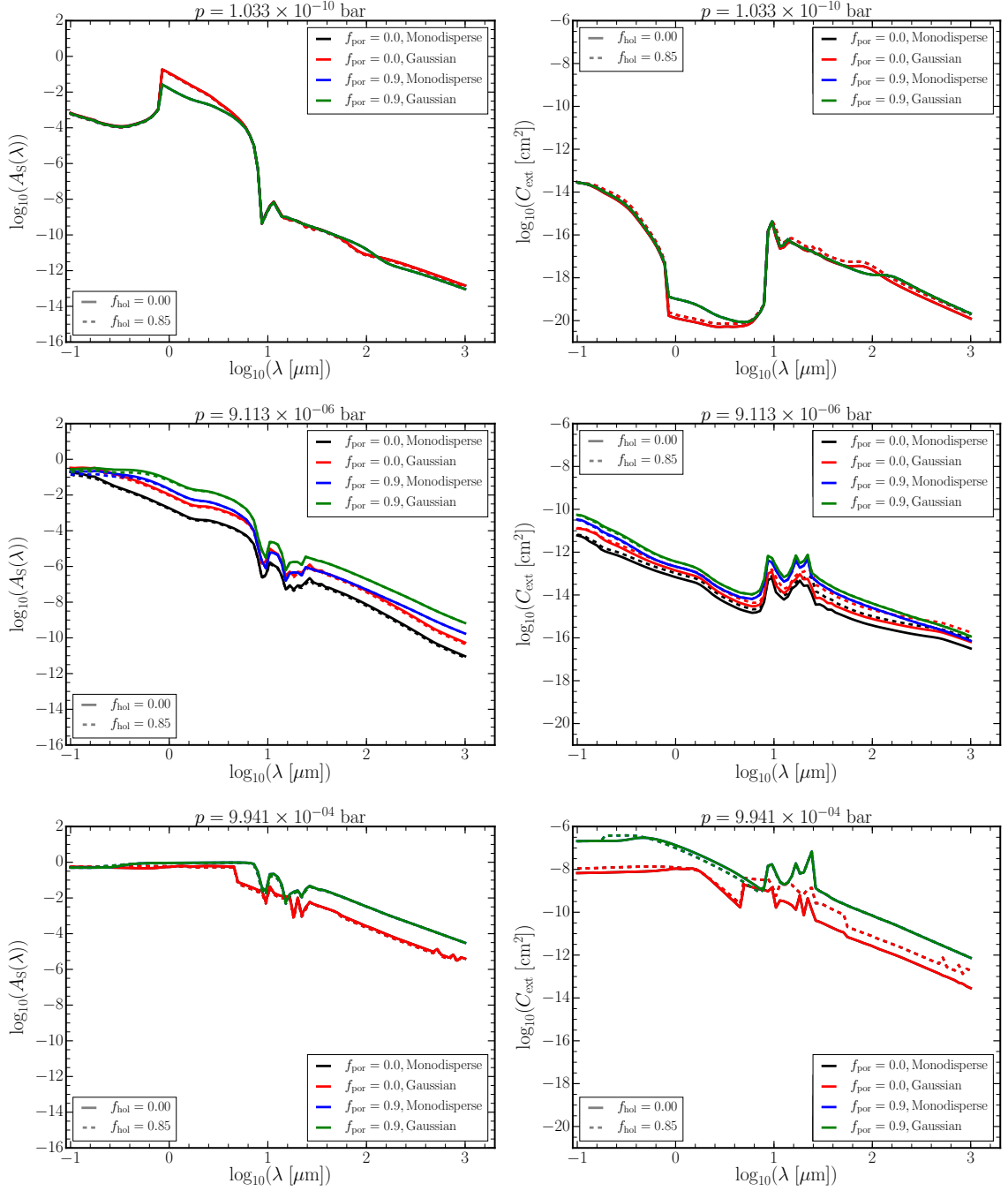
Figure 3.7: Single-scattering albedo $A_S(\lambda)$ (**Left**) and extinction cross section C_{ext} [cm^2] (**Right**) against wavelength at selected pressure levels. Calculated with (solid) and without (dashed) a distribution of hollow spheres for the T_{eff} = 1800 K, $\log(g\,[\text{cm s}^{-2}])$ = 3.0 profile. Shown are the pressure levels nearest to 10^{-10}, 10^{-5}, and 10^{-3} bar (**Top**, **Middle**, and **Bottom**). These levels are representative of the upper atmosphere, the typical lowest pressure of general circulation models, and the regime where transmission observations are sensitive, respectively. Four cloud particle cases are shown: monodisperse distribution of compact particles (black), Gaussian distribution of compact particles (red), monodisperse distribution of highly micro-porous particles $f_{\text{por}} = 0.9$ (blue), and Gaussian distribution of highly micro-porous particles (green).
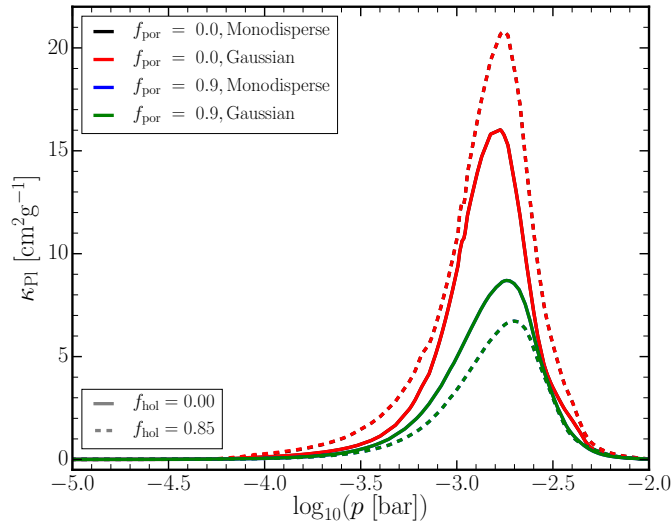
Figure 3.8: Planck mean opacity κ_{Pl} [cm^2 g^{-1}] for the T_{eff} = 1800 K, $\log(g\,[\text{cm s}^{-2}])$ = 3.0 atmosphere shown from 10^{-5} to 10^{-2} bar. Calculated with (solid) and without (dashed) a distribution of hollow spheres. Four cloud particle cases are shown: monodisperse distribution of compact particles (black), Gaussian distribution of compact particles (red), monodisperse distribution of highly micro-porous particles f_{por} = 0.9 (blue), and Gaussian distribution of highly micro-porous particles (green).
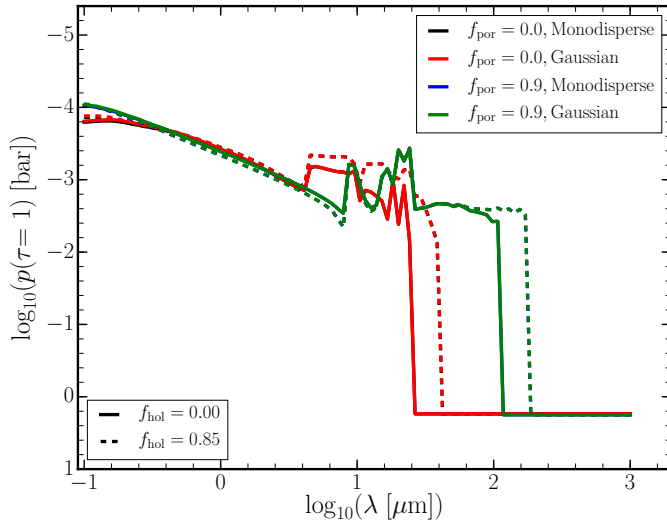
Figure 3.9: Atmospheric pressure level p [bar] at which the vertically integrated optical depth of cloud particles reaches unity ($\tau(\lambda)$ = 1). Four cloud particle cases are shown: monodisperse distribution of compact particles (black), Gaussian distribution of compact particles (red), monodisperse distribution of highly micro-porous particles f_{por} = 0.9 (blue), and Gaussian distribution of highly micro-porous particles (green). The atmosphere is T_{eff} = 1800 K, $\log(g\,[\text{cm s}^{-2}])$ = 3.0.

58
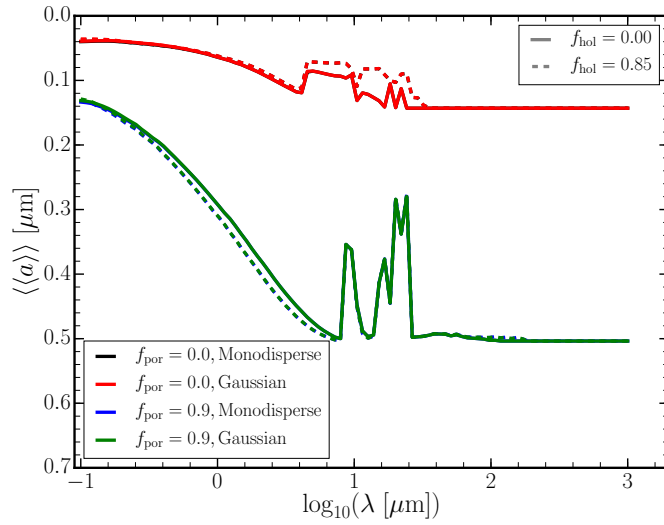
Figure 3.10: Average of the mean cloud particle size for particles in the optically thin atmosphere $\langle\langle a \rangle\rangle$ [μm], (defined as the average above the pressure, as defined in Eq. 3.17 and shown in Fig. 3.9). Four cloud particle cases are shown: monodisperse distribution of compact particles (black), Gaussian distribution of compact particles (red), monodisperse distribution of highly micro-porous particles $f_{por} = 0.9$ (blue), and Gaussian distribution of highly micro-porous particles (green).

occurs for the compact case at ~ 18 μm and for the highly micro-porous cases to > 100 μm, which means that the depth to which JWST MIRI observations are sensitive (between 5 μm and 28 μm Beichman et al. 2014) is likely an indicator of cloud micro-porosities for similar atmospheres to the warm gas giant exoplanet we considered.

MIRI observations will also include details of silicate features for similar exoplanet atmospheres. The details of these features depend on the particle micro-porosity and shape. The changes to the optical depth of the cloud particles are largely a combination of the changes to the albedo of the cloud particles and an increase in the geometrical cross-section for micro-porous particles and the larger particles in the size distribution. Hollow spheres generally also decrease the wavelength for which the clouds reach $\tau(\lambda) = 1$ by a factor of 2 consistently for the compact and micro-porous models. This occurs despite the reduction in albedo because of the large cross-sectional areas of cloud particles with large f_{hol} factors in the hollow sphere distribution.

For the silicate spectral features, the optical depth reaches unity at about the millibar level, which matches the levels anticipated by observers. Retrievals deriving the mean cloud particle size (Benneke et al. 2019) will only be affected by cloud particles in the optically thin atmosphere. We investigate this in Fig. 3.10 by approximating the optically thin regime as the atmosphere above the level at which $\tau(\lambda) = 1$. We computed the average of mean particle size for the optically thin regime using

$$\langle\langle a \rangle\rangle = \frac{\int_{TOA}^{z(\tau=1)} n_{\mathrm{d}}(z)\langle a \rangle \mathrm{d}z}{\int_{TOA}^{z(\tau=1)} n_{\mathrm{d}}(z)\mathrm{d}z}. \tag{3.17}$$

The difference in average of mean particle size for the optically thin regime at mid-infrared wavelengths is a maximum of a factor of 5 between the compact and highly micro-porous case, with minor deviations for inclusion of non-spherical particles. However, this calculation uses normal geometry because our model is limited to 1D. Fortney (2005) showed that a slanted geometry means that even small effects on the opacity in this regime can have massive implications for transmission spectra. This challenges the precision of the results by Benneke et al. (2019), who retrieved the cloud particle size to be $(0.6 \pm 0.06)\,\mu m$, but for a different atmosphere. There is no difference between the mono-disperse and Gaussian distribution because the means of the two distributions do not differ significantly (Fig. A.4).

3.8   Conclusion

We have studied the physical and spectral effects of micro-porosity on the cloud structure, particle size, and material composition on exoplanets and brown dwarfs. This allows us to asses how assumptions about cloud particles, such as sphericity, homodispersity, and compactness, affect their spectral properties. Our conclusions are listed below.

- Micro-porous cloud particles (mineral snowflakes) have lower number densities and larger particle sizes than compact particles throughout exoplanet and brown dwarf atmospheres.

- The local material composition of cloud particles is also affected by micro-porosity, with increased bulk growth across a wider range of pressure levels in an exoplanet atmosphere.

- Mineral clouds are poor reflectors and are much stronger absorbers. Even with high micro-porosity, which increases the albedo over clouds made of compact particles, they remain relatively poor reflectors.

- Mineral snowflake clouds have an increased optical depth at near-infrared wavelengths compared with clouds of compact particles.

- Clouds with a wide local particle size distribution have a significantly different single-scattering albedo in the near-UV, optical, and near-infrared wavelengths compared to monodisperse clouds, which may be detectable by transmission spectroscopy.

- The presence of non-spherical cloud particles may be observable by a distinct cut-off wavelength for $\tau(\lambda) = 1$ in the JWST MIRI bandpass.

- The effects of micro-porosity and non-spherical cloud particles can be most clearly separated in the spectral features of silicates between 5–20 μm.

Other sources of porosity may generate similar or greater effects to those examined here. One source of porosity is coagulation, which is just now beginning to be examined for exoplanet atmospheres (Powell et al. 2018; Kawashima & Ikoma 2018; Ohno & Okuzumi 2018). Collisions are examined in more detail in Chap. 4.

For gas giant atmospheres, JWST MIRI will observe at the wavelengths 5–28 μm. In this regime (Beichman et al. 2014), silicate spectral features of the clouds will be apparent, which will be sensitive to the details of the cloud particle model that is assumed. Furthermore, depending on the micro-porosity and shape of cloud particles, the clouds may be optically thin at the upper limits of the MIRI wavelength range, which can be used to test assumptions about cloud particle compactness. A distribution of hollow spheres is a simple way of calculating non-spherical cloud particle effects, and has the benefit of being defined by only one additional parameter. This makes it suitable for inclusion into retrieval codes (as has been done in Mollière et al. 2019) for cloud properties without drastically increasing the parameter space. Cloud effects on the spectra of brown dwarf and exoplanet atmospheres are a combination of the micro-porosity, non-sphericity, material composition, and cloud particle size distribution, all of which must be modelled consistently to be accurately derived. Retrieval efforts of cloud properties using simplified models must be cautiously interpreted.
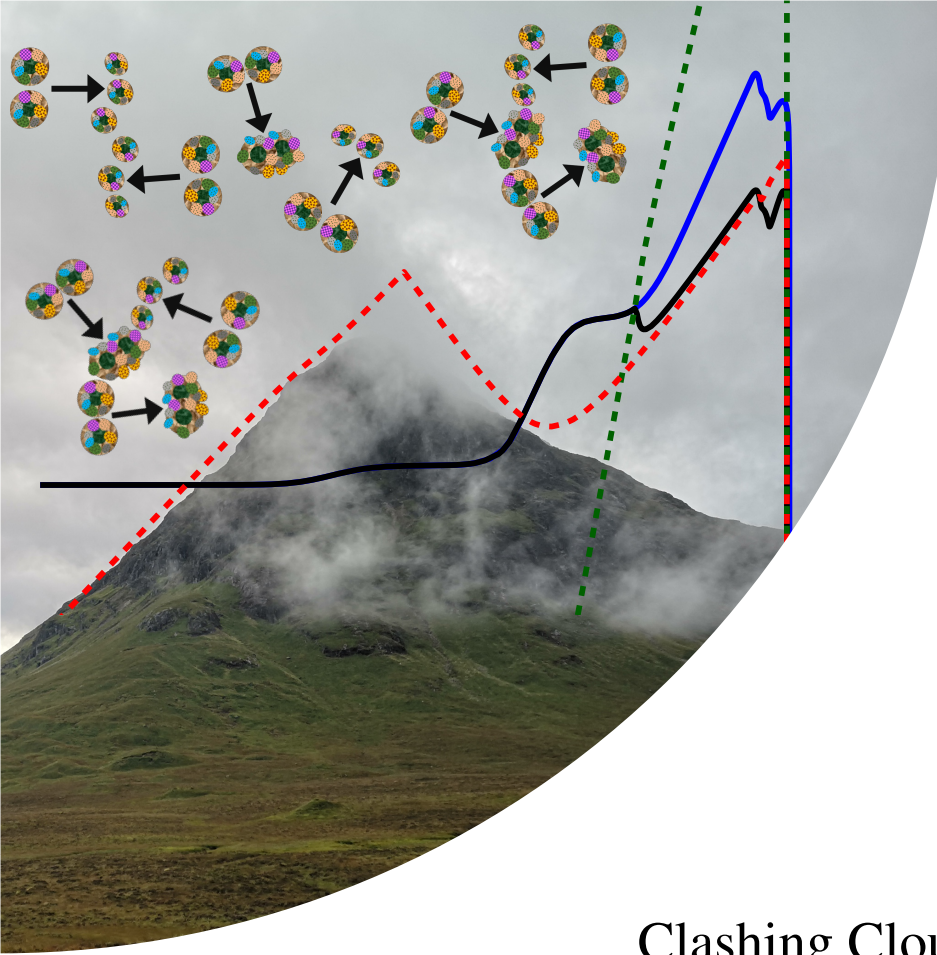
"You can measure a programmer's perspective by noting his attitude on the continuing vitality of FORTRAN."

- Adam Perlis, *Epigrams on Programming*, 1982

4

Clashing Clouds: Coagulation and Fragmentation with HʏLᴀɴᴅS

4.1 Declaration

This chapter is adapted from:

- 'Mineral snowflakes on exoplanets and brown dwarfs: Coagulation and fragmentation of cloud particles with HʏLᴀɴᴅS', Samra, D., Helling, Ch., Birnstiel, T. 2022, A&A, Accepted. All co-authors provided comments on the final manuscript of the paper.

4.2 Introduction

The most complete cloud models treat cloud formation kinetically, with rates for key processes such as nucleation, condensation/evaporation, settling, collisions, and mixing (e.g. (Helling et al. 2008b; Ohno & Okuzumi 2017; Lavvas & Koskinen 2017; Gao et al. 2018; Min et al. 2020)). A time-scale approach for particle-particle collisions as a growth process is applied by Rossow (1978), numerical solutions to the coagulation equation have been used in the context of planetesimal formation in protoplanetary discs (e.g. Dullemond & Dominik 2005; Birnstiel et al. 2010, 2012) and molecular clouds (Ormel et al. 2009, 2011; Ossenkopf 1993).

There have also recently been models including coagulation for exoplanet atmospheres. Ohno & Okuzumi (2017) consider collisions of cloud particles for terrestrial water clouds and for ammonia clouds on Jupiter, using constructive, constant density collisions and coagulation rates based on Brownian motion. The same model, with porosity evolution due to collisions included is applied to the atmosphere of mini-Neptune GJ 1214b by Ohno & Okuzumi (2018) and Ohno et al. (2020), where porous cloud particles formed by particle-particle collisions are found to be lofted into the upper atmosphere due to up-drafts. Coagulation of cloud particles has also been applied for GJ 1214b and a hot Jupiter atmosphere using a 'characteristic particle size' by Ormel & Min (2019) using the ARCiS framework. Gao & Benneke (2018); Powell et al. (2018) adapt the CARMA model, a kinetic cloud formation code for Earth, to exoplanets including hit-and-stick coagulation. In Chap 3 we investigated the effect of porous and irregularly shaped cloud particles on gas giant exoplanets and brown dwarfs, finding that highly porous cloud particles are required to have a significant impact on cloud particle properties throughout an atmosphere. Coagulation can be expected to produce large porosities if particles grow by hit-and-stick collisions (Dominik & Tielens 1997; Blum & Wurm 2000; Wada et al. 2008; Kataoka et al. 2013). However, experiments demonstrate that a range of collisional outcomes (e.g. compaction, fragmentation, sputtering, bouncing, e.t.c) are possible from particle-particle collisions (Blum & Wurm (2008); Güttler et al. (2010)).

In this chapter we present HYLANDS a cloud formation model that combines a kinetic growth description capable of predicting cloud particle sizes and material compositions (amongst others) with a description for coagulation/fragmentation, i.e. the processing of existing cloud particles through collisions and the resulting growth/destruction of cloud particles. The coagulation description has been inspired by extensive works on particle-particle processes for dust grains in the disk modelling community. Here, Birnstiel et al. (2012) have demonstrated the capacity of a simplified approach to reproduce the major characteristics of the full solution based on solving the Smolochovsky equation. However, a 1:1 adaption of the resulting code TwoPop-Py (applied, for example, in Klarmann et al. 2018; Greenwood et al. 2019) falls short of the requirements for an atmospheric environment (friction, turbulence, density) since the routine TwoPop-Py is tuned to modelling protoplanetary discs. The principle idea of TwoPop-Py, however, allows the combination of the kinetic growth moment method with a bin method for coagulation enabling to preserve the power of both for the first time, in particular the element conservation. Still, assumptions will be required (outlined in Sect. 4.3.1) compared to an in-depth modelling of the

involved physical processes (Dominik & Tielens 1997; Endres et al. 2021).

4.3 Approach

HᴙLᴀɴᴅS (the Hybrid moments (L_j) and Size method) is a **hybrid moment-bin method**. It has been developed to benefit from the advantages of the moment method used to describe particle formation (i.e. nucleation and bulk growth), alongside the advantages for a bin method for a particle size distribution in order to describe particle-particle processes. It utilizes the key idea applied in TwoPop-Py (Birnstiel et al. 2012), an approach that has been introduced to efficiently model coagulation processes within protoplanetary discs. The challenge is to identify those processes that limit or allow the particle-particle processes to occur, and the large differences in timescales for particle formation and particle-particle processes. Section 4.3.1 introduces the principle idea utilised to model coagulation and fragmentation of cloud particles through particle-particle collisions, and Sects. 4.3.2-4.3.4 defines the involved time scales. Section 4.3.7 presents the interface between the moment and the bin method. The method is summarised in Fig .4.1.

4.3.1 Coagulation Modelling

TwoPop-Py is a time dependent simple parameterisation of coagulation developed for protoplanetary discs (Birnstiel et al. 2012), it seeks to capture the complexity of a full bin model and has been calibrated to such a model as described by Birnstiel et al. (2010). It is substantially quicker than the solution of the full coagulation problem. A double Dirac delta distribution of two characteristic sizes is utilised: a collision monomer size a_0 and a second collisional product size (aggregates/fragments) a_1, where this second peak starts at the collision monomer size and increases exponentially up to some limiting maximum size a_{lim}, and thus a_1 at a time t is given by

$$a_1(t) = \min\left(a_{\text{lim}}, \quad a_0 \exp\left(\frac{t}{3\tau_{\text{coag}}}\right)\right). \tag{4.1}$$

The timescale τ_{coag} is the volume growth rate of cloud particles due to particle-particle collisions, it is calculated for differential settling and turbulence (Eq. 2.1, and Eq. 4.12), and is set to the fastest timescale considered:

$$\tau_{\text{coag}} = \min\left(\tau_{\text{coag}}^{\text{sett}}, \ \tau_{\text{coag}}^{\text{turb}}\right). \tag{4.2}$$

a_{lim} is determined by either fragmentation or settling processes, as these are the two processes by which cloud particles are removed from an atmospheric layer or destroyed. The local thermodynamic and kinetic gas conditions determine the collision monomer size, a_0, which may differ from typical dust-in-discs properties where a_0 may be fixed.

4.3.2 Timescales

A timescale analysis is utilised in order to determine where coagulation is a significant process in the atmosphere of gas giant exoplanets and brown dwarfs. Coagulation timescales are calculated by assuming a monodisperse distribution of cloud particle sizes (which for protoplanetary discs provides a good approximation to the numerical binned distribution model Birnstiel et al. (2010)). For each atmospheric layer with particle size a the collision timescale is

$$\tau_{\text{coag}} = \frac{V}{\dot{V}} = \frac{1}{3}\frac{a}{\dot{a}} = \frac{a\rho_s}{3\Delta v_{\text{coag}}\rho_d}, \tag{4.3}$$

where ρ_s is the cloud particle material density which is assumed constant through out the collisional process. ρ_d is the mass density of cloud particles in the atmosphere and the Δv_{coag} is the relative velocity between two cloud particles of size a. The factor of 1/3 in Equation 4.3 results from the collision timescale being based on the growth timescale of cloud particle radius $a/\dot{a}$, whereas the growth timescale used for the other microphysical processes (e.g. nucleation, bulk growth, evaporation) used by Woitke & Helling (2003) use the volume growth timescale $V/\dot{V}$. However, using $V = 4\pi a^3/3$ for compact spherical particles it can be shown that $V/\dot{V} = a/3\dot{a}$, thus a factor of three is applied to Eq. 4.3. This definition also aligns the collision growth timescale with the collision timescale $\tau_{\text{coag}} = \tau_{\text{coll}} = (4\pi a^2 \Delta v_{\text{coag}} n_d)^{-1}$. For a monodisperse distribution undergoing hit-and-stick collisions, each collision doubles the mass (and therefore volume when considering constant cloud particle material density ρ_s) of the cloud particle.

4.3.3 Collisional Processes Between Cloud Particles

From the moments (Eq. 2.4) it is possible to derive particle sizes, either through assuming some functional form of the size distribution, or by a direct ratio of the moments (e.g. see Chap. 2 Eqs. 2.5 and 2.6). Thus, if both particle size and gas density are known, only the relative velocity

between cloud particles remains to be determined. The collisional process between particles that are considered in the model are:

i) Differential Settling; the slightly different velocities of falling cloud particles with small variations in size.

ii) Brownian motion; the bumping of cloud particles due to the thermal velocity of gas molecules.

iii) Turbulence; turbulent eddies in the gas phase to which cloud particles frictionally couple depending on size resulting in different velocities.

The first process (i) produces ordered motion (all particles settle in the same direction, namely radially inwards), while the last two (ii and iii) produced randomly directed velocities.

i) Differential Settling

As introduced in Chapter 2, Woitke & Helling (2003) showed that cloud particles in a brown dwarf or exoplanet atmosphere quickly accelerate to their equilibrium drift velocity ($\mathring{v}_{dr}$), and for subsonic free molecular flow ($v_{dr} \ll c_T$, Kn $\gg$ 1), gravitationally settling cloud particles this has the form given in Eq. 2.1. This drift velocity depends on the local properties of the atmospheric layer, the modal gas molecule speed of a Maxwell-Boltzmann distribution (c_T), the gravitational acceleration (g) and the gas density (ρ), and the cloud particle properties of size and material density. Consequently, for a given atmospheric layer, a monodisperse, materially homogeneous population of cloud particles will all gravitationally settle at the same speed, thus having no relative velocity between each other. However, it is reasonable to assume a small variation in cloud particle size such that gravitational settling induces a differential velocity between cloud particles. Ohno & Okuzumi (2017) model collisions from differential settling for an approximately monodisperse distribution, by reducing the velocity of collisions by a factor of ϵ

$$\Delta v_{coag}^{sett} = \epsilon \mathring{v}_{dr} \tag{4.4}$$

Sato et al. (2016) fitted a simplified model for coagulation due to radial drift for icy pebbles in a protoplanetary disc to the full bin calculation of Okuzumi et al. (2012). They found a value of $\epsilon = 0.5$ fits well for compact particle coagulation. This value has subsequently been used by

Ohno & Okuzumi (2017, 2018); Krijt et al. (2016). Equation 4.4 therefore results in a lower limit for the differential gravitational settling induced coagulation timescale $\tau_{\mathrm{coag}}^{\mathrm{sett}}$.

ii) Brownian Motion

For Brownian motion the average relative velocity from the Maxwell-Boltzmann distribution for monodisperse, compact, spherical particles of size a, for a gas temperature T is

$$\Delta v_{\mathrm{coag}}^{\mathrm{Brow}} = \sqrt{\frac{12\,k_{\mathrm{B}}\,T}{\pi^2\,\rho_{\mathrm{s}}\,a^3}}. \tag{4.5}$$

By assuming the thermal velocity here, we assume that the Brownian motion collision timescale is very much smaller than the duration for which the cloud particles exist to collide with one another. In an atmosphere this is the settling timescale of a cloud particle, thus, from Eqs. 4.5, 4.3 it follows that $\tau_{\mathrm{coag}}^{\mathrm{Brow}} \ll \tau_{\mathrm{sett}}$. In addition, using Eq. 4.5 to calculate the collision timescale assumes that the cloud particle mean free path is much larger than the average distance between cloud particles (i.e. a large Knudsen number). Otherwise the cloud particles make multiple diffusive steps before colliding with one another. In this case the collision timescale is not controlled by Eq. 4.5, but rather by the diffusion coefficient.

iii) Turbulence

Turbulent fluctuations, or *turbulence* in short, are driven by large hydrodynamic, systematic motions which create a spectrum of fluctuations of different scales in time and space (also called eddies). These fluctuations can couple non-linearly and result in a non-zero vorticity of the respective fluid (e.g. Helling et al. 2004a). Prominent examples are the Kelvin-Helmholtz interface instabilities as seen in the atmosphere of Jupiter, the convective Hadley-cells on Earth, and atmospheric boundary layers. However, little is know for exoplanet and brown dwarfs beyond mere analogies or the observation of small-scale photometric variability (see Vos et al. 2020; Bailer-Jones 2002). Hence, hydrodynamic fluid models (e.g. Helling et al. 2001; Freytag et al. 2010) may provide some guidance regarding the local, large-scale fluid field. This is despite their limited suitability for turbulence consideration due to the small scale closure problem, which does effect the efficiency of chemical processes (e.g. Schmidt et al. 2006; Fistler et al. 2020). Alternative approaches utilise the Reynolds decomposition ansatz; where a unperturbed, large-scale background flow carries the small scale perturbations (e.g., Sect. 2.2. in Helling et al.

2004b). For the turbulence calculation here we follow Helling et al. (2011), where the relative velocity between two cloud particles of sizes a_i, a_j is

$$\Delta v_{\mathrm{coag}}^{\mathrm{turb}} = \langle \delta v_{\mathrm{g}}^2 \rangle^{1/2} \left(\left(1 + \frac{\tau_{\mathrm{f},i}}{\tau_{\mathrm{t}}} \right)^{-1} + \left(1 + \frac{\tau_{\mathrm{f},j}}{\tau_{\mathrm{t}}} \right)^{-1} - 2 \left(\frac{1}{\left(1 + \frac{\tau_{\mathrm{f},i}}{\tau_{\mathrm{t}}} \right) \left(1 + \frac{\tau_{\mathrm{f},j}}{\tau_{\mathrm{t}}} \right)} \right) \right)^{1/2} \tag{4.6}$$

Where $\tau_{\mathrm{f},i}$, $\tau_{\mathrm{f},j}$ are the frictional timescales for cloud particles of sizes a_i, a_j respectively and τ_{t} is the turnover timescale of a turbulent eddy. From Woitke & Helling (2003) Sect. 2.5 using Eqs. 13,21 for subsonic free molecular flow, the cloud particle frictional timescale is[1]

$$\tau_{\mathrm{f},i} = \frac{\sqrt{\pi} \rho_{\mathrm{s}} a_i}{2 \rho c_{\mathrm{T}}}, \tag{4.7}$$

The turnover timescale of a turbulent eddy is defined as

$$\tau_{\mathrm{t}} = \frac{l}{v} \tag{4.8}$$

where l is the length scale of the eddy, and v is the velocity of the eddy. For homogeneous and isotropic turbulence, energy may transfer at a constant rate from some largest eddy size where it is driven by some external process (for example, convection or large-scale hydrodynamic flows like on Jupiter) down to smaller and smaller eddy sizes. At some smallest eddy size the energy finally dissipates as heat (Kolmogorov 1941). The energy dissipation rate ϵ_{dsp} [cm^{2}s^{-3}] can be written as the following scaling relation

$$\epsilon_{\mathrm{dsp}} = \frac{C_{\mathrm{J}} v^3}{l}, \tag{4.9}$$

where $C_{\mathrm{J}} = 0.7$ (Jiménez et al. 1993). ϵ_{dsp} is constant within the inertial range of the turbulence size spectrum (Kolmogorov range). The energy dissipation rate can therefore be calculated from some eddy size and the related characteristic velocity. Here we chose an eddy size $l_{\mathrm{max}} = H_{\mathrm{p}}/10$ and velocity v_{max} given by

---

[1]We note here that Helling et al. (2011) specify τ_{f} with a numerical factor of 2/3 instead of 1/2, we use the latter as it is consistent with the drift velocity assumed in Eq. 2.1

$$\log_{10}\left(\frac{v_{\max}}{v_{\mathrm{conv}}^{\max}}\right) = \log_{10}(r_v) - \frac{\log_{10}(p/p_{\max})}{H_v/H_p} \tag{4.10}$$

where $v_{\mathrm{conv}}^{\max}$ is suggested by Freytag et al. (2010) to be modelled by the root mean square velocity of a Mixing-Length Theory (MLT) ansatz in terms of the MLT maximum velocity occurring within a 1D model. We therefore use the maximum convective velocity in the atmosphere and $p_{\max}$, the pressure level at which this velocity occurs taken from the Drift-Phoenix models. H_v/H_p is the wave amplitude velocity scale height, and $\log_{10}(r_v)$ is the ratio of maximum convection energy to wave amplitude, and r_v is itself dimensionless. Both values are calculated according to parametrisations chosen to fit the 2D sub-stellar atmospheric models by Freytag et al. (2010), where they are constant for a given set of sub-stellar parameters (Eq. 3 and Eq. 4 in Freytag et al. 2010). Hence then the turnover timescale of an eddy of size l is given by

$$\tau_{\mathrm{t}} = \left(\frac{C_{\mathrm{J}}l^2}{\epsilon_{\mathrm{dsp}}}\right)^{1/3}. \tag{4.11}$$

Thus, for monodisperse particle ensembles ($\tau_{\mathrm{f},1} = \tau_{\mathrm{f},2}$), Eq. 4.6 simplifies to

$$\Delta v_{\mathrm{coag}}^{\mathrm{turb}} = \langle \delta v_{\mathrm{g}}^2 \rangle^{1/2} \frac{\sqrt{\frac{2\tau_{\mathrm{f}}}{\tau_{\mathrm{t}}}}}{1 + \frac{\tau_{\mathrm{f}}}{\tau_{\mathrm{t}}}}. \tag{4.12}$$

$\langle \delta v_{\mathrm{g}}^2 \rangle^{1/2}$ is a systematic velocity component of the gas, following Helling et al. (2011) and from Morfill (1985), here $v_{\mathrm{conv}}^{\max}$ from Eq. 4.10 is used. The eddy size l_{edd}, for which the exchange of momentum between the gas phase and the cloud particles is most efficient, is left a free parameter. Here a typical eddy size of $l_{\mathrm{edd}} = 1\,\mathrm{cm}$ is assumed as is done by Helling et al. (2011). This assumption is discussed in Sect. 4.7.1.

The choice here of a 'typical eddy size' differs from the standard approach of choosing the maximum eddy size: the fraction $\tau_{\mathrm{f}}/\tau_{\mathrm{t}}$ is not the same as the conventional Stokes number St $= \tau_{\mathrm{f}}/\tau_{\mathrm{t,L}}$ where $\tau_{\mathrm{t,L}}$ is the turnover time of the largest eddy of the system of length $l_{\max}$. Writing Eq 4.12 in terms of the Stokes number, and rearranging one gets:

$$\Delta v_{\mathrm{coag}}^{\mathrm{turb}} = \sqrt{2}\langle \delta v_{\mathrm{g}}^2 \rangle^{1/2}\left(\left(\mathrm{St}\frac{\tau_{\mathrm{t,L}}}{\tau_{\mathrm{t}}}\right)^{-1/2} + \left(\mathrm{St}\frac{\tau_{\mathrm{t,L}}}{\tau_{\mathrm{t}}}\right)^{1/2}\right) \tag{4.13}$$

In the limits of small and large Stokes numbers, one retrieves $\Delta v_{\text{coag}}^{\text{turb}} \propto \sqrt{\text{St}} \sqrt{\tau_{\text{t,L}}/\tau_{\text{t}}}$ and $\Delta v_{\text{coag}}^{\text{turb}} \propto 1/(\sqrt{\text{St}} \sqrt{\tau_{\text{t,L}}/\tau_{\text{t}}})$ respectively. The proportionality to the Stokes number is the same as Eqs. 28,29 used by Ormel & Cuzzi (2007). The additional term relating eddy turnover timescales ($\sqrt{\tau_{\text{t,L}}/\tau_{\text{t}}}$) is a parameter which tunes the strength of turbulence and the efficiency of the coupling of turbulence and cloud particles, and therefore the relative velocities, in a similar manner to the commonly used 'α parameterisation'. Where α is dimensionless parameter determining the strength of turbulence for discs (Shakura & Sunyaev 1976). $\sqrt{\tau_{\text{t,L}}/\tau_{\text{t}}}$ acts similar to a variable α. Thus τ_{t} should not be thought of as the turnover time of the eddy with which the cloud particle is coupled, but rather a parameter either decreasing or increasing relative velocities for turbulence in certain parts of the atmosphere. A preliminary comparison of the typical eddy length scale l and α, in terms of a relative velocity comparison is conducted in Section 4.7.1.

The turbulence modelling approach used here is based on the Reynolds decomposition ansatz applied by Voelk et al. (1980); Morfill (1985) and is applied in combination with the Kolmogorov energy cascade. Both the Reynolds decomposition and the Kolmogorov cascade have severe limitations in modelling a turbulent medium: both models only represent the local interaction of neighbouring scales (similar eddy sizes), but do not describe the inherent non-linearity and non-locality of a turbulent medium that lead to non-linear interactions between different scales (e.g. Warhaft 2000). Furthermore, none of the linear models will be able to capture subsequent accelerations of cloud particles as the result of coupling to other fluctuations. This impasse in describing the effect of non-local scale interaction becomes critical, for example, in chemically reactive media in atmospheres. One simple way to represent this effect is to overemphasise the effects of linear turbulence on the chemistry. The reasonable justification is that turbulent media enable a gas to undergo chemical transformations considerably more efficiently than a laminar medium due to a larger chemically active surface as result of vorticity shaping (Schmidt et al. 2006; Fistler et al. 2020). This has been demonstrated for exoplanet and brown dwarfs by Helling et al. (2001, 2004b). Much work is still needed to fully understand appropriate selections for these parameters, and for the parameterisations in general, for exoplanet and brown dwarf atmospheres.

4.3.4 Limiting Cloud Particle Sizes

In protoplanetary discs the primary processes limiting particle growth through collisions are radial drift, settling, and fragmentation (Brauer et al. 2008; Birnstiel et al. 2016). Radial drift occurs
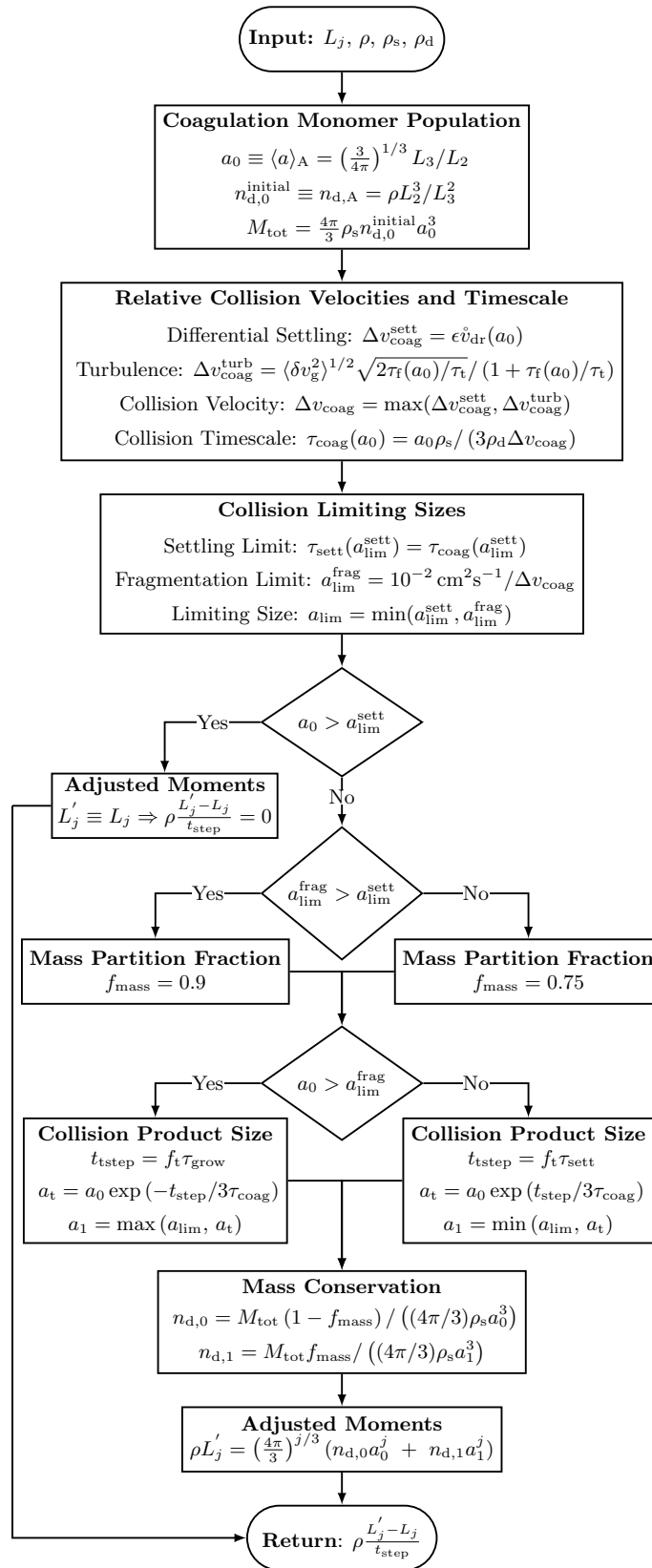
Figure 4.1: Flow chart of the collisional modelling process within HYLANDS and how it interfaces with the other cloud formation processes.

when particles orbit faster than the Keplerian velocity of the gas, thus experiencing a 'head-wind' which leads to orbit decay and the particle drifting towards the centre of the disk. Fragmentation is the result of collisions between particles being sufficiently energetic to break the colliding particles apart, rather than constructing larger particles. For an exoplanet atmosphere the processes limiting particle growth via collisions are:

i) Gravitational settling also provides a limit to the size that cloud particles can grow (Sect. 4.3.4).

ii) Fragmentation (Sect. 4.3.4) is naturally still important to consider, as cloud particle collisions may be sufficiently energetic to be destructive.

The collisional process of Brownian motion, however, is not included in the hybrid moment-binning method calculations. This is because, as seen in Eq. 4.5, Brownian motion is inversely proportional to particle size and thus provides a lower limit to fragmenting particle sizes and hence does not fit into the limiting size scheme used here.

i) Gravitational Settling limit

The process of gravitational settling still provides an analogous limit to radial drift in a protoplanetary disc: a process where the cloud particles are removed before they can be significantly affected by collisions. The timescale of this process is the time taken for cloud particles to gravitationally settle (at the equilibrium drift velocity) across a pressure scale height (Woitke & Helling 2003):

$$\tau_{\text{sett}} = \frac{H_{\text{p}}}{\mathring{v}_{\text{dr}}}. \tag{4.14}$$

This process limits the size to which cloud particles can grow to when the collisional growth timescale is faster than the settling timescale. If differential settling is the dominant collisional process, the settling limit $a_{\text{lim}}^{\text{sett}}$ is when these two timescales are equal (Eqs. 4.14 and 4.4),

$$a_{\text{lim}}^{\text{sett}} = \epsilon H_{\text{p}} \rho L_3. \tag{4.15}$$

For $\tau_{\text{coag}}^{\text{sett}} \geq \tau_{\text{coag}}^{\text{turb}}$ (turbulence is the driving timescale) the situation is more complex, resulting in a polynomial of 5$^{\text{th}}$ order which can be written as

$$a_{\mathrm{lim}}^{\mathrm{sett}}\left(1 + \frac{2\sqrt{\pi}\rho_s}{3\rho c_{\mathrm{T}}}\frac{a_{\mathrm{lim}}^{\mathrm{sett}}}{\tau_{\mathrm{t}}}\right)^{2/3} = \left(\frac{4H_{\mathrm{p}}\rho L_3\langle\delta v_g^2\rangle^{1/2}}{3g}\right)^{2/3} \tag{4.16}$$

Polynomials of 5$^{\mathrm{th}}$ order are not generally solvable algebraically. But Eq. 4.16 can be proven to always have only one positive root, less than the right hand side of Eq. 4.16. Thus, the solution can simply be found using a bisection search (see Appx. B.1).

ii) Fragmentation limit

The second limit to the growth of cloud particles by collisions is through fragmentation, where the energy of collision between two cloud particles is sufficient to destroy the cloud particles rather than constructively building up aggregates. Collisional experiments (see Blum & Wurm 2000, 2008; Güttler et al. 2010) identify three main 'modes' of collisional outcomes: sticking, bouncing, and fragmentation. The specific outcome of a collision depends on the collisional velocity, material composition, structural rigidity, and size of colliding particles.

For collisions between compact, monodisperse particles there is generally a 'bouncing barrier' (Güttler et al. 2010 Fig. 11 and Birnstiel et al. 2016 Fig. 2), where cloud particles collide but do not transfer mass (neither coagulation or fragmentation). However, this barrier can be bypassed by collisions between non-similar sized particles and by considering porosity evolution through collisions (see also Kataoka et al. 2013). The effect of neglecting bouncing in compact particle collisions can be estimated using the results of Güttler et al. (2010). The average cloud particle reference sizes or exoplanet and brown dwarf atmospheres (Table 2 Woitke & Helling 2003) are $\sim 10^{-6}$–10^{-3} cm. Consequently, compact cloud particles made purely of Mg$_2$SiO$_4$[s] ($\rho_s = 3.25\,\mathrm{g\,cm^{-3}}$) have masses between $\sim 10^{-17}$–10^{-8} g. Güttler et al. (2010) Fig. 11 shows that for silicate cloud particles with masses $\lesssim 10^{-11}$ g (radii of $\sim 1\,\mu$m) there is a direct transition from a regime of hit-and-stick collisions to a fragmentation regime. For heavier cloud particles (radii between 1–10 μm), there is an increasing range of collisional bouncing. Thus for larger cloud particles the efficiency of fragmentation may in fact be lower, as bouncing collisions occur instead. When considering collisional experiments for particle sizes spanning from $\sim 10^{-3}$–100 μm (Blum & Wurm 2008, their Fig. 13), propose a maximum velocity for sticking of dust particles in a collision dependent on size such that

$$\frac{v_{\mathrm{stick}}}{100\,\mathrm{cm\,s^{-1}}} = \left(\frac{a}{10^{-4}\,\mathrm{cm}}\right)^{-x} \tag{4.17}$$

x is largely unconstrained with $x > 1$ for particles $> 1\,\mu$m in size and potentially $x < 1$ for particle radii $< 1\,\mu$m. As exoplanet atmospheres contain cloud particles spanning a significant proportion of this size range, Eq. (4.17) is adopted as the limiting velocity between the coagulating and fragmenting regimes, with $x = 1$. This gives the inversely proportional fragmentation limit as

$$v_{\text{frag}} = \frac{10^{-2}\text{cm}^2\,\text{s}^{-1}}{a} \tag{4.18}$$

This provides that for sub-micron sized particles, where there are no collisional experiments, the fragmentation limit is larger than the typically assumed value of $v_{\text{frag}} = 100\,\text{cm}\,\text{s}^{-1}$ (e.g. Güttler et al. 2010; Kataoka et al. 2013). The fragmentation limit a_{frag} is then defined as the particle size for which this velocity equals the relative velocity of cloud particle sizes: $v_{\text{frag}}^{\text{i}}(a_{\text{frag}}) = \Delta v_{\text{coag}}^{\text{i}}$. Where i indicates if either differential settling (i = sett) or turbulence (i = turb) is the driving velocity of collisions.

Applying these to the relative velocities for differential settling and turbulence, using Eqs. 4.4 and 4.12 gives, if $\tau_{\text{coag}}^{\text{sett}} < \tau_{\text{coag}}^{\text{turb}}$:

$$a_{\text{lim}}^{\text{frag}} = \frac{1}{5}\sqrt{\frac{\rho c_{\text{T}}}{6\epsilon g\sqrt{\pi}\rho_{\text{s}}}}. \tag{4.19}$$

For $\tau_{\text{coag}}^{\text{sett}} \geq \tau_{\text{coag}}^{\text{turb}}$ one gets the cubic equation:

$$\left(\frac{\rho c_{\text{T}}\tau_{\text{t}}}{2\sqrt{\pi}\rho_{\text{s}}} + a_{\text{lim}}^{\text{frag}}\right)^2 - 2\times10^4\langle\delta v_{\text{g}}^2\rangle\frac{\rho c_{\text{T}}\tau_{\text{t}}}{2\sqrt{\pi}\rho_{\text{s}}}\left(a_{\text{lim}}^{\text{frag}}\right)^3 = 0 \tag{4.20}$$

which is solved for real roots.

4.3.5 Large Collision Monomers

The use of limiting maximum sizes (Sect. 4.3.4) is a challenge for any two representative size collision model. In a hybrid moment-bin method, other microphysical processes encapsulated in the moment equation (e.g. bulk growth) affect the average cloud particle size. Therefore, rather than having a fixed, small collision monomer size, it is possible for the collision monomer size to be larger than the cloud particle size limits of the collision model.

If the limiting size is due to settling, then this indicates that the monomers will rain out of that

atmospheric layer, without experiencing significant collisions, either fragmenting or coagulating. Thus if $a_0 > a_{\text{lim}}^{\text{sett}}$, then the cloud particle population is unchanged and the collisional product size is the same as the collision monomer size ($a_1 = a_0$). The adjusted moments are therefore the same as the input moments $L_j^{'} \equiv L_j$ (as shown in Fig. 4.1, see Sec. 4.3.7 for details).

If fragmentation is the size limiting process $a_0 > a_{\text{lim}}^{\text{frag}}$, then the cloud particles may experience a significant number of collisions. However, these are now overall destructive, resulting in a reduction of particle size. To represent this process the collisional product size exponentially decays from the collision monomer size towards the fragmentation limit,

$$a_1(t) = \max\left(a_{\text{lim}}, \ a_0 \exp\left(-\frac{t}{3\tau_{\text{coag}}}\right)\right). \tag{4.21}$$

Consequently, sufficiently fast collisional timescales lead to the collisional product size reaching this limit. Conceptually, however, this is incomplete as the fragmentation limit represents the maximum size of cloud particles that are stable to fragmentation for a particular atmospheric layer. In other words, monodisperse collisions of cloud particles of this size and smaller do not result in fragmentation. Thus, the stable cloud particle population for such an atmospheric layer could include cloud particles of this limiting size down to the minimum particle size. This results in the collisional product size now representing only the very largest cloud particles possible resultant from collisions. [2]

4.3.6 Timestep Selection

The cloud formation model used (see Chap. 2) is not time-dependent but stationary. We only consider the case that the collision monomers are small enough that they stay in an atmospheric layer and experience significant collisions (i.e. $a_0 < a_{\text{lim}}^{\text{sett}}$). In this case, in order to incorporate the effect of coagulation requires the modelling of some effective timestep to represent the amount of collisions occurring. In order to not over represent the coagulation/fragmentation with respect to the other processes, a limiting timescales for condensation growth and settling is applied such that:

---

[2]TwoPop-Py incorporates additional factors f_{sett} (f_{d} in Eq.18, Birnstiel et al. 2012) and f_{frag} into the limiting sizes, reducing the actual size limit. These factors are tuned so that the TwoPop-Py results match the full bin model simulations of Birnstiel et al. (2010). In the absence of equivalent comparable simulations for atmospheres we neglect these factors here (equivalently $f_{\text{sett}} = 1$ and $f_{\text{frag}} = 1$).

$$t_{\text{step}} = \begin{cases} f_{\text{t}}\tau_{\text{sett}} & a_0 < a_{\text{lim}}^{\text{frag}} \\ f_{\text{t}}\tau_{\text{grow}} & a_0 > a_{\text{lim}}^{\text{frag}}. \end{cases} \tag{4.22}$$

Where τ_{grow} is the condensational growth timescale (as defined by Eqs. 22, 32, 37 in Woitke & Helling 2003), f_{t} is an efficiency factor that can be used to represent effects that slow down the evolution of a cloud particle distribution from collisions, such as bouncing which preserves the mass of the colliding cloud particles. For this work, f_{t} is set to 1. τ_{sett} is used when the collision monomer is of a size that collisions are constructive (coagulation regime) as this is the other physical process which opposes growth. In the fragmentation regime it is growth by condensation that opposes reduction in the particle size due to destructive collisions.

4.3.7 The Interface

The interface between the moments and the coagulation calculation and vice-versa is a critical component of the model. Therefore combining the two approaches of kinetic cloud formation through solving moment equations with a two-bin approach for collision modelling is the core of this chapter. The effect of particle-particle processes on cloud formation is introduced by an additional source term in the master equation, similar to the introduction of mixing parameterisation in Eq. 2.9. The resulting changes of the moments, L_{j}, due to nucleation, growth/evaporation, mixing and coagulation are now calculated from

$$-\frac{\text{d}}{\text{d}z}\left(\rho_{\text{d}}\frac{L_{j+1}}{c_{\text{T}}}\right) = \frac{1}{\xi_{\text{lKn}}}\left(V_{\text{l}}^{j/3}J(V_{\text{l}}) + \frac{j}{3}\chi_{\text{lKn}}^{\text{net}}\rho L_{j-1} - \frac{\rho L_j}{\tau_{\text{mix}}} - \rho\frac{L_j' - L_j}{t_{\text{step}}}\right). \tag{4.23}$$

The collision monomer for any atmospheric layer must be selected to be representative of the size of cloud particles present in that layer. For a given layer the collision monomer size is therefore set to $a_0 = \langle a \rangle_{\text{A}}$, the surface-averaged mean particle size, and correspondingly the number density is set to $n_{\text{d},0} = n_{\text{d,A}}$, as defined in Chapter 2, Eq. 2.7.

The surface-averaged quantities are selected as the collision monomer size is used to calculate the timescale of collisions, which is the inverse of the collisional rate. As such calculations are proportional to the cross-sectional area of the cloud particles. As such for compact spherical particles this is proportional to the surface area of the cloud particle. Thus the distribution of cloud particles is better represented by this average size derived from the moments. For porous particles the relationship between surface area and cross-sectional area is more complicated.

The resultant double Dirac-delta distribution $(a_0, n_{d,0})$, $(a_1, n_{d,1})$ is converted into the collision affected moments (L'_j), according to Helling et al. (2008c), and is the inverse of the process described in Section 2.2.4.

$$\rho L'_j = \left(\frac{4\pi}{3}\right)^{j/3} (n_{d,0}a_0^j + n_{d,1}a_1^j).$$

(4.24)

4.3.8 Mass Conservation

Throughout the collision calculations, the mass of the cloud particles in the atmosphere (M_{tot}) is constant. The collision monomer size calculations assume all cloud particles to be of a single size $(a_0 = a_A)$, with corresponding number density $(n_{d,0}^{initial} = n_{d,A})$. Thus the total cloud mass is expressed as

$$M_{tot} = \frac{4\pi}{3}\rho_d n_{d,0} a_0^3.$$

(4.25)

Thus, once the collisional product size has been calculated, the cloud particle mass can then be divided between the two populations utilising a factor f_{mass}, such that:

$$n_{d,0} = \frac{M_{tot}}{\frac{4\pi}{3}\rho_d a_0^3} (1 - f_{mass})$$

(4.26)

$$n_{d,1} = \frac{M_{tot}}{\frac{4\pi}{3}\rho_d a_1^3} f_{mass}.$$

(4.27)

Where f_{mass}, like other parameters is based on protoplanetary disc numerical simulations, here the partition values used are the same as by Birnstiel et al. (2012):

$$f_{mass} = \begin{cases} 0.97, & a_{lim}^{sett} < a_{lim}^{frag} \\ 0.75, & a_{lim}^{sett} > a_{lim}^{frag}. \end{cases}$$

(4.28)
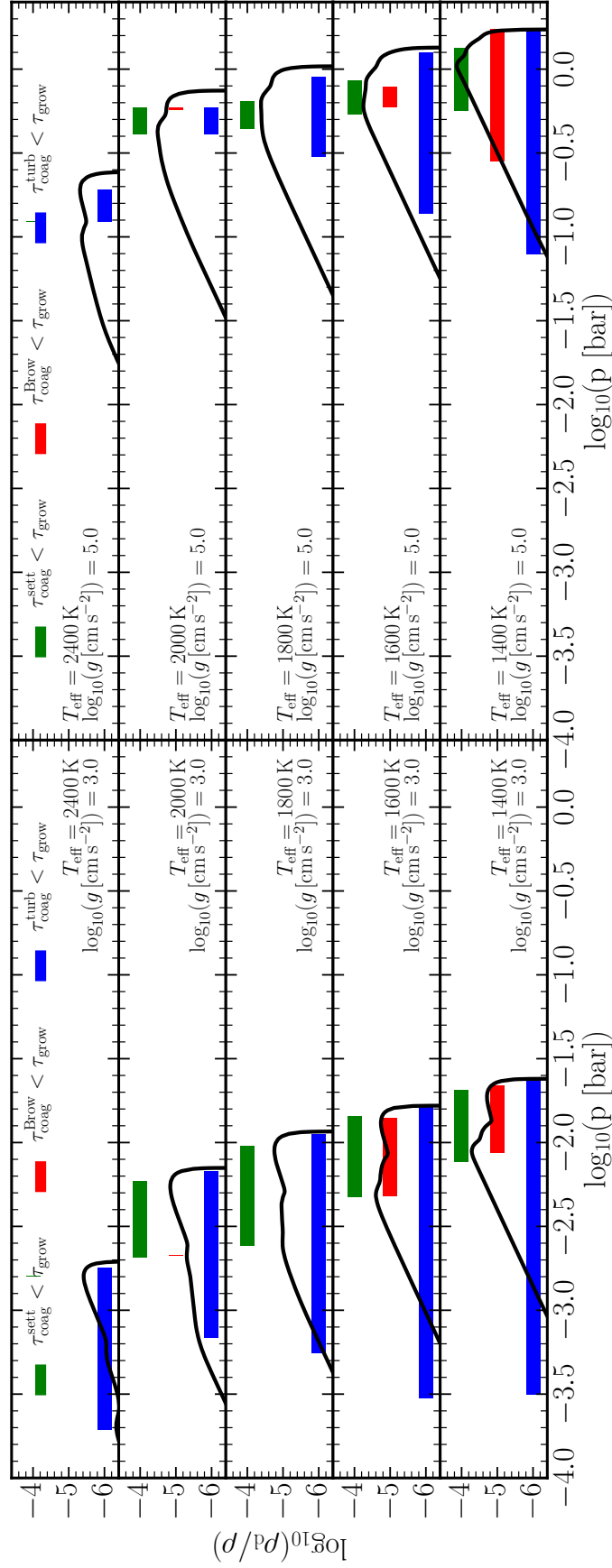
Figure 4.2: Atmosphere regions where the timescale of particle-particle collisions is faster than the gas-solid surface growth process. Shown are results for three particle collision processes: gravitational settling (green bar), Brownian motion (red bar), turbulence (blue bar). The black line shows the cloud particle mass load (ρ_d/ρ) for all DRIFT-PHOENIX atmospheric profiles used: $T_{\rm eff} = 2400, 2000, 1800, 1600, 1400$ K (top to bottom), for $\log_{10}(g\,[\rm cm\,s^{-2}]) = 3.0, 5.0$ (**Left** and **Right** respectively). Focusing only on the cloud base (10^{-4} bar $< p < 1$ bar).

4.3.9   Model Setup and Input

The atmospheric profiles used in this chapter are 1D Drift-Phoenix profiles (Dehn 2007; Helling et al. 2008c; Witte et al. 2009, 2011) for local gas temperature, pressure and vertical mixing velocity (T_{gas}, P_{gas}, v_{z}), as described in Section. 3.3.1. Here we use a grid of global atmospheric parameters of T_{eff} = 1400, 1600, 1800, 2000, 2400 K and $\log_{10}(g\,[\text{cm s}^{-2}])$ = 3.0, 5.0. These global parameters are applicable to a range of sub-stellar atmospheres, with $\log_{10}(g\,[\text{cm s}^{-2}])$ = 3.0 representing gas giant exoplanets and young brown dwarfs, and $\log_{10}(g\,[\text{cm s}^{-2}])$ = 5.0 representing old brown dwarfs. The kinetic, non-equilibrium, cloud formation model used is the same as described in Chapter 2, Section 2.2.7.

4.4   Analysis of Collision Timescales

This section compares the effectiveness of the different microphysical processes involved in cloud particle formation and particle-particle processes, as well as the likely collisional outcomes of such collisions. This is done by calculating where the coagulation timescale dominates (is shorter than) the processes of nucleation, settling, and growth/evaporation. For exoplanet and brown dwarf atmospheres, Woitke & Helling (2004) showed that atmospheres with static clouds are made of 5 typical regions: extremely cloud particle-poor and element depleted gas, efficient nucleation, cloud particle growth, drift dominated, and evaporating cloud particles. These regions are recovered in Appx. B.2, Fig. B.1, where the full set of timescales are shown.

4.4.1   Atmospheric Regions of Efficient Collisions

For the upper region of the atmosphere, efficient nucleation occurs (timescale is short) leading to the formation of small cloud particles which gravitationally settle inwards, and the number density of cloud particles rapidly increases with increasing pressure. Next, bulk growth also becomes efficient (for pressures > 10^{-8} bar for $\log_{10}(g\,[\text{cm s}^{-2}])$ = 3.0 and > 10^{-6} bar for $\log_{10}(g\,[\text{cm s}^{-2}])$ = 5.0), which grows cloud particle size and thus also increases the cloud particle settling velocity. For the lowest pressure part of this region, nucleation remains an efficient process, this leads to a dramatic increase in the cloud particle mass load ρ_{d}/ρ, as cloud particles continue to be efficiently produced and grown. At pressures of around > 10^{-2} bar for gas giant exoplanets ($\log_{10}(g\,[\text{cm s}^{-2}])$ = 3.0) and > 1 bar for brown dwarfs ($\log_{10}(g\,[\text{cm s}^{-2}])$ = 5.0) the gravitationally settling cloud particles fall into a region where they are thermally unstable and
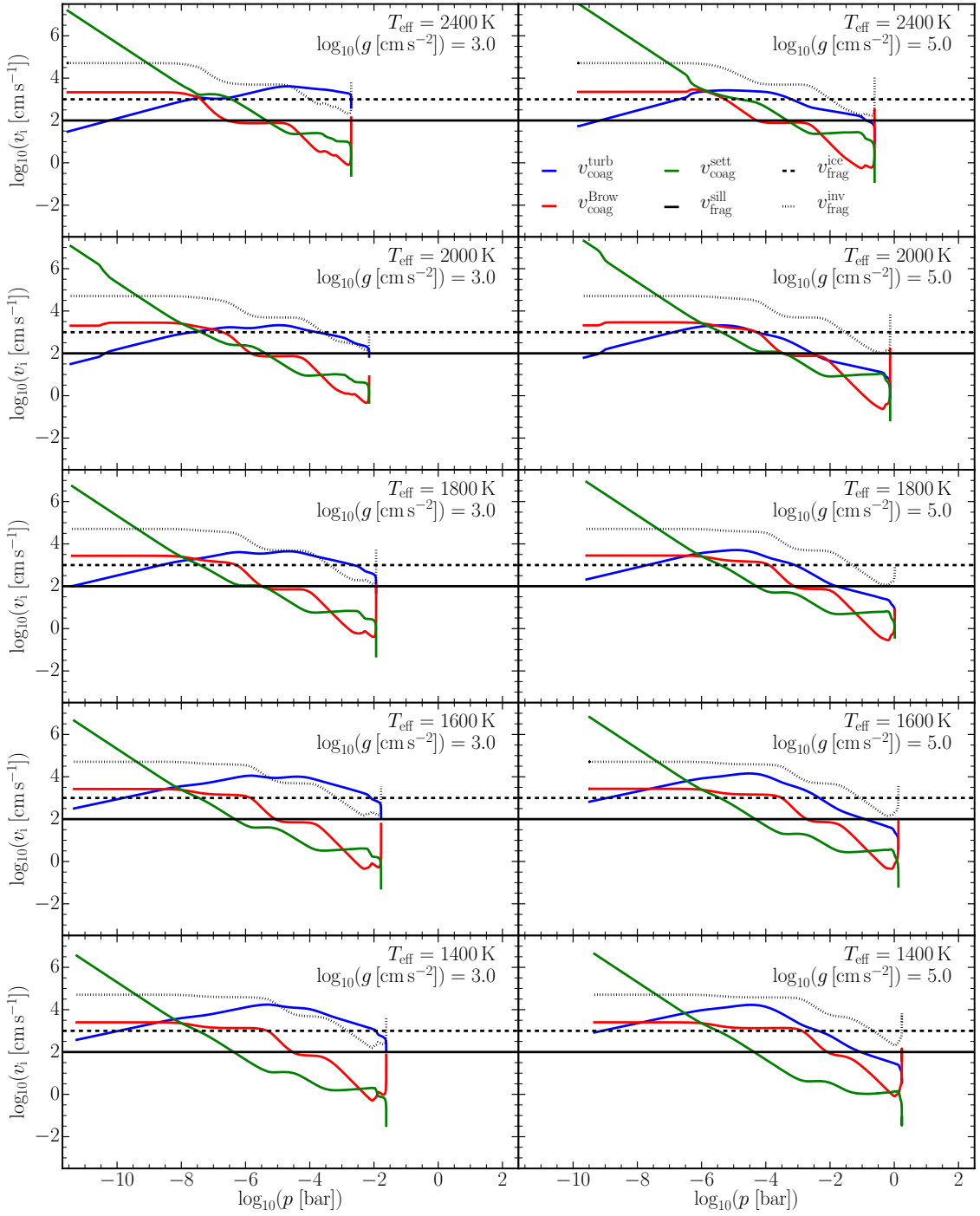
Figure 4.3: Cloud particle relative velocities generated by the three methods considered: gravitational settling (green), Brownian motion (red), turbulence (blue). Black lines show the fragmentation velocity limits for silicates (1 m s^{-1}, solid) and for ice coated particles (10 m s^{-1}, dashed). Also shown in dotted line is fragmentation limit $v_{\text{frag}}^{\text{inv}} = 10^{-2}/\langle a \rangle_{\text{A}}$ cm s^{-1}. From top to bottom are the model effective temperatures $T_{\text{eff}} = 2400, 2000, 1800, 1600, 1400$ K. Two surface gravities are also shown: $\log_{10}(g\,[\text{cm s}^{-2}]) = 3.0$ (**Left**), and $\log_{10}(g\,[\text{cm s}^{-2}]) = 5.0$ (**Right**).
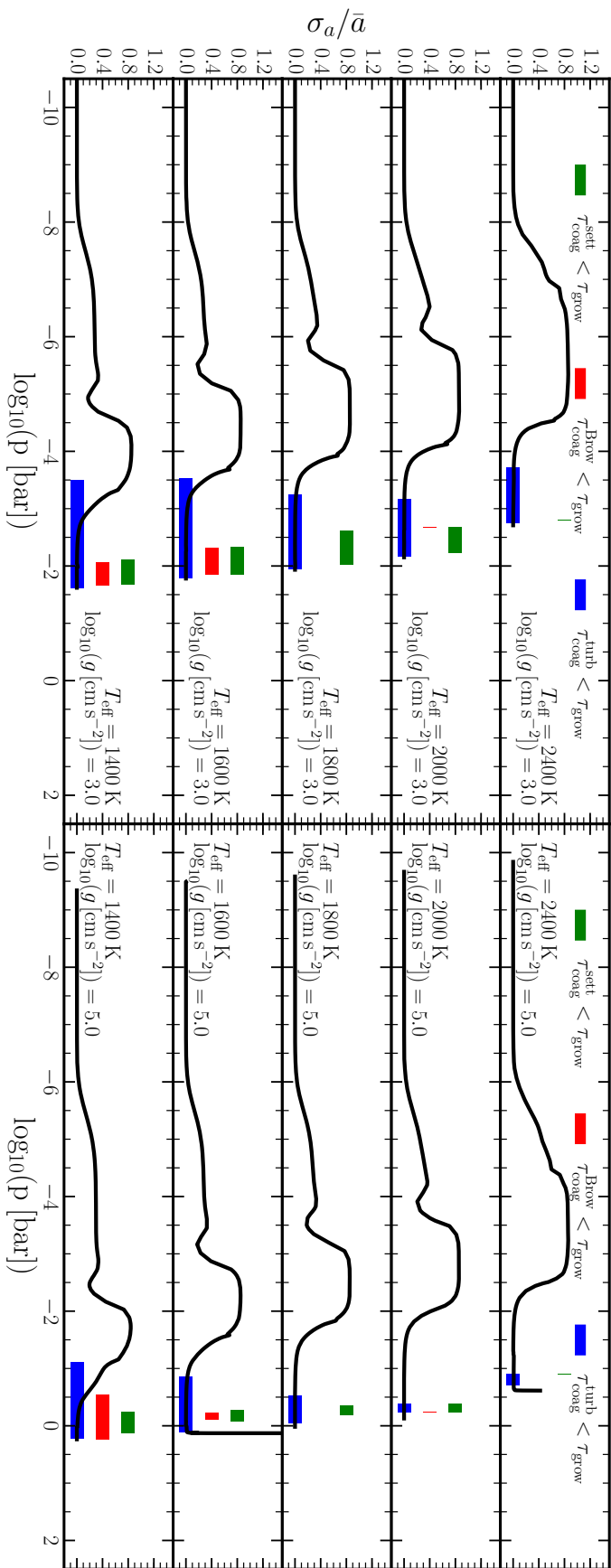
Figure 4.4: 'Broadness' of the derived Gaussian cloud particle size distribution, computed using the ratio of the standard deviation to the average Gaussian particle size, $\sigma_a / \bar{a}$. For all Dʀɪꜰᴛ-Pʜᴏᴇɴɪx atmospheric profiles used: $T_{\text{eff}} = 2400, 2000, 1800, 1600, 1400\,\text{K}$ (top to bottom), for $\log_{10}(g\,[\text{cm}\,\text{s}^{-2}]) = 3.0, 5.0$ (**Left** and **Right** respectively). The full depth of the atmospheres ($\sim 10^{-12}$–10^2 bar) is shown.

thus evaporate, which creates the sudden transition of the cloud base. Mixing is a much slower process throughout the atmosphere than the other microphysical processes, see Fig. B.1. Mixing only becomes faster than the peak of the fastest collisional timescales in the lowest (cloud-free) part of the atmosphere. Alternative mixing approaches for cloud formation have been investigated by Woitke et al. (2020).

Throughout the atmosphere, the gravitational settling timescale closely matches the timescale of the dominant growth process, excluding collisions which are calculated inconsistently. For the deepest part of the cloud structure, collisional timescales rapidly decrease. At altitudes just above the cloud base for the lowest effective temperature profiles, turbulent collisions becomes the dominant process.

Figure 4.2 summarises the regions where collisions becomes dominant – faster than the settling and growth timescales. For all atmospheric models considered collisions only dominate in the lower atmosphere, near the cloud base. This is because the collision growth timescale (Eq. 4.3) is inversely proportional to the cloud particle mass load in the atmosphere. Figure 4.3 also shows that differential settling and Brownian motion both induce lower relative velocities between cloud particles and thus fewer collisions and longer coagulation/fragmentation timescales. The collisional timescale due to Brownian motion is slower than the settling timescale (Appx. B.2 Fig. B.1). This invalidates a key assumption of Eq. 4.5 and suggests that particles make multiple diffusive step between collisions. Thus a diffusive timescale for Brownian motion induced collisions would have to be used. However, as the diffusive case is generally slower than the ballistic case, Eq. 4.5 serves to provide a lower limit on $\tau_{\mathrm{coag}}^{\mathrm{Brow}}$.

Figure 4.2 demonstrates that coagulation/fragmentation becomes an efficient and dominant process across a broader pressure range for lower effective temperatures. This timescale analysis also determines that turbulence induced collisions is the most efficient process for causing coagulation/fragmentation.

4.4.2   Relative Velocity of Collisional Processes and Fragmentation Limit

Near the cloud base, where coagulation/fragmentation is efficient , Fig. 4.3 shows that of the three considered collisional processes turbulence induced particle-particle collision occur on the shortest timescales. Thus it follows that turbulence also induces the largest relative velocities between cloud particles in these regions. Gravitational settling and Brownian motion induced collisions do
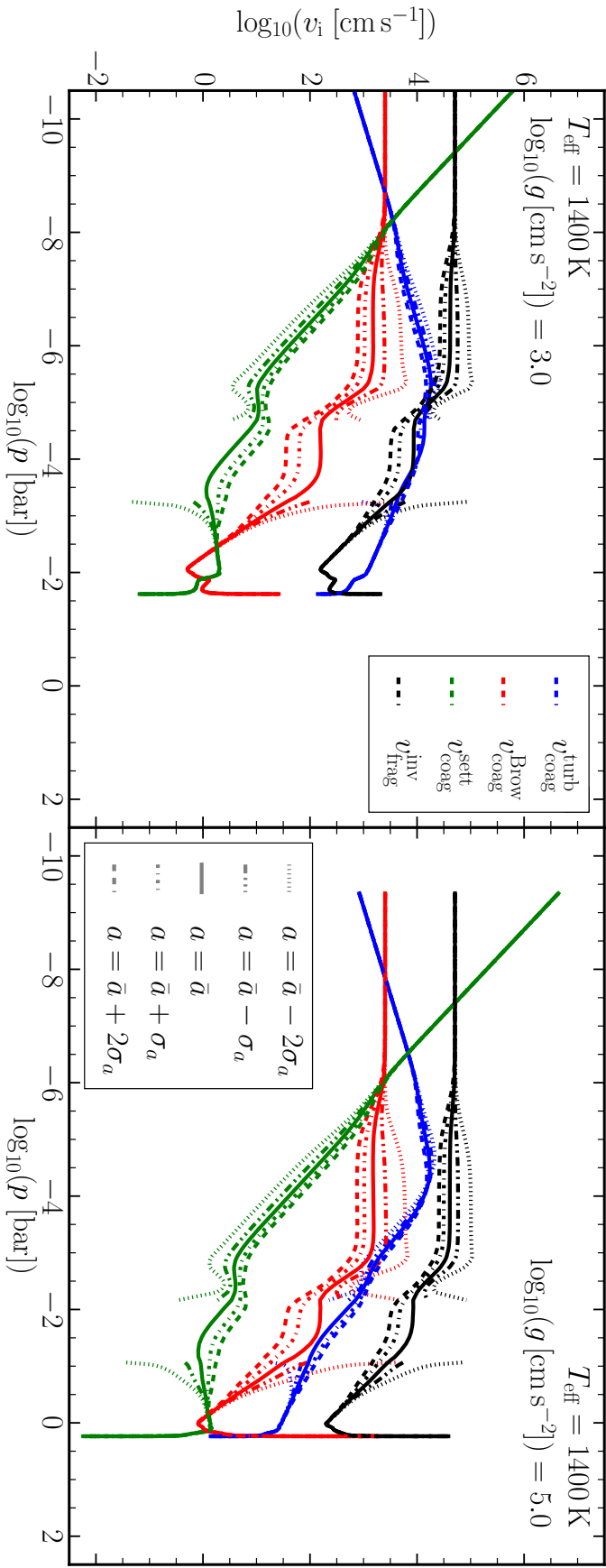
Figure 4.5: Monodisperse cloud particles relative velocities for $T_{\mathrm{eff}} = 1400\,\mathrm{K}$ for $\log_{10}(g\,[\mathrm{cm\,s^{-2}}]) = 3.0,\ 5.0$ (**Left** and **Right** respectively) as well as the fragmentation limit using Eq. 4.18, $v_{\mathrm{frag}}^{\mathrm{inv}}$ (black). Line styles represent the monodisperse velocities for particles of size $a = \bar{a} \pm k\sigma_a$ for $n = 0$, 1 and 2 as described in the legend.

occur at higher relative velocities in the upper parts of the atmospheres (low pressures). However, as cloud particle density is low in these regions, processing through particle-particle collisions in this region is very slow. Thus, the outcome of any collisions that do occur will not have a substantial impact on the overall cloud particle population.

This relative velocity analysis also highlights the important distinction in the outcomes of collisions and the limiting relative velocities between these regimes: whether they are constructive (i.e. coagulation) or destructive (i.e. fragmentation, sputtering, etc). AS discussed previously, the collisional outcome of fragmentation is often modelled by a constant velocity limit (e.g. Güttler et al. 2010; Birnstiel et al. 2011), which generally for silicates this limit is above $10^2 \, \mathrm{cm \, s^{-1}}$. Even for non-compact irregularly shaped particles of different compositions Blum & Wurm (2000) find fragmentation velocities to still consistently be around $10^2 \, \mathrm{cm \, s^{-1}}$. However, for 'icy' particle, this velocity limit may be up to $10^3 \, \mathrm{cm \, s^{-1}}$ (Wada et al. 2009). Figure 4.3 shows where the cloud particle relative velocities induced by turbulence, gravitational settling, and Brownian motion exceed these fragment velocity limits, and the inversely proportional velocity limit (Eq. 4.18).

Inside the atmospheric regions where particle-particle collisions are efficient for gas giant atmospheres (for $\log_{10}(g \, [\mathrm{cm \, s^{-2}}]) = 3.0$), turbulent collision velocities are almost always above the fragmentation limit for all three velocity limits. However, the turbulent velocities quickly fall below the fragmentation limit inversely proportional to particle size, and at very low pressures also fall below the icy fragmentation limit. Differential settling and Brownian motion both produce much lower relative velocities at high pressures, consequently their relative velocities are below all fragmentation limits for $p > 10^{-5}$ bar but do rise above the silicate fragmentation velocity limit at this pressure, and above the icy fragmentation velocity limit between 10^{-6}–10^{-8} bar. At very high altitudes the Brownian motion velocity flattens off because the size of cloud particles flattens off at the cloud condensation nuclei (condensation seeds), so it never exceeds the inversely proportional velocity limit for particle fragmentation.

In the atmospheres of old brown dwarfs ($\log_{10}(g \, [\mathrm{cm \, s^{-2}}]) = 5.0$) the cloud particle relative velocities, induced by all processes considered, never rise above the inversely proportional limit. However, the velocities still follow similar trends as for the gas giant exoplanets ($\log_{10}(g \, [\mathrm{cm \, s^{-2}}]) = 3.0$) case for the silicate and icy fragmentation velocity limits.

Thus considering the inversely proportional fragmentation velocity limit in regions where

collisions are efficient at affecting particle size, for $\log_{10}(g\,[\mathrm{cm\,s^{-2}}]) = 3.0$ fragmentation will limit growth of aggregates, but for $\log_{10}(g\,[\mathrm{cm\,s^{-2}}]) = 5.0$ collisions should always be constructive.

Overall this analysis shows that particle-particle collisions become important and dominant towards the base of the cloud deck, due largely to the cloud particle number densities increasing and that these collisions will be largely induced by turbulence. However, cloud particle-particle collisional velocities are high throughout the atmosphere so that fragmentation is likely to limit aggregate sizes. Brownian motion and differential settling could produce enough collisions and thus dominate the cloud particle sizes at higher altitudes if a sufficient number density of cloud particle were present. This might occur due to the formation of photo-chemical hazes (Barth et al. 2021; Kawashima & Ikoma 2018; Helling et al. 2020; Adams et al. 2019) or due to efficient hydrodynamic transport from deeper atmospheric regions (Ohno & Okuzumi 2017).

4.4.3 Validity of Monodisperse Timescale Calculations

For these timescale analysis a monodisperse cloud particle size distribution is assumed. We now asses for gas giant and brown dwarf atmospheres whether cloud particles of varying sizes would alter the collisional outcomes or the dominant processes for inducing particle-particle collisions. From the cloud moments a Gaussian cloud particle size distribution is derived (as done in Chap. 3). Figure 4.4 shows the ratio of the standard deviation of the Gaussian distribution (σ_a) to the mean particle size ($\bar{a}$). This illustrates that the distribution of cloud particle sizes is only broad at low pressure (high altitude) levels, where nucleation is still an efficient process. This is because without nucleation generating small cloud particles, bulk growth through condensation efficiently grows all cloud particles to the gravitational settling limiting size. Thus outside of these regions this creates a tightly peaked Gaussian cloud particle size distribution.

As seen coagulation/fragmentation timescales are shortest near the cloud base, where the nucleation timescale is long, for all but $T_\mathrm{eff} = 1400\,\mathrm{K}$, $\log_{10}(g = 3.0\,[\mathrm{cm\,s^{-2}}])$ the cloud particle size distribution is already narrow at these pressure levels. Nonetheless, the impact of adding additional particle sizes as a consequence of this size distribution for $T_\mathrm{eff} = 1400\,\mathrm{K}$, $\log_{10}(g\,[\mathrm{cm\,s^{-2}}]) = 3.0, 5.0$ is briefly considered here. Figure 4.5 reveals that the overall change to the relative velocities for monodisperse collisions with cloud particle sizes of $a = \bar{a} + k\sigma_a$ for $k = 1$ and 2 is not that dramatic. Turbulence still remains the most significant collisional process for both atmospheres. When considering the inversely proportional

fragmentation velocity limit (Eq. 4.18), qualitatively the collisional outcomes are unchanged. At the cloud base for exoplanet atmospheres ($\log_{10}(g\,[\mathrm{cm\,s^{-2}}]) = 3.0$) turbulent-induced relative velocities are still sufficiently high to cause fragmentation. For old brown dwarfs ($\log_{10}(g\,[\mathrm{cm\,s^{-2}}]) = 5.0$) all collisional processes induce cloud particle relative velocities below the fragmentation limit. However, the same cannot always be said for lower boundary values for cloud particle sizes of $a = \bar{a} - k\sigma_a$ for $k = 1$ and 2. Unsurprisingly, Brownian motion becomes more significant for smaller particles and differential gravitational settling becomes less important.

The inverse relation to cloud particle size of the fragmentation velocity limit causes turbulence induced fragmentation to remain the dominating particle-particle process near the cloud base.

## 4.5 Effect of Collisions on Cloud Particle Properties

Cloud formation results including collision processes in atmosphere of gas giant exoplanets and brown dwarfs broadly split into three categories:

  i) Fragmenting atmospheres for $\log_{10}(g\,[\mathrm{cm\,s^{-2}}]) = 3.0$ (Sect. 4.5.1)

  ii) Coagulating atmospheres for $\log_{10}(g\,[\mathrm{cm\,s^{-2}}]) = 5.0$ and $T_{\mathrm{eff}} < 1800\,\mathrm{K}$ (Sect 4.5.2)

  iii) Growth dominated atmospheres for $\log_{10}(g\,[\mathrm{cm\,s^{-2}}]) = 5.0$ and $T_{\mathrm{eff}} \geq 1800\,\mathrm{K}$ (Sect 4.5.3)

These categories are best seen in the average cloud particle size and number denisty throughout the atmospheres of the model exoplanet and brown dwarfs. These properties are shown in Figs. 4.6 and 4.7, where Fig. 4.6 also shows the fragmentation and settling limits of the collisional process.

4.5.1 Cloud Particle Fragmentation Dominated Atmospheres

For exoplanet and young brown dwarf atmospheres ($\log_{10}(g\,[\mathrm{cm\,s^{-2}}]) = 3.0$) of all temperatures, collisions between cloud particles result in a reduction in average particle size (left column of Fig. 4.6). For all these atmospheres the fragmentation limit is set by the differential settling velocity in the upper atmosphere and for the lower atmosphere it is set by the turbulent velocities, as at this point turbulence begins to generate higher relative velocities. This switch-over of dominant driving process of collisions is responsible for the inflection point around a pressure of $\sim 10^{-6}\,\mathrm{bar}$, where the fragmentation limit begins to decrease. For the upper atmosphere the fragmentation limit is small, however as the timescale for coagulation in the upper atmosphere is
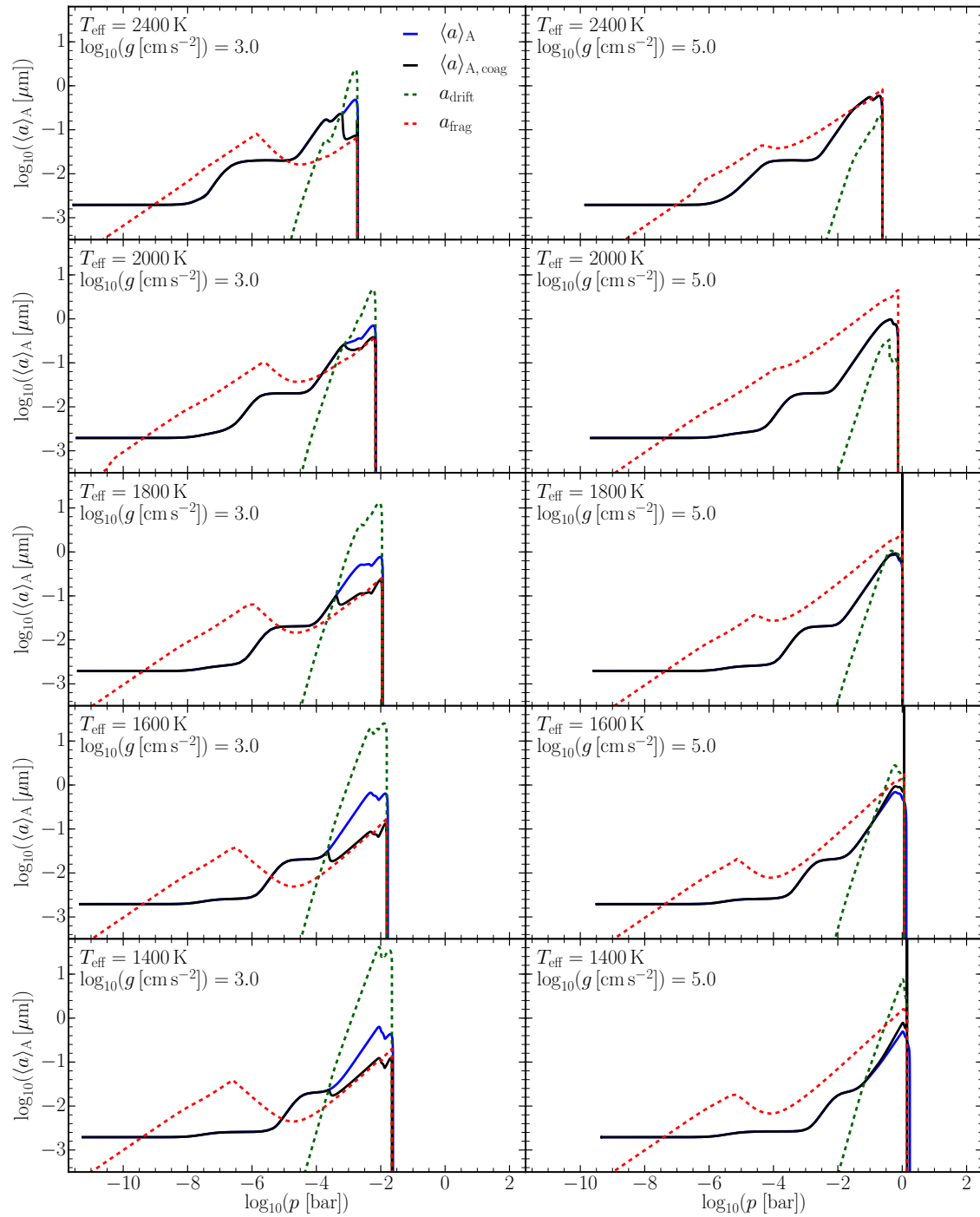
Figure 4.6: Surface-averaged particle size $\langle a \rangle_A$ without collisions (blue) and with collisions (black). From top to bottom are the model effective temperatures $T_{\mathrm{eff}} = 2400, 2000, 1800, 1600, 1400$ K for gas giant planets and young brown dwarfs ($\log_{10}(g\,[\mathrm{cm\,s^{-2}}]) = 3.0$, **Left**), and for old brown dwarfs ($\log_{10}(g\,[\mathrm{cm\,s^{-2}}]) = 5.0$, **Right**). The settling size limit $a_{\mathrm{lim}}^{\mathrm{sett}}$ is shown in red and the fragmentation size limit $a_{\mathrm{lim}}^{\mathrm{frag}}$ in green.
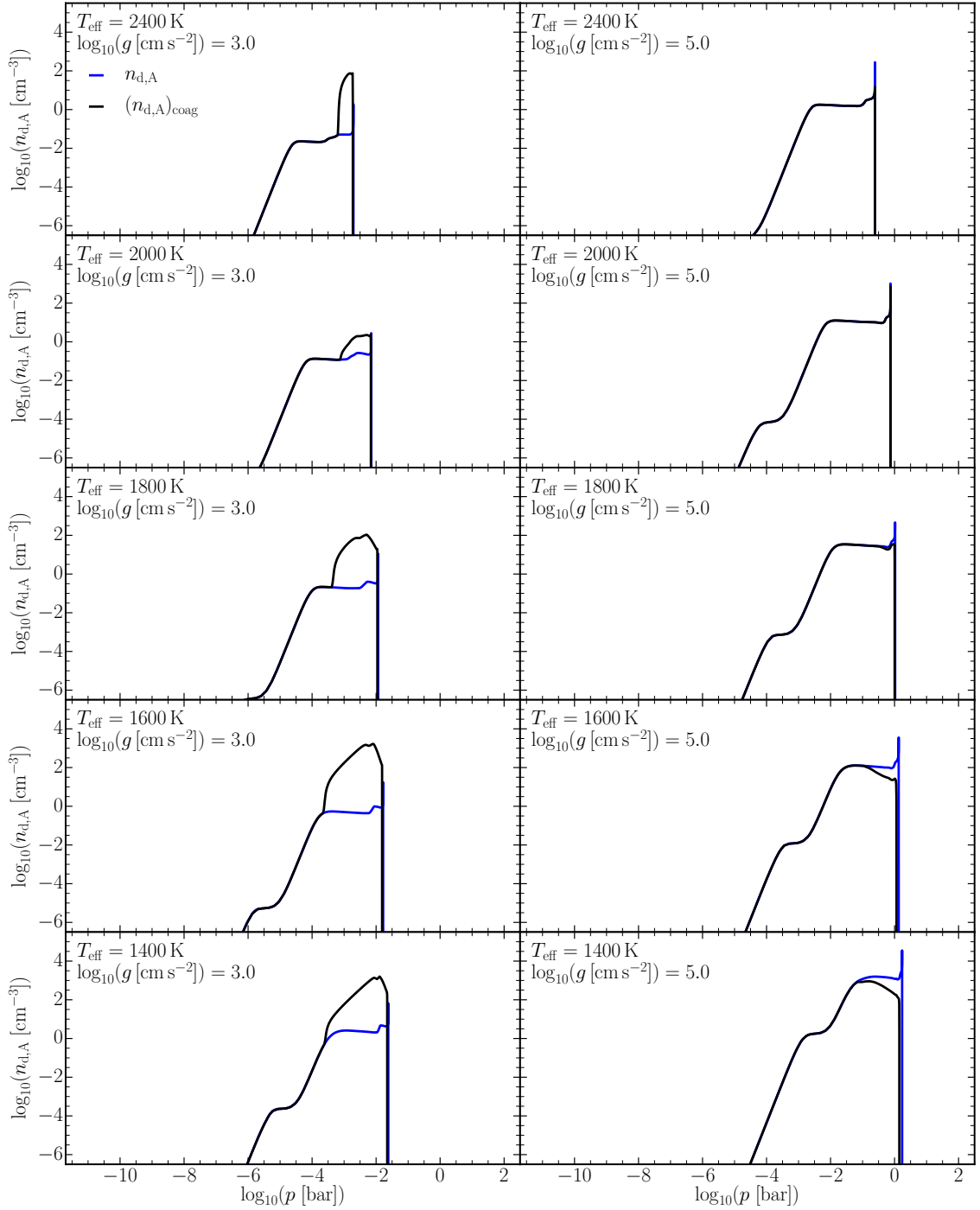
Figure 4.7: Surface-averaged number densities $n_{d,A} = \rho L_2^3/L_3^2$ without collisions (blue) and with collisions (black). From top to bottom are the model effective temperatures T_{eff} = 2400, 2000, 1800, 1600, 1400 K for gas giant planets and young brown dwarfs ($\log_{10}(g\,[\mathrm{cm\,s^{-2}}])$ = 3.0, **Left**), and for old brown dwarfs ($\log_{10}(g\,[\mathrm{cm\,s^{-2}}])$ = 5.0, **Right**).

much longer than all other processes, this does not affect the cloud particle size and number density.

The reduction of fragmentation limit with increasing pressure, in combination with increasing average particle size due to bulk growth eventually leads to the fragmentation limit in particle size, $a_{\text{lim}}^{\text{frag}}$, becoming lower than the average particle size $\langle a \rangle_{\text{A}}$ in the deeper atmosphere. Between 10^{-4} and 10^{-3} bar, the size limit due gravitational settling exceeds the average particle (and therefore collision monomer) size, therefore at greater pressure there is sufficient time for the cloud particles to collide before settling out. This results in a very sudden drop in the average cloud particle size $\langle a \rangle_{\text{A}}$ as the fast collisions rapidly fragment the cloud particle population. From here until the cloud base, the average particle size is controlled by the fragmentation limit, a_{frag}. Any growth above this limit produces cloud particles that are rapidly broken down to below this limit (red dashed line in Fig. 4.6). Figure 4.7 shows that in this region above the cloud base there is correspondingly an increase in cloud particle number density, n_{d}, due to mass conservation.

However, looking at the cloud particle mass load, ρ_{d}/ρ in Fig. B.2 one sees a substantial increase in the mass density of the cloud particles (ρ_{d}) in an atmospheric layer of up to a factor of 6 enhancement of the peak cloud particle mass load for the atmosphere $T_{\text{eff}} = 1600\,\text{K}$, and $\log_{10}(g\,[\text{cm s}^{-2}]) = 3.0$, with similarly large increases for $T_{\text{eff}} = 1400$ and $1800\,\text{K}$. As collisions are conservative of cloud particle mass, this additional increase in cloud particle material must come from increased condensation due to the increased surface area of the smaller cloud particles resultant from the fragmentation.

4.5.2 Coagulation Growth Affected Atmospheres

For cool brown dwarfs ($T_{\text{eff}} < 1800\,\text{K}$, $\log_{10}(g\,[\text{cm s}^{-2}]) = 5.0$), the peak settling limit for coagulation continues to increase with decreasing temperature. In addition, the inflection point of the fragmentation limit is much smaller than for the fragmenting type atmospheres, and consequently the fragmentation size limit always remains above the average particle size. Thus for the coolest atmospheres there is sufficient time for the cloud particles to increase in size due to collisions. For these atmospheres there is a minor increase in average particle size, however compared to the affect from fragmenting atmospheres it is much less stark. This is because the relative velocities between cloud particles are slower than for fragmenting atmospheres and thus the collisional growth timescale is also lower. Furthermore, any resultant coagulation reduces the cloud particle number density because of mass conservation, and thus reduces the collision rate

further. Figure 4.7 shows the reduction in number density can be between one and two orders of magnitude from the collision free case at the cloud base.

For these models the fragmentation limit also becomes the smaller of the two limits below 10^{-2} bar. Thus, even in the case of substantial growth, the fragmentation limit prevents significant growth greater than approximately an order of magnitude larger than the collision monomer size at most. Coagulation also affects the cloud particle mass load for these atmospheres, reducing it slightly compared with the collision free case, this is due to the increase in particle size and reduction in number density reducing the surface area available for surface growth (Fig. B.2).

4.5.3 Surface Growth Dominated Atmospheres

For hot brown dwarfs ($T_{\text{eff}} \geq 1800\,\text{K}, \log_{10}(g\,[\text{cm}\,\text{s}^{-2}]) = 5.0$), the cloud particle distribution at the cloud base is dominated by bulk growth. Figure 4.6 shows this occurs when the average cloud particle size remains below the fragmentation limit, but above the settling limit for coagulation. Physically this represents that the average cloud particles will settle out of a given atmospheric layer before collisions significantly affect the average particle size. Even for the case of $T_{\text{eff}} = 1800\,\text{K}$, where the settling limit is only marginally higher than the average particle size at its peak, any collisional growth is severely limited and the cloud particle distribution is largely unchanged.

4.5.4 Limited Impact of Collisions on Nucleation Rates and Material Composition

Section 4.4 showed that nucleation is efficient in the low pressure upper atmosphere and particle-particle collisions are efficient deeper in the atmosphere near the cloud base. However, the two processes do still occur in overlapping regions of the atmosphere. Furthermore, collisions alter the total surface area of cloud particles, and therefore the bulk growth rate. This could in turn affect the nucleation rate by reducing the element abundances in the gas phase. In particular fragmentation dramatically increases the mass of cloud particle material (Sect. 4.5.1), possibly amplifying element depletion and causing reduced nucleation rates.

The nucleation rates of the high altitude nucleation species SiO[s] is unaffected as collisional rates for pressures $< 10^{-5}$ bar are negligible. For TiO$_2$[s] though, this is not the case. Fig. B.3 shows that for cooler exoplanet and brown dwarf atmospheres ($T_{\text{eff}} \leq 1400\,\text{K}$), there may be atmospheric regions where nucleation and collisions occur efficiently simultaneously. In a fragmenting atmosphere the TiO$_2$[s] nucleation rate begins to decrease at lower pressures (higher altitude), and for the coagulating brown dwarf profile $T_{\text{eff}} = 1400\,\text{K}, \log_{10}(g\,[\text{cm}\,\text{s}^{-2}]) = 5.0$

profile there is actually a slight increase in the $TiO_2[s]$ nucleation rate before the total nucleation rate drops off at a slightly higher pressure than in the collision-free case. However, for all warmer brown dwarf ($T_{eff} \geq 1600\,K$) profiles there is no discernible effect. The reason for both these cases is similar to the situation that occurred for increased porosity in Chap. 3, where increased surface area from fragmentation of cloud particles (reducing average particle size) leads to more efficient bulk growth of the cloud particles which depletes the gas phase of the relevant nucleating species, and vice-versa for the coagulating case.

In summary, nucleation rates in exoplanet and brown dwarf atmospheres are unaffected by particle-particle collisions unless:

- The cloud particle number density is sufficient for efficient collisions (low collision timescale).

- The outcome of coagulation/fragmentation substantially changes the cloud particle average size and hence the available surface area to affect bulk growth.

- Some species has a high nucleation rate at the high pressures where collisions between cloud particle-particle collisions are efficient.

Particle-particle collisions do not change the cloud particle material composition throughout the atmospheres in our hybrid-model, because only the nucleation and the surface growth/evaporation processes are considered to interact with the gas-phase. Instead, particle-particle processes indirectly affect the material composition of the cloud particles due to an increased or decreased surface of cloud particles that allows for greater or lesser condensation of the same cloud species, as thermal stability is unchanged. However, this effect is negligible in these models.

4.6 Observable Outcomes of Particle - Particle Collisions

The optical properties of the clouds are now examined for the atmospheres with the most significant changes to the cloud distributions due to the effect of particle-particle collisions: the fragmenting type atmosphere ($T_{eff} = 1400\,K$ and $\log_{10}(g\,[cm\,s^{-2}]) = 3.0$) and the coagulating type atmosphere ($T_{eff} = 1400\,K$ and $\log_{10}(g\,[cm\,s^{-2}]) = 5.0$). Clouds are important for transmission and emission spectra (Barstow & Heng 2020) and for directly imaged exoplanets. In transmission the slant geometry observed allows for clouds to have an even larger impact on the
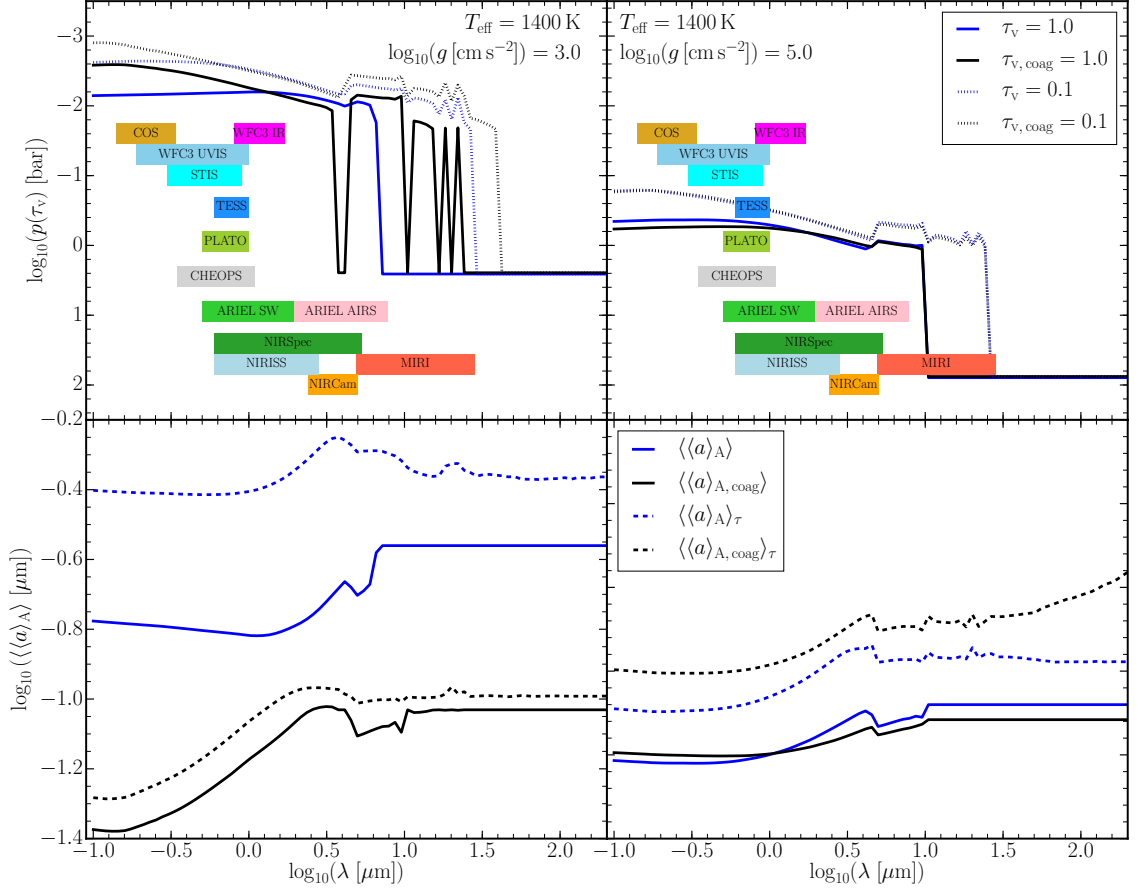
Figure 4.8: For $T_{\text{eff}} = 1400\,\text{K}$, $\log_{10}(g\,[\text{cm}\,\text{s}^{-2}]) = 3.0$ (**Left**), $T_{\text{eff}} = 1400\,\text{K}$, $\log_{10}(g\,[\text{cm}\,\text{s}^{-2}]) = 5.0$ (**Right**). Without collisions shown in blue and with collisions in black. **Top:** The pressure level at which the cloud vertical optical depth reaches certain thresholds: $p(\tau_{\text{v}} = 1)$ in solid lines and $p(\tau_{\text{v}} = 0.1)$ in dashed lines. **Bottom:** The number-density weighted, surface-averaged radius of the cloud particle population above the pressure level at which cloud optical depth reaches unity ($\langle\langle a \rangle_{\text{A}}\rangle$, solid) and the average observable particle size ($\langle\langle a \rangle_{\text{A}}\rangle_{\tau}$, dashed). Instrument wavelength ranges shown in the coloured bars, ranges taken from HST (Wakeford et al. 2020), TESS (Ricker et al. 2015), CHEOPS (Broeg et al. 2013), PLATO (Rauer et al. 2014), JWST (Greene et al. 2016). ARIEL Infrared Spectrometer (AIRS) and 'ARIEL SW' wavelengths from (Mugnai et al. 2020). 'ARIEL SW' shows the VISPhot (0.5–0.6 μm), FGS₁ (0.6–0.8 μm) and FGS₂ (0.8–1 μm) photometers, and NIRSpec (1.1–1.95 μm) spectrometer

observed spectra (Fortney 2005). For emission geometry, the depth of atmosphere visible above the clouds impacts the effective temperature of the atmosphere observed and thus the luminosity in a given infrared waveband (Baxter et al. 2020; Gao & Powell 2021). The optical depth vertically from the 'Top of the Atmosphere' (TOA) to some height z is

$$\tau(\lambda, z) = \int_{\text{TOA}}^{z} \pi Q_{\text{ext}}(\lambda, \langle\langle a\rangle_{\text{A}}\rangle, z') \left[\langle a\rangle_{\text{A}}(z')\right]^2 n_{\text{d,A}}(z')\text{d}z', \qquad (4.29)$$

with $Q_{\text{ext}}(\lambda, \langle\langle a\rangle_{\text{A}}, z)$ the extinction efficiency of the cloud particles, using effective medium theory with the Brüggemann mixing rule (Bruggeman 1935) and determined using Mie theory and assuming spherical particles of the surface-averaged mean cloud particle size (Bohren & Huffman 1983). This is integrated from the top of the atmosphere until the level at which the clouds become optically thick (optical depth $\tau_{\text{v}}(\lambda) = 1$).

4.6.1 Cloud Optical Depth

The atmosphere below the pressure level where $\tau_{\text{v}}(\lambda) = 1$ is hidden from observations, thus any results from observations are indicative of only the atmosphere above this level. Thus this level is equivalent to the cloud deck level in grey cloud model often used in parameterised atmosphere models. Although this interpretation is only valid for nadir geometry emission and reflection spectra, as it does not take into account slant geometry for other phase angles, such as transmission spectroscopy. In the case of such geometries, the optically thick pressure level is expected to be higher in the atmosphere (Fortney 2005), and the impact of clouds is biased towards the properties of high altitude clouds and hazes, and three dimensional effects becoming important (MacDonald & Madhusudhan 2017).

Figure 4.8 (top panels) shows the wavelength dependent gas pressure at which the clouds become optically thick, as well as the pressure level for $\tau_{\text{v}}(\lambda) = 0.1$ for the coolest gas giant and brown dwarf atmosphere profiles ($T_{\text{eff}} = 1400\,\text{K}$, $\log_{10}(g\,[\text{cm s}^{-2}]) = 3.0$ and 5.0). The optical depth $\tau_{\text{v}}(\lambda) = 0.1$ better illustrates the differences in the cloud silicate features around $10\,\mu\text{m}$. In the near- and mid-infrared, there are dramatic jumps in the optically thick pressure level for the collisional case of the exoplanet atmosphere (top right plot). These jumps are resulting from the enhancement of the opacity of the clouds, particularly in the silicate features. The overall enhancement of the total cloud optical depth is by a factor of ~ 3 for this atmosphere, seen in Appx. B.2 Figs. B.6 and B.7. As illustrated by these figures the overall optical depth of these

clouds is increased to the point where the peaks of the features in this region are optically thick, this leads to the severe jumps seen here.

Without the inclusions of cloud particle-particle collisions, the atmospheres exhibit relatively flat, grey, cloud decks for UV and optical wavelengths. These observable cloud decks sit around 0.01 and 1 bar for the exoplanet and brown dwarf atmospheres respectively. Beyond wavelengths of 1 μm there is a slight decrease in the optical thickness. For wavelengths > 10 μm the clouds are no longer optically thick (blue line Fig. 4.8).

With collisions included, there is relatively little change for the T_{eff} = 1400 K brown dwarf atmosphere, because the change to the cloud particle number and size density distribution is small, and affects pressure levels > 1 bar (Sect. 4.5). The $\tau_{\mathrm{v}}(\lambda)$ = 0.1 pressure level is not affected by inclusion of cloud particle-particle collisions as coagulation only becomes important at pressure levels deeper than these results. For wavelengths $\lesssim$ 1.8 μm the optically thick pressure level of clouds with collisions is marginally lower, due to a reduced density of cloud mass in the atmosphere.

For the fragmentation dominated, cold (T_{eff} = 1400 K) exoplanet atmosphere ($\log_{10}(g\,[\mathrm{cm\,s^{-2}}])$ = 3.0), it is easiest to split the effect is into two parts: silicate features and the optical regime. For the optical regime $\lesssim$ 1.25 μm the clouds are significantly more optically thick and show a trend of increasing optical thickness with decreasing wavelength until $\lesssim$ 0.15 μm. This is because fragmentation produces a large number of smaller cloud particles, compared with the collision free case for pressures greater than 10^{-4} bar for this atmosphere. Fragmentation increases the surface area of the cloud particles, decreasing particle sizes, but overall increases total cloud mass density, leading to clouds that overall are far better scatterers in the optical wavelength regime. Such differences between the flat optical depth of collision free clouds compared with the sloped optical depth of the fragmenting case could impact observations of cool exoplanets in HUBBLE observations. The short wavelength end of *Hubble* STIS and WFC3 UVIS, the later of which is suggested as a viable tool for exoplanet transit spectra by Wakeford et al. (2020), would observe the largest impact of collisions in the optical regime.

Inferences of material compositions in exoplanet atmospheres is something that has been proposed recently (Taylor et al. 2020; Luna & Morley 2021). However the material composition of clouds changes throughout the atmosphere (Appx. B.2 Fig. B.5). As the optical thick layer is quite near the cloud base for both exoplanet and brown dwarf atmospheres, the majority of these

changing material compositions will be observable. Thus a wide mix of materials are present in the observable cloud population. For comparable brown-dwarf atmospheres (T_{eff} = 1800, 2400 K $\log(g\,[\text{cm}\,\text{s}^{-2}])$ = 5.0), materials include forsterite and enstatite (Mg$_2$SiO$_4$[s], MgSiO$_3$[s]). In addition there are regions with large volume contributions of fayalite (Fe$_2$SiO$_4$[s]) in combination with forsterite (Mg$_2$SiO$_4$[s]), this could confound retrievals of specific olivine (Mg$_x$Fe$_{1-x}$SiO$_4$[s]) Fe/Mg mixing ratios. For both the cool atmospheres shown above, for wavelengths approximately < 1 μm the optically thick pressure levels are above the level where high temperature condensates form thus these would not be expected observable.

4.6.2 Average Observable Cloud Particle Size

The average cloud particle size is a property of interest for observations of clouds, as Mie scattering is an important consideration of cloud particles (and aerosols in general) for exoplanet atmospheres, particularly at longer wavelength. Mie theory is frequently used in forward models of exoplanet spectra (Wakeford et al. 2017; Morley et al. 2017; Lavvas & Koskinen 2017; Gao & Benneke 2018; Lacy & Burrows 2020a,b; Min et al. 2020), for aerosol properties (Kitzmann & Heng 2018; Mollière et al. 2019; Budaj et al. 2015), and is used in recent retrieval frameworks (e.g. Pinhas & Madhusudhan 2017; Zhang et al. 2019; Welbanks & Madhusudhan 2021).

The average particle size retrieved is dictated by the cloud particles above the optically thick level of the clouds, as below this is obscured and hence the retrieval contains no information on these atmospheric levels. We introduce two average particle sizes to investigate both the observable particle size likely derived by retrieval models, and the size of particles governing the microphysical processes of clouds in the observable atmosphere. The average observable particle size is calculated by weighting the surface-averaged mean particle size by the transmittance $\exp(-\tau_{\text{v}})$, from (Helling et al. 2019). The transmittance is the fraction of initial incident light intensity remaining at a height z into the atmosphere, thus the transmittance starts at 1 and decreases further into the atmosphere

$$\langle\langle a \rangle_{\text{A}}\rangle_\tau = \frac{\int_{\text{TOA}}^{\text{BOA}} \langle a \rangle_{\text{A}} \exp(-\tau_{\text{v}})\,\mathrm{d}z}{\int_{\text{TOA}}^{\text{BOA}} \exp(-\tau_{\text{v}})\,\mathrm{d}z} \tag{4.30}$$

This is integrated downwards from the Top of the Atmosphere (TOA) to the 'Bottom of the Atmosphere' (BOA), thus the numerator gives the average particle size contributing to the extinction of light in the atmosphere. However, this is not representative of the particle size

actually present in the optically thin atmosphere. For this we introduce the average particle size above the optically thick level weighted by cloud particle number density, from Chapter 3, Eq. 3.17:

$$\langle \langle a \rangle_{\mathrm{A}} \rangle = \frac{\int_{\mathrm{TOA}}^{z(\tau_v=1)} n_{\mathrm{d,A}} \langle a \rangle_{\mathrm{A}} \mathrm{d}z}{\int_{\mathrm{TOA}}^{z(\tau_v=1)} n_{\mathrm{d,A}} \mathrm{d}z}. \tag{4.31}$$

This average particle size is important as it typifies the surface area of the cloud particles that are existing in the observable atmosphere, and therefore will control the rates of microphysical processes such as bulk growth and collisions. The average observable particle size is larger than the number-density weighted average particle size for both the cool exoplanet and brown-dwarf atmospheres shown. This highlights that retrievals of cloud particles sizes are upper limits on the average particle size actually present in the observable part of the atmosphere.

For the cool gas giant atmosphere, the observable average particle size is significantly reduced with the inclusion of fragmentation from collisions (with radii reduced from 0.4–0.6 μm to 0.04–0.1 μm across all wavelengths). For both the collision-free and collisional models, the average observable size is roughly flat for the mid-infrared, although the collision-free case does show increases in the average observable cloud size at the silicate feature wavelengths. In the optical regime (< 1 μm) the average particle size decreases substantially in the collisional case, whilst the collision-free case is constant at 0.4 μm. This is due to the increased scattering from the smaller particles, which increase the optical thickness of the cloud at these shorter wavelengths.

Without including collisions, the average observable particle size at all wavelengths is significantly smaller for cool brown dwarfs compared with gas giants: radii of ∼ 0.4–0.6 μm compared to ∼ 0.1 μm. This is because bulk growth happens deeper in the atmosphere, but increased number density throughout the entire atmosphere, thus there are more smaller particles in the optically thin region observable compared with the gas giants. However, with the inclusion of collisions, at all wavelengths the average observable cloud particle size is increased over the collision-free case by a factor of ∼ 2.5, and is larger than the collisional case for the fragmenting type gas giant atmosphere.

Luna & Morley (2021) suggested that for sub-micron sized cloud particles there are strong silicate features which allow the distinguishing of different silicate compositions with JWST.

These features were especially strong for particles $< 0.1\,\mu m$. For a gas giant atmosphere at T_{eff} = 1400 K, with collisional fragmentation leads to an average observable particle size below this size. For the brown dwarf atmosphere at T_{eff} = 1400 K, inclusion of coagulation leads to an average observable particle size slightly above this limit, but well below 1 micron in size. For brown dwarf atmospheres, comparing with the T_{eff} = 1800, 2400 K $\log(g\,[\mathrm{cm\,s^{-2}}]) = 5.0$ models by Luna & Morley (2021), then our models would suggest there is little impact of cloud particle collisions (see Sect. 4.5.3). Both Burningham et al. (2021) and Hiranaka et al. (2016) investigate clouds in brown dwarf atmospheres and find fitting cloud particle sizes around 0.1–0.5 μm this is consistent with the average observable particle size derived here with collisions included. Ohno et al. (2020) find the slope of aggregates flattens the extinction curve for hot Jupiters for wavelengths between 1–10 μm. This conflicts with results by Pinhas et al. (2019) who find steeper 'super-Rayleigh' slopes, which Ohno et al. (2020) suggests could be caused by tiny particles. We suggest that fragmentation may be a process that prevents aggregation and leads to an accumulation of such small particles.

For wavelengths $> 30\,\mu m$, the clouds are not optically thick with or without particle-particle collisions, thus the number-density weighted average particle size is simply the average, number-density weighted particle size of the entire cloud. For the exoplanet and young brown dwarf atmosphere $(\log_{10}(g\,[\mathrm{cm\,s^{-2}}]) = 3.0)$ without collisions the average particle size is $\sim 0.28\,\mu m$, with collisions included, this is reduced to $\sim 0.09\,\mu m$. This is a result of the fragmentation reducing the average particle size and increasing the number density, skewing the average towards this fragmented particle size. Similarly, for the old brown dwarf atmospheres $(\log_{10}(g\,[\mathrm{cm\,s^{-2}}]) = 5.0)$ at long wavelengths the effect of coagulation also reduces number-density weighted average particle size from 0.20 μm to 0.16 μm. The reason for this reduction in the overall mass of cloud particles that results from coagulation reducing surface area (Sect. 4.5.2). This therefore reduces cloud particle number density of the large coagulation aggregates, and skews the average particle size towards the cloud particles at higher altitude.

The number-density weighted average particle size at shorter wavelengths is not only affected by changes to the cloud particle properties through collisions, but also the impact of these changes on the cloud optical depth, as discussed in Sect. 4.6.1. For the old brown dwarf atmosphere, the changes to the optical depth from coagulation are not that significant, therefore the corresponding changes to the number-density weighted average particle size does not diverge too much from the collision-free case. Still, for the wavelength range where silicate spectral features are located,

the number-density weighted average particle size is reduced compared with the collision-free results. At wavelengths $\lesssim 1\,\mu\mathrm{m}$, the optical depth of clouds with coagulation is less than without collisions. For these wavelengths there is an increase in the average particle size by $\approx 10\%$ as deeper atmospheric layers (larger cloud particles) are visible.

In the exoplanet and young brown dwarf atmosphere ($\log_{10}(g, [\mathrm{cm\,s^{-2}}]) = 3.0$), the reduction in average particle size is already much larger. At $\lambda \approx 6\,\mu\mathrm{m}$ the collision-free case clouds become optically thick, thus the number-density weighted average size drops dramatically, as only higher levels of cloud are observable. However, the particle-particle collision case still has a smaller average particle size. The two situations have closest particle sizes at $\lambda \approx 1.8\,\mu\mathrm{m}$, where $\langle\langle a \rangle_A\rangle =$ $0.16\,\mu\mathrm{m}$ and $\langle\langle a \rangle_{A,\mathrm{coag}}\rangle = 0.08\,\mu\mathrm{m}$, which is still a factor of two smaller. For shorter wavelengths than this (into the optical regime) the fragmentation case further diverges from the collision-free case, as the increased optical thickness of the clouds hides the deeper cloud layers which contain the larger cloud particles.

That the two average sizes are so different highlights that, even with monodisperse cloud assumptions for each layer of an atmosphere, that exoplanet atmospheres are not well represented by a single average particle size. In addition to this Powell et al. (2018) find that, including a full size distribution enhances the optical depth of clouds by a factor of ~ 3–5, when compared with opacities based on average particle sizes. Thus we can expect the optical depth here to be lower than inclusion of full particle size distributions. Although, Powell et al. (2018) Fig. 14 also shows that the optical depth of cloud particles is dominated by particles $> 1\,\mu\mathrm{m}$ in size, which is larger than the largest average particle sizes in these models even with the inclusion of coagulation. The differences in the observable cloud properties (material composition, size and number density) and the cloud particles that are present in the same region of the atmosphere has important implications for attempts to derive atmospheric properties such as the bulk C/O ratio (as is discussed in Burningham et al. 2021). This is is because the expected elemental depletion of the gas phase depends on the material composition of the clouds and overall mass of the clouds in the atmosphere.

4.7 Discussion

The key parameters of the HYLANDS hybrid moment-bin model are evaluated here to understand the uncertainties they introduce into our results. Here the cool gas giant exoplanet and brown

dwarf atmosphere profiles are used ($T_{\text{eff}} = 1400\,\text{K}$, $\log_{10}(g\,[\text{cm s}^{-2}]) = 3.0$, 5.0), as they exhibit the greatest changes resulting from the inclusion of particle-particle collisions.

4.7.1 Turbulent Eddy Length Scale

The turbulence induced relative velocity is dictated by the ratio of the frictional timescale of the cloud particles and the turnover timescale of the turbulent eddies (Sect. 4.4.2). A typical eddy size to which cloud particles couple is introduced ($l_{\text{edd}} = 1\,\text{cm}$), which is the eddy size of most efficient momentum transfer between the gas and cloud particles in all levels of the atmosphere.

The critical eddy size, l_{crit}, is defined as when $\tau_{\text{t}} = \tau_{\text{f}}$, that is that the frictional stopping time of a cloud particle is equal to the turnover time of the eddy. For eddies smaller than l_{crit} it follows that $\tau_{\text{t}} < \tau_{\text{f}}$, hence there is not sufficient time for the eddy to accelerate the cloud particle. This results in less efficient coupling and slower relative velocities. For larger eddies $\tau_{\text{t}} > \tau_{\text{f}}$, therefore the cloud particles fully couple to the eddy, matching the eddy velocity. For such eddies a monodisperse cloud particle population produces no relative velocities, as all cloud particles move with the eddy, similar to the problem for differential settling. However, as turbulence produces the velocity in a random direction there could still be some relative velocity between cloud particles, at least at the boundary between two eddies.

Further, the larger the eddy the slower the relative velocity it imparts, thus the maximal relative velocity achievable between cloud particles is when the eddy size is at the critical size. From Eq. 4.12 a maximum relative velocity of $\Delta v_{\text{coag}}^{\text{turb}} = \langle \delta v_{\text{g}}^2 \rangle^{1/2} / \sqrt{2}$ can be derived. For eddies either larger or smaller than l_{crit}, the relative velocity induced between cloud particles is lower than this peak value. The full effects of turbulence-induced collisions are captured when the typical eddies size matches the critical eddy size.

Figure 4.9 shows the critical eddy size for cloud particles in the $T_{\text{eff}} = 1400\,\text{K}$, $\log_{10}(g\,[\text{cm s}^{-2}]) = 3.0$ atmosphere, without the inclusion of particle-particle collisions. The critical eddy size for this atmosphere (and all exoplanet and brown dwarf atmospheres) spans 12 orders of magnitude, hence there is no one good pick for a 'typical' eddy size. For pressures above $\sim 10^{-8}$ bar the critical eddy size also exceeds the assumed maximum eddy size, implying that for above this pressure level cloud particles cannot couple to any turbulent eddies. However, at these pressures the collisional timescale is large, thus collisions do not affect the cloud particle population.
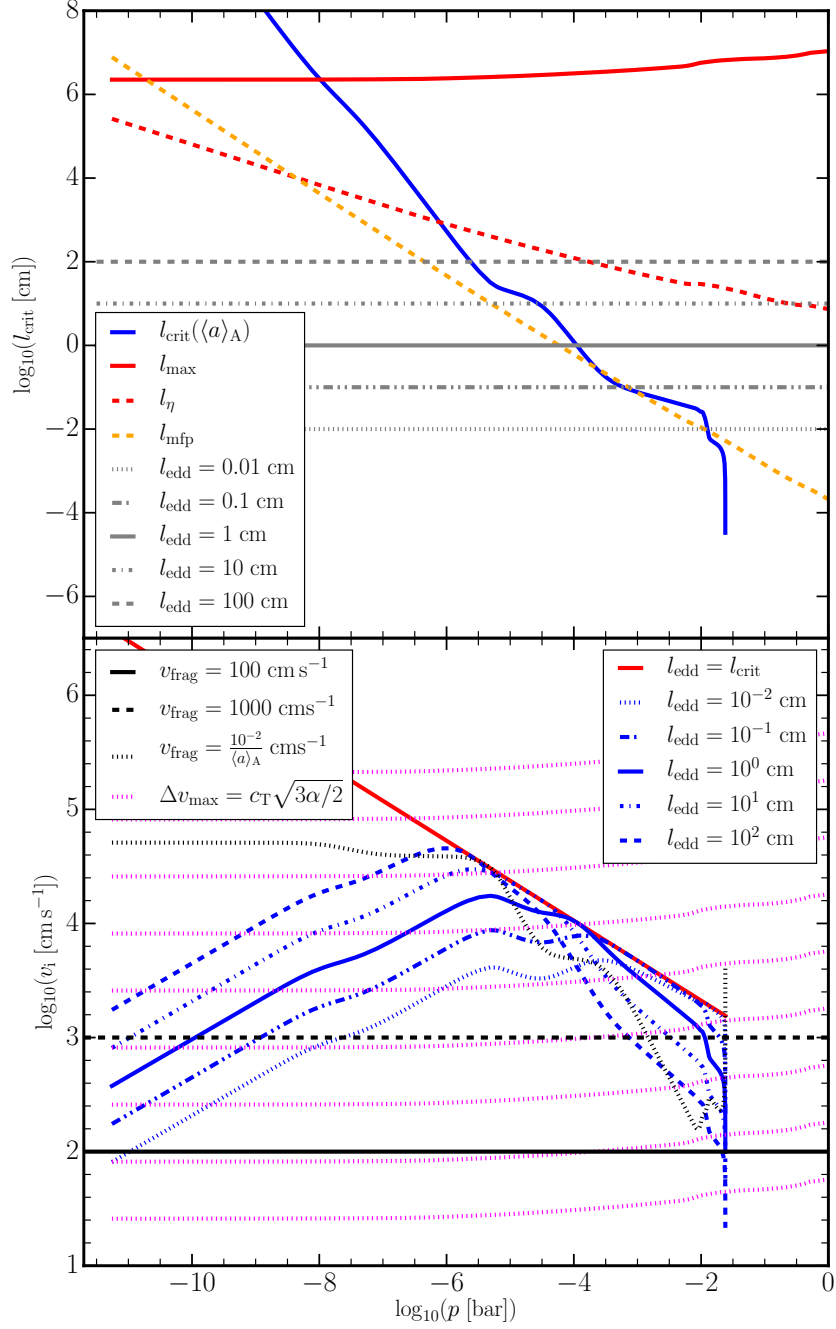
Figure 4.9: Top: Critical eddy size l_{crit} (blue) for cloud particles in the $T_{eff} = 1400\,K$, $\log_{10}(g\,[cm\,s^{-2}]) = 3.0$ profile, without inclusion of collisions. Red lines show the maximum eddy size ($l_{max} = H_p/10$) in solid and the Kolmogorov scale $l_\eta = \nu^{3/4}\epsilon_{disp}^{-1/4}$ in dashed. The mean free path (l_{mfp}) of the gas is shown in the orange dashed line. **Bottom:** Relative velocities that cloud particles would receive from turbulent eddies of the sizes l_{edd} in the upper panel in blue. Fragmentation limits discussed in Sect. 4.3.4 are in black. Magenta dashed lines show the maximum relative velocity $\Delta v_{max} = c_s\sqrt{3\alpha/2}$ using the Shakura & Sunyaev (1976) turbulence α parameterisation, and maximum velocity from Ormel & Cuzzi (2007). Lowest line shown is for $\alpha = 10^{-8}$ and the highest is $\alpha = 1$, incrementing in orders of magnitude.

However, $l_{\text{edd}} = 1\,\text{cm}$ proves to be below the Kolmogorov scale ($l_\eta = \nu^{3/4}\epsilon_{\text{disp}}^{-1/4}$, where ν is the kinematic viscosity) in the $T_{\text{eff}} = 1400\,\text{K}$ exoplanet atmosphere for pressures greater than $10^{-6}\,\text{bar}$. This is the scale at which viscosity begins to dissipate the energy of the turbulence. We note, however, that critical eddy size is around the size of the mean free path of the gas for pressures $> 10^{-4}\,\text{bar}$. The mean free path is calculated by $l_{\text{mfp}} = 3\nu/\nu_{\text{th}}$, where ν_{th} is the mean thermal velocity (see Eq. 10 in Woitke & Helling 2003). This is the length scale at which the energy of the turbulence is finally converted into heat. Thus for $l_{\text{edd}} = 1\,\text{cm}$, Kolmogorov theory does not hold. The impact of this and varying the typical eddy size is explored in the lower panel of Fig. 4.9.

We now compare the relative collision velocities for turbulent eddies of various sizes, to the fragmentation limits discussed in Sect. 4.3.4. For each assumed eddy size, the velocities peak at the point in the atmosphere where $l_{\text{crit}} = l_{\text{edd}}$ as described above, either side of this peak pressure level the relative velocities drop off steeply with pressure. Larger typical eddy sizes ($l_{\text{edd}} = 100, 10\,\text{cm}$) exceed the fragmentation limit inversely proportional to cloud particle size, for higher in the atmosphere, but around $10^{-4}\,\text{bar}$ drop below this limit. All typical eddy sizes tried induce relative velocities exceeding both the silicate and 'icy' grain fragmentation limit, for all put the upper most atmospheric levels. In general Fig. 4.9 shows that the selection of typical eddy size, along with the fragmentation limit assumed can have a significant impact on the potential collisional outcomes (i.e. fragmentation or coagulation).

In addition, Fig. 4.9 shows the maximal possible velocity produced for turbulence in the α turbulence, as taken from Birnstiel et al. (2016) using the turbulent velocity model of (Ormel & Cuzzi 2007),

$$\Delta v_{\text{max}} = c_{\text{s}} \sqrt{\frac{3}{2}\alpha}, \tag{4.32}$$

where c_{s} is the sound speed. The α parameter links the diffusion coefficient of turbulent diffusion (D_{g}) for a protoplanetary disk to the gas scale height (H_{g}) by $D_{\text{g}} = \alpha c_{\text{s}} H_{\text{g}}$ (Brauer et al. 2008). α is often taken to be some constant, with observations suggesting a value of around 10^{-2} (Hartmann et al. 1998). It is not clear what value would be expected for a gas giant exoplanet, and as α is dimensionless there is no physically justifiable value, it must come from observational fitting which is currently not possible for exoplanets. However, Fig. 4.9 shows that comparing

maximum induced relative velocities for our model, α varies between 10^{-7}–10^{-3} for the relevant pressure levels of the atmosphere ($> 10^{-4}$ bar).

The effect of different eddy timescales on the cloud structure is explored. Figure 4.10 shows that a larger typical eddy size leads to overall less destructive collisions. For gas giant exoplanets and young brown dwarf atmospheres ($\log_{10}(g\,[\mathrm{cm\,s^{-2}}]) = 3.0$), the strength of the fragmentation is reduced significantly. For typical eddy sizes of $l_{\mathrm{edd}} = 100$ cm, fragmentation only marginally decreases the mean particle size for pressures between 10^{-3} bar and the cloud base at 3×10^{-2} bar (left middle panel). Even for this largest eddy size of $l_{\mathrm{edd}} = 100$ cm, particle-particle collisions are not able to increase the average cloud particle size above the collision-free case.

For old brown dwarf atmospheres ($\log_{10}(g\,[\mathrm{cm\,s^{-2}}]) = 5.0$) case, the typical eddy size does not impact the ability of particle-particle collisions to affect the cloud particle population. As larger eddy sizes induce slower relative velocities between cloud particles, the collision rate is expected to decrease. However, for all cases the average particle size increases only slightly, by the same amount. Similarly the cloud particle number density (n_{d}) and the cloud particle mass load (ρ_{d}/ρ) are also unaffected. At the initial onset of cloud particle collisions becoming important (at 10^{-1} bar), it appears that the timescale for coagulation is fast regardless of eddy size, and thus the changes to the cloud population are the same. Thus, as the number density of cloud particles is reduced through coagulating collisions the timescale for collisions decreases rapidly, regardless of eddy size, and collisions cease to be an important factor for cloud particle growth. This means that the limiting affect of turbulence on coagulation growth is the reduction the cloud particle number density as result of collisions. As long as the induced relative velocity is sufficiently fast to start coagulation, then eventually it will stall itself as it reduces the required number density of cloud particles. In conclusion, coagulation induces a negative feedback loop, constructive collisions reduce the number density of cloud particles, and thus reduce the rate of collisions, limiting the overall growth possible due to collisions.

Finally, assuming a typical eddy size of $l_{\mathrm{edd}} = l_\eta$ has a similar impact on the exoplanet and young brown dwarf profile ($\log_{10}(g\,[\mathrm{cm\,s^{-2}}]) = 3.0$) as selecting a typical eddy size between 10–100 cm, which is to be expected as at pressures where collisions are important ($> 10^{-4}$ bar) the Kolmogorov scale is between these values. For the brown dwarf profile ($\log_{10}(g\,[\mathrm{cm\,s^{-2}}]) = 5.0$) there is no impact, as all values of typical eddy size produce the same results as previously discussed.
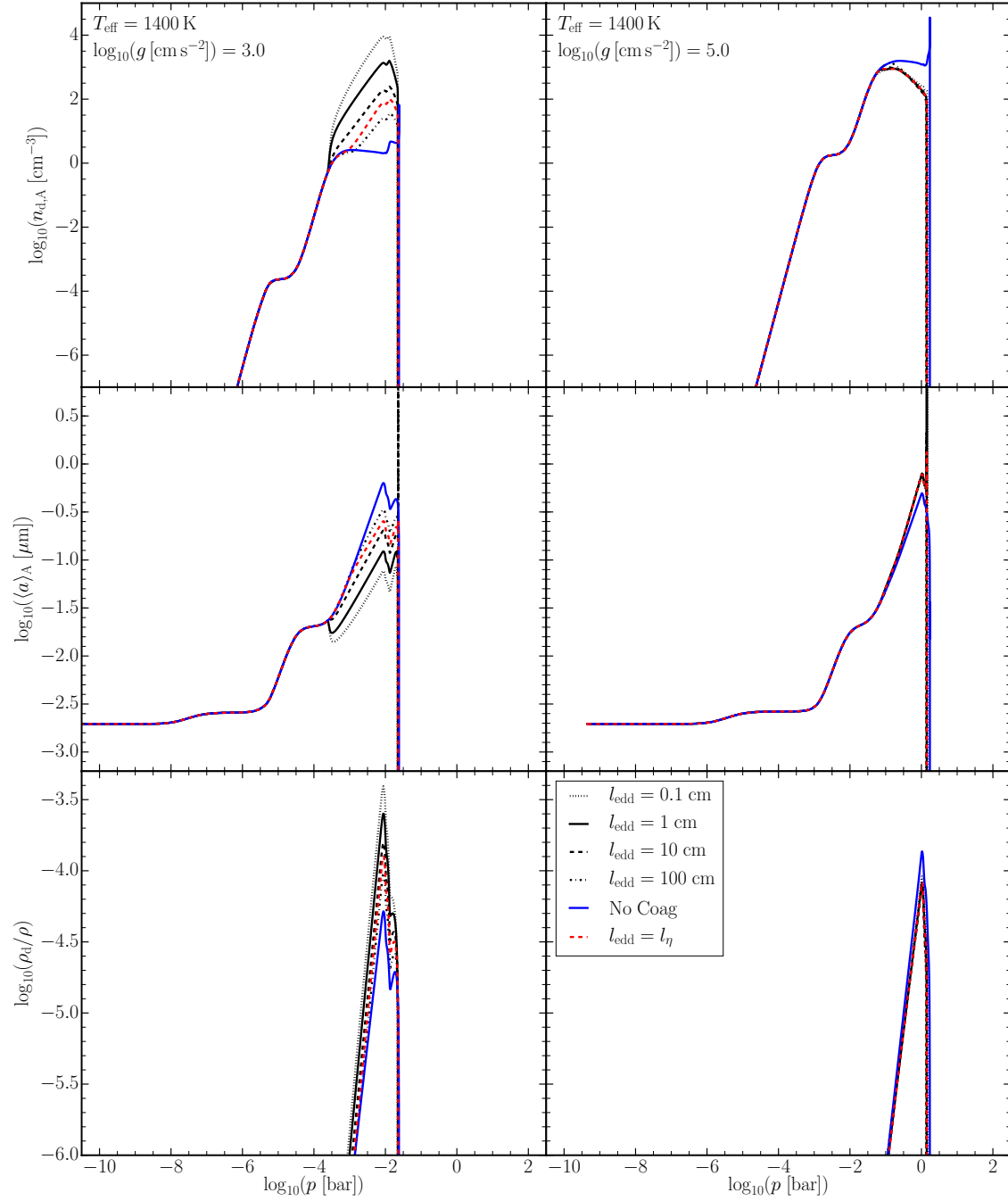
Figure 4.10: Effects of varying the typical eddy size parameter (l_{edd}) for the T_{eff} = 1400 K, $\log_{10}(g\,[\mathrm{cm\,s^{-2}}])$ = 3.0, and 5.0 profiles. **Top:** Number density of cloud particles ($n_{d,A}$), **Middle:** Surface-averaged particle size ($\langle a \rangle_A$), **Bottom:** Cloud particle mass load (ρ_d/ρ).
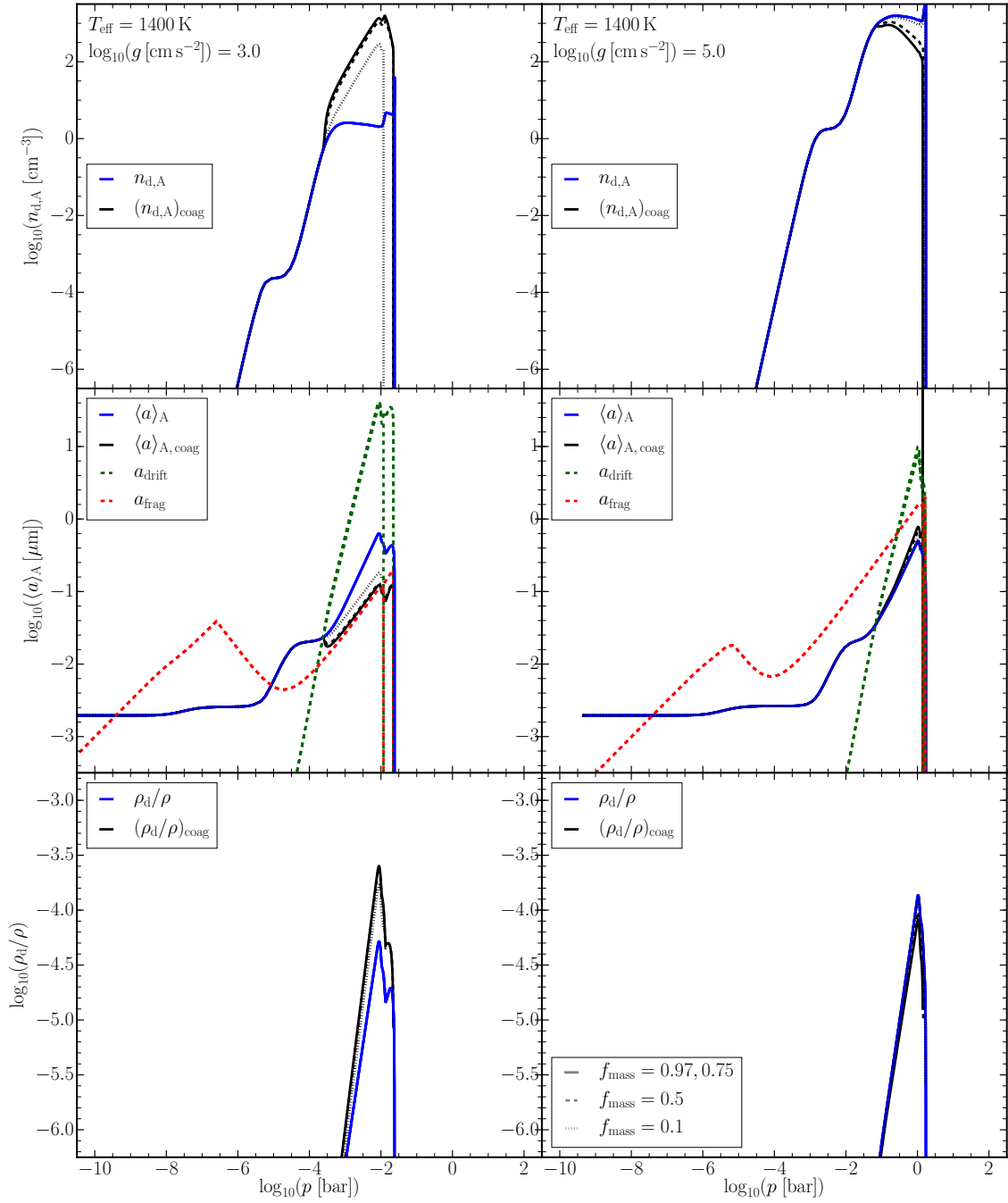
Figure 4.11: Effects of varying the mass partition fraction parameter f_{mass} (i.e. what fraction of mass is in the aggregate population). For the $T_{\mathrm{eff}} = 1400\,\mathrm{K}$, $\log_{10}(g\,[\mathrm{cm\,s^{-2}}]) = 3.0$ and 5.0 profiles. **Top:** Number density of cloud particles ($n_{\mathrm{d,A}}$), **Middle:** Surface-averaged particle size ($\langle a \rangle_{\mathrm{A}}$), **Bottom:** Cloud particle mass load (ρ_{d}/ρ).

4.7.2 Mass Partition Fraction

The mass partition fraction is a parameter that can be interpreted as a general efficiency factor for all the collisions occurring in the cloud particle population. It does this by directly controlling the total mass of cloud particles in the collisional product population and the collision monomer population. For Sect. 4.5 the mass partition fraction was set to match the values used by Birnstiel et al. (2011), which are calibrated to full numerical results of protoplanetary discs. We therefore test the sensitivity of this parameter, as exoplanets and brown dwarfs in general may not share the same partition fractions. Figure 4.11 shows the results for $T_{\text{eff}} = 1400 \, \text{K}$, $\log_{10}(g \, [\text{cm s}^{-2}]) = 3.0$ and 5.0 for $f_{\text{mass}} = 0.5$ and 0.1.

For the fragmentation limited case of a cool gas giant exoplanet ($T_{\text{eff}} = 1400 \, \text{K}$, $\log_{10}(g \, [\text{cm s}^{-2}]) = 3.0$), reducing the mass partition fraction to $f_{\text{mass}} = 0.5$ results in no qualitatively important change to the cloud particle population compared with the standard particle-particle collision case. With the mass partition fraction reduced to $f_{\text{mass}} = 0.1$, 90% of the mass remains in the coagulation monomer size set at the surface-averaged mean particle size ($a_1 = \langle a \rangle_A$). As a result, once collisions begin to affect the cloud particle population, the average particle size remains closer to the coagulation monomer size. Thus for a fragmenting type atmosphere, at the highest altitude where collisions begin to fragment cloud particles, less of the cloud particle mass is processed through collisions. Therefore, the 'transition' from the initially growth controlled size (seen by the collision-free blue case) to the fragmentation-controlled cloud particle size (the fragmentation size limit) occurs over a greater pressure range. In the case of $f_{\text{mass}} = 0.1$ the cloud particle population does not fully reach the fragmentation limited size before the cloud particles evaporate at the cloud base. However, the atmosphere still remains in the fragmenting class as the average particle size is still reduced compared with the collision-free case, and correspondingly, cloud particle density is also still increased.

For the brown dwarf, coagulating type atmosphere shown ($T_{\text{eff}} = 1400 \, \text{K}$, $\log_{10}(g \, [\text{cm s}^{-2}]) = 5.0$), with decreased mass partition fraction $f_{\text{mass}} = 0.5$, the coagulation case does see some reduction in the strength. The mean particle size is increased slightly less than the standard case, and cloud particle number density is not reduced as much from the collision-free case. For $f_{\text{mass}} = 0.1$ case particle-particle collisions make essentially no difference to the cloud particle population. This is because the coagulation impact on cloud

particle population is so weak even for the standard mass partition fraction. Thus the value of the mass partition fraction does not have significant consequences for atmospheres where collisions are not dominant (as seen for the coagulating atmosphere), or for cases where the transition to the size limited case happens over a wider pressure range.

4.7.3   Porosity

Collisional growth of aggregates often produces fractal structured particles, and this can have an impact on the outcomes of further collisions, the settling of cloud particles and their spectral properties. It is beyond the scope of this chapter to examine a full inclusion of porosity evolution due to such affects as hit-and-stick, as well as considerations for compaction in collisions and compaction due to ram pressure (see Ohno & Okuzumi 2018; Ohno et al. 2020). Furthermore, porous particles will absorb the energy of impacts differently and thus alter the boundaries between collisional regimes (e.g. fragmentation, bouncing, and hit-and-stick; Güttler et al. 2010). In addition porous particles are subject to increasingly large drag forces (Schneider & Wurm 2021).

The effects of porosity on the results presented here is explored by assuming a porosity fraction of $f_{por} = 0.9$ across the entire atmosphere (approach is the same as in Chap. 3), and then compared to the coagulation outcome for the compact case in particular focusing on the impact on particle aggregate size. The effect of porosity is studied only for atmospheres that produce increased particle sizes through coagulation, as these are the only atmospheres that could produce increased porosity aggregates. The outcomes of collisions in a fragmenting type atmosphere are likely to include compression and erosion along side the fragmentation of particles, which would reduce porosity.

Figure 4.12 shows the results for the cool brown dwarf atmosphere (T_{eff} = 1400 K, $\log_{10}(g\,[\mathrm{cm\,s^{-2}}])$ = 5.0), for cloud particles with 90% volume fraction being vacuum (f_{por} = 0.9) in comparison to the non-porous case (f_{por} = 0.0). As in Chap. 3, porous cloud particles are larger in average size (middle panel) at the top of the atmosphere (larger, porous cloud condensation nuclei), and increases in average particle size associated with surface growth also occur at lower pressures (higher altitude). Coagulation similarly becomes an efficient process at slightly lower pressure (around 10^{-2} bar), more readily seen by the reduced number density in the top panel. However, the increase in particle size for the porous cloud particles as a result of coagulation is not as large as for the compact case. Furthermore, the peak cloud particle
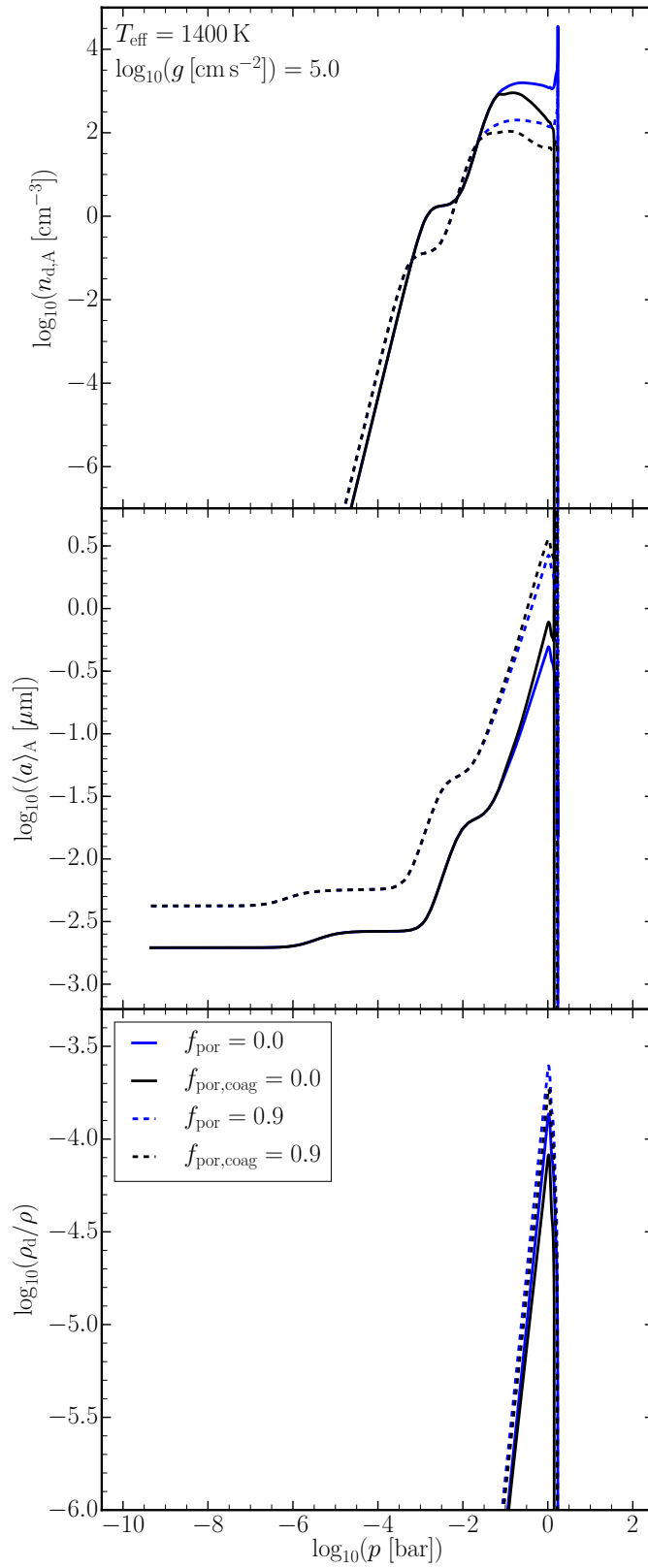
Figure 4.12: Properties of compact (f_{por} = 0.0, solid lines) and porous cloud particles (f_{por} = 0.9, dashed lines) with (black) and without (blue) collisions. For the cool brown dwarf atmosphere (T_{eff} = 1400 K, $\log_{10}(g\,[\mathrm{cm\,s^{-2}}])$ = 5.0). **Top:** Number density of cloud particles (n_d), **Middle:** Surface-averaged particle size ($\langle a \rangle_A$), **Bottom:** Cloud particle mass load (ρ_d/ρ).

mass load is not much increased even in the porous case, which is partly also a consequence of the model incorporating porosity into a spherical geometry cloud particle, thus the surface area of potentially fractal cloud particle is under-represented in this simplified approach to porosity. This also has consequences for the settling rate of these cloud particles, as a fractal cloud particle would have a larger cross-sectional area and thus a slower equilibrium drift velocity than and equivalently porous sphere.

One additional limitation of this simple approach is that because it does not account for the specific fractal dimension or size of monomers potentially comprising the aggregates, spectral properties of these cloud particles remains largely uncertain. For example, Ohno et al. (2020) found that the pressure level of optically thick clouds depends on the monomer size of the aggregates (their Fig. 5). These additional affects of porosity are not be accounted for here but remain a possibility for future work.

4.8 Conclusion

The feasibility of a hybrid method for cloud formation modelling, that combines the advantages of a moment method treating the formation processes of cloud particle and that of a bin method treating particle-particle processes has been demonstrated. The hybrid moment-bin method enables the modelling of the microphysics of the formation of chemically mixed cloud particles (by nucleation, surface growth/evaporation, gravitational settling) and the effects of agglomeration and fragmentation on the cloud particles whilst assuring element conservation. HYLANDS, a hybrid moment-bin model, includes collisions between cloud particles due to collisional processes of differential settling and turbulence, where other models have omitted the effect of turbulence. We note that there remains a strong case for investigation of turbulence parameterisations for exoplanets and brown dwarf atmospheres. In particular, there is a need for observations which could hint towards the selection of appropriate turbulence strength parameters. Nevertheless, HYLANDS, has shown robust results, with qualitative trends unchanged by varying assumed model parameters.

Particle-particle processes consistently coupled to microphysical cloud particle formation processes show that:

- Cloud particle-particle collisions affect clouds at the cloud base, where it becomes the dominant process.

- Fragmentation emerges as a crucial process for gas giant exoplanets $(\log_{10}(g\,[\mathrm{cm\,s}^{-2}]) = 3.0)$ when particle collisions are driven by turbulence in the atmosphere.

- A grid of DRIFT-PHOENIX atmospheric profiles reveals that collisional processes are more dominant at lower effective temperatures.

- Low-density atmospheres $(\log_{10}(g\,[\mathrm{cm\,s}^{-2}]) = 3.0)$ consistently show fragmentation of cloud particles, and compact atmosphere $(\log_{10}(g\,[\mathrm{cm\,s}^{-2}]) = 5.0)$ show only minor coagulation for temperatures below $T_{\mathrm{eff}} = 1800\,\mathrm{K}$.

- For fragmenting atmospheres significantly more cloud material can condense, due to an increased surface area.

- Fragmentation enhances the silicate features. Interpretations of JWST as well as of ARIEL data will be impacted by this such that complex cloud models will be needed for the data modelling process.

- The effect of particle-particle collisions will also affect the optical and near-IR wavelength accessible by HST, CHEOPS, JWST and ARIEL.

"Clouds come floating into my life,
no longer to carry rain or usher storm,
but to add color to my sunset sky."

- Rabindranath Tagore,
Stray Birds, 1916

5

Sunny Days?: Global Cloud Formation

on Hot and Ultra-hot Jupiters

5.1 Declaration

The content of this chapter is based on a number of publications to which I have contributed. All text is my own, the included figures are also my own unless as indicated in the caption and below:

- 'Understanding the atmospheric properties and chemical composition of the ultra-hot Jupiter HAT-P-7b. I. Cloud and chemistry mapping', Helling, Ch., Iro, N., Corrales, L., et al. incl. Samra, D. 2019, A&A, 631, A79. Figures for HAT-P-7b cloud properties and slice-plots were created by myself.

- 'Mineral cloud and hydrocarbon haze particles in the atmosphere of the hot Jupiter JWST target WASP-43b', Helling, Ch., Kawashima, Y., Graham, V., et al. incl. Samra, D. 2020, A&A, 641, A178. Slice plots for WASP-43b are adapted from figures produced by Victoria Graham using code written by myself.

- 'Cloud property trends in hot and ultra-hot giant gas planets (WASP-43b, WASP-103b, WASP-121b, HAT-P-7b, and WASP-18b)', Helling, Ch., Lewis, D., Samra, D. et al. 2021, A&A, 649, A44. Temperature-pressure structure plots produced by David Lewis. Cloud optical depth plot produced by myself.

5.2 Introduction

Hot Jupiters are gas giant exoplanets that orbit their host star on periods of a few hours (Dawson & Johnson 2018). The nature of such close orbits means that the planets are expected to be tidally locked, meaning that one side of the planet permanently faces the star (called the 'dayside'), whilst on faces away ('nightside'). The formation of such massive gas planets that end up on very close orbits is not well understood, but is often assumed to involve substantial migration (Dawson & Johnson 2018). Such migration histories are thought to potentially have lasting effects on the C/O ratio of these atmospheres (Madhusudhan et al. 2014). In addition, the dayside of ultra-hot Jupiters experience intense stellar irradiation, whilst having no stellar irradiation on the other. As a consequence of potential formation histories and the unique radiation environment, these planets make interesting laboratories to explore novel atmospheric composition and flow regimes, unlike anything present in our Solar System.

A further benefit of these planets is that the close orbit and large planetary radius lends itself to more easy characterisation of the atmosphere for scattered light and emission spectra (see Chap. 1). In both cases the planet-to-star flux ratio F_p/F_* is proportional to the square of planetary radius R_p and inversely to the square of their orbital distance r, $F_p/F_* \propto (R_p/r)^2$ (Seager 2010). The case for transmission spectra is a little more subtle as the property that dictates detectability is the atmosphere annulus. However, this is proportional to the planetary radius and the atmospheric pressure scale height (Seager 2010), which as gas giants are largely composed of H_2/He is also very large. Thus these planets provide the prime candidates for atmosphere characterisation, with JWST there is the potential to reveal many details of cloud formation in the near- and mid-infrared.

The distinction between hot Jupiters and ultra-hot Jupiters is somewhat nebulous, as mentioned in Sect. 1.2.1, ultra-hot Jupiters have been characterised by having dayside temperatures $\gtrsim 2200\,\text{K}$ (Parmentier et al. 2018). However, there is growing evidence for a distinction based on population studies of trends in observable properties with equilibrium temperature. Where the planetary equilibrium temperature T_{eq} is the temperature a blackbody would have to have in order to be in energy balance with the host star, therefore including effects such as aerosol albedo. Some giant planets can have non-negligible internal heat, and consequently the planetary equilibrium temperature is lower than the planetary effective temperature T_{eff} (Catling & Kasting 2017).

Population studies of gas giant exoplanets, for example Garhart et al. (2020); Baxter et al. (2020); Keating & Cowan (2022) have examined *Spitzer* data for emission spectra trends in hot

and ultra-hot Jupiters. Such studies will only become more powerful in exploring trends in planet formation and atmospheric dynamics as the number of observed atmospheres increases. So far there are indications of a transition between the ultra-hot and only 'moderately' hot Jupiters at approx $T_{eq} = 1600\,K$ (Baxter et al. 2020). Where, for planets $T_{eq} \gtrsim 1600\,K$ there is an increase in the deviation from a blackbody (when comparing $3.6\,\mu m$ and $4.5\,\mu m$ *Spitzer* bandpasses).

Wong et al. (2020) found a (weak) positive correlation between dayside temperatures and geometric albedo for dayside temperatures $T_{day} = 1500-3000\,K$, which they propose might be caused by high temperature condensate clouds on the dayside. From their microphysical models Gao et al. (2020) indicate a transition at $T_{eq} \gtrsim 1800\,K$, where increasing equilibrium temperature results in silicate clouds forming deeper in the atmosphere and thus increases the $1.4\,\mu m$ band strength.

An additional consideration is that gas giant atmospheres are, in reality, 3D (Caldas et al. 2019). Therefore, for example in transmission spectroscopy, the light rays pass through not only the terminator limbs, but a substantial amount of dayside and nightside atmosphere (MacDonald & Lewis 2021). Lacy & Burrows (2020a) showed that this region may span between $\pm 5-20°$ in longitude either side of the terminator limbs. Thus, understanding and characterising the global cloud distribution, size, and material composition will be vitally important to more detailed observations of these atmospheres.

To investigate this we examine two gas giant exoplanets 'typical' of hot and ultra-hot Jupiters: HAT-P-7b and WASP-43b. HAT-P-7b is an ultra-hot Jupiter first discovered by the HATNet[1] Exoplanet Survey (Pál et al. 2008). It is a $1.74\,M_{Jup}$ mass planet, with a radius of $1.43\,R_{Jup}$ (Van Eylen et al. 2012), with an orbital period of $\sim 2.2\,days$ (Masuda 2015) and an equilibrium temperature of $T_{eq} \sim 2200\,K$ (Heng & Demory 2013). Mansfield et al. (2018) found HAT-P-7b to have a geometric albedo of $A_g = 0.077$ from *Kepler* and *Hubble* observations which they suggest is indicative of absorbers such as TiO and VO existing in the gas phase above any potential clouds (at pressures between $10^{-1}-10^{-3}\,bar$). Another interesting observation is that, in *Kepler* data, the peak of the phase curve of HAT-P-7b was found to oscillate between west of and east of the sub-stellar point(Armstrong et al. 2016), which has been suggested to be caused by advection of clouds onto the dayside of HAT-P-7b.

Comparatively, WASP-43b is much cooler with $T_{eq} \sim 1400\,K$ (Blecic et al. 2014), this is

---

[1]Hungarian Automated Telescope Network

despite orbiting its star in just ~ 0.83 days (Hellier et al. 2011). This is because it orbits a K7 star (Gillon et al. 2012), compared with HAT-P-7 which is an F6 star and hence WASP-43b is much less strongly irradiated. In terms of mass and radius WASP-43b is much similar to HAT-P-7b (1.78 M_{Jup} and 0.93 R_{Jup}). WASP-43b has been observed multiple times, with full orbital phase curves with both *Hubble* and *Spitzer* (Stevenson et al. 2014, 2017). Retrieved dayside pressure-temperatures structures from observations of WASP-43b have suggested the possibility of dayside cloud coverage. However, this would likely need silicate clouds forming deep in the atmosphere and lofted to higher altitudes (Kataria et al. 2015). Furthermore, with *Hubble* UVIS spectroscopy Fraine et al. (2021) found WASP-43b to have a very low dayside geometric albedo $A_{\text{g}} = 0.06$, which is potentially incompatible with high-altitude reflective silicate clouds. WASP-43b is also a highly favoured target for JWST observations, with full phase curve observations in the mid-infrared with MIRI(Venot et al. 2020) and near-infrared with NIRSPEC[2], as part of the 'The Transiting Exoplanet Community Early Release Science Program for JWST' (Bean et al. 2018). With these observations in particular, longitudinally resolved mapping of WASP-43b should be possible giving a detailed picture of global cloud formation (Irwin et al. 2020; Cubillos et al. 2021).

5.3 Approach

Modelling clouds consistently in global atmospheric simulations is hard as the addition of non-equilibrium cloud formation significantly increases the computational cost, with a single cloud formation step taking 20–30 times as long as a single hydrodynamic step to compute (Lee et al. 2016). We therefore instead adopt a simpler, two step, hierarchical approach, similar to approaches used by Lee et al. (2015b), Helling et al. (2016), and Helling et al. (2019) for a number of hot and ultra-hot Jupiters. First, we use the cloud-free 3D GCM, SPARC/MITgcm (Showman et al. 2009), which solves the hydrodynamic primitive equations coupled with radiative transfer, including treatment of the main gas-phase constituents alongside non-grey radiative transfer (Mansfield et al. 2018; Parmentier et al. 2018).

The GCM uses 53 pressure levels logarithmically spaced between $\sim 10^{-6}$–10^2 bar and is run for 300 simulated Earth days, with the final 100 days providing the time averaged solution. From this we extract 1D profiles ($p_{\text{gas}}(z), T_{\text{gas}}(z), v_{\text{z}}(z)$ – pressure, temperature and vertical mixing velocities) at 97 (longitude, latitude grid) points around the planets. These are evenly spaced in

---

[2]GTO program 1224, Pi: S. Birkmann

longitude (stepping every 15°) and latitude (stepping every 22.5°) as seen in Fig. 5.1. An additional point at (90.0°, 85.5°) is included for HAT-P-7b. The generated profiles are then used as inputs for our 1D kinetic, non-equilibrium cloud formation code consistently linked with gas-phase equilibrium chemistry. For specific details of the model setups, see Chapter 2, Section 2.2.7.

This hierarchical method neglects horizontal transport of cloud particles between profiles, although an order of magnitude assessment by Helling et al. (2019) calculates the horizontal advection timescale for the equatorial morning and evening terminators of HAT-P-7b. These profiles are subject to the equatorial jet flow and therefore some of the fastest zonal winds in the atmosphere. Here the horizontal mixing timescale is approximated by the $2\pi R_{\mathrm{p}}/v_{\mathrm{h}}$, the planetary circumference divided horizontal gas velocity $v_{\mathrm{h}} = \sqrt{v_{\mathrm{x}}^2 + v_{\mathrm{y}}^2}$. Their Fig. 2 reveals that the horizontal mixing timescale ($\sim 10^5$ s) is shorter the settling timescale of the cloud particles ($\geq 10^5$ s), but slower than the vertical mixing timescale (between 10^3 and 10^5 s). Furthermore, the net growth and nucleation timescales in cloud forming regions are also faster than this horizontal mixing timescale. Thus cloud formation should still be dictated mostly by local thermodynamic conditions in situ and which will not substantially change with the cloud particle being advected around the atmosphere. However, in comparison to fully coupled models, the faster horizontal mixing timescale over the settling timescale indicates that cloud particles would be transported around the atmosphere before they can settle to deeper layers and evaporate. The effect of this would be a smearing out of particle properties in longitude compared to these results. Such an effect was seen by Lee et al. (2016) with coupled cloud formation and hydrodynamics. However, they were only able to integrate for 60 Earth days, thus vertical settling effects in this instance were neglected. The hierarchical approach gives a first order picture of global cloud formation of hot and ultra-hot Jupiters.

5.4 Pressure-Temperature Structure Differences between HAT-P-7b and WASP-43b

As the processes which form clouds are governed by local thermodynamic conditions, it is instructive to first look at the GCM results for pressure-temperature structures for the ultra-hot Jupiter HAT-P-7b versus the hot Jupiter WASP-43b. This gives an overall picture of where one may anticipate condensation of clouds, however it does not give the full picture as kinetic cloud
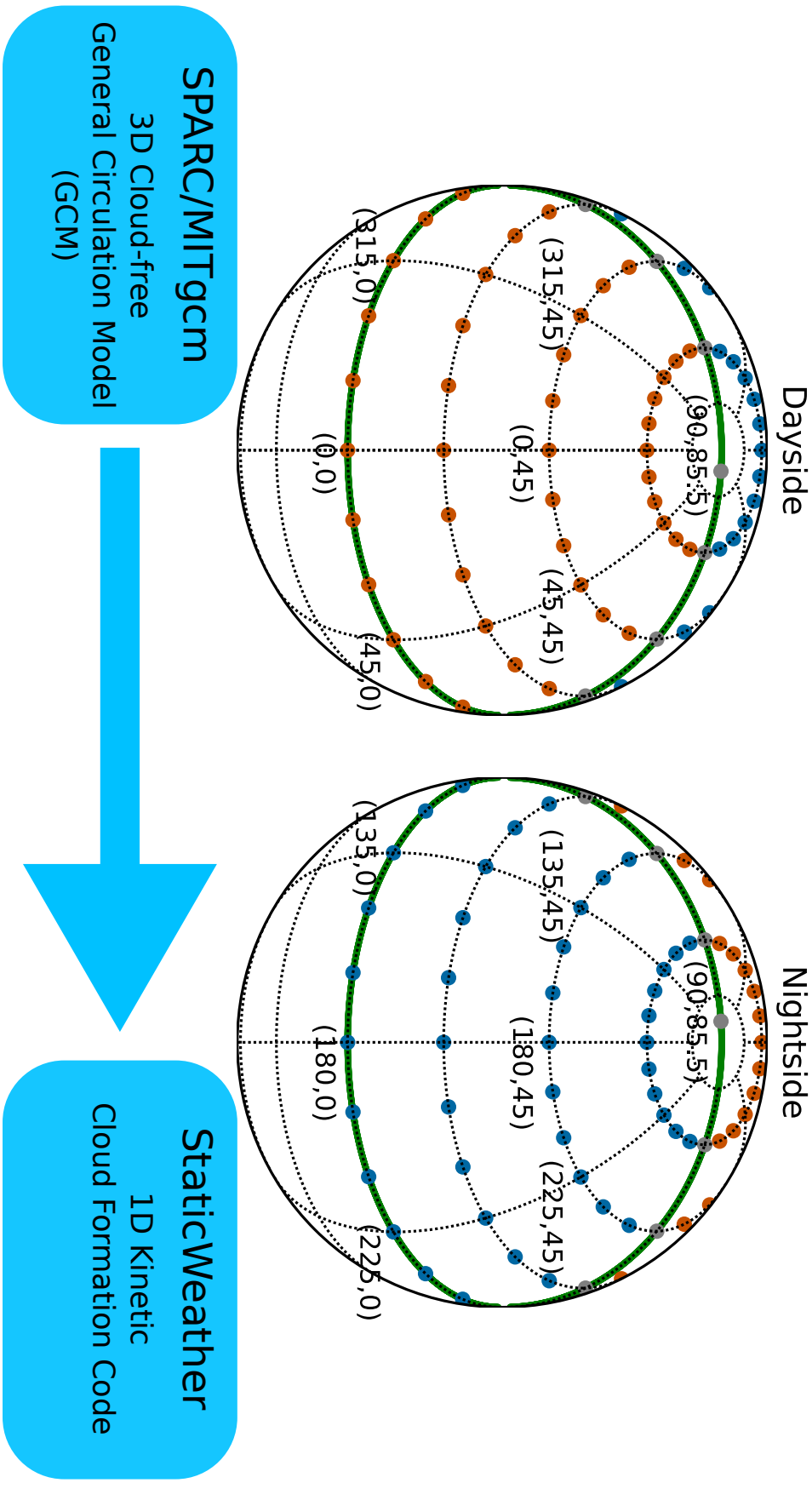
Figure 5.1: Schematic of the hierarchical procedure for global cloud modelling. The latitude and longitude grid (ϕ, and θ for longitudes, and latitudes respectively) of the 97*, 1D p_{gas}–T_{gas} profiles are shown for the two hemispheres: dayside (left, orange points) and nightside (right, blue points). Green lines show the slices through the atmosphere at the equator ($\theta = 0°$) and terminator points, at the evening ($\phi = 90°$) and morning terminators respectively ($\phi = 270°$). Grey dots represent the terminator points, at the evening ($\phi = 90°$) and morning terminators respectively ($\phi = 270°$). Grey dots represent the terminator profile. * When the additional 'polar' profile at (90°, 85.5°) is included, it is counted as an evening terminator profile.
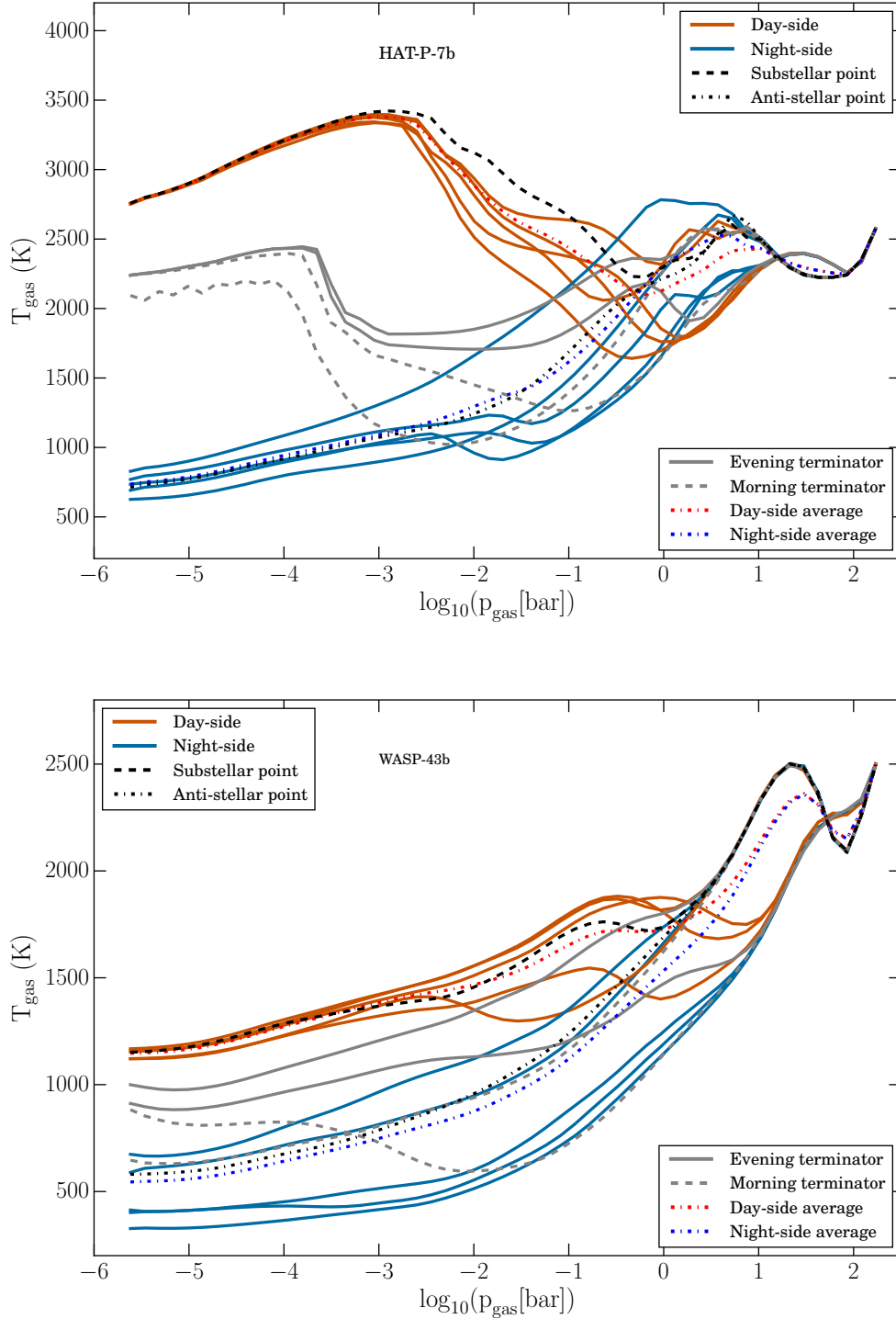
Figure 5.2: A selection of the pressure-temperature profiles for HAT-P-7b (**Top**) WASP-43b (**Bottom**), shown are profiles from $\theta = 0.0°$, and $45.0°$. Dayside profiles are shown in orange, nightside profiles in light blue. The sub-stellar point is highlighted as a black dashed line, and the anti-stellar point is similarly highlighted as a black dash-dotted line. Morning and evening terminators are in grey (dashed and solid respectively). The red and blue dotted and dashed lines show averaged dayside and nightside profiles. Taken from Helling et al. (2021), credit: David Lewis.

117

formation also includes the effects of gas phase abundances and mixing.

5.4.1 Upper Atmosphere: Temperature Inversion for Ultra-Hot Jupiter Daysides

For HAT-P-7b, and similarly for other ultra-hot Jupiters, three distinct groups of profiles are distinguishable by their Top of Atmosphere (TOA) temperatures in Fig. 5.2. With $\sim 2700\,$K, 2000–2250 K, and 500–1000 K for dayside, terminator, and nightside profiles respectively. As expected from observations the dayside profiles are typified by a hot upper atmosphere driven by stellar irradiation, with a thermal inversion peaking at $\sim 3500\,$K at $10^{-3}\,$bar, as is expected by Madhusudhan & Seager (2010). Profiles for both the morning and evening terminators also exhibit inversions, although less strongly than dayside profile. This is explained by tidal locking and the geometry of incident radiation from the star leading to lower radiative forcing.

At mid-pressures (10^{-4}–$10^{-2}\,$bar) the evening terminator plots remain significantly warmer than the morning terminator, which decreases towards the nightside average. This indicates the presence of the super-rotating jet in the GCM, transporting cooler gas from the nightside onto the terminator at levels below significant stellar irradiation forcing. The jet is driven by the extreme temperature gradient between the dayside and nightside of the planet and is biased in the direction of planetary rotation leading to an east-west jet around the planet. As a consequence of the 'night-like' morning terminator profiles and the 'day-like' evening terminator, we anticipate cloud formation to occur at the terminator asymmetrically; only on the morning terminator.

The most striking thing in Fig. 5.2 for WASP-43b is the lack of a strong inversion, contrary to the case for HAT-P-7b. Whilst the upper atmosphere of WASP-43b is substantially hotter for the dayside than the nightside, the difference is at most $\sim 700\,$K. Furthermore, for pressure $\lesssim 10^{-3}\,$bar the temperature still decreases with decreasing pressure. The only exception to this is the equatorial morning terminator profile, which is a result of zonal winds deeper in the atmosphere transporting cooler gas across the terminator. However, the effect is not as strong as for the equatorial morning terminator of HAT-P-7b as discussed previously because of the smaller dayside-nightside temperature gradients on WASP-43b. Finally, because of the lack of strong instellation from the host star WASP-43, the dayside of WASP-43b is cooler than 1500 K for $p_{\text{gas}} < 10^{-3}\,$bar. This substantially cooler temperature, when compared to the dayside of HAT-P-7b, should allow for condensation of cloud material.

5.4.2 Lower Atmosphere: Effects of GCM Boundary Conditions

For both HAT-P-7b and WASP-43b the two latitude groups ($\theta = 0.0°$, $45.0°$) are distinguishable at the inner atmospheric boundary, as first the pressure-temperature profiles converge for each latitude, with the equatorial latitudes in general being hotter. For WASP-43b the mid- to low-atmosphere ($p_{\mathrm{gas}} > 10^{-3}$ bar) is host to a number of minor temperature inversions for the dayside profiles. These inversions are typically of the order of ~ 200 K, and occur at different pressure levels for different points around the globe, unlike the consistent peak of the thermal inversion for HAT-P-7b at 10^{-3} bar.

All profiles converge deep in the atmosphere ($p_{\mathrm{gas}} \sim 100$ bar) where internal heating is the driving thermal source for both exoplanets. The nature of this convergence is specific to the GCM used (Carone et al. 2020), so interpretations of specific features here is dubious. However, for both exoplanets this region lies below the cloud formation region and as the kinetic 1D cloud formation code produces a solution from the bottom to the top of the atmosphere, the nature of cloud formation is only affected by the changing pressure-temperature structure resultant from different GCM assumptions (Helling et al. 2021). One good example of this is for WASP-43b for equatorial points at around 1 bar there is one further steep temperature inversion of about ~ 500 K. As explored by Helling et al. (2021) this can have a dramatic impact on the inner edge of the cloud deck, as ~ 2500 K is significantly hotter than the condensation curve at those pressures (their Fig. 15). When comparing to a GCM with a higher pressure internal boundary (Carone et al. 2020), such inversion is not present with the inner atmosphere ($p_{\mathrm{gas}} > 0.1$ bar) being significantly cooler and thus able to form clouds (again Fig. 15 Helling et al. 2021).

5.4.3 Hemispherical Averages: The Need for Phase Resolution

In addition Fig. 5.2 shows the projected surface area-averaged pressure-temperature profiles for the dayside and nightside hemispheres. The area element on the surface of a sphere[3] is $dA = r^2 \cos(\theta) d\theta\, d\phi$. Projecting this area element into the plane perpendicular to the observer yields another factor of $\cos(\theta)\cos(\phi)$, as areas at the limb contribute zero additional area to the projected disc. Finally integrating over the observed hemisphere (dayside or nightside) and dividing by the projected area of the disc (πr^2), gives the projected surface area-averaged pressure-temperature as

---

[3]Note the $\cos(\theta)$ term arises because latitude is defined from the equator rather than from the polar axis.

$$\langle T_{\text{gas}}(p_{\text{gas}}) \rangle = \frac{1}{\pi} \int_{\theta=-90°}^{90°} \int_{\phi=-90°}^{90°} T_{\text{gas}}(p_{\text{gas}}, \theta, \phi) \cos(\phi) \cos^2(\theta) \mathrm{d}\theta \mathrm{d}\phi. \qquad (5.1)$$

The $1/\pi$ factor arises from the normalisation factor for the projected area of the disc, as the radius of the planet cancels out. In practice this is done as a discreet summation over the selected (longitude, latitude) points. Furthermore, as only the northern hemisphere is calculated, latitude is only averaged from $\theta = 0°$ to $\theta = 90°$ and the result doubled. For both the dayside and nightside averages the terminators ($\phi = 90.0°, 270.0°$) are excluded, as they contribute nothing to the projected area. For the dayside this gives a good impression of the effective pressure-temperature structure observed by secondary eclipse emission observations, as at this point the exoplanet is 'face-on' to the observer, so points around the sub-stellar point dominate the projected area of the planet disc.

In general, for HAT-P-7b and WASP-43b, both the dayside and nightside averages prove to be poor matches for any individual given pressure-temperature profile, particularly for the inner atmospheres. However, for the upper atmospheres ($p_{\text{gas}} \lesssim 10^{-3}$), there is reasonable agreement between the profiles and the appropriate hemisphere average. This is particularly true for the dayside profiles as at such pressure the pressure-temperature profiles are very similar due to stellar radiation. In both cases the hemisphere averages are far from isothermal, indicating this a poor choice for simple atmospheric models.

5.5 How Clouds Form on an Ultra-hot Jupiter (HAT-P-7b)

To illustrate general trends in the properties of cloud particles on HAT-P-7b we initially examine three points around the equator. Fig. 5.3 shows the nucleation rate, number density, material composition, cloud particle size, and drift velocity at the evening terminator, anti-stellar point, and the morning terminator. The sub-stellar point is not shown as no clouds form at this point due to the strong stellar irradiation.

Of the three nucleating species treated for HAT-P-7b ($TiO_2[s]$, $SiO[s]$, $C[s]$), carbon is not found to nucleate anywhere on HAT-P-7b. Furthermore, no nucleation occurs at all on the evening terminator as the temperature is too great for nucleation, at any altitude, for all species. $TiO_2[s]$ is responsible for the majority of nucleation (top row, left axis, Fig. 5.3) for the two cloud forming profiles ($\phi = 180.0°, 270.0°$). However, for the anti-stellar point, at high altitudes ($p \leq 10^{-5}$ bar) $SiO[s]$ is briefly the dominant nucleating species. From Fig. 5.3 it appears that nucleation is
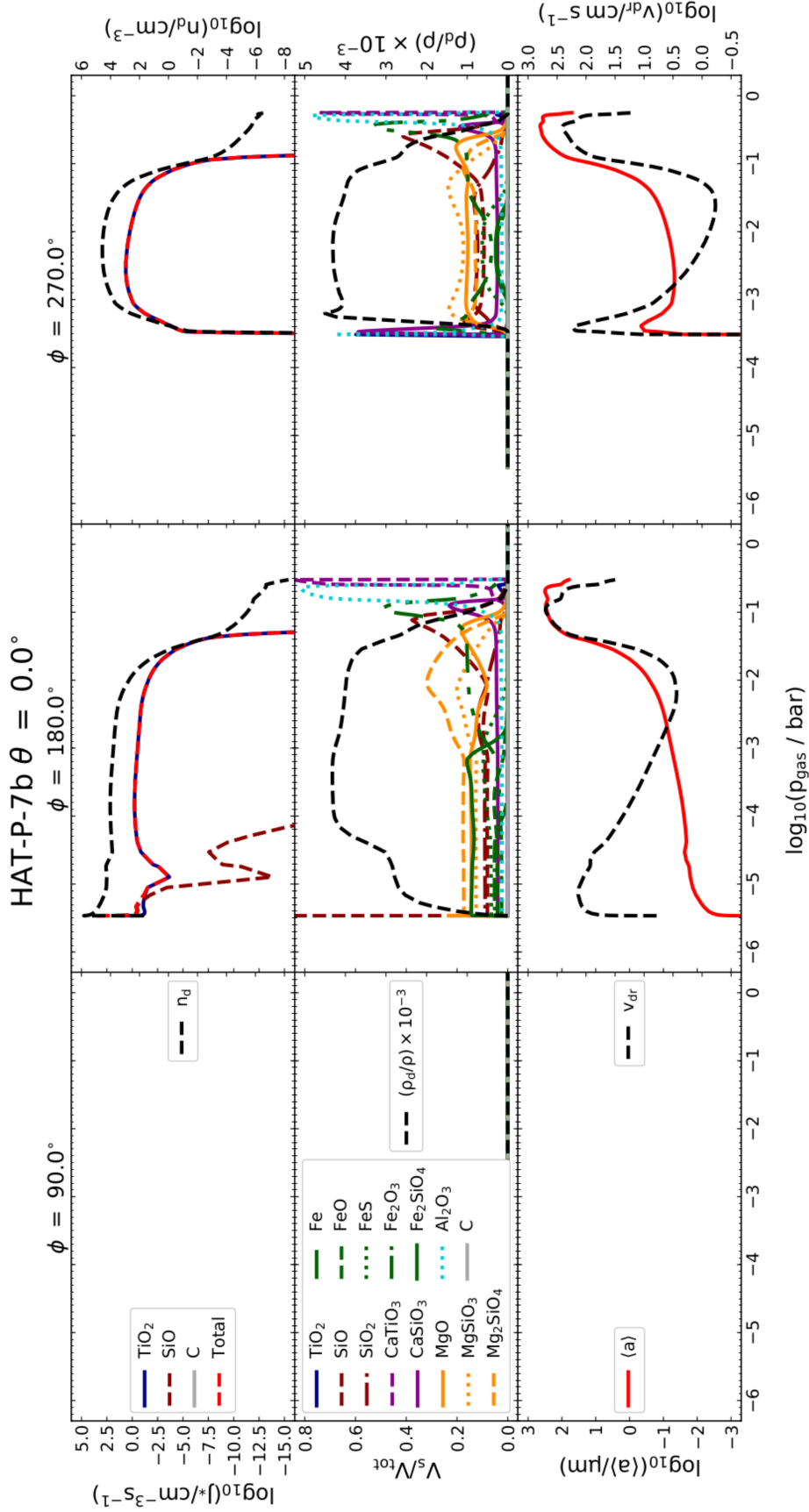
Figure 5.3: Properties of cloud particles and their formation at the evening terminator(ϕ = 90°), anti-stellar point(θ = 0°) of HAT-P-7b. **Top:** Left axis shows the total nucleation rates $J_* = \sum_i J_i$ as well as the individual components, J_i for i=TiO$_2$[s], SiO[s], C[s]. Right axis shows the number density of cloud particles, n_d [cm^{-3}] (black dashed line). **Middle:** Left axis shows the material volume fractions (V_s/V_{tot}) for all 15 condensate species in the cloud particles (see legend). Right axis shows the cloud particle mass load ρ_d/ρ scaled by a factor of 10^3 (black dashed line). **Bottom:** Left axis shows the mean cloud particle size, $\langle a \rangle$ [μm] (red solid line). Right axis shows the vertical drift velocity, v_{dr} [cm s^{-1}] for a cloud particle of size $\langle a \rangle$ (black dashed line).

121

almost entirely restricted to the cool nightside of HAT-P-7b, apart from around the morning side terminator, where the GCM provides cooler 'night-like' profiles due to the equatorial jet. We see the nucleation of cloud particles deeper in the atmosphere at the morning terminator compared with nucleation up to the TOA for the anti-stellar point, which is due to the thermal inversion at this part of the atmosphere and hence cloud condensation nuclei are not stable at high altitudes.

The number density of cloud particles (top row, right axis, Fig. 5.3) closely follows the nucleation rate, as there is no other way for particles to form; bulk growth only affects the mass of cloud particles condensed, as it relies on the presence of condensation nuclei which set the number density. However, there is a 'tail' of cloud particles present on both the cloud forming profiles below where the nucleation rate rapidly decreases ($p_{gas} \gtrsim 5 \times 10^{-2}$ bar for the anti-stellar point and $p_{gas} \gtrsim 10^{-1}$ bar for the morning terminator). This is due to gravitational settling of cloud particles from higher in the atmosphere. Although settling occurs at all levels of the atmosphere – as seen by the drift velocities of the particles (bottom row, right axis, Fig. 5.3) – at deep atmospheric levels nucleation all but ceases, leaving only settling and growth/evaporation processes in these regions. At the deepest atmospheric levels growth also stops, due to the high temperatures, and so particles 'raining' in from higher levels begin to evaporate leading to the disappearance of clouds for $p_{gas} \approx 1$ bar.

Thus we see that the extent of the cloud deck at a given location on HAT-P-7b is controlled by two main factors; the thermal stability of cloud particles at the inner atmosphere and the nucleation rate in the upper atmosphere. At high pressures, the profiles have a much lower spread in temperatures (seen in Fig. 5.2), meaning that in cloud-forming regions (the nightside and morning terminator) the lower boundary of clouds are roughly uniform. However, the thermal inversion for the morning terminator at low pressures ($\sim 5 \times 10^{-4}$ bar) limits high altitude nucleation. This is also seen in the cloud particle mass load ρ_d/ρ (middle, right axis, Fig. 5.2) which remains relatively flat for pressures between 5×10^{-6}–5×10^{-2} bar at the anti-stellar point, and only 10^{-3}–10^{-1} bar at the morning terminator. The overall lower cloud top at the morning terminator has implications for transmission spectra and phase curve observations. The changing altitude of clouds could potentially impact retrieved atmospheric abundances as well as the average particle size (see Sect. 5.7).

In the case of assuming a cloud particles to be of a single size equal to the mean cloud particle size, the mean particle drift velocity (bottom row, right axis, Fig. 5.2) is proportional to the mean

cloud particle size. This explains the peak in drift velocity at high pressures below the region of efficient nucleation (reduced nucleation rate). As nucleation has almost completely ceased in this region of the atmosphere, there is a dearth of small particles. Furthermore, cloud particles present due to settling from higher layers have experienced significant growth and are therefore large. This leads to a large average cloud particle size. These cloud particles continue to grow, and as such the mean cloud particle size increases until the point where the drift velocity becomes high enough that the largest cloud particles rapidly rain out of these layers, once again decreasing the mean particle size. Those particles that do remain at theses deep levels also experience some evaporation, which may also contribute to the decreasing average size of cloud particles.

For both cloud forming profiles, moving towards higher altitudes, there is an increase in drift velocity owing to a decreasing atmospheric density (cf. inverse proportionality in Eq. 2.1) and thus less resistance to gravitational settling. This trend continues until the uppermost atmosphere, where the vast majority of cloud particles are recently formed cloud condensation nuclei that have experienced minimal growth, and hence are very small and buoyant, even in a rarefied environment. The peak in average cloud particle size seen only at the morning terminator is explained by the shift of the cloud top to lower altitudes, as discussed previously. This atmosphere is much more suitable to growth, and thus particles rapidly grow after nucleation to an average size of $\sim 1 \, \mu m$.

Composition of the cloud particles varies dramatically both throughout the pressure levels and at different points around HAT-P-7b. For the anti-stellar point, at high altitudes the composition is briefly $\sim 80\%$ SiO[s] which is the main nucleating species at this profile and altitude, as mentioned before, indicating that almost all particles are pure condensation nuclei and significant growth is yet to occur. At higher pressures, growth species dominate over the nucleating species and particles become highly mixed – leading to the predicted heterogeneous cloud particles. Down to $p_{\text{gas}} \sim 3 \times 10$ bar the particle composition is dominated by silicates such as Fe_2SiO_4[s] and Mg_2SiO_4[s], with a lesser component of MgO[s]. At greater pressures this only high temperature species (Al_2O_3[s] and $CaTiO_3$[s]) survive, as other species become thermally unstable and evaporate. At the morning terminator a different regime appears, as cloud particles develop at lower layers in the atmosphere with higher temperatures, they are easily dominated immediately high temperature species Al_2O_3[s] and $CaTiO_3$[s], before following a broadly similar variation in composition for deeper in the atmosphere as for the anti-stellar point.

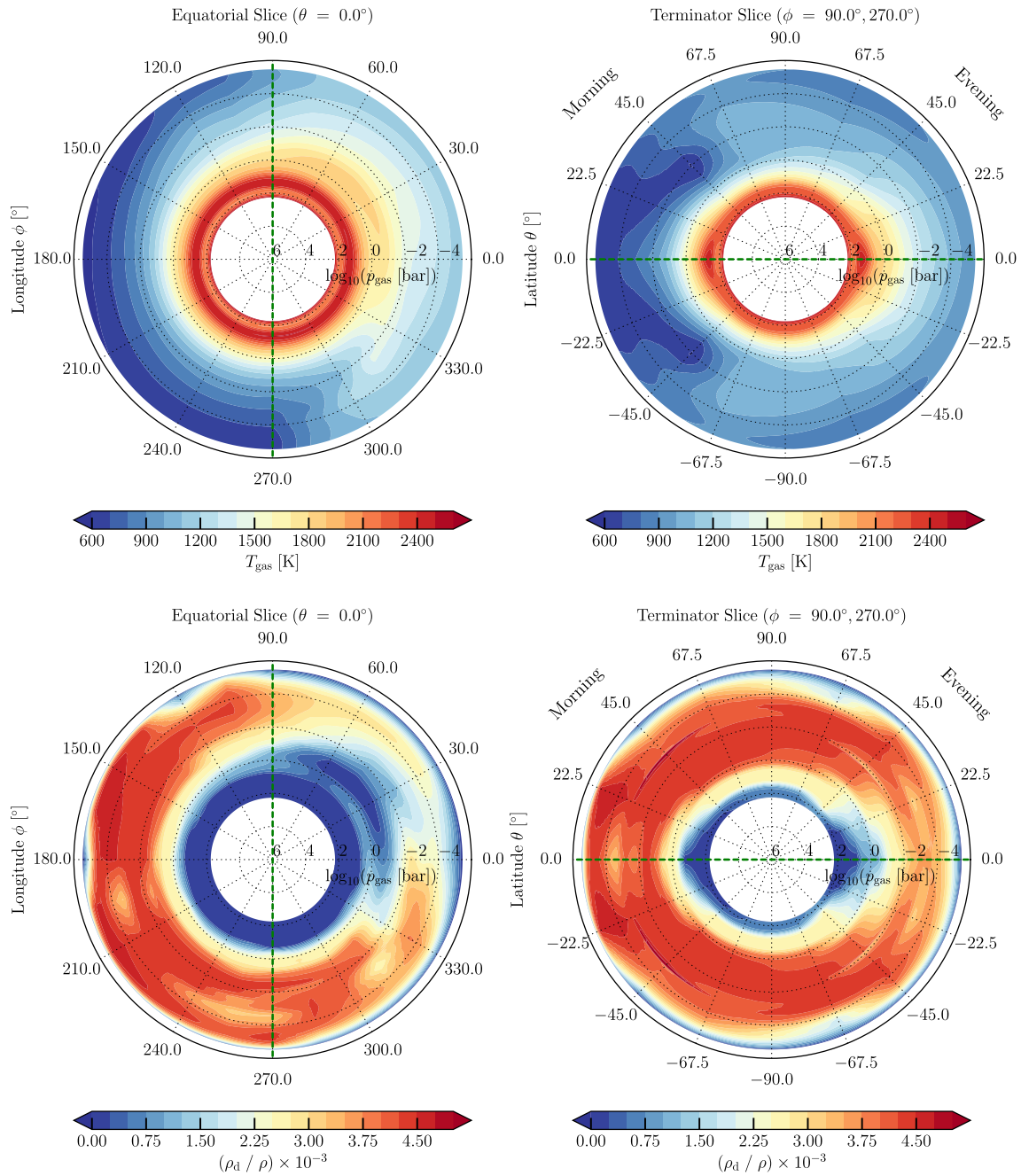## 5.6   Equatorial and Terminator Slices Through HAT-P-7b and WASP-43b

We now broaden our picture towards the global structure of cloud formation on HAT-P-7b and WASP-43b. We do so by looking at 'slices' through the atmospheres of the planets. We take two orientations of slices: around the equator to illustrate the differences between the dayside and nightside cloud particle formation; and around the terminator, which demonstrates the atmosphere probed by transmission spectroscopy. A representative central disk (white) extends below the modelled atmosphere, from 10^2–10^6 bar, this arbitrary scaling was chosen for best visibility of the data. A true physical scaling would have an extensive 'core' with only a small annulus for the atmosphere. The equatorial plots are oriented such that the star is located to the right of the diagram. The terminator plots are oriented with the star located out of the page, as only the northern hemisphere was modelled, thus the data is mirrored across the equator (dotted green line).

Comparing Fig. 5.4 and Fig. 5.5 we now get a better picture of the global pressure-temperature structure differences between WASP-43b and HAT-P-7b. Firstly examining the equatorial temperature distribution (top left of figures), the dayside/nightside temperature contrast discussed in the previous section is apparent. In both planets the convergence of the pressure-temperature structure occurs at around 10 bar, which aligns with the selected equatorial profiles in Fig. 5.2. In addition we see that for HAT-P-7b for $p_{gas} < 10^{-2}$ bar the temperature is dominated by the amount of stellar irradiation globally. The most notable feature is the effects of the super-rotating equatorial jet on the mid-pressure ($\sim$ 5–10^{-2} bar) in the morning terminator transition region. Figure 5.4 shows an extension of cooler material round to longitudes for $\phi = 300.0°$ on the dayside. Higher altitude atmospheric levels do not exhibit the same cooling around the morning terminator, owing to stellar irradiation. The top right of Fig. 5.4 shows the thermal inversions present around the terminator of HAT-P-7b, with a sharp drop off at 10^{-4} bar, although the inversion is less strong than for the dayside as expected.

Fig. 5.5 for WASP-43b also shows dayside heating, but substantially weaker than for HAT-P-7b. In addition, there is also evidence of west-east flow; the hotspot (the hottest profile in the atmosphere) is offset from the sub-stellar point by approximately 45° at 10 bar. However, the location of the hotspot is dependent on the pressure probed, potentially being less than 30° for $p_{gas} \sim 0.1$ bar. These hotspot offsets at the equator are broadly in line with retrieved hotspots observed in the phase curves of WASP-43b. Although these observations naturally integrate over
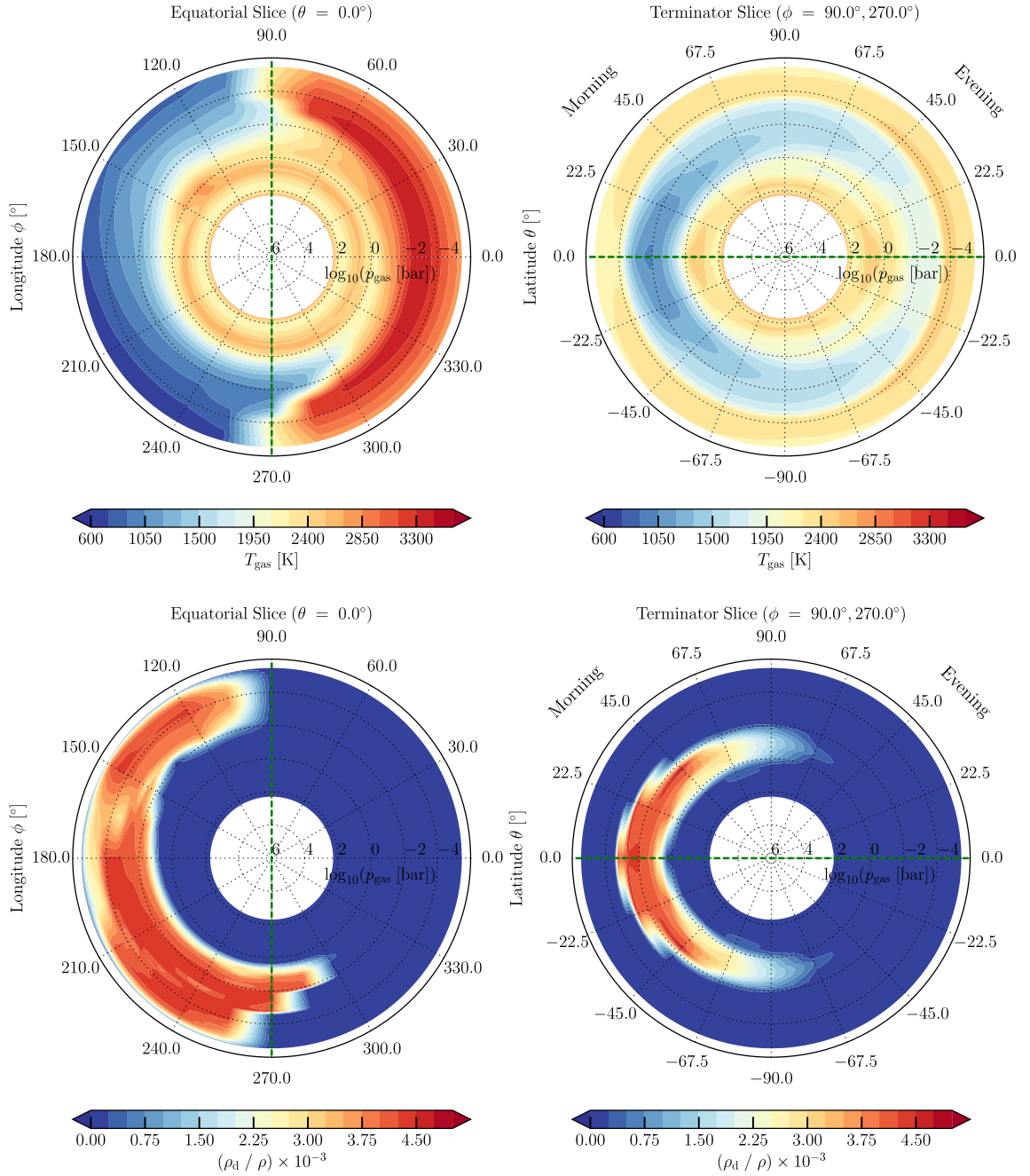
Figure 5.4: Equatorial ($\theta = 0.0°$, **Left**) and terminator ($\phi = 90.0°, 270.0°$, **Right**) slices through the atmosphere of HAT-P-7b. Dashed green lines show the equivalent positions of the terminator and equator for the alternate plots. Equatorial and terminator plots use the same colour-bars to aid comparison. **Top:** Local gas temperature. **Bottom:** Cloud particle mass load $\rho_{\rm d}/\rho$ scaled by a factor of 10^3.

Figure 5.5: Equatorial ($\theta = 0.0°$, **Left**) and terminator ($\phi = 90.0°, 270.0°$, **Right**) slices through the atmosphere of WASP-43b. Dashed green lines show the equivalent positions of the terminator and equator for the alternate plots. Equatorial and terminator plots use the same colour-bars to aid comparison. **Top:** Local gas temperature. **Bottom:** Cloud particle mass load ρ_d/ρ scaled by a factor of 10^3. Adapted from Helling et al. (2020), credit: Victoria Graham.

126

the full observable disc, not just the equator. Stevenson et al. (2017) found an offset of $\sim (12 \pm 3)°$ at $\lambda = 3.6 \, \mu m$ and $\sim (21 \pm 2)°$ at $\lambda = 4.5 \, \mu m$, although analysis by Mendonça et al. (2018); Morello et al. (2019) found significantly smaller offsets. There is also evidence of a similar equatorial jet as on HAT-P-7b, but again weaker, for longitudes $\phi = 270°$–$300.0°$, this is aided by the rapid rotation rate of WASP-43b. The jet is found at similarly deep pressures to HAT-P-7b, inline with the structures shown by Kataria et al. (2015) who use the same MITgcm model.

The terminator regions (right panel) for WASP-43b is dramatically different than for HAT-P-7b, the morning terminator shows a particularly interesting structure, of which a little glimpse was seen in the inversion for the $\theta = 45°$ morning terminator profile discussed in Sec. 5.4.1. For the equatorial terminator the temperature decreases with decreasing pressure, however for mid-latitudes ($\sim 30°$–$67.5°$) the atmosphere exhibits inversions for pressures around 10^{-2} bar. In comparison, the evening terminator limb ($\phi = 90°$) is straightforward; with temperature decreases with decreasing pressure for all latitudes, with the equator remaining warmer than higher latitudes.

After applying our 1D kinetic cloud formation model, we can examine where most of the cloud density is located globally, this is shown in the bottom plots of Fig. 5.4 and Fig. 5.5. For HAT-P-7b, at the equator, we see that clouds (high cloud particle mass load ρ_d/ρ) are almost exclusively limited to the nightside. Furthermore, for nightside profiles moving from the morning to the evening terminator (i.e. going from $\phi = 270.0°$ to $\phi = 90.0°$ via the nightside), the cloud base can be seen to rise from 1 to 10^{-2} bar, significantly reducing the overall cloud depth. However, some amount of cloud particles are present on the dayside of the planet round to longitudes of $\phi = 300.0°$. Comparing to the equatorial slice of T_{gas} we can see that cloud extension in the atmosphere closely follows the cooler temperatures at mid-pressures from the equatorial jet. It is worth reiterating at this point that due to the hierarchical nature of our modelling process this is not material swept from the nightside onto the dayside by the jet. Rather, cloud particles are forming on the dayside due to favourable thermodynamic conditions, namely the gas temperature, which are generated by the hydrodynamics of the jet as captured by the profiles from the 3D cloud-free GCM.

The effects of the thermal inversions on the top of the cloud deck around the equator can also be seen for the morning terminator. The cloud top is roughly constant near the top of the atmosphere for all nightside profiles, but the cloud top moves inwards to deeper pressures for

$\phi \approx 270°$–$300.0°$. The sharp steps in cloud particle mass load in both bottom plots is due to the spacing of our GCM profiles and the interpolation used in these plots. The terminator region of HAT-P-7b (lower right, Fig. 5.4) shows that the bias in winds from east-west leads to a massive asymmetry in the cloud particle distribution around the terminator. Furthermore, cloud particle formation again aligns with regions of cooler gas temperatures, with high cloud particle mass load in the atmosphere limited to below the thermal inversion on the morning side of the terminator. As the jet is only bringing cool material from the nightside for a narrow range of latitudes around the equator, the terminator is actually warmer at higher latitudes, leading less cloud formation (lower cloud particle mass load ρ_d/ρ) and the cloud top migrating inwards for higher latitudes. The evening terminator limb is almost entirely cloud free aside from the polar latitudes, where there is a region of very low density cloud.

WASP-43b shows cloud formation around the entire equator (Fig. 5.5), however, on the warmer dayside cloud formation is again restricted to cooler temperature regions. The equatorial hotspot is particularly apparent and as a result $\phi = 45°$ has only a thin cloud deck between $p_{\text{gas}} \sim 10^{-6}$–$10^{-3}$ bar. Cloud formation on the nightside is also more efficient, producing atmosphere cloud particle mass loads of around $\rho_d/\rho \sim 4.5 \times 10^{-3}$ which is not achieved anywhere on the dayside equator. For the terminator region, clouds form for both limbs, with a greater cloud particle mass load condensing on the cooler morning terminator near the mid-latitudes. The cloud decks extend down to ~ 1 bar, compared to the limited pressure range of the cloud deck at the morning terminator of HAT-P-7b. Thus we expected less asymmetric spectral properties for transmission spectra of the terminators of WASP-43b and similar temperate gas giants.

Figure 5.6 shows the nucleation rate and average cloud particle size around the equator and terminators of HAT-P-7b, comparison between the two shows a clear trend: average cloud particle size remains low in regions with high nucleation rates. As discussed in Sect. 5.5 the nucleation rate determines the number density of cloud particles in a layer, high nucleation rates results in a large number of cloud particles. These freshly formed particles are at the cloud condensation nuclei size and hence the lower average cloud particle size. For HAT-P-7b nucleation occurs across the nightside up to the top of the atmosphere, with two regions of high nucleation rate ($J_* \gtrsim 100 \, \text{cm}^{-3} \, \text{s}^{-1}$) around $\phi = 150.0°$ and between $\phi = 210.0°$–$240.0°$ for $p_{\text{gas}} < 10^{-4}$ bar. These regions align closely with regions of high cloud particle mass load in Fig. 5.4 as expected. The lower limit of efficient nucleation (set at $J_* = 10^{-20} \, \text{cm}^{-3} \, \text{s}^{-1}$) follows similar patterns to the cloud
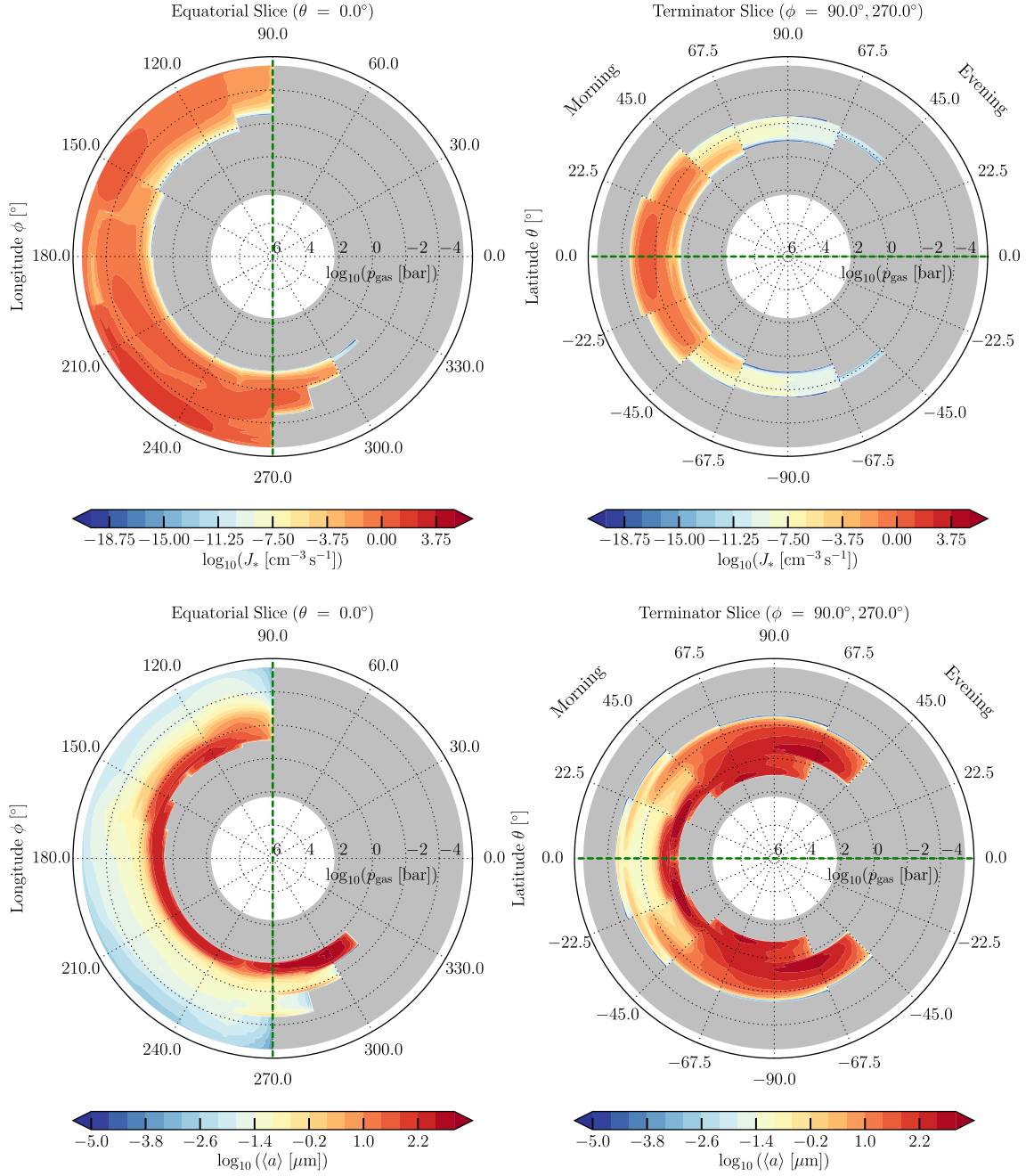
Figure 5.6: Equatorial ($\theta = 0.0°$, **Left**) and terminator ($\phi = 90.0°, 270.0°$, **Right**) slices through the atmosphere of HAT-P-7b. Dashed green lines show the equivalent positions of the terminator and equator for the alternate plots. Equatorial and terminator plots use the same colour-bars to aid comparison. **Top:** Total nucleation rate, the grey regions are those where the nucleation rate falls below the cut-off value of $J_* = 10^{-20} \, \text{cm}^{-3} \, \text{s}^{-1}$. **Bottom:** Average cloud particle size in micrometers, the grey regions represent those where no cloud particles exist.
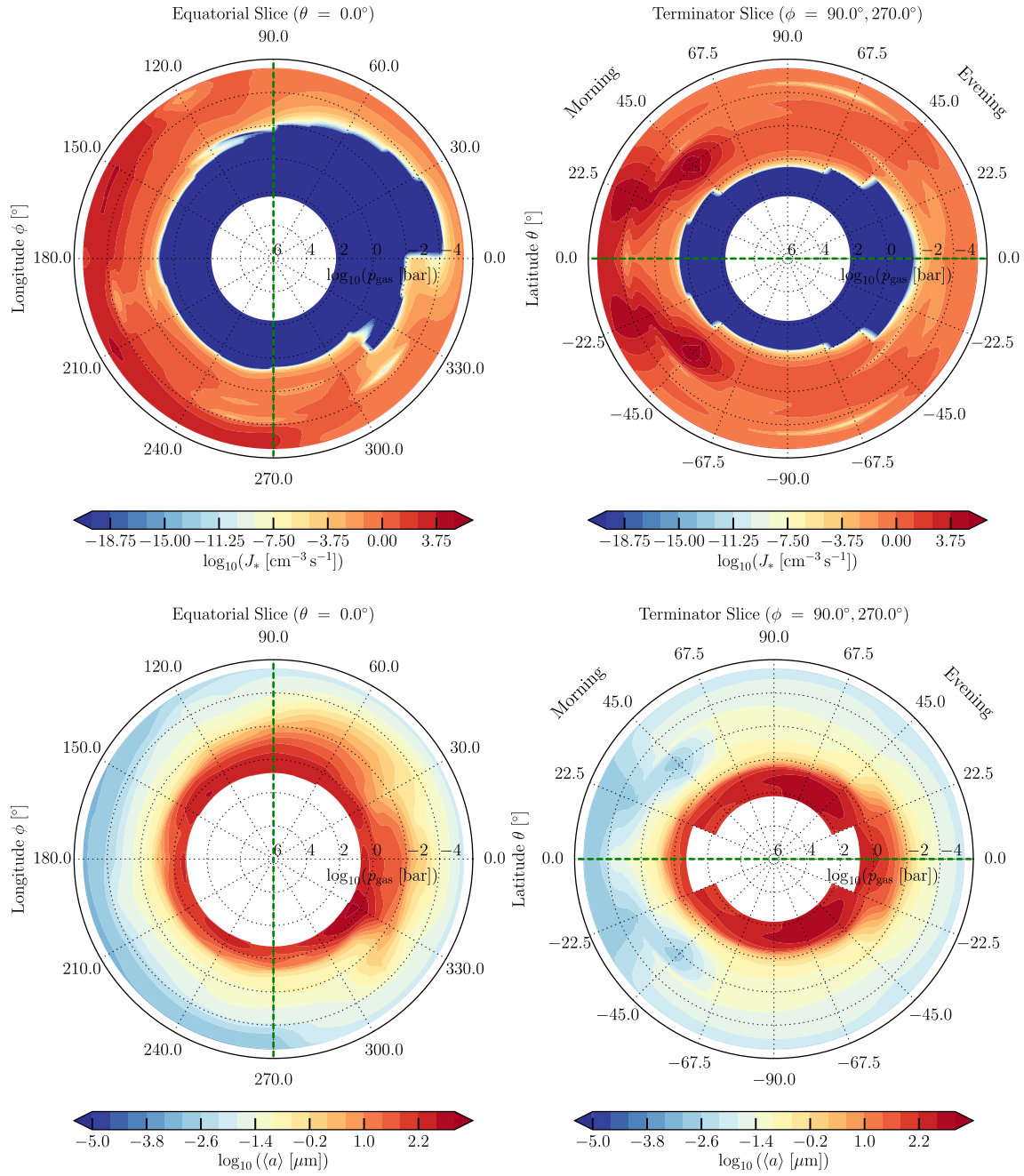
Figure 5.7: Equatorial ($\theta = 0.0°$, **Left**) and terminator ($\phi = 90.0°, 270.0°$, **Right**) slices through the atmosphere of WASP-43b. Dashed green lines show the equivalent positions of the terminator and equator for the alternate plots. Equatorial and terminator plots use the same colour-bars to aid comparison. **Top:** Total nucleation rate, note the colour-bar is again cut-off at $J_* = 10^{-20}\,\mathrm{cm}^{-3}\,\mathrm{s}^{-1}$. **Bottom:** Average cloud particle size in micrometers. Adapted from Helling et al. (2020), credit: Victoria Graham.

particle mass load and temperature plots, although the lowest pressure levels at which nucleation occurs are slightly higher than the cloud base due to cloud particle settling. For example, between 1–5 bar at the morning terminator, here the mean cloud particle size rapidly increases as only cloud particles that have undergone significant bulk growth in higher levels and then settled out are present, furthermore smaller grains evaporate more quickly and thus the average particle size increases.

For the evening terminator of HAT-P-7b, at high latitudes there is low overall cloud particle mass load, but high mean cloud particle size at deep pressure levels. This indicates rapid bulk growth onto the small number of cloud condensation nuclei formed by the low nucleation rate. This is because of the thermal inversion and generally warmer temperatures of the profile. This means the very upper atmosphere is not stable for nucleation, thus the cloud material nucleates deeper in the atmosphere, here the cloud condensate materials are also thermally stable to growth which is efficient. Correspondingly, this results in a large average particle size of $\langle a \rangle > 100\,\mu$m.

Nucleation rates and average particle size for WASP-43b tell a similar story as for HAT-P-7b. Figure 5.7 very clearly shows nucleation in the upper atmosphere, followed by settling and growth. To pick a very obvious example, at $\phi = 15°$ the nucleation rate drops below $J_* < 10^{-20}\,\mathrm{cm}^{-3}\,\mathrm{s}^{-1}$ at $p_{\mathrm{gas}} \approx 10^{-4}$ bar and therefore there is no new cloud particle formation below this layer. However, cloud particles exist down to pressures of ~ 10 bar at this longitude. These cloud particles eventually reach average sizes of $\sim 160\,\mu$m, which is slightly smaller than the average particle size formed at the deepest cloud levels for HAT-P-7b. Finally the average particle size for the terminator of WASP-43b is smaller than at the same size for HAT-P-7b (c.f. bottom right Fig. 5.6 and Fig. 5.7). This is due to nucleation occurring over a much wider range of pressures than the comparatively thin region for HAT-P-7b. This is especially true for the evening terminator polar regions, which is where some of the largest average particle sizes are found for the terminator of HAT-P-7b. We note that for both atmospheres cloud particles reach much larger average sizes than we have dealt with in previous chapters, up to nearly 400 μm compared with a maximum of $\langle a \rangle \sim 1\,\mu$m in the 1D DRIFT-PHOENIX atmosphere profiles.

## 5.7 Optical Depth of Clouds on gas giant Exoplanets and Ultra-hot Jupiters

Finally we turn our attention to the observable properties of these exoplanets. To do this we examine the optical depth of clouds at the equatorial terminators ($\theta = 0°$, $\phi = 90°, 270°$) for WASP-43b and HAT-P-7b. The optical depth is the property of clouds that dictates the observable atmosphere, neglecting additional gas-phase opacity. As shown by Lacy & Burrows (2020a), the width of the terminator probed in transmission spectra differs for different gas giants, for WASP-43b they find it to be $\sim \pm10°$ and for HAT-P-7b $\sim \pm17°$. The former value is below the resolution of the longitude spacing used in this investigation, thus we can gain a first order insight into the spectral effects of clouds for transmission spectra by examining just the terminator profiles. However, we recognise that to get a true picture of cloud optical depth this 'wedge' must be integrated over. For HAT-P-7b in particular this wedge is much wider and includes points at the evening terminator that demonstrate cloud formation in our results (see bottom left panel Fig. 5.4 $\phi = 105°$), which is neglected here.

We, however, do correct for the fact that instead of light rays travelling vertically along the individual equatorial terminator profiles, light rays rather passes through the atmosphere at an angle. This 'slant' correction adjusts for the geometry of transmission observations by increasing the optical depth by a factor (Fortney 2005):

$$\tau_s(\lambda) = \tau_v(\lambda) \sqrt{\frac{2\pi R_p}{H_p}}. \tag{5.2}$$

Where τ_s is the called the 'slant optical depth' and τ_v is the 'vertical optical depth' calculated as in Eq. 2.23. This still neglects full 3D effects, as we calculate the optical depth for only one latitude, longitude profile. For example, the evening terminator of ultra-hot Jupiter there are clouds located at the poles. Therefore a major limitation of this method is that for the evening terminator interpreting the actual impact of clouds in the transmission spectra of HAT-P-7b is not possible, instead we can only state that the evening terminator limb at the equator does not contribute to the optical depth of clouds for HAT-P-7b.

Figure 5.8 shows the pressure at which clouds become optically thick at the two terminators, as discussed above there is no optical depth calculation shown for the evening terminator of
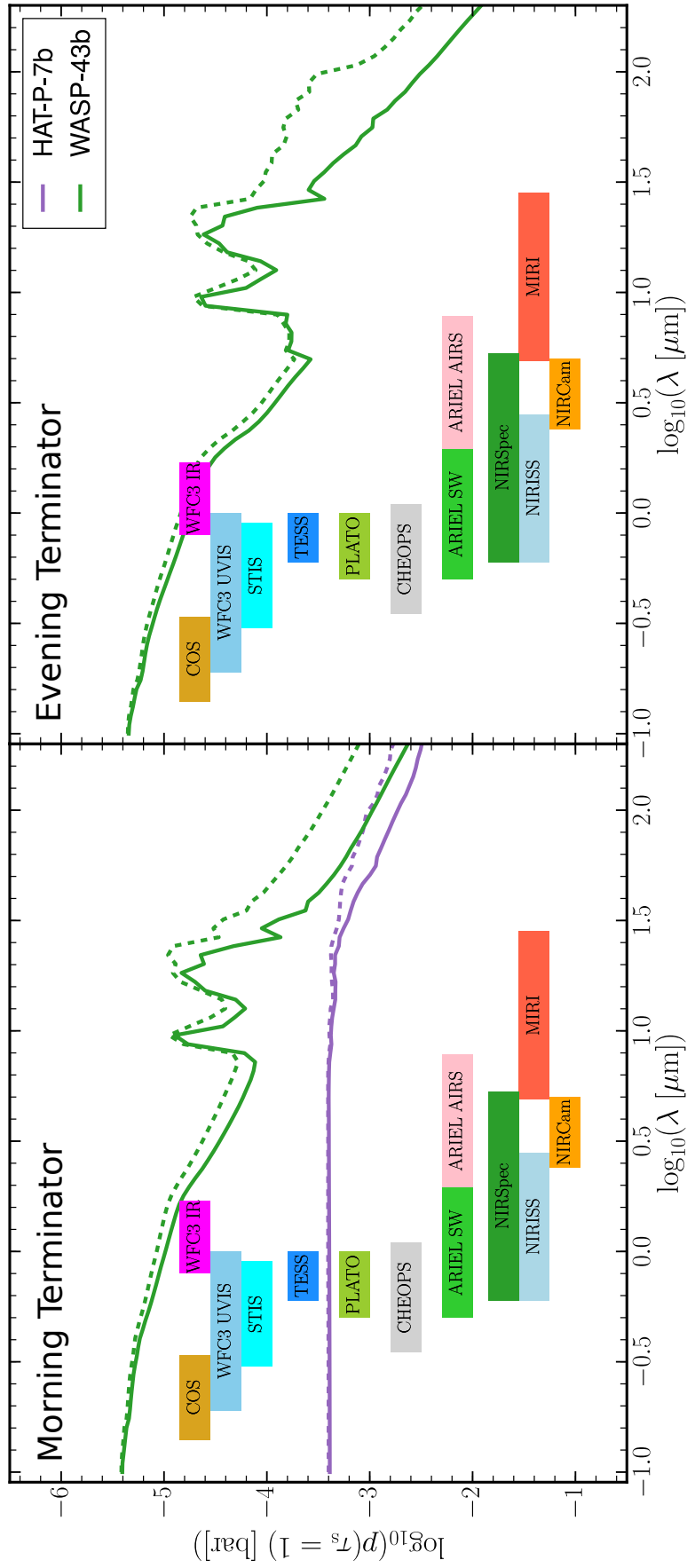
Figure 5.8: Pressure levels at which the slant-corrected optical depth reaches unity ($\tau_s = 1$) for the ultra-hot Jupiter (HAT-P-7b, purple) and the gas giant (WASP-43b, green). **Left:** Morning terminator, $\phi = 270.0°$. **Right:** Evening terminator, $\phi = 90.0°$. The coloured bars indicate the wavelength ranges of a number of present and future instruments. Solid lines show the opacity assuming compact clouds, whilst dashed lines assume a distribution of hollow spheres as is introduced in Chap. 3. Adapted from (Helling et al. 2021).

HAT-P-7b. Therefore, initially looking at the morning terminator the two planets produce dramatically different optical depths. HAT-P-7b exhibits a completely flat opaque pressure level (at $p_{gas} = 3 \times 10^{-4}$ bar) for wavelengths $\lambda < 10\,\mu$m. Comparing this to Fig. 5.4, we can see this is close to the initial occurrence of cloud particles for this profile. However, we have consider that the slant correction increased the optical depth and therefore decreased the pressure at which the clouds became optically thick. Nonetheless, the clouds at equatorial evening terminator for HAT-P-7b become optically thick near the top of the cloud deck. As the clouds at this point only form relatively deep in the atmosphere, thus cloud condensation is efficient and any cloud condensation nuclei formed experience rapid bulk growth. The cloud particles at these levels have an average particle size around $0.25\,\mu$m, which equates to a transition in size parameter of $x > 1$ to $x < 1$ at around $1.6\,\mu$m. These large (mostly silicate) cloud particles are therefore in the geometric optics regime for $\lambda \lesssim 10\,\mu$m, hence the flat, featureless opaque pressure level, even in the silicate feature range. For $\lambda \gtrsim 15\,\mu$m the cloud particles enter the Rayleigh regime ($x \lesssim 1/10$), leading the slope seen in optically thick pressure level.

In comparison, the cloud optical depth of the equatorial evening terminator of WASP-43b can be broken down into three regions: $\lambda \lesssim 6\,\mu$m, $6\,\mu$m $\lesssim \lambda \lesssim 40\,\mu$m, and $\lambda \gtrsim 40\,\mu$m. The optically thick pressure level varies from 4×10^{-6} bar down to 2.5×10^{-3} bar, thus the pressure in the atmosphere observed depends strongly on wavelength. As particle size also changes with pressure in the atmosphere it is consequently less easy to define the average particle size that is observed, but looking at Fig. 5.7 we see that the average particle size in the observable atmosphere at the morning terminator ranges between $\langle a \rangle = 10^{-3}$–$2.5\,\mu$m in average size. The lower limit of average particle size corresponds to the size of cloud condensation nuclei that kickstart the cloud formation process. The Rayleigh scattering from these small particles is responsible for the increasing opacity of the clouds (i.e. lower pressure opaque cloud level) in the UV, optical, and near-infrared wavelength regime $\lambda \lesssim 6\,\mu$m, and hence the slope in the optically thick pressure level.

In the mid-infrared regime $6\,\mu$m $\lesssim \lambda \lesssim 40\,\mu$m, the cloud optical depth of the the equatorial evening terminator of WASP-43b is governed by the silicate features located at $9.7\,\mu$m and $18\,\mu$m. These features increase the opacity of the clouds by enough that the clouds become optically thick nearly an order of magnitude lower in pressure than out of the feature. This wavelength range is covered by JWST MIRI, and thus it should provide a good test of the material composition of the clouds based on the strength and shape of these features. At $\lambda \gtrsim 40\,\mu$m, the scattering from

the small cloud particles in the upper atmosphere is largely insubstantial, thus the clouds remain transmissible down to deeper atmospheric layers. Here the $\sim 1\ \mu$m average sized cloud particles begin scatter the light.

Cloud formation on the evening terminator of WASP-43b is very similar to the morning terminator and thus the opaque pressure level looks largely the same. However, from Fig. 5.7 we see that at the same pressure level, the cloud particles are on average larger than the morning terminator. Thus even with a roughly similar observable atmospheric column, the average cloud particle size is not a single, easily definable value. Furthermore, the features in the mid-infrared regime display a different shape, due to slightly different material composition of the clouds between the two terminators. Lastly we discuss the impact of irregular particle shapes, this is done by assuming a distribution of hollow spheres (DHS, Min et al. (2005)) for the cloud particles, see Chap 3 for details of the implementation. In general for irregular cloud particle sizes the optical depth is increased across all wavelengths, thus the clouds become opaque at lower pressure.

5.8 Conclusion

In general the results of this analysis indicate that cloud formation of tidally locked gas giant exoplanets is highly dynamic and not easily characterisable for by a single value for any single parameter, be that material composition, particle size, or optically thick cloud pressure depth. For HAT-P-7b, and ultra-hot Jupiters more generally, it has highlighted cloud formation occurs on the nightside, and equatorial winds produce an asymmetry in cloud formation around the terminator. Such asymmetry could affect retrieved properties in a similar way to how MacDonald et al. (2020) found assumptions of uniform pressure-temperature structures for transmission spectra bias temperatures towards cooler values. Although, Welbanks & Madhusudhan (2021) point out the dependence on model assumptions in atmospheric retrievals and that these also crucial impact inferences of terminator inhomogeneities. Asymmetric terminator cloud formation has also been found by Powell et al. (2019) for gas giants using the CARMA microphysical model. Such asymmetry may also be observable in ingress and egress transmission photometry by missions such as CHEOPS.

WASP-43b, typical of hot Jupiters, albeit with a very fast rotation rate due to its small orbit, is found to easily form clouds globally. This conflicts with observations suggesting very low

geometric albedos for the dayside (Fraine et al. 2021). However, the nightside formation of clouds agrees with results by Kataria et al. (2015), who invoked nightside clouds to explain lack of flux in both *Hubble* and *Spitzer* observations for WASP-43b. Parmentier et al. (2021) suggest that when nightside clouds are present the day-night re-distribution of heat is very poor on hot Jupiters. Furthermore, nightside clouds decrease phase curve offset, but this is sensitive to nightside cloud material composition. However, Parmentier et al. (2021) use MnS[s] clouds, which currently we do not include, which is proposed to be a good cloud candidate for $T_{eq} < 1600 \, K$ gas giants (Parmentier et al. 2016). Silicate clouds on the nightside of gas giants should cause an increase in the phase curve offset for exoplanets from $T_{eq} = 1200$–$2000 \, K$, we find silicate clouds form on the nightside of hot Jupiters across this temperature range.

The terminators of WASP-43b are both found to exhibit strong silicate spectral features, increasing the opacity of clouds at 9.7 and 18 μm and thus increasing the height of the optically thick cloud level. Comparing this to HAT-P-7b, we expect ultra-hot Jupiters in the same wavelength range (observable with JWST MIRI and eventually also ARIEL) to have a flat, deeper cloud deck due to thermal inversions at the terminator. Ultra-hot Jupiters should also have much deeper opaque cloud levels in the visible wavelength range (observable with *Hubble*, and also affecting observations with CHEOPS and PLATO) compared to a more temperate hot Jupiter like WASP-43b.

The hierarchical approach here is a step towards fully consistent kinetic cloud formation in GCM simulations, such modelling has previously also been undertaken by Lee et al. (2016). Fully consistent modelling of clouds is essential to investigate variability in observations of hot and ultra-hot Jupiters, which is often attributed to clouds (Line & Parmentier 2016; Armstrong et al. 2016; Beatty et al. 2019). A limitation of this study is that the results have only been shown utilising one GCM, results with an alternative GCM (e.g. Carone et al. 2020) can give very different cloud material compositions due to different thermodynamic conditions (Fig.15 in Helling et al. 2021), which result from deep atmosphere wind structures, at high-pressure (down to $p_{gas} \sim 700 \, bar$). Such higher pressure levels are not included in this GCM and the lower boundary flow structure is not converged as Parmentier et al. (2018) assume that this does not alter the photospheric pressure-temperature structure. A major result of Carone et al. (2020) is that they found a westward (retrograde) flow alongside super-rotation, although more recent work without temperature forcing at deep layers found only super-rotation (Schneider & Wurm 2021). However, both these results serve to highlight the importance of expanding GCM computational

domains to gain a full picture of gas giant dynamics, which govern the local thermodynamic conditions, which in turn dictate cloud formation.

However this hierarchical approach is computationally feasible and has allowed for modelling of disequilibrium chemistry effects and to investigate the ionisation of the ultra-hot Jupiter HAT-P-7b (Molaverdikhani et al. 2020; Helling et al. 2021). As well as investigating the impact of photochemical haze formation alongside clouds for WASP-43b (Helling et al. 2020). This study found photochemical hazes to occur at much lower pressures (higher altitudes) thus occupying a different atmospheric regime from clouds. Despite the higher altitude, the hazes but do not become optically thick (Helling et al. 2020).
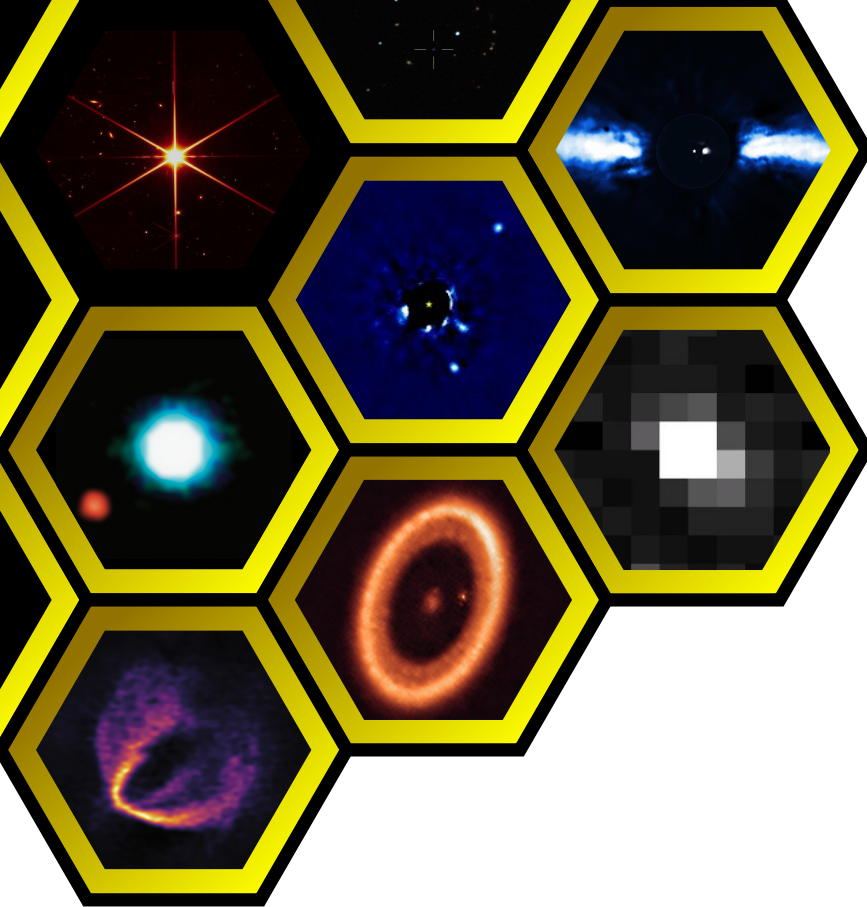
"I love deadlines. I like the whooshing noise they make as they go by."

- Douglas Adams, *The Salmon of Doubt*, 2002

6

Summary, Conclusion, and Future Work

6.1 Summary

In this thesis we have used a kinetic, non-equilibrium cloud formation model consistently linked with gas-phase equilibrium chemistry, to investigate the formation of cloud particles in the atmospheres of gas giant exoplanets and brown dwarfs. Below we briefly summarise what has been presented, and the main results derived from these investigations.

Chapter 3 investigated the effects of micro-porous cloud particles ('mineral snowflakes') with a simple parametrised model; reducing cloud material density of represent highly porous cloud particles. We found that such micro-porosity shifts the onset of condensational growth for mineral clouds to higher in the atmosphere, and that these effects are robust for a range of planetary effective temperatures and surface gravities. We also investigated the spectral effects of porous, irregularly shaped cloud particles, and a particle size distribution. We find that such properties likely impact near- and mid-infrared observations, such as those that will be undertaken by JWST MIRI.

Chapter 4 detailed the development of the HYLANDS hybrid moment and bin cloud particle-particle collision model, which retains the advantages of the mixed material kinetic cloud formation modelling with equilibrium gas-phase chemistry, whilst incorporating a parametrised

cloud particle collision model to capture the trends of coagulation and fragmentation of cloud particles. The advantage of this approach is that it remains computationally cheap, avoiding issues of full bin models, such as challenges with element conservation and the large numbers of bins necessary. We find turbulence is the main driving process of cloud particle collisions in exoplanets and brown dwarfs. For exoplanets these collisions are likely to fragment the particles. For cool brown dwarfs, limited increase in average particle size is possible through coagulation. For atmospheres with fragmentation, observations in the optical and infrared regimes (*Hubble*, CHEOPS, JWST, and ARIEL) are likely affected, potentially impacting cloud particle material and size retrievals.

Chapter 5 used a hierachical approach to model global cloud formation in the atmosphere of hot and ultra-hot Jupiters WASP-43b and HAT-P-7b, using 1D p_{gas}-T_{gas} profiles extracted from 3D cloud-free GCM results as input into kinetic cloud formation. We found the terminators of ultra-hot Jupiters to exhibit highly asymmetric cloud formation. Furthermore, for both hot and ultra-hot Jupiters clouds readily form on the nightside. However, only for hot Jupiters are clouds present on the dayside, due to the strong thermal inversions for ultra-hot Jupiters on the dayside. These differences agree with population studies already undertaken, but as a greater number of observations come in we expect that the detailed differences of microphysical cloud formation will become more apparent.

6.2 Future Work

As is so frequently the case with science, investigation produces more, new, interesting questions than they answer. These further questions are, necessarily by the pressure of actually finishing the work, left unanswered. In this section we suggest such unresolved questions and the opportunities they provide for further exploration.

- Incorporating porosity evolution as a result of collisions to investigate fluffy cloud particles and their impact on exoplanet spectra. Recently, fluffy hazes have shown to be a good method of generating flat spectra (Adams et al. 2019), and a key question would be whether fluffy clouds produce similar effects.

- Integrate the collision model into the time dependent DiffuDrift model (Woitke et al. 2020), this would allow the exploration of the time evolution of the system. Alongside this, introducing a fully binned collisional model, this more computationally intensive approach

would allow the calibration of the faster hybrid HʏLᴀɴᴅS approach.

- Applying the microphysical modelling to cooler and smaller planets, such as the mini-Neptune GJ 1214b, incorporating more condensate species and cooler chemistry.

- For application of microphysical cloud models a key aim would be to produce spectra from microphysical cloud modelling, which will be possible through the use of ARCiS (Min et al. 2020). These include optical properties of non-compact cloud particles, as well as investigating the impacts of mixed cloud particles on mid-infrared retrievals. One example is the low albedo of dayside gas giant exoplanets WASP-43b (e.g. Fraine et al. 2021) which remains a challenge, but one that mixed cloud particles has the potential to resolve.

- Using microphysical modelling to inform attempts to derive material composition of clouds from observations with, for example, JWST (e.g. Luna & Morley 2021). As well as this microphysical cloud models could act as a means to set priors on cloud properties (such as cloud deck height) for atmospheric retrievals, potentially helping with degeneracies between properties such as clouds and atmospheric metallicities (Carone et al. 2021).

- Furthermore, the scattering properties of mixed and porous grains will be important for reflected light observations of exoplanets, for high resolution spectra which probes the upper atmosphere, and for polarisation observations in the UV.

6.3 Conclusion

Clouds have been a defining feature of exoplanets since the first observation of an exoplanet atmosphere (Charbonneau et al. 2002), obscuring the deeper atmosphere and thus producing flat transmission spectra with muted gaseous absorption features. The importance of clouds in the atmospheres of sub-stellar mass objects had also been well known from brown dwarfs (Lunine et al. 1986; Tsuji et al. 1996a,b). Whilst many models parametrise clouds (e.g. Ackerman & Marley 2001), self-consistent microphysical modelling is required to fully capture the complexity of the cloud formation. The size, shape and material composition of cloud particles, as well as their global distribution in the atmosphere, all affect the impact clouds have on observations. As observations continue to improve from new missions such as JWST (Gardner et al. 2006) and future missions (e.g. ARIEL), cloud modelling will be crucial to understanding other atmosphere properties such as the composition.

However, attempts to infer cloud material composition from observations (e.g. Taylor et al. 2020; Luna & Morley 2021) may be confounded by the additional affects resulting from the processing of cloud particles by collisions, irregular particle shape, and porosity of the cloud particles. Furthermore, as observations of gas giant exoplanets are treated more completely in their full, glorious three dimensions, the asymmetries in terminator properties of clouds for ultra-hot Jupiters as well as the asymmetry between the daysides and nightsides of gas giant exoplanets need to be properly incorporated.

The silver lining is that as observations improve, the insights generated by microphysical modelling only become more relevant. Details of microphysical cloud formation on hot Jupiters has already been exploited to explain trends in observed populations (e.g. Baxter et al. 2020; Gao & Powell 2021). We will, in the fullness of time, gain a deeper understanding of what is happening in the clouds of exoplanets. For example, retrieval of cloud particle size variations with depth in the atmosphere, which would be possible through multi-wavelength, high-resolution observations can expose the collisional affects on the cloud particle distribution. The difference between exoplanet science and a typically overcast summer's day in the UK is that we may eventually peer into the clouds and perhaps be surprised by what we find. If one can be a little bold, it is the firm opinion of the author of this thesis that the future of the field of exoplanet science is exceptionally bright, even if it is for the moment hidden just behind the clouds.
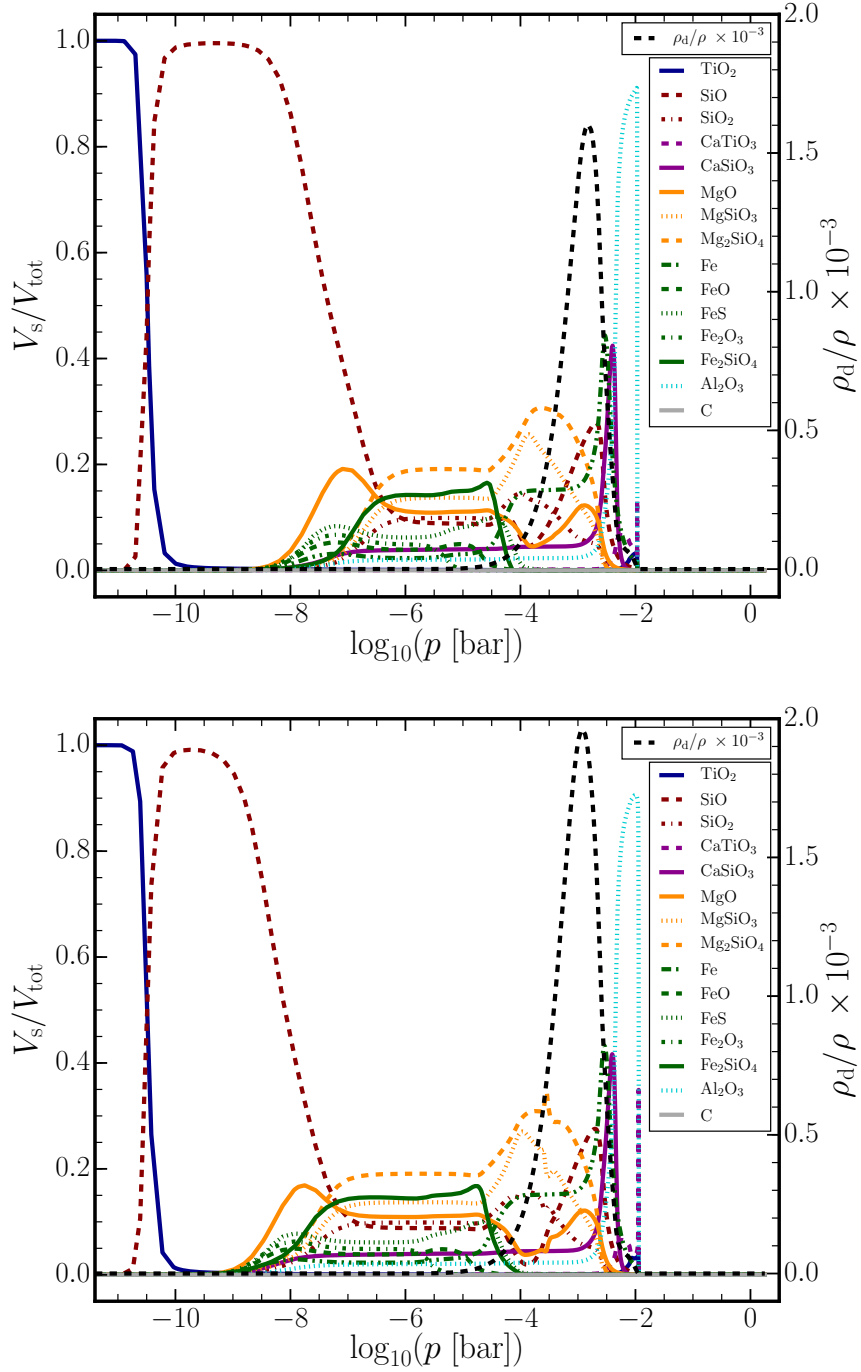
A

Appendix: Mineral Snowflakes

A.1 Additional Figures
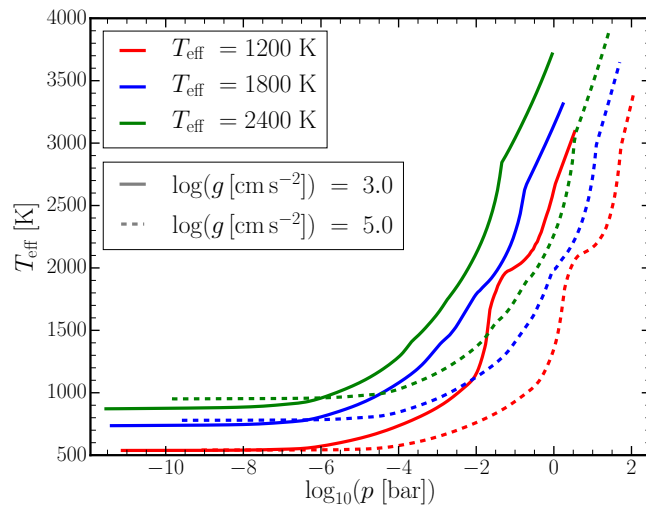
Figure A.1: DRIFT-PHOENIX (T_{gas}-p_{gas}) profiles for $T_{\mathrm{eff}} = 1200, 1800,$ and $2400\,\mathrm{K}$ (red, blue, and green, respectively) and $\log(g\,[\mathrm{cm\,s^{-2}}]) = 3.0$ and 5.0 (solid and dashed, respectively).

Figure A.2: Material properties of cloud particles in the T_{eff} = 1800 K, $\log(g\,[\mathrm{cm\,s^{-2}}])$ = 3.0 atmosphere. **Top:** For compact cloud particles (f_{por} = 0.0). **Bottom:** For highly micro-porous cloud particles (f_{por} = 0.9). **Left axis:** Material volume fractions of cloud particles. **Right axis:** Cloud particle mass load ρ_{d}/ρ scaled by a factor of 10^3 (black dashed line).
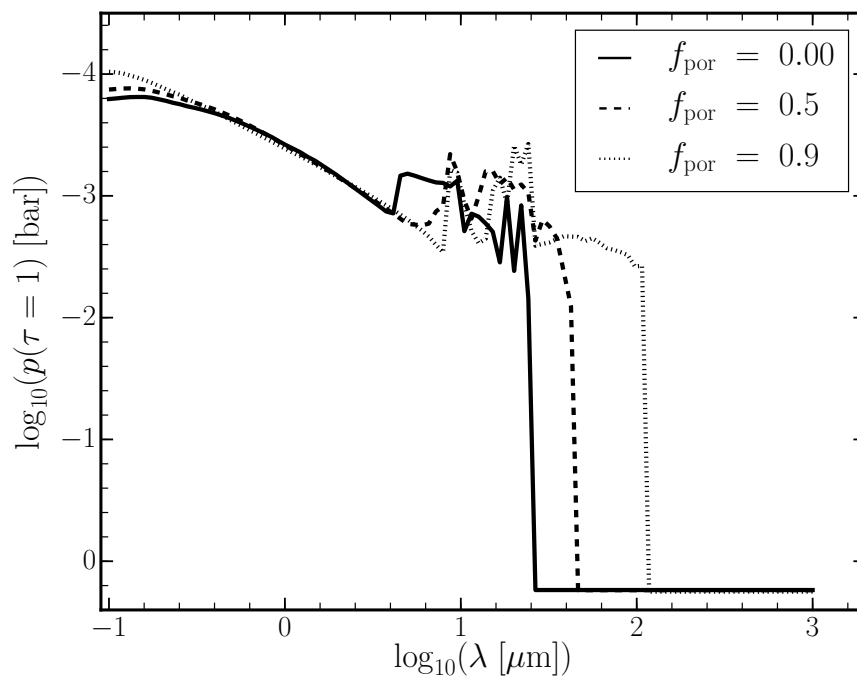
Figure A.3: Pressure level at which the cloud deck optical depth reaches unity $p(\tau(\lambda) = 1))$ for wavelengths in the range $\lambda = 0.1$–1000 μm integrated from the top of the atmosphere.
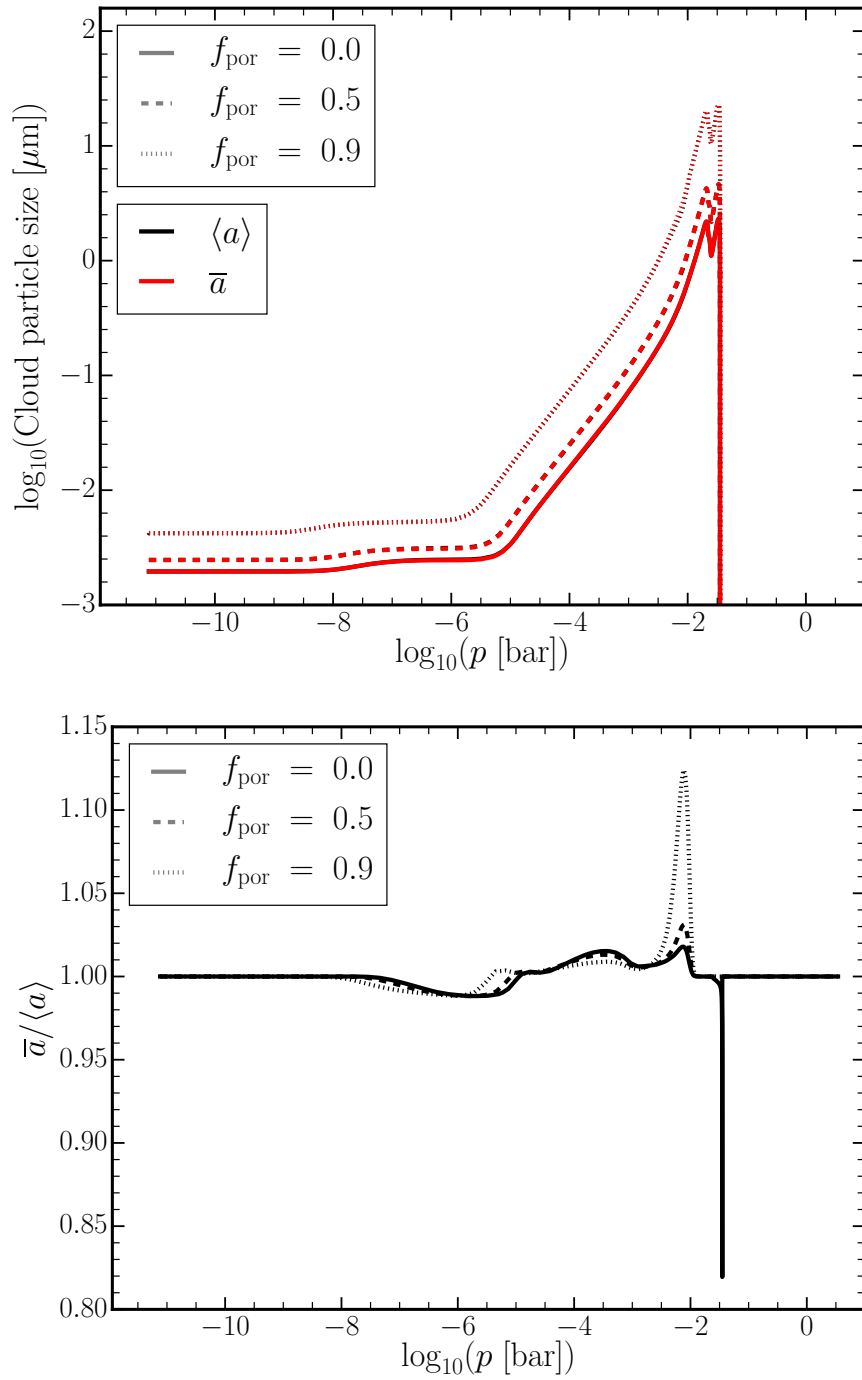
Figure A.4: Comparison of the two methods of calculating the cloud particle size, the mean particle size from the moments $\langle a \rangle$ according to Eq. 2.6, and from the size distribution $\bar{a}$ using Eq. 3.5. **Top:** $\langle a \rangle$ and $\bar{a}$ throughout the atmosphere for $T_{\text{eff}} = 1200\,\text{K}$, $\log(g\,[\text{cm}\,\text{s}^{-2}]) = 3.0$, and three micro-porosity cases $f_{\text{por}} = 0.0, 0.5, \text{and } 0.9$. **Bottom:** $\bar{a}$ as a fraction of $\langle a \rangle$ for the same atmosphere and micro-porosity cases as above. This atmosphere shows the largest difference between the two average cloud particle sizes across all profiles.

B

Appendix: Clashing Clouds

B.1 Derivation of Maximum Cloud Particle Size for Turbulence-Induced Collisions

Starting with $\tau_{\text{coag}}^{\text{turb}} = \tau_{\text{sett}}$, using Eq. 20 from Woitke & Helling (2003) and using Eqs. 4.3 and 4.12, and given that $\rho_{\text{d}}/\rho_{\text{s}} = \rho L_3$ one arrives at

$$\frac{H_{\text{p}}}{v_{\text{dr}}^{\circ}} = \frac{a}{\rho L_3 \langle \delta v_{\text{g}}^2 \rangle^{1/2}} \frac{1 + \frac{\tau_{\text{f}}}{\tau_{\text{t}}}}{\sqrt{2\frac{\tau_{\text{f}}}{\tau_{\text{t}}}}}. \tag{B.1}$$

However, both v_{dr}° and τ_{f} are dependent on cloud particle size. Substituting Eqs. 2.1 and 4.7 into Eq. B.1 and re-arranging gives the 5th order polynomial

$$f(a) = \left(1 + \frac{2\sqrt{\pi}\rho_{\text{s}}}{\rho c_{\text{T}}\tau_{\text{t}}}a\right)^2 a^3 - \left(\frac{4H_{\text{p}}\rho L_3 \langle \delta v_{\text{g}}^2 \rangle^{1/2}}{3g}\right)^2 \frac{2\rho c_{\text{T}}}{2\sqrt{\pi}\rho_{\text{s}}\tau_{\text{t}}}. \tag{B.2}$$

Solutions to Eq. B.2 for limiting particle size are when $f\left(a_{\text{lim}}^{sett}\right) = 0$. Defining the parameter z

147

for the final term, as it is independent of cloud particle size a:

$$z = \left(\frac{4H_\mathrm{p}\rho L_3 \langle \delta v_\mathrm{g}^2 \rangle^{1/2}}{3g}\right)^2 \frac{2\rho c_\mathrm{T}}{2\sqrt{\pi}\rho_\mathrm{s}\tau_\mathrm{t}}. \tag{B.3}$$

From the Eq. B.2 and Eq. B.3, one can see that for $a = z^{1/3}$

$$f(z^{1/3}) = z\left(1 + \frac{2\sqrt{\pi}\rho_\mathrm{s}}{\rho c_\mathrm{T}\tau_\mathrm{t}} z^{1/3}\right)^2 - z, \tag{B.4}$$

which is strictly positive. Similarly, $f(0) = -z$ and hence is negative. Thus a real positive root of $f(a)$ exists for $0 < a < z^{1/3}$. For there to be further real roots would require a turning point for $f(a)$ for positive a. This can be checked by taking the derivative of Eq. B.2 with respect to a, which yields

$$f'(a) = 5\left(\frac{2\sqrt{\pi}\rho_\mathrm{s}}{\rho c_\mathrm{T}\tau_\mathrm{t}}\right)^2 a^4 + 8\left(\frac{2\sqrt{\pi}\rho_\mathrm{s}}{\rho c_\mathrm{T}\tau_\mathrm{t}}\right) a^3 + 3a^2. \tag{B.5}$$

Turning points of the function are at $f'(a) = 0$, as trivially a factor of a^2 cancels out, this gives an inflection point at $a = 0$. The remaining quadratic yields solutions for turning points at $a = -\rho c_\mathrm{T}/\sqrt{\pi}\rho_\mathrm{s}\tau_\mathrm{t}$ and $-3\rho c_\mathrm{T}/10\sqrt{\pi}\rho_\mathrm{s}\tau_\mathrm{t}$. This guarantees that there is only one positive root and thus one solution between $a = 0$ and $a = z^{\frac{1}{3}}$. Which can be solved for numerically.

B.2 Additional Figures
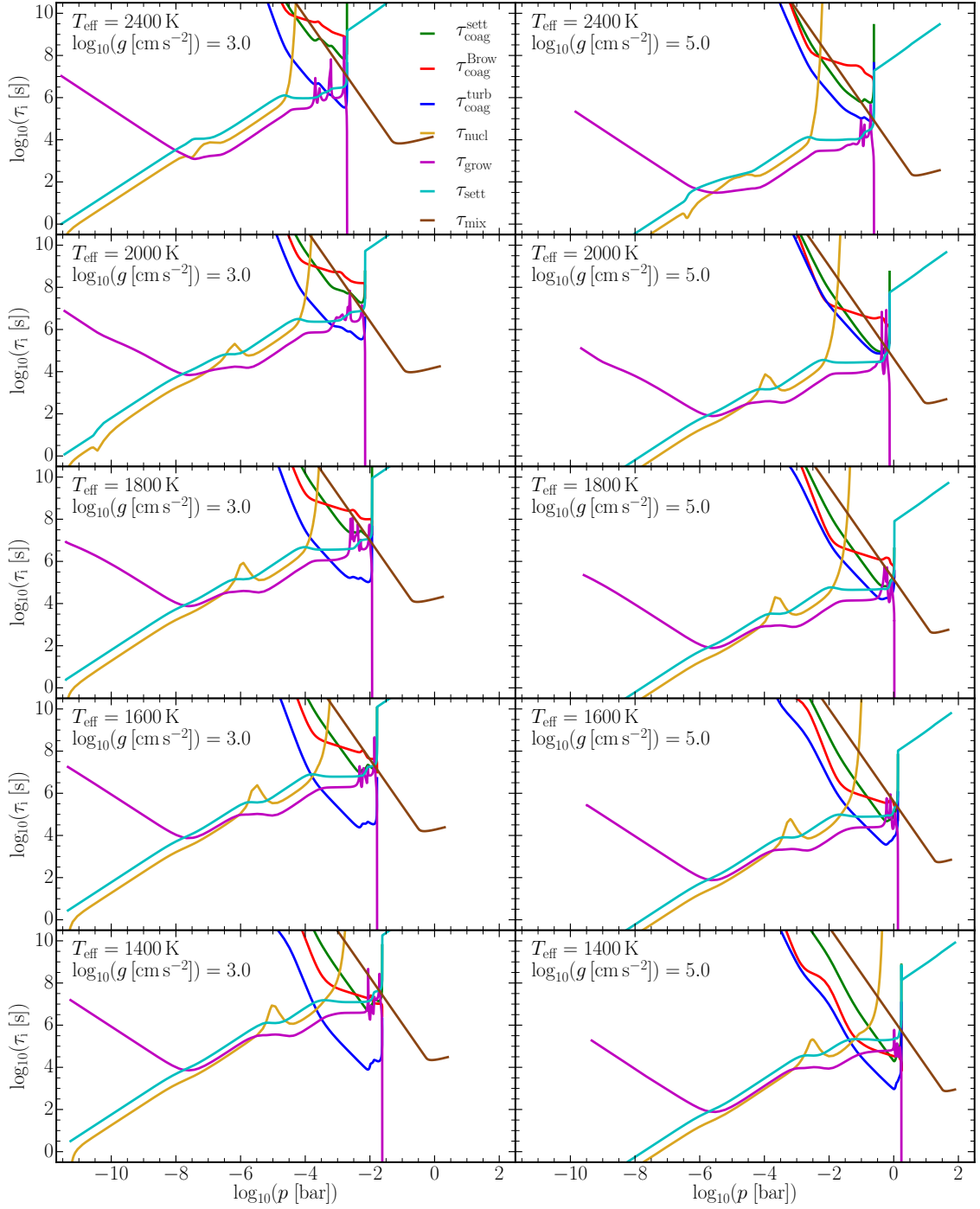
Figure B.1: Timescales for physical processes controlling cloud particle formation and distribution in the atmosphere. For monodisperse distributions, the timescales of collisions are shown for the three driving processes considered: gravitational settling (green), Brownian motion (red), and turbulence (blue). Also shown are the timescales of the other microphysical processes: gravitational settling (τ_{sett}, cyan), condensational growth (τ_{grow}, magenta), nucleation (τ_{nucl}, gold), and mixing (τ_{mix}, brown). Effective temperatures from top to bottom are: T_{eff} = 2400, 2000, 1800, 1600, 1400 K. Two surface gravities are shown: $\log_{10}(g\,[\mathrm{cm\,s^{-2}}]) = 3.0$ (**Left**), and $\log_{10}(g\,[\mathrm{cm\,s^{-2}}]) = 5.0$ (**Right**)
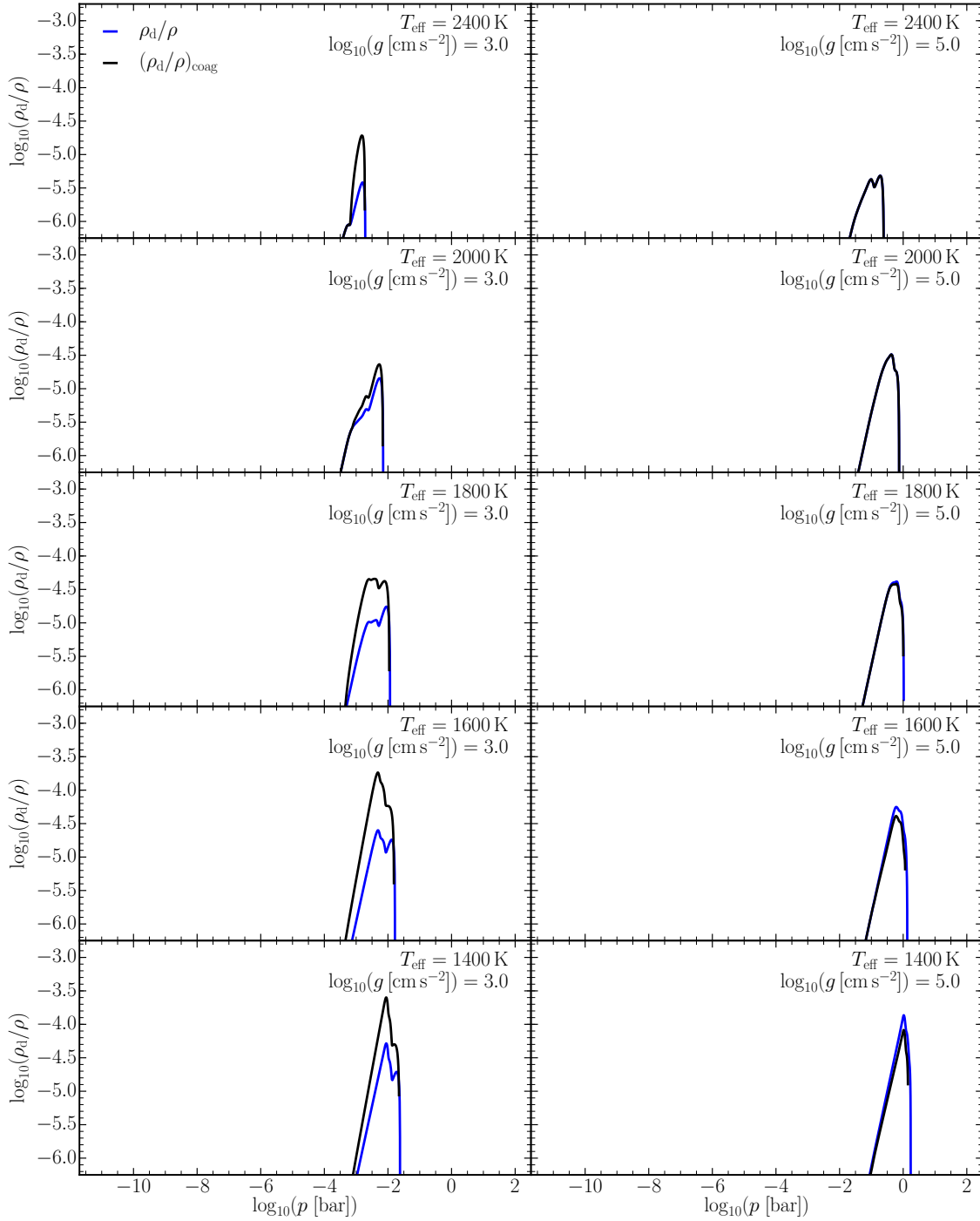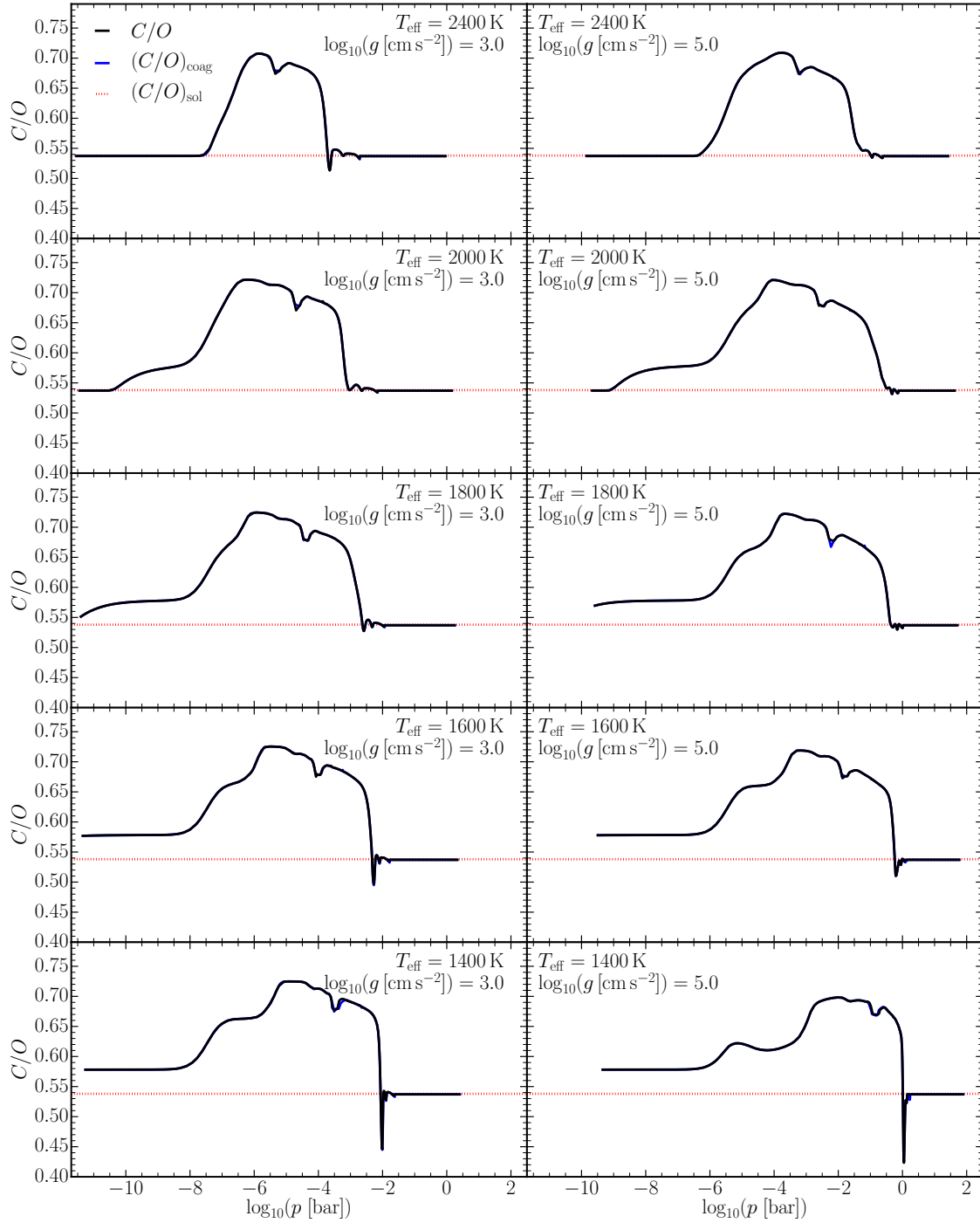
Figure B.2: Cloud particle mass load ρ_d/ρ, without coagulation (blue) and with coagulation (black). Effective temperatures from top to bottom are: T_{eff} = 2400, 2000, 1800, 1600, 1400 K. Two surface gravities are shown: $\log_{10}(g\,[\mathrm{cm\,s^{-2}}])$ = 3.0 (**Left**), and $\log_{10}(g\,[\mathrm{cm\,s^{-2}}])$ = 5.0 (**Right**)
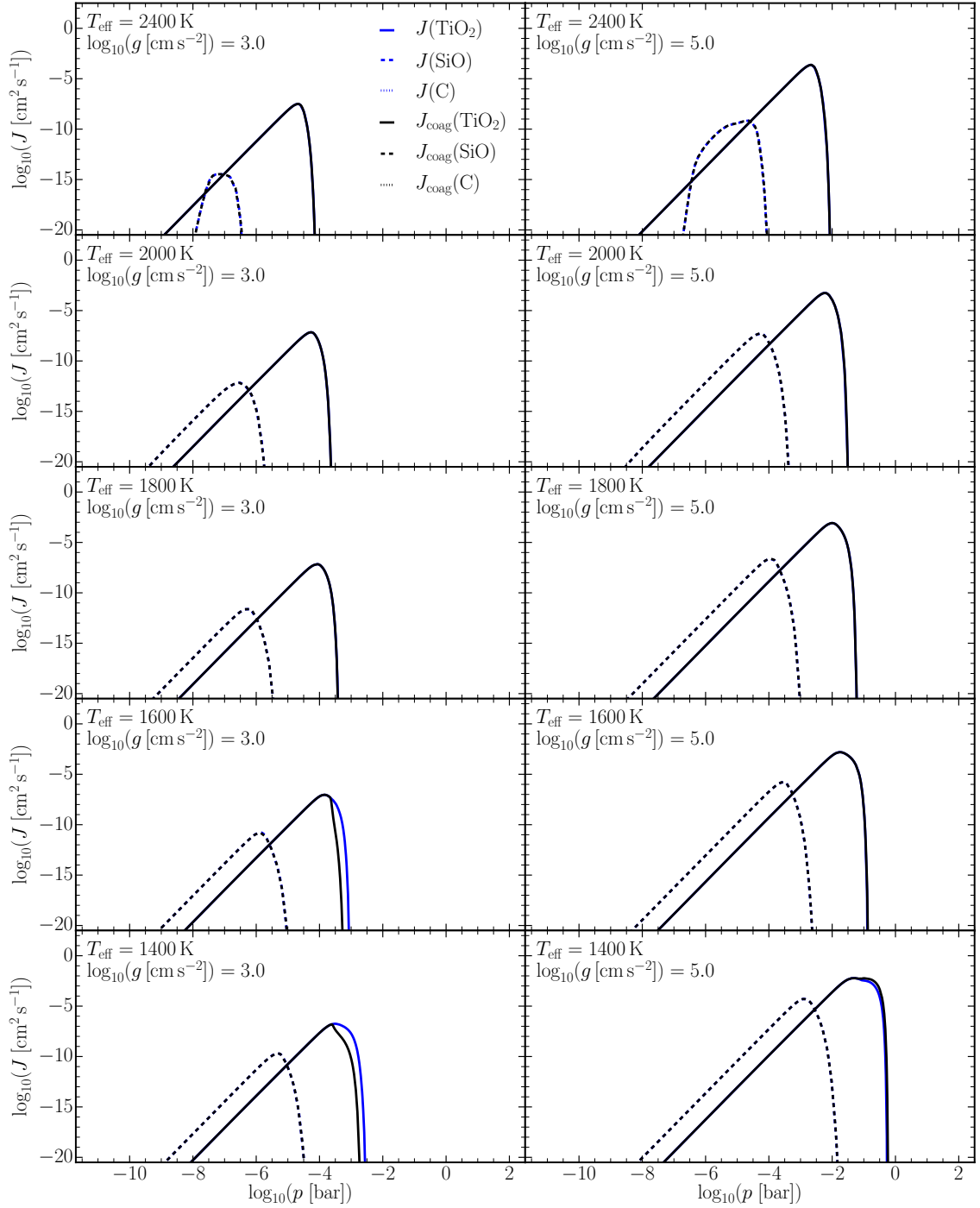
Figure B.3: Nucleation rates J of nucleating species TiO_2[s], SiO[s], and C[s] (solid, dashed, and dotted lines respectively), without coagulation (blue) and with coagulation (black). Effective temperatures from top to bottom are: T_{eff} = 2400, 2000, 1800, 1600, 1400 K. Two surface gravities are shown: $\log_{10}(g \, [\text{cm s}^{-2}])$ = 3.0 (**Left**), and $\log_{10}(g \, [\text{cm s}^{-2}])$ = 5.0 (**Right**)
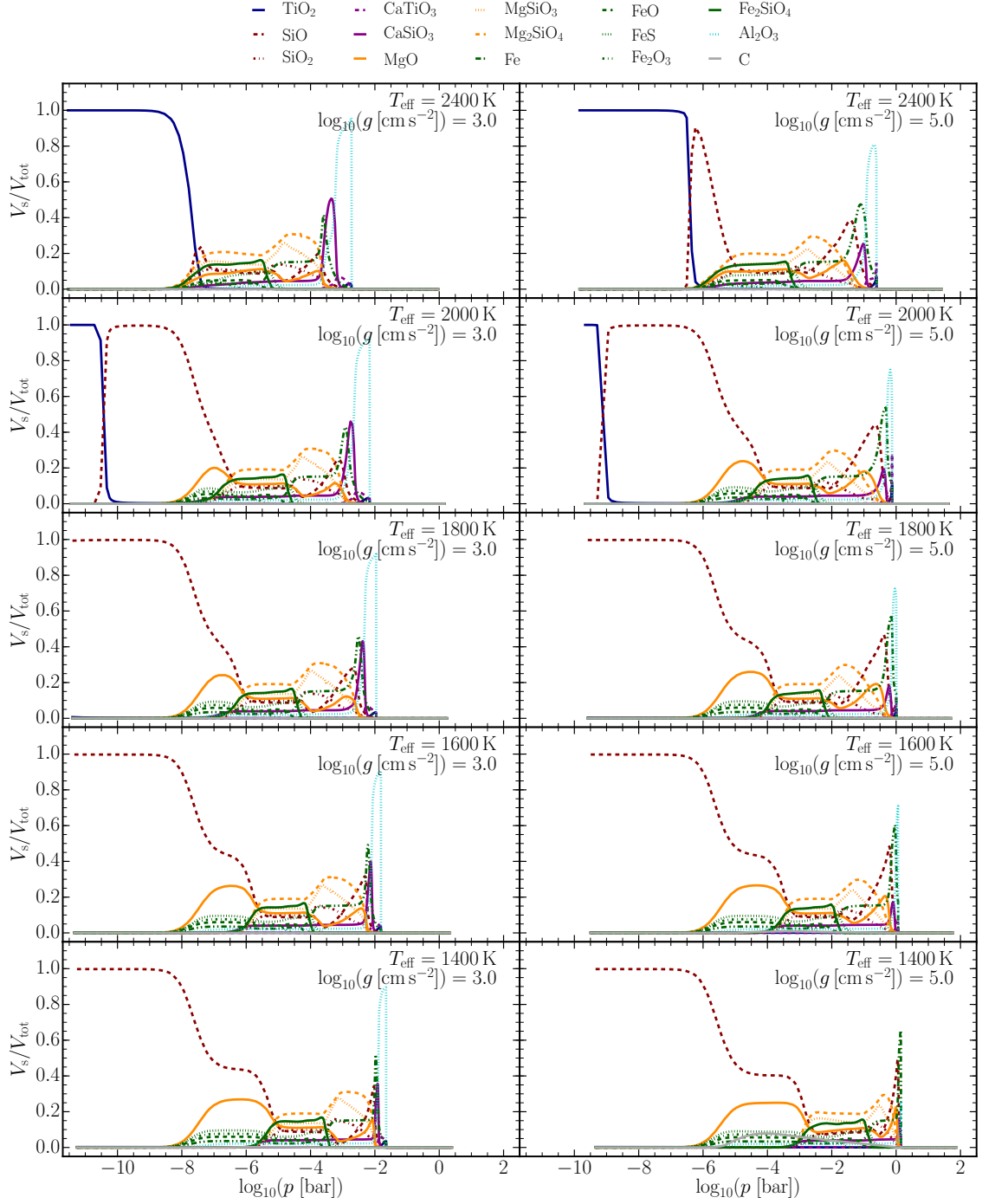
151

Figure B.4: C/O in the gas phase, without coagulation (blue) and with coagulation (black). Effective temperatures from top to bottom are: $T_{\rm eff}$ = 2400, 2000, 1800, 1600, 1400 K. Two surface gravities are shown: $\log_{10}(g\,[{\rm cm\,s}^{-2}])$ = 3.0 (**Left**), and $\log_{10}(g\,[{\rm cm\,s}^{-2}])$ = 5.0 (**Right**)

Figure B.5: Material composition of cloud particles expressed as volume fractions V_s/V_{tot} for each species s. Effective temperatures from top to bottom are: T_{eff} = 2400, 2000, 1800, 1600, 1400 K. Two surface gravities are shown: $\log_{10}(g\,[\text{cm}\,\text{s}^{-2}])$ = 3.0 (**Left**), and $\log_{10}(g\,[\text{cm}\,\text{s}^{-2}])$ = 5.0 (**Right**)
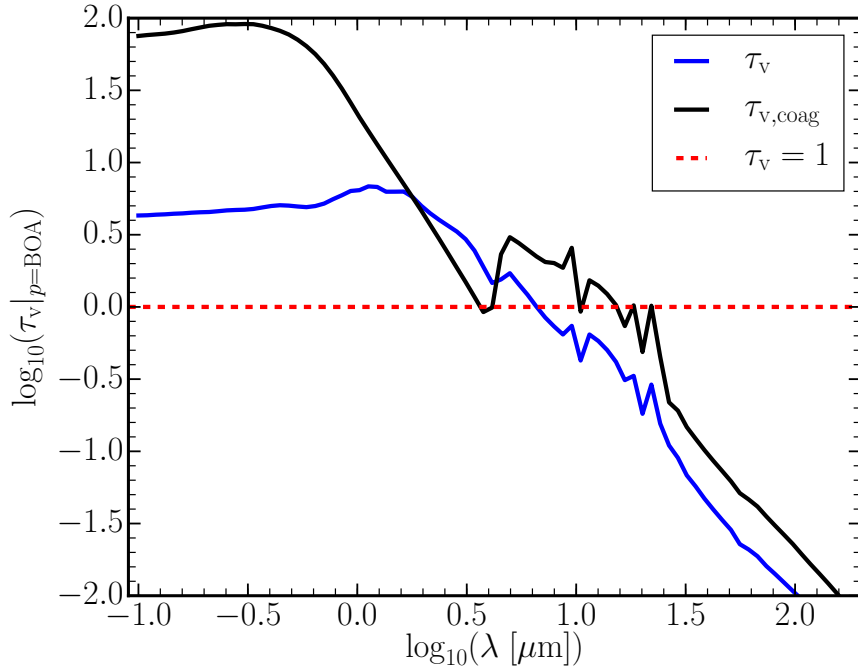
Figure B.6: For $T_{\text{eff}} = 1400\,\text{K}$, $\log_{10}(g\,[\text{cm s}^{-2}]) = 3.0$, the optical depth of clouds vertically integrated to the bottom of the atmosphere (BOA): $\tau_{\text{v}}(\lambda)|_{p=\text{BOA}}$.
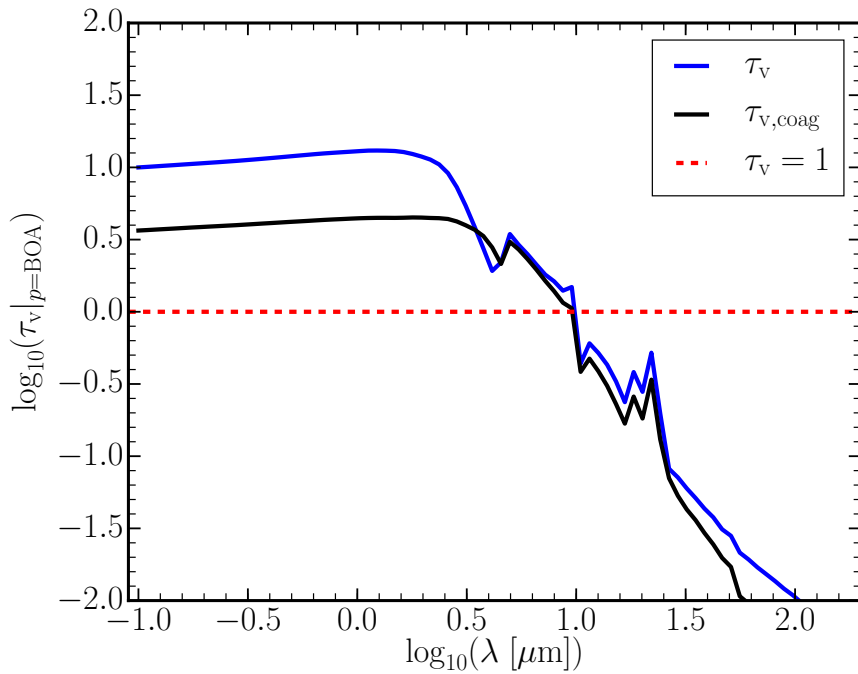
Figure B.7: For $T_{\text{eff}} = 1400\,\text{K}$, $\log_{10}(g\,[\text{cm s}^{-2}]) = 5.0$, the optical depth of clouds vertically integrated to the bottom of the atmosphere (BOA): $\tau_{\text{v}}(\lambda)|_{p=\text{BOA}}$.

Bibliography

Ackerman, A. S. & Marley, M. S. 2001, ApJ, 556, 872

Adams, D., Gao, P., de Pater, I., & Morley, C. V. 2019, ApJ, 874, 61

Adibekyan, V. 2019, Geosciences, 9, 105

Allard, F., Hauschildt, P. H., Alexander, D. R., Tamanai, A., & Schweitzer, A. 2001, ApJ, 556, 357

Alonso, R. 2018, in Handbook of Exoplanets, ed. H. J. Deeg & J. A. Belmonte (Springer International Publishing AG, part of Springer Nature), 40

Armstrong, D. J., de Mooij, E., Barstow, J., et al. 2016, Nature Astronomy, 1, 0004

Asplund, M., Grevesse, N., Sauval, A. J., & Scott, P. 2009, ARA&A, 47, 481

Bailer-Jones, C. 2002, A&A, 389, 963

Bakos, G., Noyes, R. W., Kovács, G., et al. 2004, PASP, 116, 266

Barman, T. S., Konopacky, Q. M., Macintosh, B., & Marois, C. 2015, ApJ, 804, 61

Barstow, J. K. 2020, MNRAS, 497, 4183

Barstow, J. K. & Heng, K. 2020, Space Sci. Rev., 216, 82

Barth, P., Helling, Ch., Stüeken, E., et al. 2021, MNRAS, 502, 6201

Baxter, C., Désert, J.-M., Parmentier, V., et al. 2020, A&A, 639, A36

Bean, J. L., Stevenson, K. B., Batalha, N. M., et al. 2018, PASP, 130, 114402

Beatty, T. G., Marley, M. S., Gaudi, B. S., et al. 2019, AJ, 158, 166

Begemann, B., Dorschner, J., Henning, T., et al. 1997, ApJ, 476, 199

Beichman, C., Benneke, B., Knutson, H., et al. 2014, PASP, 126, 1134

Benneke, B., Knutson, H. A., Lothringer, J., et al. 2019, Nature Astronomy, 3, 813

Benneke, B. & Seager, S. 2012, ApJ, 753

Benneke, B., Wong, I., Piaulet, C., et al. 2019, ApJ, 887, L14

Beuzit, J.-L., Feldt, M., Dohlen, K., et al. 2008, in SPIE Conference Series, Vol. 7014, Ground-based and Airborne Instrumentation for Astronomy II, ed. I. S. McLean & M. M. Casali, 701418

Bibliography

Biller, B. A., Vos, J., Bonavita, M., et al. 2015, ApJ, 813, L23

Birnstiel, T., Dullemond, C., & Brauer, F. 2010, A&A, 513, A79

Birnstiel, T., Fang, M., & Johansen, A. 2016, Space Sci. Rev., 205, 41

Birnstiel, T., Klahr, H., & Ercolano, B. 2012, A&A, 539, A148

Birnstiel, T., Ormel, C., & Dullemond, C. 2011, A&A, 525, A11

Blecic, J., Harrington, J., Madhusudhan, N., et al. 2014, ApJ, 781, 116

Blum, J. & Wurm, G. 2000, Icarus, 143, 138

Blum, J. & Wurm, G. 2008, ARA&A, 46, 21

Bohren, C. & Huffman, D. 1983, Absorption and scattering of light by small particles (Wiley)

Borucki, W. J., Koch, D., Basri, G., et al. 2010, Science, 327, 977

Boss, A. P., Basri, G., Kumar, S. S., et al. 2003, in Brown Dwarfs, ed. E. Martín, Vol. 211, 529

Brahm, R., Espinoza, N., Jordán, A., et al. 2018, MNRAS, 477, 2572

Brauer, F., Dullemond, C., & Henning, T. 2008, A&A, 480, 859

Broeg, C., Fortier, A., Ehrenreich, D., et al. 2013, in European Physical Journal Web of Conferences, Vol. 47, European Physical Journal Web of Conferences, 3005

Bruggeman, D. 1935, Annalen der Physik, 416, 636

Budaj, J., Kocifaj, M., Salmeron, R., & Hubeny, I. 2015, MNRAS, 454, 2

Burningham, B., Faherty, J. K., Gonzales, E. C., et al. 2021, MNRAS, 506, 1944

Caldas, A., Leconte, J., Selsis, F., et al. 2019, A&A, 623, A161

Carone, L., Baeyens, R., Mollière, P., et al. 2020, MNRAS, 496, 3582

Carone, L., Mollière, P., Zhou, Y., et al. 2021, A&A, 646, A168

Carrión-González, Ó., García Muñoz, A., Santos, N. C., et al. 2021, A&A, 651, A7

Catling, D. C. & Kasting, J. F. 2017, Atmospheric Evolution on Inhabited and Lifeless Worlds (Cambridge University Press)

Chabrier, G., Baraffe, I., Allard, F., & Hauschildt, P. 2000, ApJ, 542, 464

Chabrier, G., Johansen, A., Janson, M., & Rafikov, R. 2014, in Protostars and Planets VI, ed. H. Beuther, R. S. Klessen, C. P. Dullemond, & T. Henning, 619

Charbonneau, D., Brown, T., Noyes, R., & Gilliland, R. 2002, ApJ, 568, 377

Chen, J. & Kipping, D. 2017, ApJ, 834, 17

Cooper, C. S., Sudarsky, D., Milsom, J. A., Lunine, J. I., & Burrows, A. 2003, ApJ, 586, 1320

Crossfield, I. J., Barman, T., Hansen, B. M., & Howard, A. W. 2013, A&A, 559, A33

Crossfield, I. J. M., Biller, B., Schlieder, J. E., et al. 2014, Nature, 505, 654

Cubillos, P. E., Keating, D., Cowan, N. B., et al. 2021, ApJ, 915, 45

Dawson, R. I. & Johnson, J. A. 2018, ARA&A, 56, 175

Dehn, M. 2007, PhD thesis, Universität Hamburg, Von-Melle-Park 3, 20146 Hamburg

Deming, D., Wilkins, A., McCullough, P., et al. 2013, ApJ, 774, 95

Desidera, S., Chauvin, G., Bonavita, M., et al. 2021, A&A, 651, A70

Dominik, C., Gail, H. P., & Sedlmayr, E. 1989, A&A, 223, 227

Dominik, C. & Tielens, A. 1997, ApJ, 480, 647

Dominik, M. 2010, General Relativity and Gravitation, 42, 2075

Dorschner, J., Begemann, B., Henning, T., Jaeger, C., & Mutschke, H. 1995, A&A, 300, 503

Draine, B. T. 2003, ARA&A, 41, 241

Draine, B. T. & Flatau, P. J. 1994, J. Opt. Soc. Am. A, 11, 1491

Dullemond, C. & Dominik, C. 2005, A&A, 434, 971

Endres, S. C., Ciacchi, L. C., & Mädler, L. 2021, Journal of Aerosol Science, 153, 105719

Fischer, D. A., Howard, A. W., Laughlin, G. P., et al. 2014, in Protostars and Planets VI, ed. H. Beuther, R. S. Klessen, C. P. Dullemond, & T. Henning, 715

Fistler, M., Kerstein, A., Wunsch, S., & Oevermann, M. 2020, PhysRev Fluids, 5, 1243039

Follert, R., Dorn, R., Oliva, E., et al. 2014, in Proc. SPIE, Vol. 9147, Ground-based and Airborne Instrumentation for Astronomy V, 914719

Fortney, J. J. 2005, MNRAS, 364, 649

Fortney, J. J., Shabram, M., Showman, A. P., et al. 2010, ApJ, 709, 1396

Fraine, J., Mayorga, L. C., Stevenson, K. B., et al. 2021, AJ, 161, 269

Freytag, B., Allard, F., Ludwig, H.-G., Homeier, D., & Steffen, M. 2010, A&A, 513, A19

Gail, H.-P. & Sedlmayr, E. 1988, A&A, 206, 153

Gail, H.-P., Zhukovska, S. V., Hoppe, P., & Trieloff, M. 2009, The Astrophysical Journal, 698, 1136

Gao, P. & Benneke, B. 2018, ApJ, 863, 165

Gao, P., Marley, M. S., & Ackerman, A. S. 2018, ApJ, 855, 86

Gao, P. & Powell, D. 2021, ApJ, 918, L7

Gao, P., Thorngren, D. P., Lee, E. K., et al. 2020, Nature Astronomy, 4, 951

Gao, P., Wakeford, H. R., Moran, S. E., & Parmentier, V. 2021, JGR (Planets), 126, e06655

Gardner, J. P., Mather, J. C., Clampin, M., et al. 2006, Space Sci. Rev., 123, 485

Garhart, E., Deming, D., Mandell, A., et al. 2020, AJ, 159, 137

Gaudi, B. S., Seager, S., Mennesson, B., et al. 2020, arXiv e-prints, arXiv:2001.06683

Gauger, A., Gail, H., & Sedlmayr, E. 1990, A&A, 235, 345

Gillon, M., Triaud, A. H. M. J., Fortney, J. J., et al. 2012, A&A, 542, A4

Goeres, A. 1996, in Astronomical Society of the Pacific Conference Series, Vol. 96, Hydrogen Deficient Stars, ed. C. S. Jeffery & U. Heber, 69

Greene, T. P., Line, M. R., Montero, C., et al. 2016, ApJ, 817, 17

Greenwood, A., Kamp, I., Waters, L., Woitke, P., & Thi, W. F. 2019, A&A, 626, A6

Grevesse, N., Noels, A., & Sauval, A. 1993, A&A, 271, 587

Griffith, C. A. 2014, Philosophical Transactions of the Royal Society of London Series A, 372, 20130086

Güttler, C., Blum, J., Zsom, A., Ormel, C., & Dullemond, C. 2010, A&A, 513, A56

Hales, T. 2005, Annals of Mathematics, 162, 1065

Hanaor, D. A. H. & Sorrell, C. C. 2010, Journal of Materials Science, 46, 855

Hartmann, L., Calvet, N., Gullbring, E., & D'Alessio, P. 1998, ApJ, 495, 385

Hauschildt, P. & Baron, E. 1999, Journal of Computational and Applied Mathematics, 109, 41

Hellier, C., Anderson, D. R., Collier Cameron, A., et al. 2011, A&A, 535, L7

Helling, C., Woitke, P., Rimmer, P. B., et al. 2014, Life, 4, 142

Helling, Ch. 2019, Annual Review of Earth and Planetary Sciences, 47, 583

Helling, Ch., Ackerman, A., Allard, F., et al. 2008a, MNRAS, 391, 1854

Helling, Ch. & Casewell, S. 2014, A&A Rev., 22, 80

Helling, Ch., Dehn, M., Woitke, P., & Hauschildt, P. 2008b, ApJ, 675, L105

Helling, Ch. & Fomins, A. 2013, Phil. Trans. R. Soc. London, Ser. A, 371, 20110581

Helling, Ch., Gourbin, P., Woitke, P., & Parmentier, V. 2019, A&A, 626, A133

Helling, Ch.., Iro, N., Corrales, L., et al. 2019, A&A, 631, A79

Helling, Ch., Jardine, M., & Mokler, F. 2011, ApJ, 737, 38

Helling, Ch., Kawashima, Y., Graham, V., et al. 2020, A&A, 641, A178

Helling, Ch., Klein, R., Woitke, P., Nowak, U., & Sedlmayr, E. 2004a, A&A, 423, 657

Helling, Ch., Klein, R., Woitke, P., Nowak, U., & Sedlmayr, E. 2004b, A&A, 423, 657

Helling, Ch., Lee, E., Dobbs-Dixon, I., et al. 2016, MNRAS, 460, 855

Helling, Ch., Lewis, D., Samra, D., et al. 2021, A&A, 649, A44

Helling, Ch., Oevermann, M., Lüttke, M., Klein, R., & Sedlmayr, E. 2001, A&A, 376, 194

Helling, Ch. & Rietmeijer, F. 2009, International Journal of Astrobiology, 8, 3

Helling, Ch., Thi, W. F., Woitke, P., & Fridlund, M. 2006, A&A, 451, L9

Helling, Ch. & Woitke, P. 2006, A&A, 455, 325

Helling, Ch., Woitke, P., & Thi, W.-F. 2008c, A&A, 485, 547

Heng, K. & Demory, B.-O. 2013, ApJ, 777, 100

Henning, T., Begemann, B., Mutschke, H., & Dorschner, J. 1995, A&AS, 112, 143

Hiranaka, K., Cruz, K. L., Douglas, S. T., Marley, M. S., & Baldassare, V. F. 2016, ApJ, 830, 96

Hoeijmakers, H. J., Seidel, J. V., Pino, L., et al. 2020, A&A, 641, A123

Hörst, S. M. 2017, JGR (Planets), 122, 432

Irwin, P. G. J., Parmentier, V., Taylor, J., et al. 2020, MNRAS, 493, 106

Jiménez, J., Wray, A. A., Saffman, P. G., & Rogallo, R. S. 1993, Journal of Fluid Mechanics, 255, 65

Johnson, S. A., Penny, M., Gaudi, B. S., et al. 2020, AJ, 160, 123

Jontof-Hutter, D., Rowe, J. F., Lissauer, J. J., Fabrycky, D. C., & Ford, E. B. 2015, Nature, 522, 321 EP

Juncher, D., Jørgensen, U. G., & Helling, Ch. 2017, A&A, 608, A70

Jung, S.-C. & Imaishi, N. 2001, Korean Journal of Chemical Engineering, 18, 867

Kataoka, A., Tanaka, H., Okuzumi, S., & Wada, K. 2013, A&A, 557, L4

Kataria, T., Showman, A. P., Fortney, J. J., et al. 2015, ApJ, 801, 86

Kawashima, Y. & Ikoma, M. 2018, ApJ, 853, 7

Keating, D. & Cowan, N. B. 2022, MNRAS, 509, 289

Kerker, M. 1969, in Physical Chemistry: A Series of Monographs, Vol. 16, The Scattering of Light and Other Electromagnetic Radiation, ed. M. Kerker (Academic Press), 27–96

Khare, B. N., Sagan, C., Thompson, W. R., et al. 1984, Advances in Space Research, 4, 59

Kirkpatrick, J. D. 2005, ARA&A, 43, 195

Kitzmann, D. & Heng, K. 2018, MNRAS, 475, 94

Klarmann, L., Ormel, C., & Dominik, C. 2018, A&A, 618, L1

Knutson, H. A., Charbonneau, D., Cowan, N. B., et al. 2009, ApJ, 690, 822

Köhn, C., Helling, Ch., Bødker Enghoff, M., et al. 2021, A&A, 654, A120

Kok, J. F., Parteli, E. J. R., Michaels, T. I., & Karam, D. B. 2012, Reports on Progress in Physics, 75, 106901

Kolmogorov, A. 1941, Akademiia Nauk SSSR Doklady, 30, 301

Kreidberg, L., Bean, J. L., Désert, J. M., et al. 2014, Nature, 505, 69

Kreidberg, L., Line, M. R., Thorngren, D., Morley, C. V., & Stevenson, K. B. 2018, ApJ, 858, L6

Krijt, S., Ormel, C., Dominik, C., & Tielens, A. 2016, A&A, 586, A20

Krueger, D., Woitke, P., & Sedlmayr, E. 1995, A&AS, 113, 593

Lacy, B. I. & Burrows, A. 2020a, ApJ, 905, 131

Lacy, B. I. & Burrows, A. 2020b, ApJ, 904, 25

Langlois, M., Gratton, R., Lagrange, A. M., et al. 2021, A&A, 651, A71

Lavvas, P. & Koskinen, T. 2017, ApJ, 847, 32

Lavvas, P., Lellouch, E., Strobel, D. F., et al. 2021, Nature Astronomy, 5, 289

Lecavelier Des Etangs, A., Pont, F., Vidal-Madjar, A., & Sing, D. 2008, A&A, 481, L83

Lee, E., Helling, Ch., Giles, H., & Bromley, S. 2015a, A&A, 575, A11

Lee, G., Dobbs-Dixon, I., Helling, Ch., Bognar, K., & Woitke, P. 2016, A&A, 594, A48

Lee, G., Helling, Ch., Dobbs-Dixon, I., & Juncher, D. 2015b, A&A, 580, A12

Lee, G., Helling, Ch., Giles, H., & Bromley, S. 2015c, A&A, 575, A11

Lewis, N. K., Wakeford, H. R., MacDonald, R. J., et al. 2020, ApJ, 902, L19

Line, M. R. & Parmentier, V. 2016, ApJ, 820, 78

Looyenga, H. 1965, Physica, 31, 401

Lothringer, J. D. & Casewell, S. L. 2020, ApJ, 905, 163

Lothringer, J. D., Fu, G., Sing, D. K., & Barman, T. S. 2020, ApJ, 898, L14

Luna, J. L. & Morley, C. V. 2021, ApJ, 920, 146

Lunine, J. I., Hubbard, W. B., & Marley, M. S. 1986, ApJ, 310, 238

MacDonald, R. J., Goyal, J. M., & Lewis, N. K. 2020, ApJ, 893, L43

MacDonald, R. J. & Lewis, N. K. 2021, arXiv e-prints, arXiv:2111.05862

MacDonald, R. J. & Madhusudhan, N. 2017, MNRAS, 469, 1979

Macintosh, B. A., Graham, J. R., Palmer, D. W., et al. 2008, in SPIE Conference Series, Vol. 7015, Adaptive Optics Systems, ed. N. Hubin, C. E. Max, & P. L. Wizinowich, 701518

Madhusudhan, N., Agúndez, M., Moses, J. I., & Hu, Y. 2016, Space Sci. Rev., 205, 285

Madhusudhan, N., Amin, M. A., & Kennedy, G. M. 2014, ApJ, 794, L12

Madhusudhan, N., Burrows, A., & Currie, T. 2011, ApJ, 737, 34

Madhusudhan, N. & Seager, S. 2009, ApJ, 707, 24

Madhusudhan, N. & Seager, S. 2010, ApJ, 725, 261

Mansfield, M., Bean, J., Line, M., et al. 2018, AJ, 156, 10

Marcy, G., Butler, R. P., Fischer, D., et al. 2005, Progress of Theoretical Physics Supplement, 158, 24

Marley, M. S., Ackerman, A. S., Cuzzi, J. N., & Kitzmann, D. 2013, in Comparative Climatology of Terrestrial Planets, ed. S. J. Mackwell, A. A. Simon-Miller, J. W. Harder, & M. A. Bullock (University of Arizona Press), 367–392

Marley, M. S., Gelino, C., Stephens, D., Lunine, J. I., & Freedman, R. 1999, ApJ, 513, 879

Masuda, K. 2015, ApJ, 805, 28

Mayor, M. & Queloz, D. 1995, Nature, 378, 355

McCullough, P. R., Crouzet, N., Deming, D., & Madhusudhan, N. 2014, ApJ, 791, 55

Mendonça, J. M., Tsai, S.-m., Malik, M., Grimm, S. L., & Heng, K. 2018, ApJ, 869, 107

Ménétrey, M., Markovits, A., Minot, C., & Pacchioni, G. 2004, The Journal of Physical Chemistry B, 108, 12858

Mie, G. 1908, Annalen der Physik, 330, 377

Min, M. 2015, in European Physical Journal Web of Conferences, Vol. 102, European Physical Journal Web of Conferences, 5

Min, M., Hovenier, J., & de Koter, A. 2003, A&A, 404, 35

Bibliography

Min, M., Hovenier, J., & de Koter, A. 2005, A&A, 432, 909

Min, M., Hovenier, J., Waters, L., & de Koter, A. 2008, A&A, 489, 135

Min, M., Ormel, C. W., Chubb, K., Helling, Ch., & Kawashima, Y. 2020, A&A, 642, A28

Molaverdikhani, K., Helling, Ch., Lew, B. W. P., et al. 2020, A&A, 635, A31

Mollière, P., Wardenier, J., van Boekel, R., et al. 2019, A&A, 627, A67

Morello, G., Danielski, C., Dickens, D., Tremblin, P., & Lagage, P. O. 2019, AJ, 157, 205

Morfill, G. 1985, in Birth and Infancy of Stars, 693–792

Morley, C. V., Fortney, J. J., Kempton, E. M. R., et al. 2013, ApJ, 775, 33

Morley, C. V., Fortney, J. J., Marley, M. S., et al. 2012, ApJ, 756, 172

Morley, C. V., Knutson, H., Line, M., et al. 2017, AJ, 153, 86

Mugnai, L. V., Pascale, E., Edwards, B., Papageorgiou, A., & Sarkar, S. 2020, Experimental Astronomy, 50, 303

Naud, M.-E., Artigau, É., Malo, L., et al. 2014, ApJ, 787, 5

Öberg, K. I., Murray-Clay, R., & Bergin, E. A. 2011, ApJ, 743, L16

Ohno, K. & Kawashima, Y. 2020, ApJ, 895, L47

Ohno, K. & Okuzumi, S. 2017, ApJ, 835, 261

Ohno, K. & Okuzumi, S. 2018, ApJ, 859, 34

Ohno, K., Okuzumi, S., & Tazaki, R. 2020, ApJ, 891, 131

Ohno, K., Zhang, X., Tazaki, R., & Okuzumi, S. 2021, ApJ, 912, 37

Okuzumi, S., Tanaka, H., Kobayashi, H., & Wada, K. 2012, ApJ, 752, 106

Ormel, C. & Cuzzi, J. 2007, A&A, 466, 413

Ormel, C., Min, M., Tielens, A., Dominik, C., & Paszun, D. 2011, A&A, 532, A43

Ormel, C., Paszun, D., Dominik, C., & Tielens, A. 2009, A&A, 502, 845

Ormel, C. W. & Min, M. 2019, A&A, 622, A121

Ossenkopf, V. 1993, A&A, 280, 617

Pál, A., Bakos, G., Torres, G., et al. 2008, ApJ, 680, 1450

Palik, E. 1985, Handbook of optical constants of solids (Academic Press)

Parmentier, V., Fortney, J. J., Showman, A. P., Morley, C., & Marley, M. S. 2016, ApJ, 828, 22

Parmentier, V., Line, M., Bean, J., et al. 2018, A&A, 617, A110

Parmentier, V., Showman, A. P., & Fortney, J. J. 2021, MNRAS, 501, 78

Patapis, P., Nasedkin, E., Cugno, G., et al. 2022, A&A, 658, A72

Pinhas, A. & Madhusudhan, N. 2017, MNRAS, 471, 4355

Pinhas, A., Madhusudhan, N., Gandhi, S., & MacDonald, R. 2019, MNRAS, 482, 1485

Pollacco, D. L., Skillen, I., Collier Cameron, A., et al. 2006, PASP, 118, 1407

Pont, F., Sing, D. K., Gibson, N. P., et al. 2013, MNRAS, 432, 2917

Posch, T., Kerschbaum, F., Fabian, D., et al. 2003, ApJS, 149, 437

Powell, D., Louden, T., Kreidberg, L., et al. 2019, ApJ, 887, 170

Powell, D., Zhang, X., Gao, P., & Parmentier, V. 2018, ApJ, 860, 18

Purcell, E. M. & Pennypacker, C. R. 1973, ApJ, 186, 705

Randall, K., Ewing, E. T., Marr, L. C., Jimenez, J. L., & Bourouiba, L. 2021, Interface Focus, 11

Rappaport, S., Levine, A., Chiang, E., et al. 2012, ApJ, 752, 1

Rauer, H., Catala, C., Aerts, C., et al. 2014, Experimental Astronomy, 38, 249

Ricker, G. R., Winn, J. N., Vanderspek, R., et al. 2015, Journal of Astronomical Telescopes, Instruments, and Systems, 1, 14003

Rossow, W. B. 1978, Icarus, 36, 1

Rupprecht, G., Pepe, F., Mayor, M., et al. 2004, in SPIE Conference Series, Vol. 5492, Ground-based Instrumentation for Astronomy, ed. A. F. M. Moorwood & M. Iye, 148–159

Samra, D., Helling, Ch., & Birnstiel, T. 2022, arXiv e-prints, arXiv:2203.07461

Sanghavi, S., West, R., & Jiang, J. 2021, ApJ, 907, 30

Sato, T., Okuzumi, S., & Ida, S. 2016, A&A, 589, A15

Schaaf, S. A. 1963, Handbuch der Physik, 3, 591

Schmidt, H., Oevermann, M., Münch, M., & Klein, R. 2006, in European Conference on Computational Fluid Dynamics, ed. P. Wesseling, E. Onate, & J. Périau, 1

Schneider, N. & Wurm, G. 2021, A&A, 655, A50

Scholz, A., Moore, K., Jayawardhana, R., et al. 2018, ApJ, 859, 153

Seager, S. 2010, Exoplanet Atmospheres: Physical Processes, Princeton Series in Astrophysics (Princeton University Press)

Seager, S. & Sasselov, D. D. 2000, ApJ, 537, 916

Sedaghati, E., Boffin, H., MacDonald, R., et al. 2017, Nature, 549, 238

Shakura, N. & Sunyaev, R. 1976, MNRAS, 175, 613

Showman, A. P., Fortney, J. J., Lian, Y., et al. 2009, ApJ, 699, 564

Sing, D. K., Fortney, J. J., Nikolov, N., et al. 2016, Nature, 529, 59

Siverd, R., Beatty, T., Pepper, J., et al. 2012, ApJ, 761, 123

Sood, S. & Gouma, P. 2013, Nanomaterials and Energy, 2, 82

Spergel, D., Gehrels, N., Baltay, C., et al. 2015, arXiv e-prints, arXiv:1503.03757

Spring, E. F., Birkby, J. L., Pino, L., et al. 2022, arXiv e-prints, arXiv:2201.03600

Sreejith, A. G., Fossati, L., Fleming, B. T., et al. 2019, Journal of Astronomical Telescopes, Instruments, and Systems, 5, 018004

Stam, D. M., Hovenier, J. W., & Waters, L. B. F. M. 2004, A&A, 428, 663

Stevenson, K. B., Désert, J.-M., Line, M. R., et al. 2014, Science, 346, 838

Stevenson, K. B., Line, M. R., Bean, J. L., et al. 2017, AJ, 153, 68

Stolker, T., Min, M., Stam, D. M., et al. 2017, A&A, 607, A42

Suto, H., Sogawa, H., Tachibana, S., et al. 2006, MNRAS, 370, 1599

Taylor, J., Parmentier, V., Line, M. R., et al. 2020, arXiv e-prints, arXiv:2009.12411

The LUVOIR Team. 2019, arXiv e-prints, arXiv:1912.06219

Tinetti, G., Drossart, P., Eccleston, P., et al. 2018, Experimental Astronomy, 46, 135

Toon, O. B., Turco, R., Hamill, P., Kiang, C., & Whitten, R. 1979, Journal of Atmospheric Sciences, 36, 718

Tsuji, T., Ohnaka, K., & Aoki, W. 1996a, A&A, 305, L1

Tsuji, T., Ohnaka, K., Aoki, W., & Nakajima, T. 1996b, A&A, 308, L29

Turco, R., Hamill, P., Toon, O., Whitten, R., & Kiang, C. 1979, Journal of Atmospheric Sciences, 36, 699

Van Eylen, V., Kjeldsen, H., Christensen-Dalsgaard, J., & Aerts, C. 2012, Astronomische Nachrichten, 333, 1088

Venot, O., Drummond, B., Miguel, Y., et al. 2018, Experimental Astronomy, 46, 101

Venot, O., Parmentier, V., Blecic, J., et al. 2020, ApJ, 890, 176

Voelk, H., Jones, F., Morfill, G., & Roeser, S. 1980, A&A, 85, 316

Vos, J. M., Biller, B. A., Allers, K. N., et al. 2020, AJ, 160, 38

Wada, K., Tanaka, H., Suyama, T., Kimura, H., & Yamamoto, T. 2008, ApJ, 677, 1296

Wada, K., Tanaka, H., Suyama, T., Kimura, H., & Yamamoto, T. 2009, ApJ, 702, 1490

Wakeford, H., Sing, D., Stevenson, K., et al. 2020, AJ, 159, 204

Wakeford, H. R. & Sing, D. K. 2015, A&A, 573

Wakeford, H. R., Visscher, C., Lewis, N. K., et al. 2017, MNRAS, 464, 4247

Warhaft, Z. 2000, Annual Review of Fluid Mechanics, 32, 203

Welbanks, L. & Madhusudhan, N. 2021, ApJ, 913, 114

Welbanks, L. & Madhusudhan, N. 2021, arXiv e-prints, arXiv:2112.09125

Witte, S., Helling, Ch., Barman, T., Heidrich, N., & Hauschildt, P. 2011, A&A, 529, A44

Witte, S., Helling, Ch., & Hauschildt, P. 2009, A&A, 506, 1367

Woitke, P. & Helling, Ch. 2003, A&A, 399, 297

Woitke, P. & Helling, Ch. 2004, A&A, 414, 335

Woitke, P., Helling, Ch., & Gunn, O. 2020, A&A, 634, A23

Woitke, P., Min, M., Pinte, C., et al. 2016, A&A, 586, A103

Wolf, S. & Voshchinnikov, N. 2004, Computer Physics Communications, 162, 113

Wolszczan, A. & Frail, D. A. 1992, Nature, 355, 145

Wong, I., Shporer, A., Daylan, T., et al. 2020, AJ, 160, 155

Wright, G. S., Rieke, G. H., Colina, L., et al. 2004, in SPIE Conference Series, Vol. 5487, Optical, Infrared, and Millimeter Space Telescopes, ed. J. C. Mather, 653–663

Zeidler, S., Posch, T., & Mutschke, H. 2013, A&A, 553, A81

Zeidler, S., Posch, T., Mutschke, H., Richter, H., & Wehrhan, O. 2011, A&A, 526, A68

Zhang, M., Chachan, Y., Kempton, E. M. R., & Knutson, H. A. 2019, PASP, 131, 34501

Zhu, W. & Dong, S. 2021, ARA&A, 59, 291

"Poo-tee-weet?"